

Doctoral Dissertation
Doctoral Program in Metrology (31st cycle)

^{171}Yb optical frequency standards towards the redefinition of the second

Filippo Bregolin
* * * * * *

Supervisors
Dr. Davide Calonico, INRIM
Prof. Hidetoshi Katori, The University of Tokyo and RIKEN

Doctoral Examination Committee:
Dr. Andrew D. Ludlow, Referee, NIST and University of Colorado
Dr. Ekkehard Peik, Referee, PTB

Politecnico di Torino
September 23, 2019

This thesis is licensed under a Creative Commons License, Attribution - Noncommercial-NoDerivative Works 4.0 International: see www.creativecommons.org. The text may be reproduced for non-commercial purposes, provided that credit is given to the original author.

I hereby declare that, the contents and organisation of this dissertation constitute my own original work and does not compromise in any way the rights of third parties, including those relating to the security of personal data.

. . . . . .

Filippo Bregolin
Turin, September 23, 2019

Summary

The optical frequency standards clearly surpass in terms of accuracy and stability the microwave Cs primary standards, whose performance limits the realisation of the second as defined in the International System of Units (SI). In 2006 several atomic optical transitions have been recommended as secondary representations of the second, and recently a roadmap towards the redefinition of the SI second on an optical transition has been delineated defining requirements and targets.

Among the optical clocks realising a secondary representation of the second, lattice clocks based on neutral ^{171}Yb have demonstrated feasibility and performances competitive with the best frequency standards realised to date. Several research laboratories around the world develop such frequency standards, including metrology institutes in Japan, USA, Korea, China and Italy.

These frequency standards exploit an optical lattice to trap hundreds of neutral atoms, and probe the narrow $^1S_0$-$^3P_0$ clock transition with a ultra-stable laser at the frequency of 518 THz.

The work presented in this thesis has been carried out with ^{171}Yb lattice frequency standards developed at the National Metrology Institute (NMI) of Italy, the Istituto Nazionale di Ricerca Metrologica (INRIM), and at the Institute of Physical and Chemical Research (RIKEN), in Japan, where I have been guest researcher.

The thesis discusses in details the evaluation of the systematic frequency shifts of the Yb clock transition frequency due to external perturbations. The INRIM Yb clock has been characterised with a fractional uncertainty of 2.8×10^{-17}, while the RIKEN Yb clock with an uncertainty of 6.0×10^{-18}.

Furthermore, several frequency measurements are presented: at INRIM we measure the absolute frequency of the ^{171}Yb clock transition directly against a Cs fountain, which is the Italian primary frequency standard employed for the steering of the Italian time scale. The frequency is evaluated with an uncertainty of 5.9×10^{-16}. We also perform an optical frequency ratio measurement of the Yb clock against the ^{87}Sr transportable lattice clock developed at the NMI of Germany (PTB), with a final fractional uncertainty of 2.8×10^{-16}. At RIKEN we measure the frequency ratio between the Yb clock and the RIKEN ^{87}Sr lattice clock with a fractional uncertainty of 1.1×10^{-17}.

Acknowledgements

I would like to thank my supervisors Davide Calonico and Hidetoshi Katori for giving me the opportunity to join their laboratory and for supporting my activity along these years. My greatest gratitude goes to Marco Pizzocaro, Nils Nemitz and Pierre Thoumany, who advised me continuously. Working closely with them has been inspiring and enriching. Many thanks goes to my fellow PhD colleagues Anna Tampellini, Piero Barbieri, Matteo Barbiero, Michele Gozzelino, Gianmaria Milani, Benjamin Rauf, Tadahiro Takahashi, Ryotatsu Yanagimoto, Ray Mizushima, Carolina Cardenas, Martina Gertosio and Haixiao Lin, for their continuous support, collaboration and sympathy. I want to thank my INRIM and RIKEN colleagues Elio Bertacco, Cecilia Clivati, Marco Tarallo, Salvatore Micalizio, Filippo Levi, Giacomo Cappellini, Giovanni Costanzo, Claudio Calosso, Alberto Mura, Noriaki Ohmae, Masao Takamoto and Ichiro Ushijima for their support, collaboration and helpful discussions. Finally I want to thank the PTB Sr transportable clock team and the NPL trasportable frequency comb team for the research collaboration.

Funding. This work has been funded by the "European Metrology Program for Innovation and Research" (EMPIR) project 15SIB03 OC18. This project has received funding from the EMPIR programme co-financed by the participating states and from the European Union's Horizon 2020 research and innovation programme.

Contents

Chapter 1

Introduction

The unit of time, the second, is among the base units in the International System of Units (SI). In the new revision of the SI [1] coming into force this year (2019) the second is defined

> by taking the fixed numerical value of the caesium frequency ν_{Cs}, the unperturbed ground-state hyperfine transition frequency of the caesium 133 atom, to be 9 192 631 770 when expressed in the unit Hz, which is equal to s^{-1}.

This means that

$$\nu_{\mathrm{Cs}} = 9\,192\,631\,770\ \mathrm{Hz} \quad \Longleftrightarrow \quad 1\ \mathrm{Hz} = \frac{\nu_{\mathrm{Cs}}}{9\,192\,631\,770}.$$

In other words, the definition fixes the absolute frequency of the microwave transition between the two hyperfine ground states of ^{133}Cs unperturbed by external fields.

This definition improves a previous version [2] elaborated in 1967 which states that the SI second is the *duration of 9 192 631 770 periods of the radiation corresponding to the transition between the two hyperfine levels of the ground state of the caesium 133 atom*. While the new definition does not differ from the previous one in substance, it improves the wording clearly introducing the ^{133}Cs ground state transition frequency as a universal constant, assumed not to vary in space and time, and specifying that the transition has to be unperturbed by any external field, such as the blackbody radiation.

The Cs frequency standards [3] realise the primary representation of the SI second, and are used to calibrate local and international time scales [4, 5] such as the International Atomic Time (TAI) [6], which is obtained steering the weighted average [7] of more than 400 atomic standards operated around the world to maintain agreement with the SI second definition. The steering correction is evaluated with several primary and secondary atomic standards. Secondary frequency standards

are based on atomic species different from Cs: they have been selected to provide a secondary representation of the second based on their characterized performances, shown to be competitive with the best Cs standards [8].

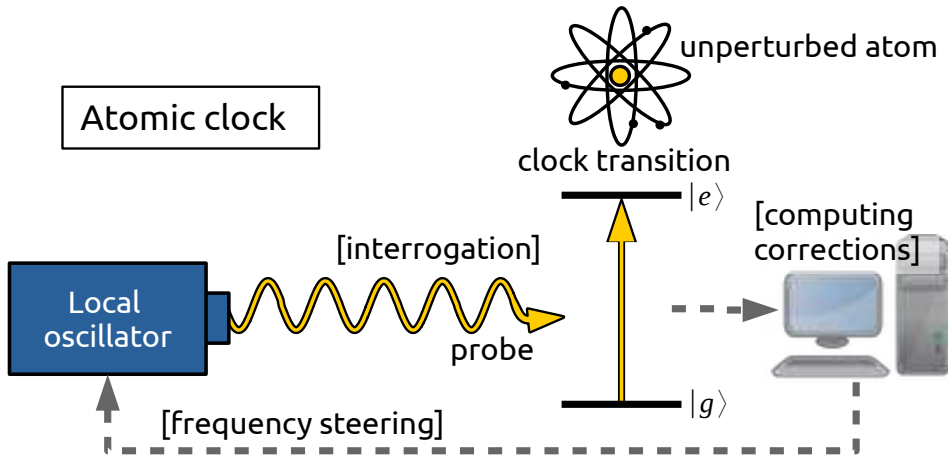

Figure 1.1: Scheme of the principle of operation of an atomic clock.

The basic principle of operation of an atomic frequency standard consists in tracing a local oscillator (LO) frequency to a reference, provided by the frequency of a specific atomic transition, called the clock transition. In other words the LO is characterized so that its frequency is known against the atomic reference, and differs from it by a constant factor. This is realised probing the frequency reference, in a process named clock interrogation, using a slave radiation with a fixed phase relation with the LO (see figure 1.1). In the interrogation process the probe radiation interacts with the atomic sample: if its frequency is reasonably close to the atomic reference atoms can be excited along the clock transition. A frequency correction is then applied to the LO according to the observed excitation and an active feedback control loop is implemented to maintain its frequency constant against the resonance frequency.

The best performing primary frequency standards are the Cs fountains [9–17], which are able to realise the SI second with a fractional uncertainty in the low 10^{-16} regime and show a white frequency noise instability in terms of Allan deviation of few parts in 10^{13} in 1 s averaging time. For example the German Cs fountain frequency standard contributes to TAI with a systematic uncertainty of 1.7×10^{-16}, and a statistical uncertainty of 9×10^{-17} in 35 days of measuring time [18].

The Cs clock performances are now greatly surpassed by the optical frequency standards, both in terms of accuracy and stability. Optical standards may be based on several different atomic species, such as ytterbium, strontium, mercury, aluminium or magnesium; they all share the common property of using a reference clock transition with frequency ν_0 in the optical domain, five orders of magnitude

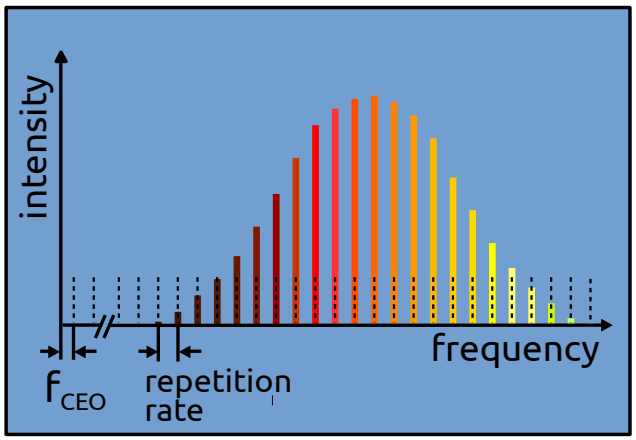

Figure 1.2: Frequency spectrum of an optical frequency comb.

larger than the microwave clock transition frequency of Cs-like standards. The higher reference frequency allows to improve the quality factor $Q \propto 1/\nu_0$, and thus the clock stability, triggering the interest in developing these frequency standards.

In order to be measured against the SI second the optical frequencies require to be down-converted in a regime where they can be compared with a primary standard. This is performed with an optical frequency comb [19], which is a mode-locked femtosecond laser whose frequency spectrum consists of a series of evenly spaced lines, or teeth, covering a wide frequency range (see fig. fig:comb). Since the frequency comb has optical spectral components in the infrared domain, it can be used to realise beat notes with infrared radiations directly. A single frequency doubling stage of the comb spectrum is typically sufficient to provide spectral components in the visible frequency range and realise beat notes with visible lasers.

The frequency comb spectrum is characterized by two quantities, the carrier-envelope offset frequency f_{CEO} initiating the sequence of teeth and the repetition rate f_{rep}, which defines the separation between two consecutive spectral lines. The frequency of the m^{th} tooth of the optical comb is then

$$f_{\mathrm{m}} = f_{\mathrm{CEO}} + m \times f_{\mathrm{rep}}, \tag{1.1}$$

where m is the integer corresponding to the mode number of the spectral line considered. The accuracy and stability of f_{CEO} and f_{rep}, which translate in the comb teeth frequency and linewidth, depends on the frequency reference provided to the comb. Tracing the comb frequency reference to a Cs primary standard allows to use the optical comb as a frequency bridge between the optical and the microwave domain, providing an optical signal referenced to the SI second.

There are two main designs of optical clocks: the single ion clocks and the neutral atoms lattice clocks. While both systems exploit laser cooling techniques

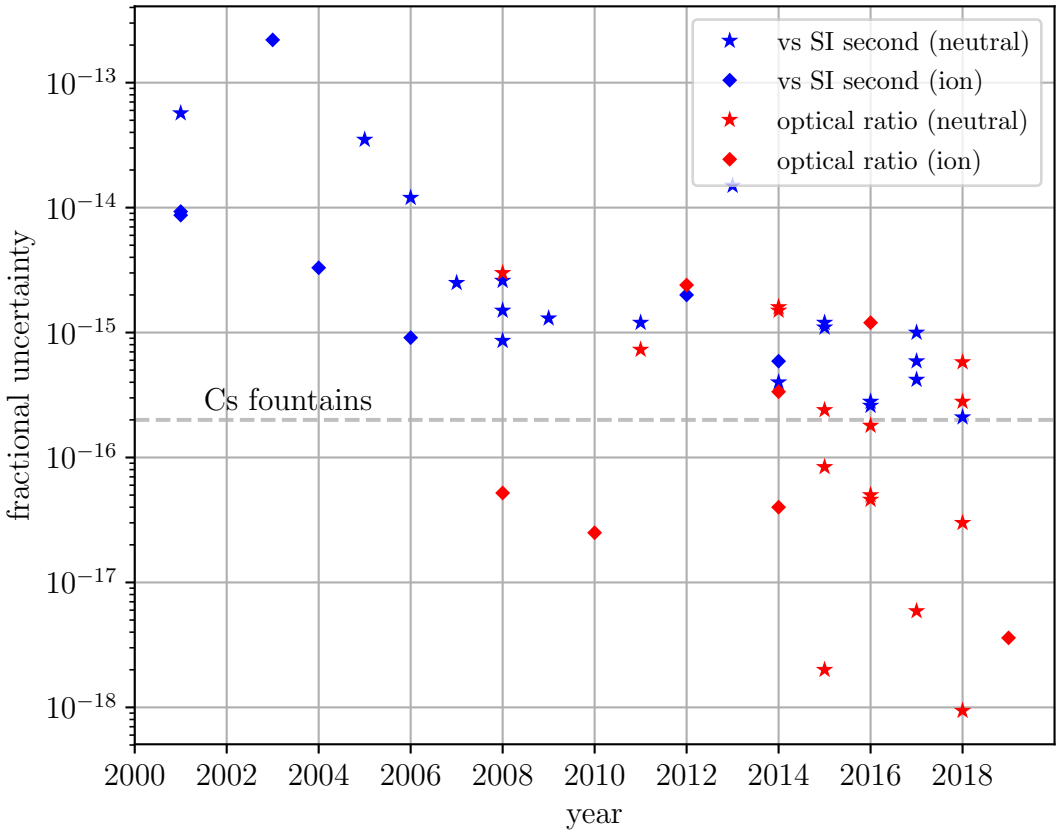

Figure 1.3: Overview of the fractional uncertainties reported for several optical frequency comparisons performed worldwide over time, either with lattice clocks based on neutral atoms (stars) or with ion clocks (diamonds). Both absolute frequency measurements performed against Cs fountains or through TAI (blue) and optical frequency ratio measurements (red) are reported. While the collected data is a subset of the results available in literature, it still succeeds to show the trend in the optical clock improvement over time, showing the ability of such clocks to realise frequency comparisons beyond the SI limit, provided by the uncertainty of the best Cs fountains (dashed line).

to cool atoms down to microkelvin temperatures [20, 21], the firsts implement a Paul trap to confine a single ion [22], while the seconds confine several hundreds of neutral atoms in the potential wells of an optical lattice [23].

Optical clocks can now realise frequency comparisons with a fractional uncertainty below 10^{-16}, which is the Cs fountain's uncertainty limit, and comparisons between identical clocks have been demonstrated with uncertainties of few parts in 10^{18} [24–26] (see fig. 1.3). Besides, statistical uncertainty contributions at 1 s averaging time smaller than 10^{-16} have been shown [27, 28]. Such clock stability allows to reach the clock systematic uncertainty limit in few hours of measuring

time, compared to Cs fountains which require more than 20 days to average down their statistical noise to the 10^{-16} level. The realisation of optical frequency comparisons with unprecedented accuracy is also allowed by the availability of devices and technologies for frequency dissemination which do not deteriorate the measurement uncertainty. These are the optical frequency combs, able to bridge the frequency gap between two optical frequencies with an uncertainty contribution in the 10^{-19} regime [29], and the optical fibre links [30, 31], which disseminate clock optical signals between distant locations with an uncertainty contribution $< 10^{-18}$ in 10 000 s averaging time [32].

Because of general relativity, the comparison of frequency standards requires to include corrections accounting for the different gravity potentials at the clock locations (see also section 3.5.4). Unless the two compared standards are sufficiently close to be able to measure their differential gravity potential with high accuracy, the relativistic redshift effect has to be evaluated with respect to a conventional equipotential reference surface [33, 34]; this is accomplished relying on the geoid model, whose uncertainty currently provides a limit for frequency measurements. State-of-the-art redshift evaluations are performed with an uncertainty of $\sim 2 \times 10^{-18}$ [35]. Some clocks have been already characterized and compared beyond this level [25, 36], becoming tools to measure geopotential differences with unprecedented uncertainty. This comes at the expense of the reciprocal validation of distant frequency standards at the 10^{-18} uncertainty level, limited by the redshift evaluation.

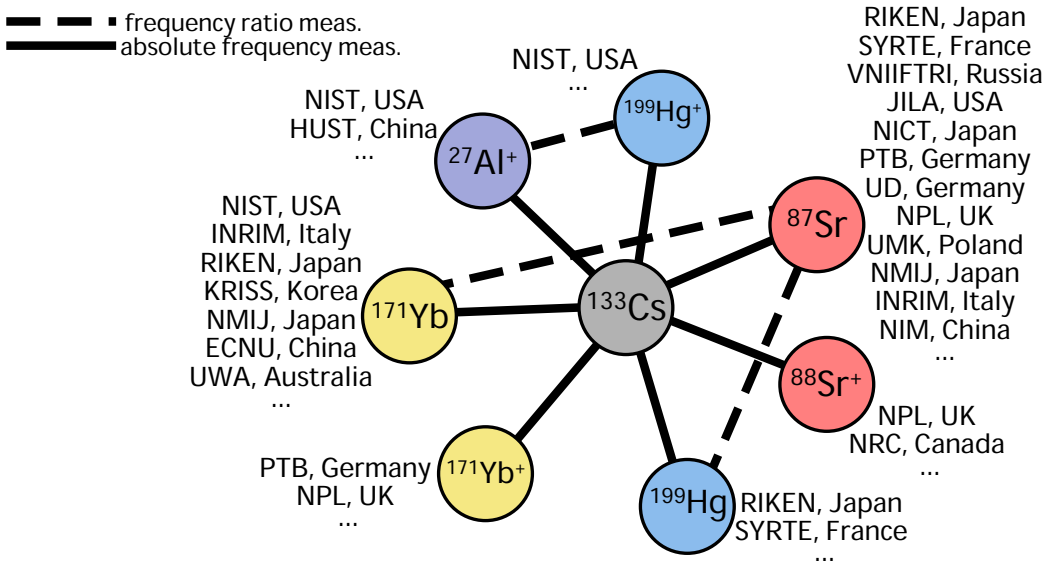

Figure 1.4: Optical frequency measurements of secondary frequency standards performed to date. A list of the worldwide laboratories developing optical standards is provided for each of the atomic species whose clock transition frequency is chosen as secondary representation of the second.

The demonstrated performance of the optical frequency standards led the International Committee of Weight and Measures[a] (CIPM) since 2006 to recommend several optical transitions as secondary representations of the second [37]. The list of recommended frequencies as of 2017 includes the clock transitions of $^{199}Hg^{+}$, $^{171}Yb^{+}$($E2$ and $E3$), $^{88}Sr^{+}$, ^{87}Sr, ^{171}Yb, ^{199}Hg and $^{27}Al^{+}$ (see figure 1.4).

Some optical clocks are now being successfully used to contribute to the realisation of TAI and for the generation of optical time scales [38–43], duties currently fulfilled by microwave standards.

All these advances show that optical clocks are suitable candidates for a future redefinition of the SI second. Because of the current uncertainty limit in the evaluation of the redshift against the geoid at $\sim 10^{-18}$, this level of uncertainty may be adopted as a reasonable target for the optical clocks to validate their performance and prove reproducibility, in light of a redefinition [37]. From this perspective, a roadmap towards a redefinition of the second has been articulated in ref. [37]. Prerequisites of a redefinition are firstly the demonstration of at least three different and independent optical standards characterized and compared with uncertainties in the low 10^{-18} regime; secondly, the continuity from the current definition has to be assured with several independent absolute frequency measurements of the optical frequencies considered with uncertainties lower than 3×10^{-16}. Finally, optical clocks have to be regular contributors to TAI, and several independent optical frequency ratios have to be demonstrated with an uncertainty $< 5 \times 10^{-18}$, so as to realise frequency ratio closures.

Thesis overview. The work presented in this dissertation is part of this framework, providing a contribution towards the redefinition of the SI second on an optical atomic transition. The thesis discusses the operation and characterization of two optical lattice frequency standards based on neutral ^{171}Yb, developed at INRIM, the Italian National Metrology Institute (Istituto Nazionale di Ricerca Metrologica), in Torino and at RIKEN, the Japanese National Institute of Physical and Chemical Research in Wako, Saitama.

The detailed characterization of the two frequency standards is reported, discussing all uncertainty contributions to be accounted for in the evaluation of the Yb lattice clock uncertainty budget. The discussion includes strategies and methods to overcome major uncertainty contributions in such frequency standards, with the aim of developing reliable and reproducible procedures to characterize this type of frequency standard, towards the demonstration of reliable performance at the 10^{-18} level.

Several frequency measurements involving the Yb frequency standards are reported. Firstly the absolute frequency measurement of the $^{1}S_0$-$^{3}P_0$ clock transition

[a] https://www.bipm.org/en/committees/cipm/

frequency of neutral ^{171}Yb is discussed; this is the most accurate measurement of this kind performed directly against a primary frequency standard. Additionally two independent measurements of the optical frequency ratio between the ^{171}Yb lattice frequency standards and ^{87}Sr lattice frequency standards are discussed. These results together with those of other research groups make the ^{171}Yb/^{87}Sr frequency ratio the only interspecies frequency ratio independently measured by four different research groups, providing a metrological insight of this quantity.

We believe that these results contribute in building confidence in the optical frequency standards, and provide a small advance towards the redefinition of the unit of time on an optical transition.

Chapter 2

^{171}Yb optical lattice clocks

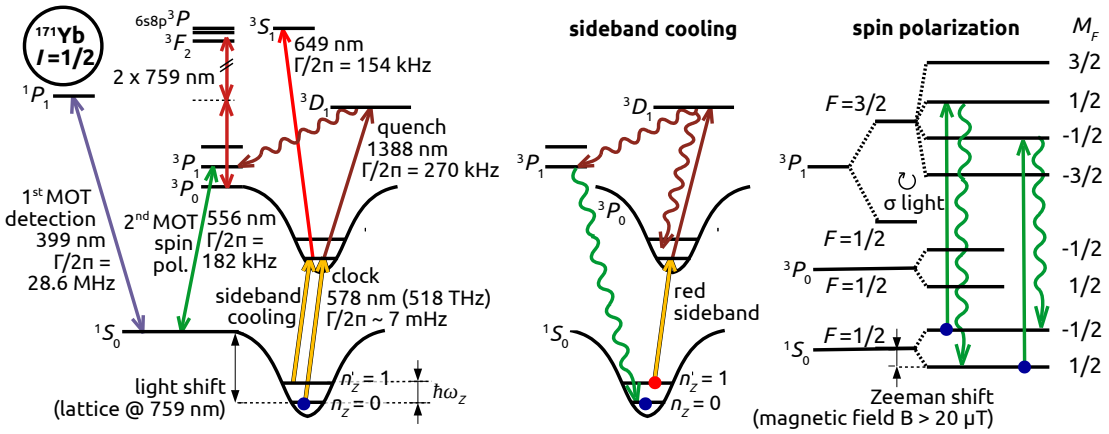

Figure 2.1: Left: ^{171}Yb relevant energy levels, with transition frequencies and linewidths. The lattice light modifies the clock transition energy levels allowing to confine the atoms in a potential well, as shown in the figure. The effect of the lattice light is not displayed for all energy levels. Centre: Atoms can be axially cooled to the lowest vibrational state through the sideband cooling scheme depicted. Right: Atoms are spin polarized to a specific ground Zeeman state through the shown optical pumping cycles. The process can be realised to either populate the $^1\mathrm{S}_0(M_F = +1/2)$ state (arrows in the left side) or to populate the $^1\mathrm{S}_0(M_F = -1/2)$ state (arrows in the right)

In a optical lattice clock several hundreds of neutral atoms are collected in an optical lattice and interrogated by the so-called probe laser, provided by the optical local oscillator (LO), along an optical clock transition.

Lattice clocks based on ^{171}Yb atoms exploit as the clock transition the narrow $^1\mathrm{S}_0$-$^3\mathrm{P}_0$ transition at $\nu_{\mathrm{Yb}} = 518$ THz (see figure 2.1) [44]. Other possible clock transitions have been recently proposed [45, 46], but they have not been experimentally investigated yet.

The clock transition has a natural linewidth $\gamma_{\mathrm{Yb}} \approx 7$ mHz [47] small enough to

represent a suitable frequency reference if it is not perturbed by the environment. However, even in a quiet environment free of external perturbations if the atoms are in motion when the interrogation process is performed the Doppler effect, the atoms' recoil and the short available interaction time induce line broadening and a frequency shift of the atomic resonance.

2.1 The optical lattice

In a lattice clock these issues are solved confining the atomic sample in the potential wells of a far-off-resonance (red-detuned) optical lattice realised as a standing wave [23, 48]. The interaction of the lattice light with the atomic electronic structure results in a dipole force which succeeds in confining the atoms near the lattice intensity maxima (see also section 3.2.1). Figure 2.1 shows how the lattice modifies the clock transition energy levels inducing a spatially-depended light shift which realises a potential well. Atoms confined inside a lattice site may be ejected from the trap because of collisions with the background gas or because of lattice-induced heating, however with a residual vacuum pressure below 10^{-7} Pa and implementing an active stabilization of the lattice intensity is possible to keep a large ensemble of atoms confined for several seconds (see also section 3.4.2).

In the simplest and most common configuration of lattice frequency standards the lattice is established by two counter-propagating beams along the selected z-axis, which interfere and generate a standing wave pattern. This realises a 1-dimensional lattice providing dipole traps which can be approximated along the z-axis and in the vicinity of the intensity maxima to harmonic potentials with vibrational energy levels identified by quantum numbers n_z, as shown in figure 2.1. An atom trapped in this potential well may be excited either along a purely electronic transition ($n_z^{\mathrm{g}} = n_z^{\mathrm{e}}$, where "g" and "e" refer to the clock ground and excited states) or on a sideband transition where a motional excitation or de-excitation takes place ($n_z^{\mathrm{e}} - n_z^{\mathrm{g}} = \Delta n_z \neq 0$).

The lattice depth, usually referred as the trap depth U_0 and corresponding to the on-axis maximum depth at the centre of the potential well, can be retrieved from the lattice axial trap frequency $\omega_z = 2\pi\nu_z$ and the lattice recoil energy E_{r} such that

$$U_0 = \frac{h^2\nu_z^2}{4E_{\mathrm{r}}} \quad \text{with} \quad E_{\mathrm{r}} = \frac{h^2\nu_{\mathrm{L}}^2}{2m_{\mathrm{Yb}}c^2} = h \times 2.03\ \mathrm{kHz} = 1.34 \times 10^{-30}\ \mathrm{J}, \tag{2.1}$$

where ν_{L} is the lattice frequency and $m_{\mathrm{Yb}} = 2.838\,464\,470(43) \times 10^{-25}$ kg is the ^{171}Yb atomic mass.

The Gaussian radial profile of the lattice beams leads to radial trap frequencies $\omega_r \ll \omega_z$, with

$$\omega_r(z) = 2\pi\nu_r = \sqrt{\frac{2U_0}{m_{\mathrm{Yb}}w^2(z)}}, \tag{2.2}$$

which varies along the z-axis according to the lattice $1/e^2$ radius $w(z)$.

The trap depth can be chosen to satisfy the Lamb-Dicke condition [49], where the spatial extension of the harmonic vibrational wavefunction[a] $z_0 = \sqrt{\hbar/(2m_{\mathrm{Yb}}\omega_z)}$ is much smaller than the wavelength of the probing light $\lambda_{\mathrm{Yb}} = 2\pi/k_{\mathrm{Yb}} = c/\nu_{\mathrm{Yb}}$, so that the Lamb-Dicke parameter

$$\eta = k_{\mathrm{Yb}} z_0 = \sqrt{\frac{\hbar k_{\mathrm{Yb}}^2}{2m_{\mathrm{Yb}}\omega_z}} = \sqrt{\frac{E_{\mathrm{r}}^{\mathrm{Yb}}}{h\nu_z}} \ll 1, \tag{2.3}$$

where $E_{\mathrm{r}}^{\mathrm{Yb}} = h^2\nu_{\mathrm{Yb}}^2/(2m_{\mathrm{Yb}}c^2) = h \times 3.48$ kHz is the probe photon recoil energy. Here we assume that the atoms occupy the ground vibrational state $n_z = 0$ and the probe beam propagates along the lattice axis, so that $\boldsymbol{k_{\mathrm{Yb}}} = k_{\mathrm{Yb}}\boldsymbol{z}$.

When the Lamb-Dicke condition is satisfied, the atom recoil energy $E_{\mathrm{r}}^{\mathrm{Yb}}$ obtained absorbing and re-emitting a photon of frequency ν_{Yb} is much smaller than the spacing $\hbar\omega_z$ between two neighbouring vibrational states.

In addition, in these conditions the linewidth $\Gamma = 2\pi\gamma$ of the clock transition spectroscopy feature is sufficiently smaller than the axial trap frequency so that $\Gamma/\omega_z \ll 1$; this means that the sidebands are resolved from the purely electronic transition, which can be selectively probed during the interrogation process. This is called the resolved sideband regime and has to be satisfied to discriminate the electronic excitation.

With these conditions satisfied, probing the atomic ensemble along the lattice axis allows to perform Doppler and recoil free spectroscopy.

Since the lattice polarizability is different for the clock ground and excited states, in general the energy shifts affecting the two states because of the interaction with the lattice light are different and vary according to the lattice frequency. As a consequence, the clock transition frequency and line shape are affected by the lattice perturbation. In order to overcome this problem the lattice frequency is tuned to a so-called E1-magic frequency $\nu_{\mathrm{L}} = \nu_{\mathrm{E1}}$ at which the electric dipole polarizability α_{E1} of the two clock states is same [50]. For ^{171}Yb, $\nu_{\mathrm{E1}} \simeq 394\,798.3$ GHz ($\lambda_{\mathrm{E1}} = 759$ nm). In this condition, as shown in fig. 2.1, the light shifts of the two clock states are the same (neglecting higher order effects, see also section 3.2.1), hence the purely electronic clock transition is almost unperturbed by the lattice light. If the lattice frequency is moved away from the magic frequency the clock transition line shape becomes asymmetric and broader, and at certain frequencies even the confinement of the atoms is undermined.

In the standard clock operation of the work presented in this thesis the lattice trap depth U_0 is chosen within 60 $E_{\mathrm{r}} \leq U_0 \leq 300$ E_{r}, corresponding to lattice average temperatures $T_{\mathrm{L}} = U_0/(\frac{3}{2}k_{\mathrm{B}})$ of 4 µK $\leq T_{\mathrm{L}} \leq$ 20 µK. Such lattice depths

[a] z_0 is the average value of the position operator $\hat{z} = z_0(\hat{a}^\dagger + \hat{a})$ in the ground vibrational state of the lattice potential $n_z = 0$, such that $z_0 = (\langle 0|\,\hat{z}^2\,|0\rangle)^{1/2}$.

are realised with lattice beams having an optical power 0.5 W $\lesssim P_{\mathrm{L}} \lesssim$ 1 W each and setting the lattice waist $w_0 \sim 50$ µm. Other lattice configurations exploiting enhancement cavities to build up the lattice optical power allow to work with deeper traps and larger waists [51, 52] even with the same lattice beam power. Despite large depths allow to trap a larger ensemble of atoms, if possible it is preferred to work with shallow depths $U_0 < 100\ E_{\mathrm{r}}$ to limit and better control the lattice light shift.

2.2 Magneto optical traps

The hot vapour of Yb atoms as produced by the atomic source requires to be cooled to temperatures $T \lesssim 20$ µK before it is possible to trap the atoms in a lattice. This is performed through two magneto-optical traps (MOTs) performed in sequence. A MOT exploits laser cooling techniques together with magnetic field gradients to cool and confine atoms in a small region of space [21]. The first MOT is realised making the atoms interact with laser beams at 399 nm on the ^{1}S$_0$-^{1}P$_1$ atomic transition, while the second MOT interacts with the0.213 ^{1}S$_0$-^{3}P$_1$ transition at 556 nm, as shown in figure 2.1. The MOT makes use of three pairs of laser beams counter-propagating along the three spatial directions, to decelerate atoms in all the three degrees of freedom through radiation pressure; the crossing point between the beams coincides with the minimum of a magnetic field gradient generated by a pair of coils in anti-Helmholtz configuration. The magnetic field gradient generates the trap making the radiation pressure force spatially dependent so that it reduces together with the atom getting closer to the trap centre.

The thermal balance between the energy dissipation provided by the photon radiation pressure and the heating induced by the atom recoil after spontaneous emission determines a lower limit in the temperature of the atomic ensemble cooled by the MOT. The temperature limit T_{D}, called Doppler temperature, depends on the linewidth $\Gamma = 2\pi\gamma$ of the cooling transition exploited

$$T_{\mathrm{D}} = \frac{\hbar\Gamma}{2k_{\mathrm{B}}}, \tag{2.4}$$

where k_{B} is the Boltzmann constant. The first MOT on the blue transition as a Doppler temperature $T_{\mathrm{D}}^{\mathrm{blue}} \simeq 0.7$ mK, while for the green MOT $T_{\mathrm{D}}^{\mathrm{green}} \simeq 3$ µK. Therefore, after the second MOT the atomic ensemble is sufficiently cold to be contained in a lattice generated by feasible laser intensities.

Once atoms are loaded in the lattice, MOT laser beams and magnetic field gradients can be turned off, leaving atoms trapped in the lattice sites. Details about the MOT sequence and performance for the RIKEN Yb clock can be found in [53], while for the INRIM Yb clock can be found in [54, 55].

2.3 State preparation

Sideband cooling. When atoms are loaded in the lattice, they are thermally distributed among the lattice vibrational levels. In order to cool the atoms along the direction where atoms are probed, namely the lattice axis (or longitudinal direction), in the RIKEN Yb clock we implement quenched sideband cooling [56] on the clock transition. This is realised applying a high power (i.e. $\gtrsim 1$ mW) laser pulse linearly polarized along the quantization axis (as defined in the following section) and frequency tuned to a fixed frequency $\nu_{\mathrm{l}} \approx \nu_{\mathrm{Yb}} - \nu_z$ to address the clock transition red sideband ($\Delta n_z = n_z^{\mathrm{e}} - n_z^{\mathrm{g}} = -1$).

Atoms in a vibrational state with $n_z \neq 0$ are excited to a vibrational state with quantum number $n_z - 1$, as shown in figure 2.1. The cycling of the atoms back to the $^1\mathrm{S}_0$ state is ensured by the quenching beam at 1388 nm resonant with the $^3\mathrm{P}_0$-$^3\mathrm{D}_1$ transition, which optically pumps the excited atoms to the $^3\mathrm{D}_1$ short-lived state. The decay through spontaneous emission to the ground $^1\mathrm{S}_0$ state occurs through the $^3\mathrm{P}_1$ state, and strongly favours the ground vibrational state with same quantum number $n_z - 1$ (see fig. 2.1). The process thus succeeds in lowering the atom vibrational quantum number by one. Over multiple excitation cycles most of the atoms populate the lowest vibrational state.

Because of the atomic radial motion the red sideband excitation frequency varies across the atomic sample, thus the sideband cooling can address all atoms with the same efficiency only if the irradiation time is comparable with the atom radial oscillation time. We satisfy such condition implementing a sequence of multiple pulses. The sideband cooling sequence consists of four pulses with optical power of ~ 1 mW delivered along the lattice axis in the opposite direction of the probe laser. The first pulse lasts 30 ms, while the following last 20 ms each. We finally achieve a mean vibrational quantum number of the atomic ensemble of $\bar{n}_z \approx 0.1$.

In the INRIM Yb clock we currently do not implement this state preparation sequence.

Spin polarisation. Among the odd isotopes of Yb, ^{171}Yb has a nuclear spin $I = 1/2$, providing a simple hyperfine structure convenient for the atom manipulation. The ground and the excited clock states are characterized by a single degenerate hyperfine state $F = 1/2$. In the presence of an external magnetic field, the degeneracy is broken and both energy levels are split in two Zeeman states identified by the quantum numbers $M_F = \pm 1/2$. The suppression of the external magnetic field is experimentally challenging, and small residual fields result in a broadening of the spectroscopic feature. Additionally, an unbalanced atom distribution between the Zeeman levels leads to an asymmetric line shape. The issue is tackled applying an external magnetic field of intensity $B > 20$ µT able to resolve the different transitions between the Zeeman states, inducing a separation of the energy levels larger than the transition linewidths (see fig. 2.1).

The axis of the external magnetic field defines the quantization axis of the atomic system. This allows to selectively excite the different transitions between Zeeman states by choosing the appropriate orientation of the probe laser polarisation and its frequency (see also section 3.1). Transitions satisfying $\Delta M_F = M_F^e - M_F^g = 0$ are excited with linearly polarized π light parallel to the quantization axis, while $\Delta M_F \neq 0$ transitions are excited either with circularly polarized σ light or linearly polarized light orthogonal to the quantization axis.

When the atoms are loaded in the lattice they are distributed among both Zeeman ground states, thus just part of the population can be driven on the π clock transition at a time. As a consequence the acquired signal-to-noise ratio is lower than expected for the number of trapped atoms. The maximum signal is recovered optically pumping the entire atomic ensemble to a specific Zeeman spin-state. This spin polarisation process also suppresses line pulling effects between the Zeeman transitions, and reduce atomic collisions, which are prohibited between identical fermions by the Pauli exclusion principle (see section 3.4.1).

Spin polarisation is performed quenching one of the Zeeman ground states with σ-polarized light at 556 nm, resonant with the $^1S_0$-$^3P_1$, $\Delta M_F = \pm 1$ transition. Atoms then preferentially decay along the $\Delta M_F = 0$ transition, with twice the branching ratio of the $\Delta M_F = \mp 1$ transition, to populate the desired Zeeman spin state as shown in figure 2.1 and 2.2.

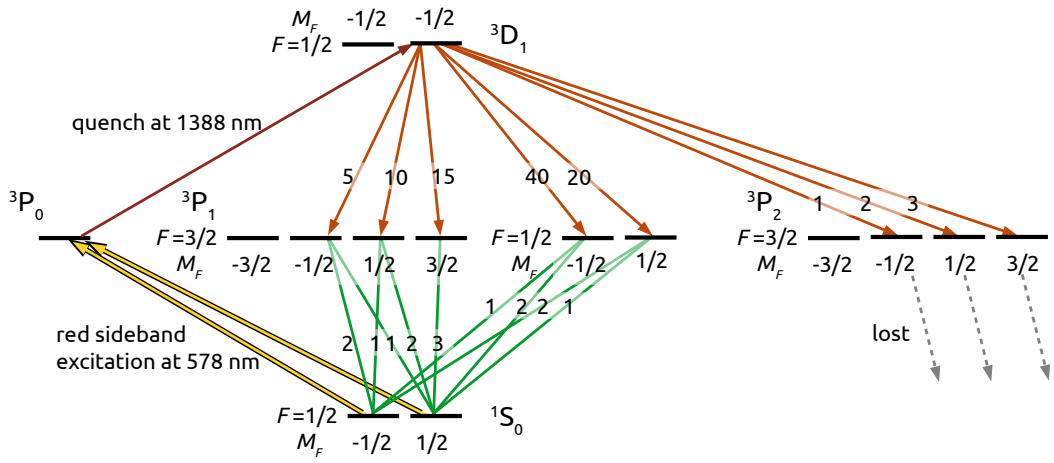

Figure 2.2: Atomic transitions involved in the spin polarisation process and their branching ratios to the ground $^1S_0$, $M_F = \pm 1/2$ states from the $^3D_1$, $M_F = +1/2$ state. The figure and the calculated values are taken from [57]. The figure allows to understand how the sideband cooling process can be tuned to assist spin polarisation, preferentially populating the $^1S_0$, $M_F = +1/2$ state for the case shown in the figure.

In the INRIM Yb clock, an external bias magnetic field of about 0.03 mT is used to resolve the Zeeman states, and the optical pumping is implemented with a

single 1 ms pulse of σ-polarized light propagating along the quantization axis.

In the RIKEN clock, we apply an external field of ~ 0.08 mT. Spin polarizing light is delivered with the same optical fibre used for the sideband cooling laser and propagates along the lattice axis. Its polarisation is chosen to be linear and aligned orthogonal to the quantization axis. Since the spin polarisation and sideband cooling processes both rely on the spontaneous decay of atoms from the $^3P_1$ state, their effects may interfere. In the sideband cooling cycle atoms may decay to both Zeeman ground states, degrading the spin polarisation performance (see fig. 2.2). On the other hand spin polarizing light heats up atoms eventually increasing their vibrational state.

Sideband cooling can be optimized to assist the spin polarisation process populating a specific Zeeman component of the $^3D_1(F = 1/2)$ state with a favourable branching ratio to the $^1S_0$ desired Zeeman state [57, 58], as shown in figure 2.2. The address of a specific $^3D_1(F = 1/2)$ Zeeman level is allowed by retaining both quenching beam polarisation components parallel and orthogonal to the quantization axis.

Optimal state-preparation sequence minimising the pumping cycles is found interleaving 20 ms pulses for sideband cooling with 10 ms pulses for spin polarisation.

In both the RIKEN and INRIM clocks we achieve spin polarisation with an efficiency ≥ 98 %.

2.4 Interrogation and detection.

The interrogation of the atomic sample is performed probing the $^1S_0$-$^3P_0$ clock transition. Typically, the probe laser is continuously active during the clock operation, but frequency detuned from resonance by ≥ 100 kHz not to interact with the atoms; the interrogation is implemented bringing the laser to resonance for the required interrogation time.

Rabi interrogation. The simplest interrogation scheme, the Rabi interrogation, consists in a single resonant light pulse of duration T_i. In the standard clock operation the probe laser intensity and the pulse duration T_i are chosen to coherently excite all atoms from the ground state of the clock transition to the excited state. In this case, the interrogation pulse is called a π-pulse and the pulse area $T_i\Omega_R = \pi$. Ω_R is the Rabi frequency, which depends on the clock transition light-coupling strength and is proportional to the squared-root of the probe laser intensity I_p, $\Omega_R \propto \sqrt{I_p}$ (see also section 3.2).

Visualising the Rabi interrogation on the Bloch sphere [21], a resonant Rabi π-pulse moves the Bloch vector from the south pole to the north pole of the sphere. With a pulse area $T_i\Omega_R < \pi$ the Bloch vector does not reach the north pole, and specifically a π/2-pulse brings the vector to the equator, where the atom is in a

superposition of the ground and excited states; this means that if the atoms were detected after this pulse both the ground and excited states populations would have been measured to be 50 % of the total number of trapped atoms. Similarly, pulse areas larger than π, obtained with either a longer interrogation time or with higher optical power, make the vector overtake the pole and eventually bring the atoms back to the ground state for a 2π-pulse.

The interrogation pulse has to be delivered along the lattice axis to probe the atoms in the Lamb-Dicke regime. The polarisation of the probe light has to be linear and aligned along the quantization axis, which is also the lattice polarisation axis. This is required to suppress the two σ transitions with $\Delta M_F = \pm 1$ from the clock transition spectrum, avoiding the loss of atoms along these transitions.

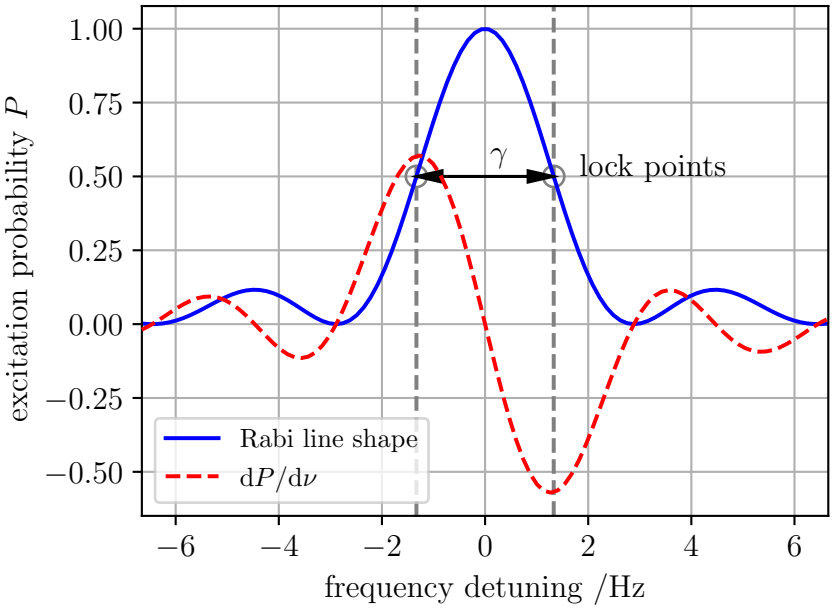

Figure 2.3: Line shape obtained from Rabi interrogation (blue), corresponding to the excitation probability P at different probe frequency detuning from resonance. Its derivative is shown with the red dashed curve. The plot is performed assuming a Rabi π-pulse of duration $T_\mathrm{i} = 300$ ms.

After interrogation a detection sequence is implemented to measure the excitation probability P, which is the atom excitation fraction at the end of the interrogation pulse. A frequency scan of the probe laser across the atomic resonance allows to retrieve the Fourier-limited line shape of the clock transition in terms of the excitation probability. in the frequency domain the Rabi interrogation provides

a line shape of the form

$$P = \frac{\Omega_{\mathrm{R}}^2}{\Omega_{\mathrm{R}}^2 + \Delta\omega^2} \sin^2\left(\sqrt{\Omega_{\mathrm{R}}^2 + \Delta\omega^2}\frac{T_{\mathrm{i}}}{2}\right), \tag{2.5}$$

where $\Delta\omega = 2\pi(\nu_{\mathrm{l}} - \nu_{\mathrm{Yb}})$, with ν_{l} the probe laser frequency and ν_{Yb} the resonant frequency.

A Rabi π-pulse leads to a spectroscopy feature of linewidth $\gamma \approx 0.8/T_{\mathrm{i}}$ and maximum excitation probability at resonance of $P_{\max} \approx 1$ (see figure 2.3).

The plot of an experimental Rabi line shape is reported in a later section, in figure 2.15.

As shown in figure 2.3, Rabi spectroscopy of the clock transition provides a line shape whose derivative, and thus sensitivity to LO frequency variations $\delta\nu_{\mathrm{l}}$, is maximal close to the line half-height points (i.e. the lock points), which are thus suitable to be probed to check the probe laser frequency deviation from resonance. Lock points are probed detuning the probe laser frequency by $\pm\Delta\nu_{\mathrm{step}} = \gamma/2$ from resonance, where γ is the full-width at half-maximum of the spectroscopy line, and according to eq. (2.5) correspond to an excitation probability $P = 0.5$.

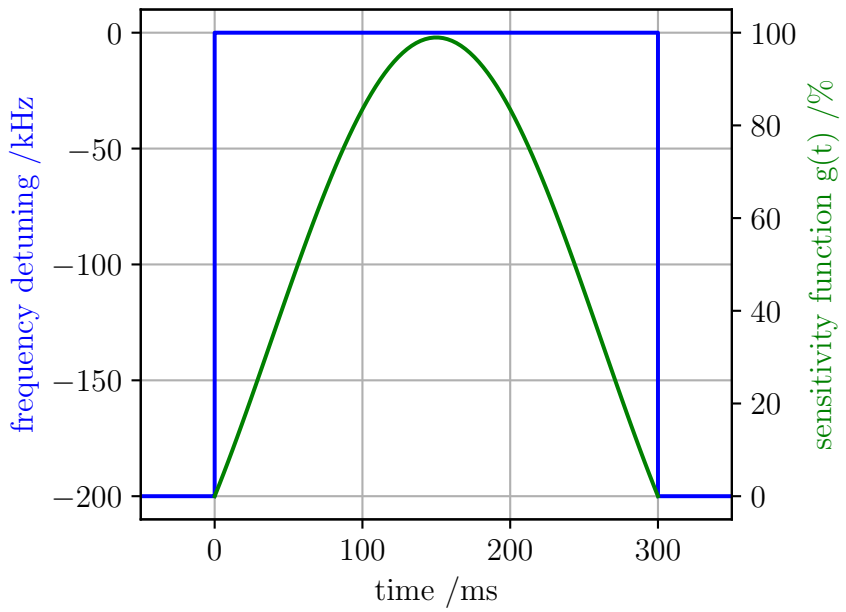

Figure 2.4: Blue: Rabi interrogation sequence in the time domain shown as the probe laser frequency detuning from resonance. Green: corresponding sensitivity function $g(t)$ over the Rabi pulse. Example provided for a π-pulse of duration $T_{\mathrm{i}} = 300$ ms probing the clock transition at the half-height points.

Frequency fluctuations $\delta\nu_{\mathrm{l}}(t)$ of the probe laser with respect to the clock resonance, either induced by the LO noise or by external fields perturbing the clock

transition, reflects in a variation δP of the excitation probability outcome. The excitation probability sensitivity to such time-dependent fluctuations varies along the interrogation pulse, and it is zero outside of it. It is possible to define a sensitivity function $g(t)$ which depends on both the clock interrogation sequence and the lock points such that [59, 60]

$$\delta P = \pi \int_0^{T_\mathrm{i}} g(t)\delta\nu_\mathrm{l}\,\mathrm{d}t\,. \tag{2.6}$$

For a Rabi π-pulse and lock points defined above by frequency steps $\pm\Delta\nu_\mathrm{step} = \gamma/2$ the sensitivity function reads [61]

$$g(t) = \left\{ \begin{array}{ll} \sin^2(\theta)\cos(\theta)\left[\sin(\Theta_1)(1-\cos\Theta_2)+\sin(\Theta_2)(1-\cos\Theta_1)\right] & \text{for } 0 \le t \le T_\mathrm{i} \\ 0 & \text{for } t > T_\mathrm{i} \end{array} \right\} \tag{2.7}$$

where

$$\begin{aligned} \Delta &= 2\Delta\nu_\mathrm{step}T_\mathrm{i} \approx 0.799 \\ \theta &= \tfrac{\pi}{2} + \arctan(\Delta) \\ \Theta_1 &= \pi\sqrt{1+\Delta^2}\left(\tfrac{t}{T_\mathrm{i}}\right) \\ \Theta_2 &= \pi\sqrt{1+\Delta^2}\left(1-\tfrac{t}{T_\mathrm{i}}\right). \end{aligned} \tag{2.8}$$

Figure 2.4 shows the Rabi interrogation sequence as performed detuning the probe laser frequency (blue), together with the shape of the corresponding sensitivity function according to eq. (2.7).

The derivative $\mathrm{d}P/\mathrm{d}\nu$ at the lock points can be written in terms of g as [59]

$$\left.\frac{\mathrm{d}P}{\mathrm{d}\nu}\right|_{\Delta\nu_\mathrm{step}} = \pi\int_0^{T_\mathrm{i}} g(t)\,\mathrm{d}t\,. \tag{2.9}$$

Experimentally the excitation probability is obtained measuring the population N_e of the clock transition excited state normalized over the total number of atoms N, which in turn is the sum of the ground and excited state populations $N = N_\mathrm{g} + N_\mathrm{e}$:

$$P = \frac{(N_\mathrm{e} - N_\mathrm{bkg})}{(N_\mathrm{g} - N_\mathrm{bkg}) + (N_\mathrm{e} - N_\mathrm{bkg})}, \tag{2.10}$$

where N_bkg is the background signal acquired in the absence of atoms.

The ground state population is measured exciting the atoms along the ^{1}S$_0$-^{1}P$_1$ transition with a 399 nm pulse and collecting the fluorescence signal emitted from the atom spontaneous decay. The process is destructive, since atoms are are heated out from the trap by the detection pulse. Once the ground state is emptied, a second pulse measures the background signal. The population of the clock transition metastable excited state is then pumped to ^{1}S$_0$ through excitation to ^{3}D$_1$ and decay along the^{3}D$_1$-^{3}P$_1$-^{1}S$_0$ channel (see fig. 2.1). It is then measured

with a third detection pulse at 399 nm. The pumping of the $^3P_0$ population to the ground state has an efficiency η which is estimated and included in the calculation of P. Typically, $\eta = 0.8$ in the INRIM Yb clock, while $\eta = 0.9$ in the RIKEN clock.

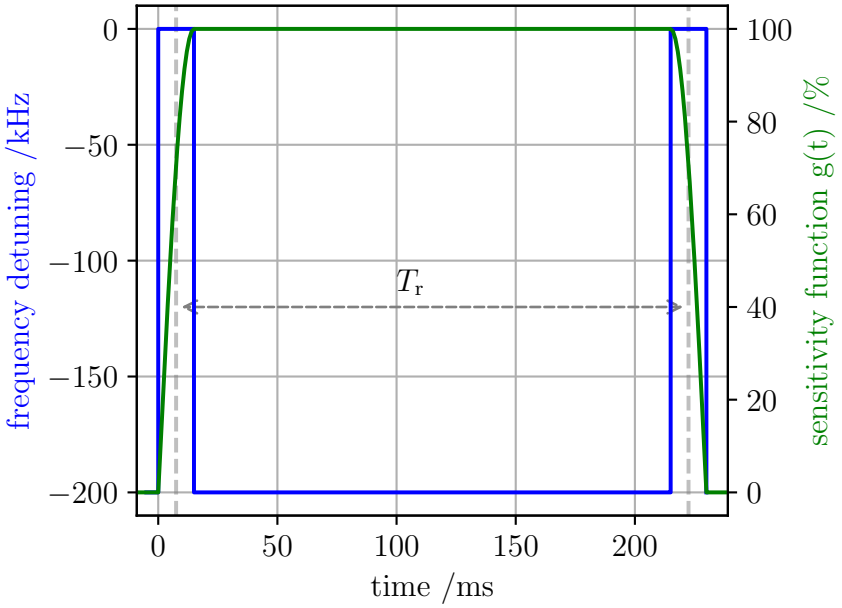

Figure 2.5: Blue: pattern of the Ramsey interrogation sequence performed frequency detuning the probe laser out of resonance outside the interrogation pulses. The shown sequence has interrogation pulses of $T_p = 15$ ms, and $T_{dark} = 200$ ms. Green: corresponding Ramsey sensitivity function to probe beam intensity variations.

Ramsey interrogation. In addition to the Rabi interrogation, another possible technique to probe the clock transition is the Ramsey interrogation. The Ramsey sequence is composed of two resonant $\pi/2$ pulses of duration $T_p = \pi/(2\Omega_R)$ each, separated by a dark time T_{dark} in which the probe laser does not interact with the atoms; this can be achieved turning the laser off, however since this approach leads to technical difficulties it can be preferred to keep the laser on and frequency detuned from resonance. For $T_{dark} \to 0$ the Ramsey sequence effectively converges to the Rabi interrogation.

The first resonant $\pi/2$-pulse brings the atoms in a superposition of the ground and excited clock states, moving the Bloch vector from the Bloch-sphere south pole to the equator. During the dark time, also called free-evolution time, the atomic phase is let evolve along the Bloch sphere equator up to the second $\pi/2$-pulse, which completes the interrogation process ideally bringing all the atoms to the excited state (represented as the north pole in the Bloch sphere). If the probe

laser is not perfectly resonant, the Bloch vector at the end of the sequence points below the North pole, and the final excitation probability $P < 1$ reflects the laser frequency detuning from resonance.

The linewidth of the Ramsey spectroscopy fringe is determined by the Ramsey time $T_\mathrm{r} = T_\mathrm{p} + T_\mathrm{dark}$, defined as the time separation between the centre of the two short pulses (see fig. 2.5), such that the linewidth (as the full width at half maximum) $\gamma \approx 1/(2T_\mathrm{r})$.

The time-dependent sensitivity function $g(t)$ for the Ramsey interrogation pattern used in this experiment is shown in figure 2.5, and can be written for a general Ramsey scheme with $T_\mathrm{dark} \gg T_\mathrm{p}$ as [60]

$$g(t) = \left\{ \begin{array}{ll} a\sin(\Omega_\mathrm{R} t) & \text{for } 0 \leq t \leq T_\mathrm{p} \\ a\sin(\Omega_\mathrm{R} T_\mathrm{p}) & \text{for } T_\mathrm{p} < t < T_\mathrm{p} + T_\mathrm{dark} \\ a\sin(\Omega_\mathrm{R}(T_\mathrm{dark} + 2T_\mathrm{p} - t)) & \text{for } T_\mathrm{p} + T_\mathrm{dark} < t \leq T_\mathrm{i}' \\ 0 & t > \text{for } T_\mathrm{i}' \end{array} \right\} \tag{2.11}$$

with $a = \pm\sin(\Delta\omega_\mathrm{step} T_\mathrm{dark})\sin(\Omega_\mathrm{R} T_\mathrm{p})$, where $\Delta\omega_\mathrm{step} = \pm 2\pi\Delta\nu_\mathrm{step}$ is the frequency modulation applied to the probe laser frequency to probe either the left or right side (according to the sign) of the clock transition to perform the frequency lock. $T_\mathrm{i}' = 2T_\mathrm{p} + T_\mathrm{dark}$ is the total interrogation time.

In the standard clock operation, $\Omega_\mathrm{R} T_\mathrm{p} = \pi/2$ and the clock transition is probed at the half-heigh points of the spectroscopy signal as with Rabi interrogation. In this case $\Delta\nu_\mathrm{step} = \gamma/2 = 1/(4T_\mathrm{dark})$, thus $a = 1$.

2.5 Sequence of the clock cycle

The cycle of operation of a lattice frequency standard is shown in figure 2.6. Firstly atoms are collected in the blue MOT at 399 nm. When a sufficient number of trapped atoms is reached, atoms are transferred and trapped in the green MOT at 556 nm, which is overlapped on the blue one, until a sufficiently low temperature is reached. MOT fields are then turned off and atoms are left confined in the lattice, which is continuously present and crosses the MOT region during the clock operation.

Once atoms are in the lattice potential wells, their internal state can be changed to optimize the clock performance, in the state preparation sequence. Atoms are then probed at the half-height lock points implementing an interrogation sequence.

The atomic state readout after the interrogation is concluded, i.e. the detection process, retrieves the excitation fraction P, which is used to quantify the discrepancy between the LO frequency and the transition resonance in order to apply a frequency correction. Since the detection process is destructive, atoms have to be loaded again to perform another interrogation: this defines an operational cycle time Δt_c required to load, interrogate and detect the atoms.

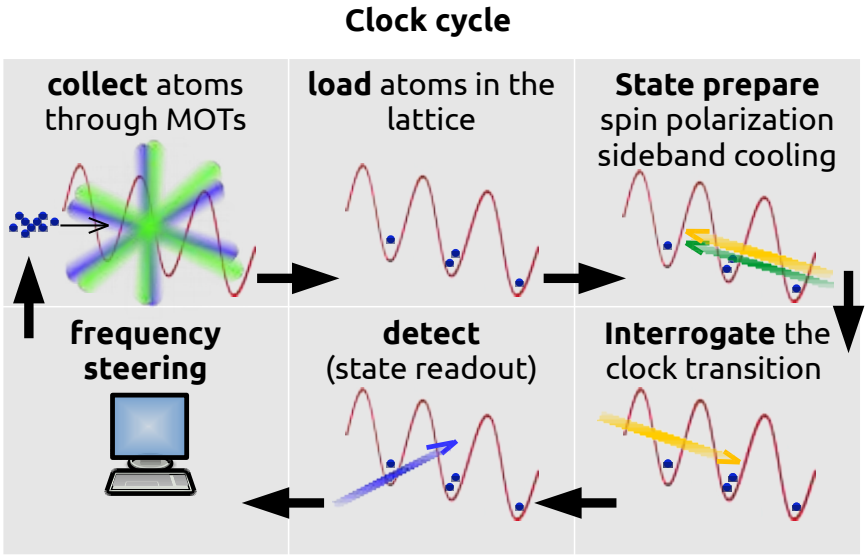

Figure 2.6: Sequence of the clock cycle of operation. Since the frequency steering involves a digital process, it can be overlapped to the beginning of the next cycle to shorten the clock cycle.

A side-of-the-fringe frequency stabilization, probing just one side of the spectroscopy line, would stabilise the LO frequency with an offset from the desired resonance frequency. Instead, the probe laser frequency is modulated interleaving clock cycles with opposite frequency detuning $\pm\Delta\nu_{\text{step}} = \pm\gamma/2$. The finite difference between the signal at the two lock points is used to implement a LO frequency stabilization control loop with an error signal which zeros at resonance.

This approach requires two interrogations of the clock transition, hence two clock cycles are necessary to evaluate the error signal and compute a frequency correction. The frequency correction is then applied to an acousto-optic modulator (the lock AOM) to frequency steer the LO frequency and continuously satisfy the resonance condition.

2.6 Stability of lattice frequency standards

The fractional instability of a frequency standard is expressed in terms of the Allan deviation [62] and can be calculated according to [63, 64]

$$\sigma_y(\tau) = \frac{1}{K}\frac{1}{Q}\frac{1}{S/N}\sqrt{\frac{\Delta t_c}{\tau}}. \tag{2.12}$$

In the equation $Q = \nu_{\text{Yb}}/\gamma$ is the clock transition quality factor, where γ is the linewidth of the clock transition spectroscopy feature, which is Fourier-limited

by the finite interrogation time T_i (see eq.(2.5) for Rabi interrogation). $S/N = S_\mathrm{max}/\delta S$ is the signal-to-noise ratio, where δS is the noise (i.e. instability) evaluated at a measuring time $\tau = 1$ s and S_max is the signal maximum value. The signal S can be written in terms of the number of probed atoms N times the measured excitation probability P so that $S = NP$.

Equation 2.12 does not consider instability contributions corresponding to other than white frequency noise processes. This is reflected in the dependence of the frequency instability to the averaging time τ such that $\sigma_y(\tau) \propto 1/\sqrt{\tau/\mathrm{s}}$: performing a sequence of M uncorrelated frequency measurements, the instability averages down by a factor $\sqrt{M}$, with $M = \tau/\Delta t_\mathrm{c}$ since the duration of a single measurement corresponds to the clock cycle time Δt_c .

The factor K is a positive constant near unity which depends on the line shape, and on the way the frequency modulation $\pm\Delta\nu_\mathrm{step}$ employed to extract the clock transition centre is performed [63]:

$$K = \left| \left.\frac{\mathrm{d}S}{\mathrm{d}\nu}\right|_{\Delta\nu_\mathrm{step}} \frac{\gamma}{S_\mathrm{max}} \right|. \tag{2.13}$$

In the following we assume that the probe interrogation performs a π-pulse.

According to the treatment of [63] (page 77), the maximum signal S_max used as normalisation value is taken as the value acquired probing the clock transition resonance, such that S_max/γ is the slope at the lock points of a triangular line shape with same height and width; therefore $S_\mathrm{max} = NP_\mathrm{max} = N$. Note that this value is the same S_max appearing in the signal-to-noise calculation.

Since the signal at the lock points, i.e. the half-height points, is acquired applying a frequency modulation with step size $\pm\Delta\nu_\mathrm{step} = \pm\gamma/2 \approx \pm 0.399/T_\mathrm{i}$ [61], in the following we introduce the notation $P_{\pm\Delta} = P(\pm\Delta\nu_\mathrm{step})$, and $P_{\pm\Delta} \approx 0.5$ if the probe laser frequency $\nu_\mathrm{l} \approx \nu_\mathrm{Yb}$.

The slope of the spectroscopy signal evaluated at the lock points is [61]

$$\left.\frac{\mathrm{d}S}{\mathrm{d}\nu}\right|_{\Delta\nu_\mathrm{step}} = N \left.\frac{\mathrm{d}P}{\mathrm{d}\nu}\right|_{\Delta\nu_\mathrm{step}} \approx N\pi\ 0.604\ T_\mathrm{i}. \tag{2.14}$$

Therefore the factor K can be calculated as

$$K \approx N\pi\ 0.604\ T_\pi \frac{2 \times 0.399}{T_\pi N} \approx 1.52. \tag{2.15}$$

2.6.1 Quantum projection noise and technical noise processes

The fundamental limit to the clock stability is provided by the quantum projection noise (QPN) [65]: when the signal S is measured, the atomic wave functions

collapse (i.e. are projected) into a particular state (either the ground state $|g\rangle$ or the excited state $|e\rangle$). The measurement outcome finds atoms in $|e\rangle$ with a probability P, or in $|g\rangle$ with a probability $1-P$. The statistical fluctuation δS of the measurement result, called the quantum projection noise (QPN), deteriorates the clock stability. Such fluctuation is calculated as the variance of the projection operator $|e\rangle\langle e|$ or equivalently as the variance of the binomial probability distribution of finding an atom in the excited state [65]

$$(\delta S)^2 = NP_\Delta(1-P_\Delta), \tag{2.16}$$

leading to a signal-to-noise ratio $S/N = S_{\max}/\delta S = NP_{\max}/\sqrt{NP_\Delta(1-P_\Delta)} \approx 2\sqrt{N}$ (note that $P_{\max}$ here has to match the normalisation value used in eq. (2.13) and (2.15)). As a consequence, using eq. (2.15) the QPN instability of a frequency standard performing a Rabi interrogation is

$$\sigma_y^{\mathrm{QPN}}(\tau) = \frac{1}{K}\frac{1}{Q}\frac{\sqrt{NP_\Delta(1-P_\Delta)}}{N}\sqrt{\frac{\Delta t_\mathrm{c}}{\tau}} \approx \frac{1}{K}\frac{1}{Q}\frac{1}{2\sqrt{N}}\sqrt{\frac{\Delta t_\mathrm{c}}{\tau}} \approx \frac{0.26}{\nu_0 T_\mathrm{i}}\sqrt{\frac{\Delta t_\mathrm{c}}{N\tau}}. \tag{2.17}$$

Since the LO frequency stabilization is performed with a digital lock acquiring the finite difference between the signal at the two lock points, the signal to be considered is $S = NP_{-\Delta} - NP_{+\Delta}$, and the calculation of the QPN instability has to be modified accordingly. The signal derivative, which is the error signal used in the frequency-steering control loop, is thus $\mathrm{d}S/\mathrm{d}\nu = 2N\,\mathrm{d}P/\mathrm{d}\nu$. The QPN obtained probing both lock points is

$$\delta S = \sqrt{\delta S_{-\Delta}^2 + \delta S_{+\Delta}^2} = \sqrt{2NP_\Delta(1-P_\Delta)}. \tag{2.18}$$

Since the required time to probe both sides of the spectroscopy line shape is twice the operation cycle time Δt_c, than the QPN-limited instability is

$$\sigma_y^{\mathrm{QPN}}(\tau) = \frac{1}{2K}\frac{1}{Q}\frac{\sqrt{2NP_\Delta(1-P_\Delta)}}{N}\sqrt{\frac{2\Delta t_\mathrm{c}}{\tau}} \approx \frac{0.26}{\nu_0 T_\mathrm{i}}\sqrt{\frac{\Delta t_\mathrm{c}}{N\tau}}, \tag{2.19}$$

which comes out to be the same result obtained in eq. (2.17).

In a lattice clock the number of atoms N interrogated varies according to the operating conditions: the efficiency of the loading procedure and the properties of the optical lattice such as the trap depth play an important role. Beside physical constraints, N can be limited by purpose to contain the amount of collisions. Therefore, in the experiments reported here $100 \leq N \leq 1000$. For an operational cycle time $\Delta t_\mathrm{c} = 1.6$ s, and $N = 300$ the QPN instability would be $\sigma_y^{\mathrm{QPN}} = 1.2 \times 10^{-16}\,/\sqrt{\tau/\mathrm{s}}$.

Other noise sources deteriorating the stability of lattice frequency standards are related to the detection apparatus efficiency [66]. Including this terms, the

instability limit provided by the atomic and technical noise processes can be written [66, 67]

$$\sigma_y(\tau) = \frac{1}{2K}\frac{1}{Q}\sqrt{\left(\frac{1}{N} + \frac{1}{Nn_{\mathrm{ph}}} + \frac{2\delta N^2}{N^2}\right)\frac{\Delta t_{\mathrm{c}}}{\tau}}, \tag{2.20}$$

where the first term in the parenthesis is the QPN, the second is the photon shot noise determined by the limited number of detected photons n_{ph} per probed atom due for instance to the angle of view of the detection system, while the third term represents the effect of the single channel electronic detection noise, which is intrinsic of the state readout process, with δN^2 being its variance and N the number of probed atoms. The factor 2 in front of the variance δN^2 arises because the total atom number N is retrieved with two detection channels, measuring the ground and excited populations [68].

At RIKEN, for typical operating conditions where $N \sim 300$ atoms are probed the rms fluctuation of the atom number due to electronic detection noise is evaluated to be $\delta N \sim 5$. Accounting for a cycle time of $\Delta t_{\mathrm{c}} = 1.6$ s the instability due to technical atom number fluctuation is $\sigma_y^{\delta N} \sim 5 \times 10^{-17}\ /\sqrt{\tau/\mathrm{s}}$.

2.6.2 The Dick effect and the LO instability

The instability of the local oscillator is usually the dominant contribution to the lattice frequency standard instability. The LO frequency noise affects the clock stability because of the Dick effect [61], named after G. J. Dick, who firstly explained the phenomenon.

The effect arises because in the clock operation the atomic sample is not continuously probed, instead the interrogation process is performed with a duty cycle $T_{\mathrm{i}}/\Delta t_{\mathrm{c}} < 1$.

The presence of a dead time between two consecutive interrogations leads to aliasing of the LO frequency noise, whose components near the harmonics $mf_{\mathrm{c}} = m/\Delta t_{\mathrm{c}}$ (with m an integer factor) are downconverted into the detection band. The clock instability limited by the Dick effect can be estimated in terms of the Allan deviation as [60, 61]

$$\sigma_y^{\mathrm{Dick}}(\tau) = \sqrt{\frac{1}{\tau}\sum_{m=1}^{\infty}\left(\frac{g_{\mathrm{c},m}^2}{g_0^2} + \frac{g_{\mathrm{s},m}^2}{g_0^2}\right) S_y\!\left(\frac{m}{\Delta t_{\mathrm{c}}}\right)}, \tag{2.21}$$

where $S_y\!\left(\frac{m}{\Delta t_{\mathrm{c}}}\right)$ is the one-sided power spectral density (PSD) of LO phase noise evaluated at the Fourier frequencies $m/\Delta t_{\mathrm{c}}$, while $g_{\mathrm{c},m}$, $g_{\mathrm{s},m}$ and g_0 are parameters

defined as

$$\begin{aligned} g_{\mathrm{s},m} &= \frac{1}{\Delta t_\mathrm{c}} \int_0^{\Delta t_\mathrm{c}} g(t) \sin\left(\tfrac{2\pi m t}{\Delta t_\mathrm{c}}\right) \mathrm{d}t \\ g_{\mathrm{c},m} &= \frac{1}{\Delta t_\mathrm{c}} \int_0^{\Delta t_\mathrm{c}} g(t) \cos\left(\tfrac{2\pi m t}{\Delta t_\mathrm{c}}\right) \mathrm{d}t \\ g_0 &= \frac{1}{\Delta t_\mathrm{c}} \int_0^{\Delta t_\mathrm{c}} g(t)\, \mathrm{d}t\,. \end{aligned} \tag{2.22}$$

The function $g(t)$ is the sensitivity function of the interrogation process to laser frequency fluctuations, defined by eq. 2.7.

For a LO instability described by a PSD of

$$S_y(f) = 1.41 \times 10^{-29} f^{-1} + 1.86 \times 10^{-31}\ \mathrm{Hz}^{-1}, \tag{2.23}$$

which is the LO frequency noise measured at INRIM in 2012 [69], the Dick effect instability is calculated to be $2.1 \times 10^{-15}\ /\sqrt{\tau/\mathrm{s}}$, assuming a cycle time of $\Delta t_\mathrm{c} = 320$ ms and an interrogation time of $T_\mathrm{i} = 120$ ms.

Increasing the operational duty cycle does help in the reduction of the Dick effect instability; however, technical limits related to the destructive detection process, and consequently the atom loading time, bound the improvement and have triggered the interest in investigating non-destructive detection schemes [70]. Besides, a direct way of tackling the Dick effect is the realisation of stable oscillators. These are usually achieved using ultra-stable Fabry-Pérot cavities as frequency references. Materials and design of the optical cavities, together with the environment where they are enclosed, are chosen to provide the best isolation from temperature and seismic noise [71–73]. Currently, the ultimate limit is provided by the thermal noise of the cavity mirror coatings [74]. New generations of optical LOs based on a cryogenic silicon cavity have demonstrated a short term instability dominated by a flicker frequency noise as low as $\sigma_y(\tau) = 4 \times 10^{-17}$ [75], which corresponds to a PSD of $S_y(f) \approx 1.2 \times 10^{-33} f^{-1}$: in these conditions the Dick effect is suppressed at $\sigma_y^{\mathrm{Dick}}(\tau) = 2 \times 10^{-17}\ /\sqrt{\tau/\mathrm{s}}$. A recent measurement with this LO has demonstrated an instability where the Dick effect provides a contribution comparable with that of the quantum projection noise [28].

While the Dick limit for the stability of a single frequency standard cannot be avoided, combining two frequency standards in a single zero-dead-time clock allows for the suppression of the Dick effect [27]. This is realised operating two frequency standards based on the same LO in an anti-synchronized way, such that a clock performs the interrogation while the other prepare and detect the atomic sample; as a result the composite clock has no dead time and a 100 % duty cycle. While this approach is effective in suppressing the Dick effect, it requires that two clocks are operated at the same time to realise a frequency standard, and an additional pair of clocks is necessary to perform a frequency comparison. Another

approach to perform frequency measurements beyond the Dick limit between two standards consists of correlating the frequency noise of the two LOs and performing synchronous clock interrogations [67, 76]: the two LOs may be referenced to each other through a phase lock, eventually mediated by a frequency comb; in this way, if the atom interrogation is performed synchronously the LO frequency noise is common mode between the two frequency standards, and cancels out in the frequency comparison, not limiting the stability.

The frequency comparison between a Sr and Yb frequency standards performed at RIKEN and reported in section 4.3 exploits this technique to suppress the instability provided by the Dick effect.

2.7 Yb lattice clock at INRIM

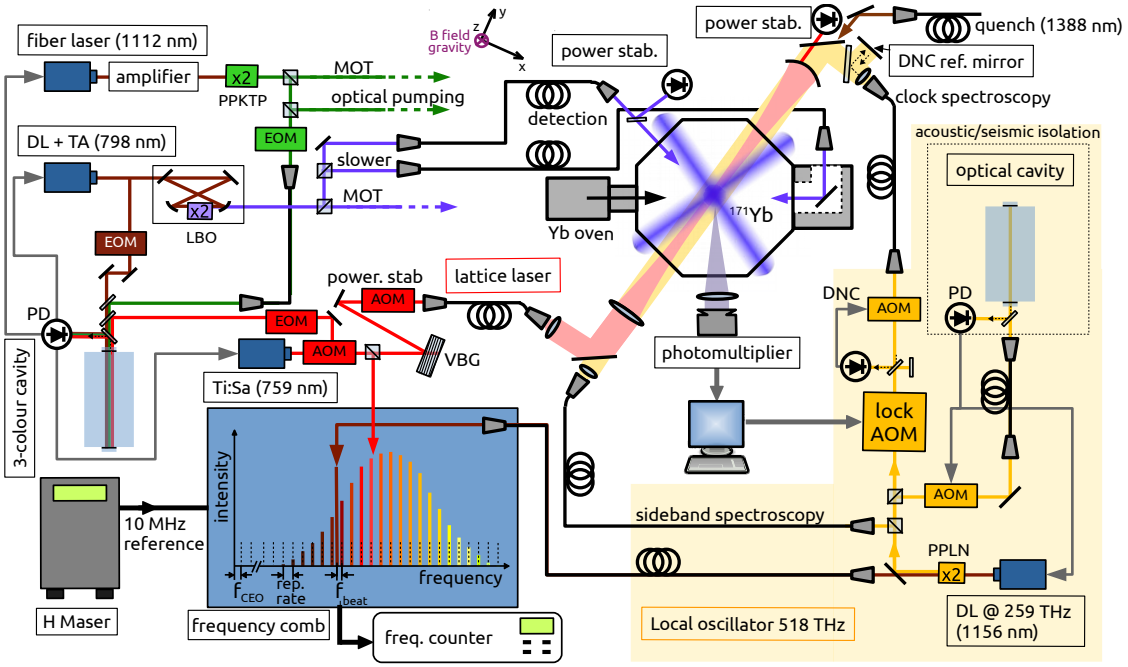

Figure 2.7: Scheme of the INRIM Yb lattice clock setup.

Figure 2.7 shows a scheme of the INRIM Yb lattice clock setup, whereas fig. 2.8 is a picture of it. An atomic oven source [77] at about 400 °C sublimates a sample of solid ytterbium and generates a collimated flux of atoms. A differential vacuum tube separates the oven region, with a residual vacuum pressure of 2×10^{-6} Pa, from the main vacuum chamber for the light-atom interaction, which instead has a residual vacuum pressure of 6×10^{-8} Pa.

The main chamber view ports are designed to provide wide optical access, with a diameter of either 40 mm for the 6 lateral view ports on the horizontal (x,y) plane

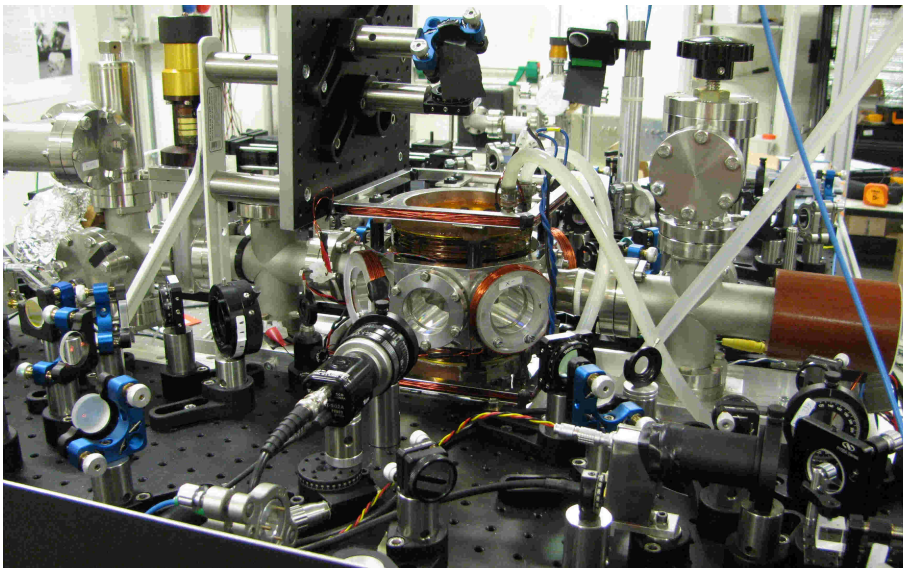

Figure 2.8: Picture of the INRIM Yb lattice clock.

or 70 mm for the two ports on top and bottom of the chamber. The 1 cm thick windows are installed with an indium wire sealing, which is UHV compatible and require a small retaining force which avoids to induce birefringence in the glass. All fused silica-glass windows are provided with an anti-reflection coating at the relevant optical wavelengths, namely at 759 nm for the lattice laser, and at 399 nm and 556 nm for the MOT beams. Of particular importance is the coating at the lattice wavelength providing a residual reflectivity of $R = 0.05$ %, since the lattice beam has a large optical power of about 1 W compared to other beams.

The oven and the main chamber are installed close to each other (the separation distance is $\sim$ 20 cm) to have a sufficient flux of atoms in the MOT region not to require a Zeeman slower decelerating tube (see ref. [78] for details). The atomic flow is slowed with a counter-propagating slower beam at 399 nm and while crossing the main vacuum chamber interact with the three MOT beams. In order to avoid that Yb atoms coat the window for the slower beam access, the slower beam accesses the vacuum chamber from a lateral view port, and it is then reflected on a 45° mirror. The mirror performance degrades over time because of the deposition of material emitted by the oven expected to be mainly Yb, despite Yb is a reflective metal, and require to be replaced with a time scale of about one year. A discussion about mirror coating materials able to maintain good reflectivity when subjected to a flow of Sr atoms (which possibly have similar chemical properties of Yb) can be found in ref. [79].

The lattice is established almost horizontally (with a 60 mrad tilt from the horizontal plane orthogonal to gravity), retro-reflecting the incoming beam on a curved mirror, as shown in figure 2.7. The lattice is focused to a waist $w_0 = 45$ µm,

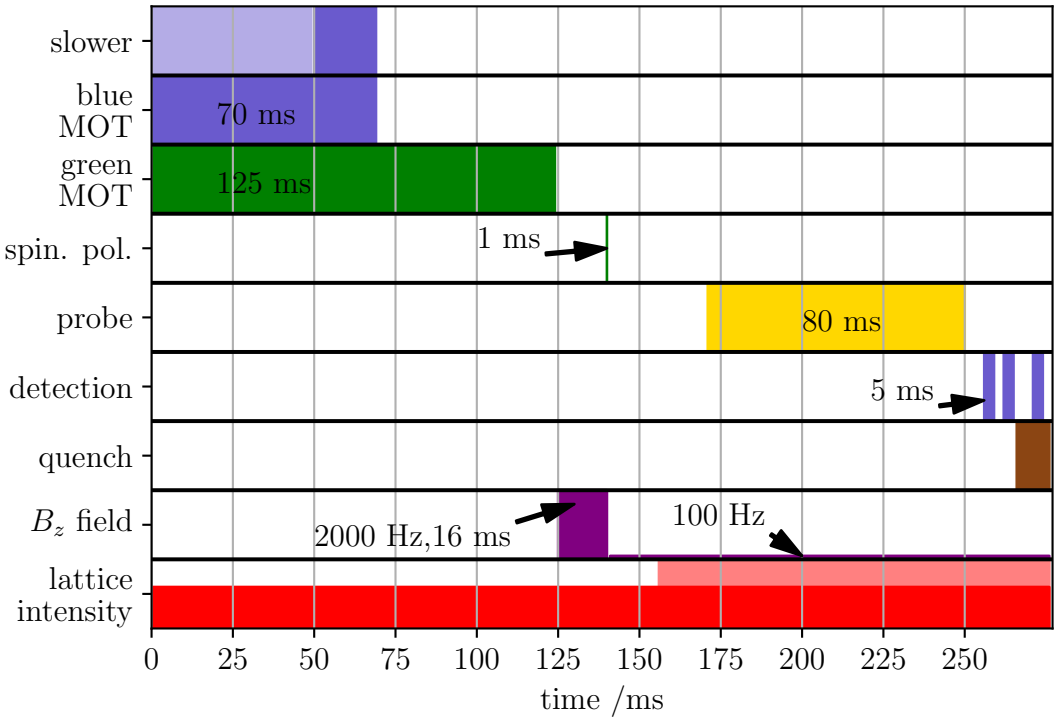

Figure 2.9: Sequence of operation of the Yb clock at INRIM. The slower beam time, as shown by the shaded area, is tuned to load a small or large amount of atoms; this is specially implemented when measuring the collisional shift by alternating the clock operation with a high and a low atomic density condition. MOT magnetic fields are not displayed. The B_z field refer to the external bias magnetic field along the z-axis (along gravity) added to a pre-set offset value constant during operation (see text). The value of B_z corresponds to a splitting between the clock transition π lines as indicated in the figure. The lattice intensity is either maintained at fixed depth $U_0 \sim 250\ E_\mathrm{r}$ (solid area) or increased to the maximum depth $U_0 \sim 400\ E_\mathrm{r}$ (shaded area) for the interrogation and detection. The detection process is performed with three pulses: the first detects the ground state population, the second the background signal, while the third measures the excited state population.

and delivers a maximum trap depth $U_0^{\max} \sim 400\ E_\mathrm{r}$. The deformation of the radial confinement because of the gravitational force determines a minimum trap depth $U_0^{\min} \sim 250\ E_\mathrm{r}$ below which the lattice cannot reliably trap atoms.

The clock sequence of operation is detailed in figure 2.9. The cycle time is $\Delta t_\mathrm{c} = 277$ ms, and it can be increased to accommodate a longer loading time or longer interrogation time.

Bias magnetic fields along the three spatial axes are set to fixed offset values to compensate the magnetic field of the environment. Then an additional magnetic

field term B_z is added along the vertical axis to define the quantization axis and split the Zeeman levels, as shown in fig. 2.9. Optimised bias offset settings are reached at $B_z = 0$ when the splitting between the two π lines is not observed and the degenerate unpolarised transition excitation is maximal, as done in ref. [80]. We typically achieve an excitation of the unpolarised line of $P \sim 0.8$. This technique provides a reference setting for the bias fields.

2.7.1 Optical radiations

The 399 nm radiation, as shown in fig. 2.7, is obtained though resonant second-harmonic generation (SHG) [81] in a non-linear lithium-triborate (LBO) crystal of a 798 nm laser source [82], provided by a diode laser (DL) injected in a tapered amplifier (TA). Both the DL and TA are manufactured by TOPTICA Photonics and the combined system delivers an output power of 2.7 W at full TA current of 3780 mA, with a linear current-to-output power characteristic. The mode of the beam is cleaned to a TE00 mode by coupling the laser to an optical fibre, whose transmission efficiency is 50 % to 70 %.

The frequency doubling is performed in a bow-tie enhancement cavity [82], frequency locked exploiting the Hänsch-Couillaud technique [83]. With an input power to the cavity of 1.2 W and optimized conditions the output power at 399 nm is 400 mW.

The radiation at 556 nm is generated through SHG in a non-linear periodically-poled potassium titanyl phosphate (PPKTP) crystal from a 1112 nm laser. The input laser is a 10 mW doped fiber laser (Koheras Adjustik, NKT), amplified in a fibre amplifier (Keopis) to obtain an optical power of 1.3 W. Frequency doubling is performed in single pass, and generates 10 mW of green light.

The lattice laser is a Ti:Sapphire tuned to 759 nm (SolsTiS, M squared), using as a pump a 532 nm, 10 W solid-state laser (Sprout, Lighthouse Photonics). The output power with optimized operation is 2.4 W. The spectrum of the output mode is filtered with a volume Bragg grating (VBG) with 20 GHz bandwidth centred at the lattice magic frequency to remove undesired spectral components which may contribute with unexpected light shifts. The cavity-stabilised lattice laser has a frequency drift of 2 kHz h^{-1} [84], and its frequency is continuously measured by acquiring the beatnote with an optical frequency comb. We conservatively assign an uncertainty of 100 kHz in its estimation.

As shown in figure 2.7, these three radiation sources are all frequency stabilized to a single 10 cm optical Fabry-Pérot cavity [55, 84], called 3-colour cavity, whose mirrors are provided with reflection coatings at the three wavelengths of interest, namely 399 nm, 556 nm and 759 nm. We observe that in the presence of the 399 nm light in the cavity, the cavity frequency drift hugely increases; we attribute this to mirror thermal effects induced by the optical absorption of the energetic 399 nm photons. We thus decide to frequency stabilize the 399 nm radiation by sending

to the cavity the fundamental laser at 798 nm, whose wavelength is close to the lattice wavelength and thus is included in the mirror reflectivity band.

The radiation at 1388 nm radiation required to quench the $^3P_0$ state is generated with a pigtail distributed feedback diode laser (NKT) with an output power of about 10 mW which is sent to the atoms without attenuation, beside the extraction of a pick-up beam for wavelength monitor. The $^3P_0$-$^3D_1$ transition is power broadened to a linewidth $\gamma \sim 300$ MHz. Since the laser frequency drift in one day of operation is smaller than the transition linewidth, it does not affect the performance of the repumping process, and therefore the laser frequency does not require an additional stabilization system.

Power broadening the transition allows to easily perform the detection process, however it induces a light shift of the clock excited state breaking the sideband cooling process. While we currently do not implement such state preparation stage, in the future we plan to include it in the operation sequence, thus we will reduce its power and stabilize its frequency.

Local oscillator

The local oscillator is a frequency stabilized laser at 578 nm. The laser source is a quantum dot DL laser (DL-PRO, TOPTICA Photonics) at 1156 nm, operated

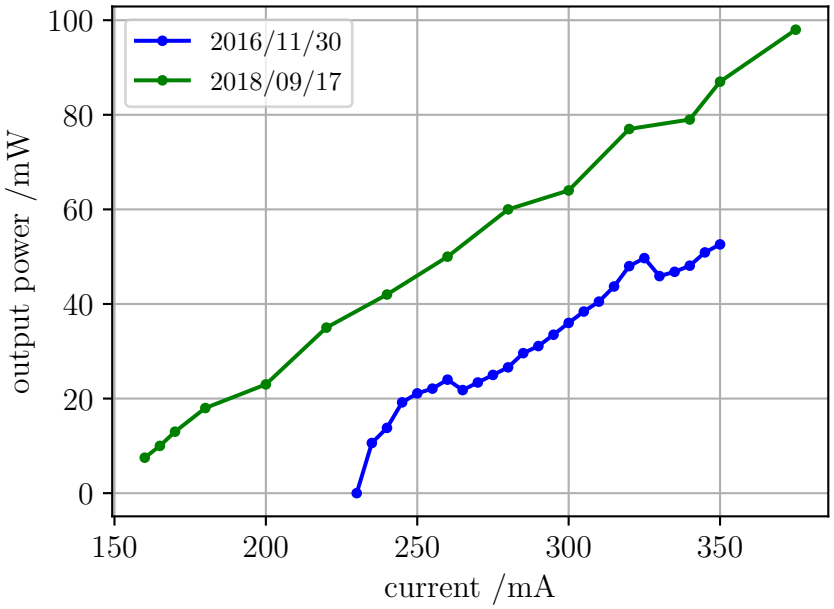

Figure 2.10: Output power of the 1156 nm DL in terms of the diode current for the original diode (measurement performed on Nov. 2016) and the replacement diode currently in use (measurement performed on Nov. 2018).

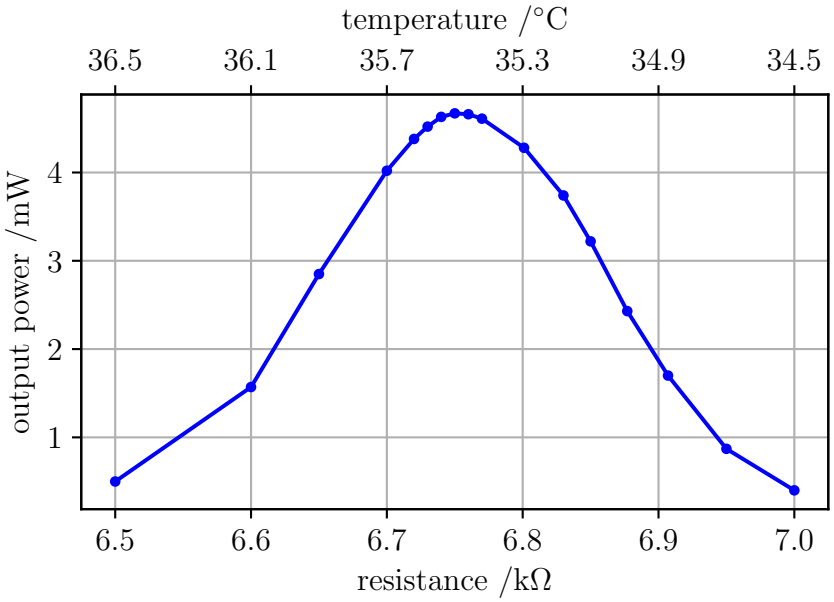

Figure 2.11: Output power at 578 nm generated by the SHG module with an input power at 1156 nm of ~ 40 mW.

at a controlled temperature of 20 °C. Figure 2.10 shows the laser output power in terms of the diode current, relative to either the original diode installed in the system (blue dots) or the replacement diode currently in use (green dots). The original diode broke after about one year of intensive operation; as shown in the figure the replacement diode showed from the beginning a better performance in terms of lasing threshold and output power.

The 1156 nm laser beam is fibre coupled, with a coupling efficiency of ~ 70 %, and injected for SHG in a non-linear periodically-poled lithium niobate (PPLN) crystal (NEL Crystal, NTT). The module consists of a PPLN waveguide enclosed in a case provided with a thermoelectric cooler (TEC) and a thermistor for resistance-based temperature readings. The SHG is performed in single pass through the crystal. Figure 2.11 shows the output power at 578 nm generated by the SHG module with an input power at 1156 nm of ~ 40 mW. The reading of the resistance R is converted to a temperature value T according to the equation

$$\frac{1}{T} = \frac{1}{T_0} + \frac{\ln\left(\frac{R}{R_0}\right)}{B}, \tag{2.24}$$

with $T_0 = 25$ °C, $R_0 = R(T_0) = 10$ kΩ and $B = 3450$. With an input power of about 60 mW, corresponding to the usual current working point of 325 mA, the output power is ~ 7.5 mW.

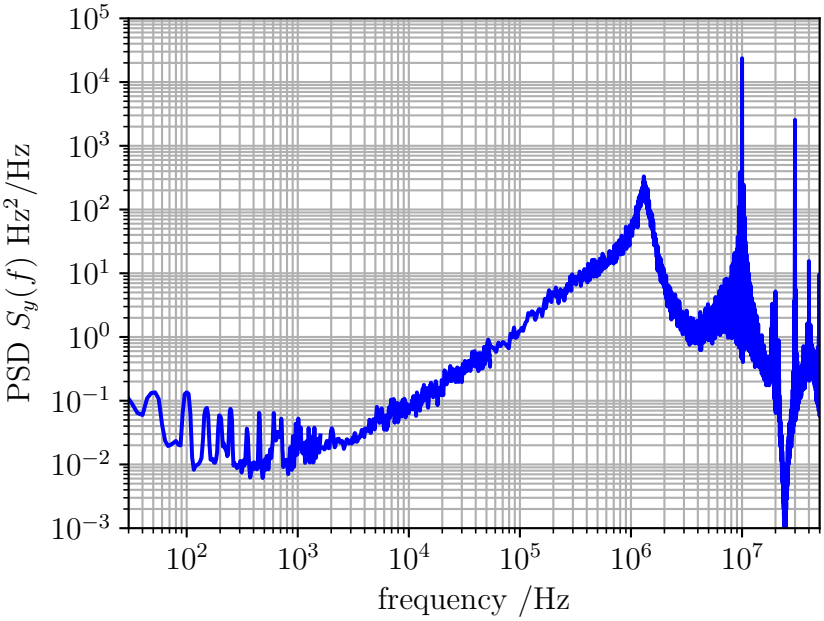

Figure 2.12: In-loop power spectral density of the 578 nm laser locked to the optical cavity, showing a control loop bandwidth of ~ 1.3 MHz.

The DL frequency can be coarsely tuned either with the alignment of the laser grating or the temperature set point. The temperature tuning allows for frequency variations of about 10 GHz °C^{-1}, however an increase or decrease of the temperature set point by 0.5 °C is sufficient to induce a mode hop, which results in a frequency jump back to the original frequency making the tuning ineffective. Fine tuning of the output frequency is performed acting on the diode current and the voltage of the laser cavity piezoelectric device, which induces frequency variations of about 260 MHz V^{-1}.

The DL is frequency stabilized to a 10 cm Fabry-Pérot optical cavity with a finesse $F = 224\,000$ [69], with a spacer made of Corning ultra low expansion glass (ULE) and fused silica mirrors provided with high-reflection coatings at 578 nm and ULE compensation rings. The frequency stabilization is realised through the Pound-Drever-Hall technique [85, 86] delivering to the cavity a EOM-modulated 578 nm beam and acquiring the backreflection signal from the cavity input mirror. The frequency stabilization control loop has a bandwidth of about 1.3 MHz, as shown by the in-loop power spectral density of figure 2.12. The beam is power stabilized at 10 µW.

The cavity is enclosed in a stainless steel vacuum chamber with a thermal insulation provided by an external layer of foam and aluminium foil. An in-vacuum copper shield reflecting the black body radiation provides thermal homogeneity

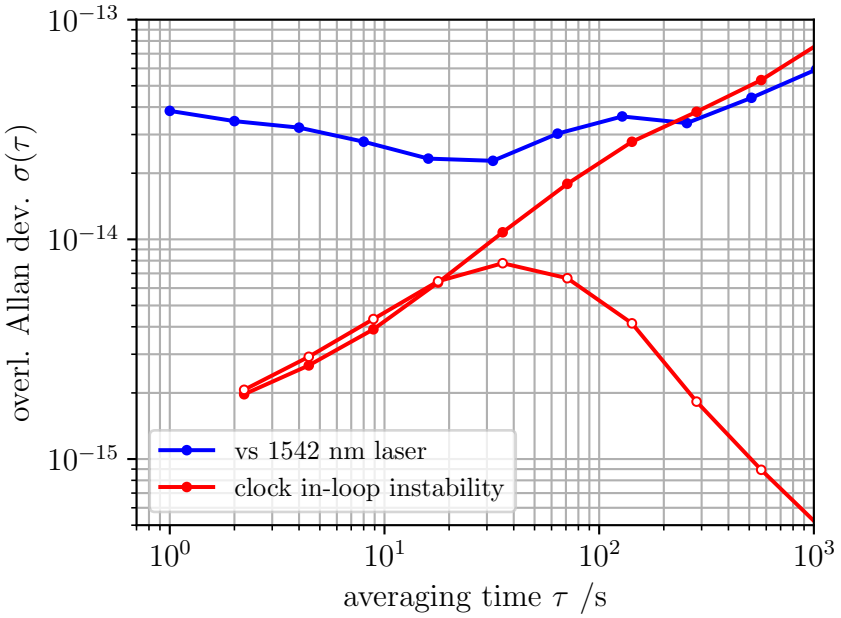

Figure 2.13: Instability of the LO either measured against a 1542 nm laser stabilized on a separate cavity (blue curve), or acquired through the clock in-loop frequency corrections applied to the lock AOM to stabilize the LO to the atomic reference (red filled markers). Open markers show the in-loop stability retrieved from frequency correction data while implementing an additional low-bandwidth drift-compensation loop.

and stability. Further details of the vacuum package are reported in ref. [69, 78]. The cavity is temperature controlled implementing an active disturbance rejection control (ADRC) [87], with heaters installed on the external surface of the vacuum chamber.

We measure the instability of the local oscillator against a 1542 nm laser frequency stabilized on a separate Fabry-Pérot ULE cavity, whose long-term frequency drift is controlled with a low-bandwidth digital lock to an H maser. The ratio stability, shown in figure 2.13 (blue curve) in terms of the overlapping Allan deviation, shows a flicker floor of $\sim 3 \times 10^{-14}$ $(\tau/\mathrm{s})^0$ for short averaging times dominated by the 1542 nm laser instability, and a drift for longer averaging times due to the residual thermal expansion of the 578 nm cavity.

The measured instability is compared with that extracted from the frequency corrections applied lo the lock AOM (shown in fig. 2.7) to maintain the LO locked to the atomic reference (red filled markers in figure 2.13). Like the filled markers, open markers are obtained from the lock data, but in this other case an additional digital real-time low-bandwidth dedrift of the cavity frequency (with a time constant of 50 s) is implemented in addition to the main control loop. Open markers thus show

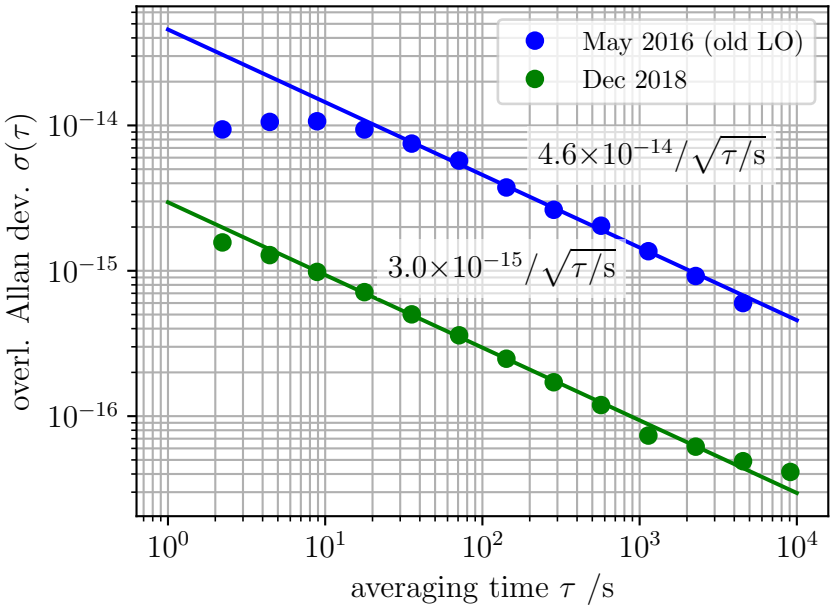

Figure 2.14: Interleaved stability of the Yb frequency standard in term of the overlapping Allan deviation.

the de-drifted in-loop stability.

The current local oscillator is an improvement from a earlier system, whose laser source was obtained through sum frequency generation from two infra-red lasers at 1030 nm and 1319 nm in a waveguide PPLN crystal, and stabilized with a different cavity-based setup. Details of the previous system can be found in [69, 88]. The new LO generation allows for a more reliable operation in terms of output power, while the improved LO frequency stabilization system now allows to perform frequency measurements with an instability reduced by more than a factor 10 from earlier results, as shown in figure 2.14. The frequency standard interleaved stability is still limited by the LO frequency noise, and is assessed to be $2 \times 10^{-15}\ /\sqrt{\tau/\mathrm{s}}$ to $3 \times 10^{-15}\ /\sqrt{\tau/\mathrm{s}}$ according to the level of optimization of the cavity optical setup and the duration of the clock cycle time.

The improved coherence time of the local oscillator now allows to probe the clock transition with interrogation pulses of duration $T_\mathrm{i} \leq 240$ ms, leading to a Fourier limited rabi spectroscopy showing a linewidth of $\gamma = 3.3$ Hz with $T_\mathrm{i} = 240$ ms (see fig. 2.15). The Rabi line shape fit shown in the figure is obtained through eq. (2.5) fixing the interrogation time and allowing a Rabi frequency inhomogeneity according to the atomic sample temperature, which is left as a free parameter. Since we do not apply axial cooling of the atomic ensemble, the temperatures along the three spatial directions are same and included in the model with a single

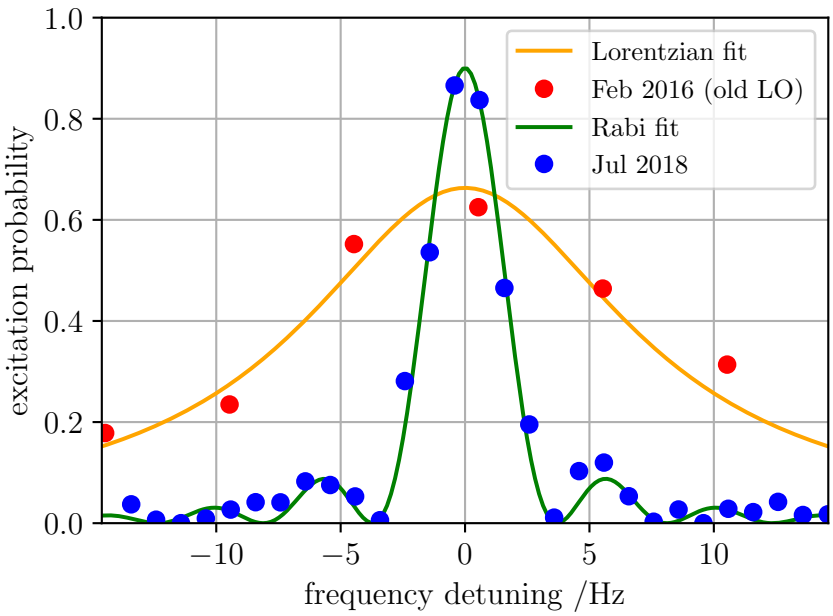

Figure 2.15: Rabi spectroctrocopy of the clock transition performed either with the current LO (blue) allowing an interrogation time $T_\mathrm{i} = 240$ ms, which leads to a Fourier limited linewidth $\gamma = 3.3$ Hz, or with the old system (red), whose smaller coherence time allowed for pulses of duration $T_\mathrm{i} = 60$ ms leading to a Lorentzian linewidth $\gamma = 16$ Hz.

parameter, which is estimated to be $T = 4.4$ µK [89].

2.8 Yb lattice clock at RIKEN

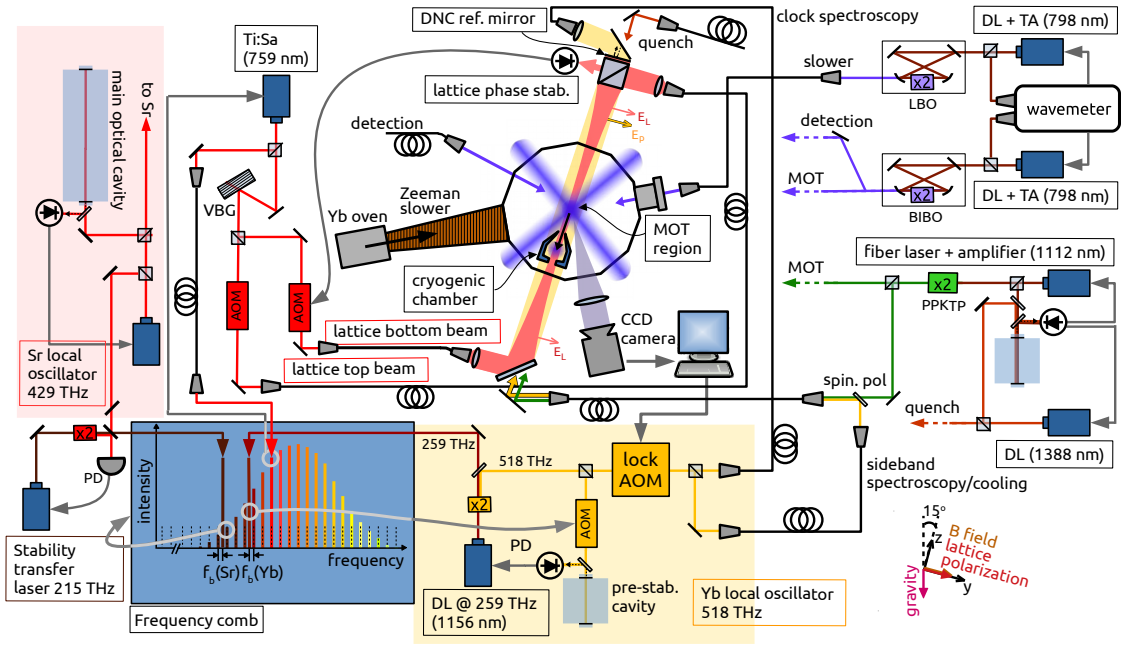

Figure 2.16: Scheme of the RIKEN Yb lattice clock setup.

The experimental setup of the Yb lattice clock at RIKEN is shown in figure 2.16, while figure 2.17 shows a picture of the clock. A complete description of the system can be found in ref. [53]. The Yb effusive oven is a custom system with a similar design of ref. [77], and it is operated at a temperature of about 400 °C. The collimated flux of atoms propagates along a Zeeman slower pipe before reaching the main vacuum chamber. The Zeeman slower realises a magnetic field gradient along the pipe shifting the energy of the $^1S_0$-$^1P_1$ transition through the Zeeman effect: in combination with a circularly polarised 399 nm slower beam counter-propagating with the atomic flux it allows to laser cool the atoms, which are maintained resonant with the laser light all along the pipe despite the change in velocity thanks to the carefully tuned magnetic field gradient.

The main vacuum chamber is provided with twelve view ports allowing the access of the laser beams propagating in the vertical (z,y) plane, and with a single view port allowing the access along the x-axis: an intra-vacuum mirror back-reflects the MOT beam propagating along this direction, while other MOT beams are back-reflected with out-of-vacuum mirrors.

This lattice clock can be operated in cryogenic configuration (see ref. [24]) to suppress the effect of the black body radiation (BBR) emitted by the environment on the atomic energy levels (see section 3.3). The BBR-induced energy shift of the clock transition becomes critical when the atoms are interrogated, as it results

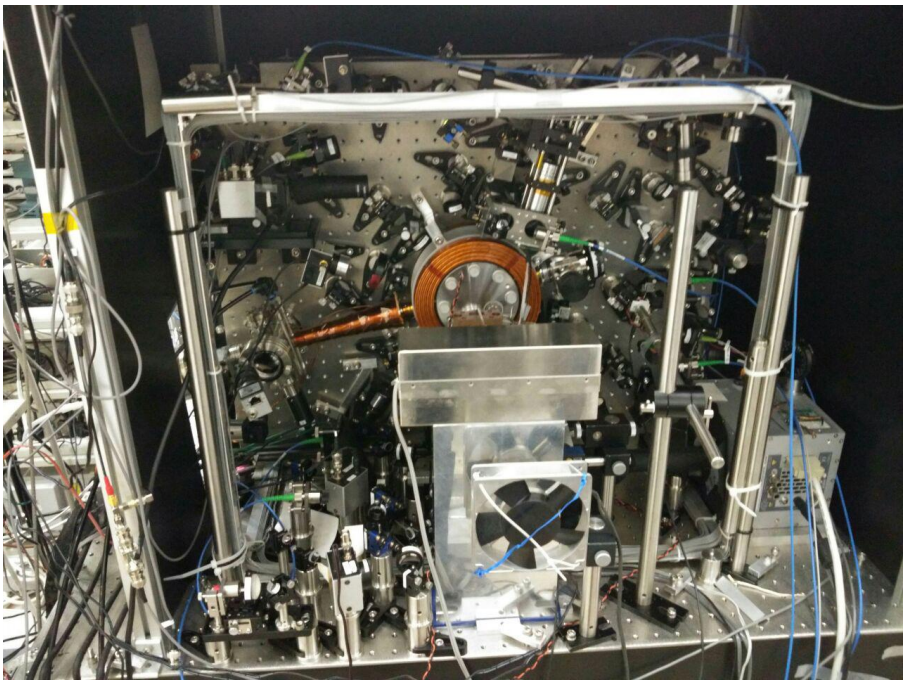

Figure 2.17: Picture of the RIKEN Yb lattice clock.

in a systematic shift of the measured frequency from the unperturbed value. To suppress the perturbation, atoms are interrogated in a small cryogenic chamber installed within the main vacuum chamber and kept at a temperature $T \leq 100$ K by a Stirling refrigerator.

The lattice is established vertically, with a tilt of 15° from the axis defined by gravity. In the clock operation atoms are loaded in the lattice in a room-temperature environment, transported into the cryogenic chamber to interact with the probe laser and transported back outside of the cryogenic chamber for the detection process. Atoms can be transported along the lattice axis by establishing the lattice with two separate beams counter-propagating with each other; a controlled frequency detuning between the beams forms a moving lattice. The transport is realised gradually ramping the frequency detuning up to 2 MHz in 30 ms, corresponding to a peak velocity of 76 $\mathrm{cm\,s^{-1}}$, and then applying a similar ramp with opposite detuning to gradually decelerate the atoms to the desired location in the cryogenic chamber [24]. This moves the atoms by 20.5 mm from the MOT region, to a position 7.5 mm inside the cryogenic chamber. When the transport is concluded the relative phase of the two lattice beams is actively stabilized with respect to the phase reference surface shown in figure 2.16. This is performed phase-modulating one of the two beams and acquiring the beat note signal between the two laser beams with the photodetector shown in the drawing, and based on that applying frequency corrections to one of the two beams [24].

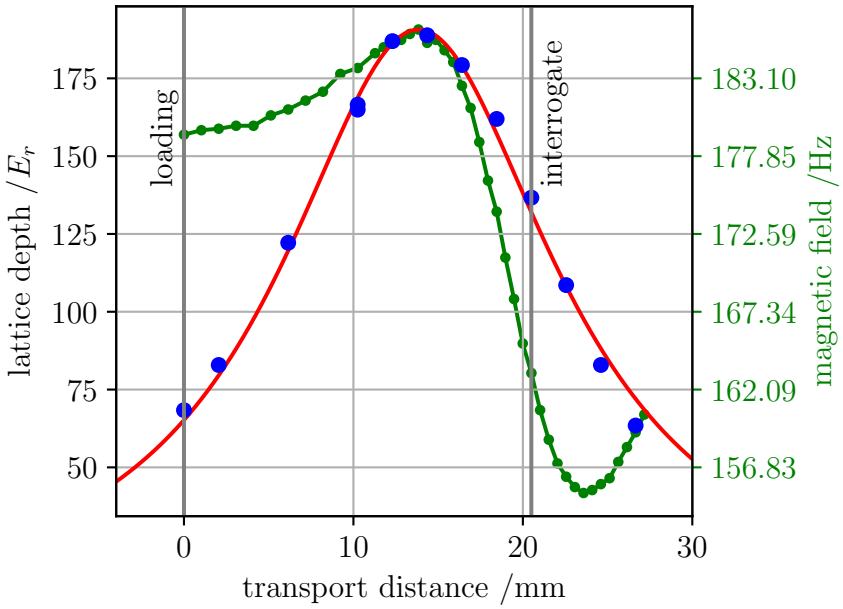

Figure 2.18: Axial trap depth measured at different transport distance (blue dots), with the loading position at the origin of the axis. Red curve is a fit assuming an intensity profile provided by two identical overlapping Gaussian beams, with the beam waist position and size, together with a scaling factor, as the only free parameters. Green label and scale refer to the green data, which is the magnetic field profile measured along the transport distance in terms of the Zeeman linear shift of the clock π transitions.

The cryogenic chamber, to allow the access of the atoms, is crossed by the lattice through two narrow apertures of diameter $\phi_1 = 0.5$ mm and $\phi_2 = 1$ mm. To provide thermal homogeneity the chamber is made of copper, and the inner surface is black-coated to avoid BBR reflections. The estimation of the residual BBR leaking thorough the apertures and affecting the atomic sample is the limiting contribution in the evaluation of the BBR-induced clock transition frequency shift [24].

The chamber also works as a Faraday cage isolating from external DC electric fields [90].

The lattice beams are focused near the entrance to the cryogenic chamber. This is chosen as a compromise to have a sufficient lattice depth U both in the MOT region, where atoms are loaded in the lattice, and inside the cryogenic chamber where atoms are interrogated (see figure 2.18). Moreover, loading atoms at lower trap depth than where they are probed ensures that radially hot atoms, initially at the edge of the trap, once are moved to the cryogenic chamber do not occupy far-off axis regions of the lattice.

A large lattice waist is desirable to allow atoms spread over a large number of

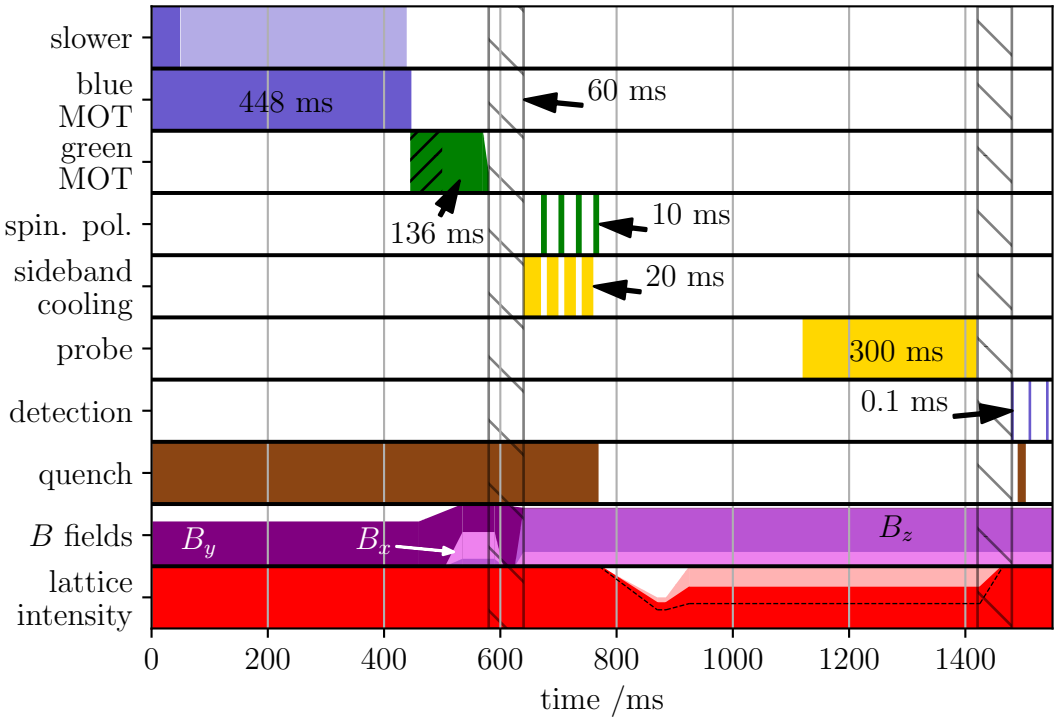

Figure 2.19: Sequence of operation of the Yb clock at RIKEN. The long hatched areas indicate the 60 ms atom transport phases to and from the cryogenic chamber. During the green hatched interval, the green MOT laser is frequency modulated at increased detuning in order to increase the capture velocity and allow for an efficient transfer of the atoms from the blue to the green MOT. The interaction time of the slower beam can be tuned as shown by the shaded area to load either a low density or a high density lattice. The lattice intensity solid profile is implemented during standard clock operation, while the shaded area and the dashed level indicate the two sequences adopted in the light shift measurements for the high and low intensity cases respectively. Maximum intensity provides a trap depth $U_0 \sim 135\ E_\mathrm{r}$. The total cycle time is 1.6 s; the duration of the cycle is deliberately set to match that of the Sr clock to perform synchronous interrogations during the frequency ratio measurement discussed in section 4.3. The clock can be operated without effects on the performance with a shorter cycle of $\Delta t_\mathrm{c} \sim 1.1$ s.

lattice sites with similar trap depth and thus suppress cold collisions, however this has to be balanced with the available optical power and required trap depth.

These criteria are all considered when defining the lattice geometry. The final shape of the lattice is retrieved measuring the trap depth at different transport distances, as shown in figure 2.18.

The fit (red curve) of the experimental data (blue dots) is obtained assuming that the two beams are identical and perfectly overlapping along the z-axis (the

lattice axis) with a profile of the form

$$U = 4\alpha_{\mathrm{E1}} \frac{2P_{\mathrm{L}}}{\pi w_0^2 \left(1 + \left(\frac{z-z_0}{z_{\mathrm{R}}}\right)^2\right)}, \tag{2.25}$$

where $P_{\mathrm{L}} = 0.5$ W is the power of each beam, w_0 and z_0 are the size and position of the lattice waist and $z_{\mathrm{R}} = \pi w_0^2/\lambda_{\mathrm{L}}$ is the Rayleigh range in terms of the lattice wavelength λ_{L}. The free parameters of the fit are $z_0 = 13.8(1)$ mm, $w_0 = 49.1(6)$ µm and $\alpha_{\mathrm{E1}} = h \times 7.3(1)$ kHz/(kW/cm^2) , which can be compared with a theoretical value calculated at the magic wavelength $\lambda_{\mathrm{L}} = \lambda_{\mathrm{magic}}$ of $\alpha_{\mathrm{E1}} = h \times 8.7$ kHz/(kW/cm^2) [91].

The vacuum chamber windows attenuate the lattice beam power by some percent. Assuming a maximum attenuation of 10 %, then $P_{\mathrm{L}} = 0.45$ W and the fitted parameters result unchanged except for the dipole polarizability which becomes $\alpha_{\mathrm{E1}} = h \times 8.1(2)$ kHz/(kW/cm^2), in better agreement with the theoretical expectation.

From the extracted parameters is possible to estimate the lattice radius at the loading position to be $w_{\mathrm{load}} \sim 84$ µm, while inside the cryogenic chamber where atoms are probed the radius is $w_{\mathrm{interr}} \sim 59$ µm. This also allows to estimate the radial trap frequency of the atoms in the cryogenic chamber, which is $\nu_r \sim 80$ Hz according to eq. (2.2).

Figure 2.18 shows also the spatial profile of the magnetic field measured in terms of the linear Zeeman shift of the clock π transitions. Near the cryogenic chamber entrance there is a steep change of the profile because of the chamber shielding effect. The chamber conductive material deviates the field lines which preferentially propagate within the material; as a result the magnetic field intensity reduces in the shielded volume.

Figure 2.19 shows the clock sequence of operation. Atoms are firstly loaded in the full intensity lattice ($U_0^{\mathrm{load}} \sim 68\ E_{\mathrm{r}}$) and moved in the cryogenic chamber, then they are state-prepared through a sequence of interleaved pulses of either axial sideband cooling or spin polarisation [58] (details are provided in section 2.3). State preparation is also performed at full lattice intensity, corresponding to a trap depth $U_0^{\mathrm{cryo}} \sim 137\ E_{\mathrm{r}}$.

The lattice intensity is then ramped down to a value between 30 % to 50 % of the maximum intensity in 100 ms, and after 15 ms is ramped to the desired level for the interrogation process over an interval of 40 ms. This sequence is a cleaning intensity dip which removes from the trap atoms in highly excited radial states to reduce the radial temperature. In general, to be effective the level of the intensity dip is chosen to be some tens percent lower than the final intensity level during interrogation. In typical operation the interrogation is performed at $U_0^{\mathrm{interr}} = 92\ E_{\mathrm{r}}$ (corresponding to the 65 % of the available intensity), with a cleaning dip at $U_0^{\mathrm{dip}} \sim 55\ E_{\mathrm{r}}$.

Intensity ramps are performed adiabatically over several tens of milliseconds

to avoid that the intensity gradient may lead to synchronous radial oscillations of the atoms in the trap. Such radial oscillation may result in a systematic radial Doppler shift if a residual misalignment of the probe beam from the lattice axis is present. In addition, where the atomic cloud is located the lattice wavefront is curved, defining a radial intensity gradient towards the lattice waist; an atomic cloud radially displaced from the lattice axis is then pushed towards the lattice waist, inducing an axial Doppler shift. The dephasing of radial oscillations that might persist after the intensity ramp is ensured by delaying the interrogation process by > 100 ms from the end of the ramp. In general, long interrogation pulses allow to average such Doppler shifts over the entire (or multiple) oscillation period, further reducing the probability of a residual systematic shift.

Similar intensity sequences are implemented during the light shift measurements, where high and low lattice intensity conditions are interleaved. In these cases intensity levels of the cleaning dip are varied along with the ultimate intensity, set either to 40 % intensity ($U_0^{\mathrm{dip}} = 45\ E_{\mathrm{r}}$ / $U_0^{\mathrm{interr}} = 60\ E_{\mathrm{r}}$) or 100 % intensity ($U_0^{\mathrm{dip}} = 65\ E_{\mathrm{r}}$ / $U_0^{\mathrm{interr}} = 135\ E_{\mathrm{r}}$).

2.8.1 Optical radiations

The 399 nm radiation is provided by two laser sources. Both sources are custom systems based on a 798 nm external cavity diode laser (ECDL) amplified by a tapered amplifier (TA) and frequency doubled with second harmonic generation (SHG) in a bow-tie cavity locked with the PDH technique. The SHG is realised in the first system with a BIBO crystal, while the second system uses a LBO crystal which shows better performances in terms of efficiency and stability of the output intensity. The laser diodes are manufactured by eagleyard Photonics, while the tapered amplifiers by m2k-laser.

The 798 nm laser beams are frequency stabilized on a wavemeter, as shown in fig. 2.16.

The first system has an output power at 399 nm of 180 mW, and provides the laser beams for the MOT and detection. The second system has an output power of 240 mW and it is used as the beam for the Zeeman slower.

The radiation at 556 nm is generated through single-pass SHG in a waveguide PPLN crystal (NTT Electronics), using as fundamental laser an amplified fibre laser at 1112 nm (Orange One-1PM, MenloSystems). The frequency of the seed laser is stabilized on a vertical cavity with spacer in ULE glass with the PDH technique. The same cavity is used to frequency stabilize the quenching laser at 1388 nm, which is generated with a custom grating-stabilized ECDL based on a gain chip (Thorlabs).

The lattice laser is a Ti:Sapphire tuned at 759 nm (SolsTiS, M squared), pumped with a 532 nm, 18 W solid-state laser (Sprout, Lighthouse Photonics). The laser output power with optimized performance is 5 W; for the clock standard cryogenic

operation, a minimum beam power of 4 W is required for the operation of the lattice. The laser is spectrally filtered by a reflective VBG with 40 GHz bandwidth and then split in two beams whose power before the injection in the optical fibre is $\sim$ 1 W. The lattice frequency is stabilized on a erbium-fibre optical frequency comb developed at NMIJ/AIST [92].

Local oscillator

The local oscillator is based on a laser source at 578 nm (518 THz) generated though single-pass SHG in a waveguide PPLN crystal (NTT Electronics). The fundamental laser at 1156 nm (259 THz) is realised as a custom grating-stabilized ECDL with laser diode manufactured by Innolume. The laser frequency is stabilized on a vertical 75 mm ULE cavity at 578 nm though the PDH technique. To improve the LO stability performance, the IR laser is phase locked to an optical frequency comb [93] (a commercial erbium-fibre frequency comb FC1500-250-ULN, by Menlo Systems) referenced to the ultra-stable local oscillator of a different frequency standard operated at RIKEN based on strontium (Sr) atoms [24]. With such local oscillator we achieve a clock interleaved stability of $\sigma(\tau) \sim 6 \times 10^{-16} \, / \sqrt{\tau/\mathrm{s}}$.

The Sr local oscillator is realised stabilizing an ECDL at 429 THz on a 40 cm-long optical cavity whose spacer is made in low thermal expansion AZ glass and mirrors are in fused-silica [24]. Its spectral purity is transferred to the optical frequency comb through phase locks [94]. This is realised through an additional ECDL at 215 THz (half the Sr frequency) frequency doubled in a waveguide PPLN crystal. The frequency-doubled transfer laser is phase-locked to the Sr oscillator after acquiring the beat note between the two lasers on a photodiode (PD) as shown in figure 2.16, while its fundamental harmonic is delivered to the frequency comb. The frequency comb is phase locked to the transfer laser to stabilise its repetition rate, so as to transfer the stability properties of the reference Sr LO oscillator to the comb. This realises a universal oscillator which provides a stable frequency reference over a range of more than a hundred nanometres [93].

The frequency stability of the Sr local oscillator is transferred to the Yb oscillator at $\nu_{\mathrm{Yb}} = 518$ THz through the optical frequency comb by a phase lock loop, realised acquiring the beat note between the fundamental radiation at 259 THz and the comb and applying frequency corrections to an AOM located in the path to the pre-stabilisation cavity (see fig. 2.16, details are in ref. [53]).

The short pre-stabilization cavity of the Yb oscillator provides an additional stabilization stage which makes the bandwidth requirements of the phase-lock-loop used to lock the Yb laser to the Sr laser less stringent. In addition it allows to operate the Yb clock when either the frequency comb, the transfer laser or the Sr laser are not available.

Chapter 3

Clock systematic frequency shifts

This chapter is aimed at discussing all relevant perturbations of the atomic clock transition leading to systematic frequency shifts. Strategies to either cancel or properly measure the effect of such perturbation on the clock frequencies are presented, together with results obtained with the INRIM and RIKEN Yb lattice clocks.

3.1 Zeeman shift

The presence of an external magnetic field $\boldsymbol{B}$ perturbs the atomic electronic structure, inducing shifts of the energy levels.

As far as the $^1S_0$ and the $^3P_0$ clock states are concerned, since the nuclear spin of ^{171}Yb is $I = 1/2$ and the angular momentum $J = 0$, then the total angular momentum operator $\boldsymbol{F} = \boldsymbol{I} + \boldsymbol{J} = \boldsymbol{I} + \boldsymbol{S} + \boldsymbol{L}$ generating the hyperfine structure is described by the quantum numbers $F = 1/2$, $M_F = \pm 1/2$ for both states, where M_F is the eigenvalue of the operator F_z resulting from the projection of the total angular momentum along the quantization axis defined by the magnetic field axis (e.g. the z-axis). This results in doubly degenerate clock states. The most visible effect of the field perturbation on the clock transition is the break of the hyperfine degeneracy, inducing a splitting into sublevels (see fig. 3.1, inset).

Even if both the ground and the excited clock states are affected by the perturbation, the energy difference between clock states is not conserved because of the fine and hyperfine interactions, which induce a mixing of the $^3P_0$ state with the $^3P_1$, $^3P_2$ and $^1P_1$ states [96] (without affecting the ground state). As a consequence the magnetic field generates a frequency shift of the clock transition termed Zeeman shift.

The interaction between the atoms and an external magnetic field depends on the atomic total magnetic moment $\boldsymbol{\mu_Z}$, and it is described by the Hamiltonian

$$H_Z = -\boldsymbol{\mu_Z} \boldsymbol{B}. \tag{3.1}$$

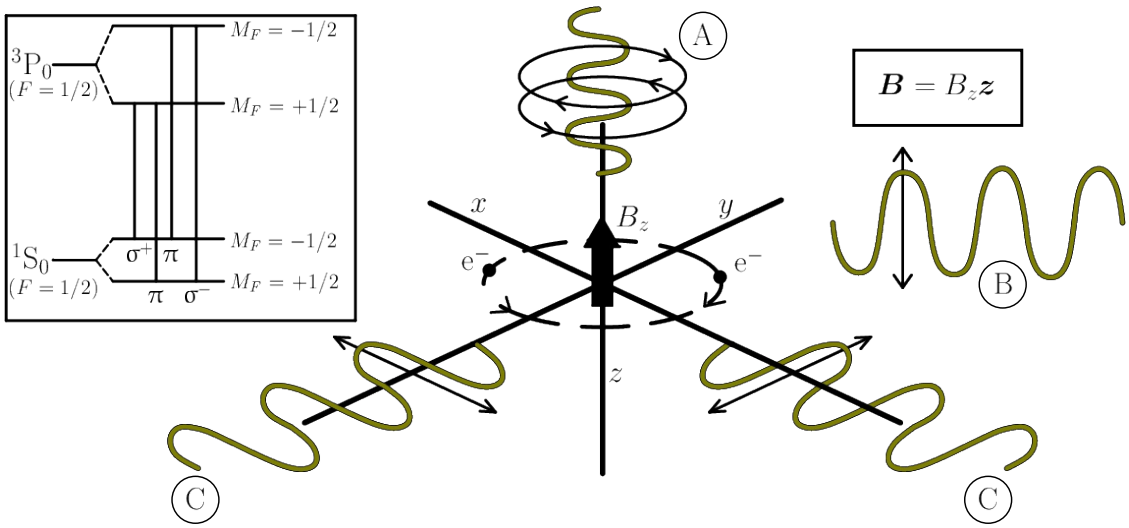

Figure 3.1: Inset: Scheme of the π and σ Zeeman transitions arising between the two clock states because of the external magnetic field. Drawing of the classical picture of the light-atom interaction in the presence of an external magnetic field $\boldsymbol{B}$ along the z-axis to figuratively understand the light polarisation required to excite the specific Zeeman transitions [95]. A, B and C letters indicate the different light polarisation orientations discussed in the text. The π transitions are excited with light linearly polarised along the quantization axis, while σ transitions are excited with circularly polarised light propagating along the quantization axis or linearly polarised light propagating perpendicularly to the quantization axis.

The atomic magnetic moment arises from the coupling between the electronic spin $\boldsymbol{S}$, the angular momentum $\boldsymbol{L}$ and the nuclear spin $\boldsymbol{I}$ (all in units of $\hbar$) according to [95]

$$\boldsymbol{\mu_Z} = -g_J\mu_B\boldsymbol{J} + g_I\mu_B\boldsymbol{I} = -\mu_B\boldsymbol{L} - g_s\mu_B\boldsymbol{S} + g_I\mu_B\boldsymbol{I}, \tag{3.2}$$

where $\mu_B = e\hbar/2m_e = 9.274 \times 10^{-24}$ J T^{-1} is the Bohr magneton, with m_e the electron mass, and $g_s \simeq 2$ is the Landé g factor.

In the weak coupling limit where the external field is sufficiently smaller than the hyperfine structure constant A_{hfs} so that $\mu_B B < A_{hfs}$ and assuming that the field is aligned along the z-axis the interaction is described by the Hamiltonian [96]

$$H_Z = -\boldsymbol{\mu_Z}B\boldsymbol{z} = (L_z + g_sS_z - g_II_z)\mu_BB \simeq g_F\mu_BBF_z, \tag{3.3}$$

where F_z is in units of $\hbar$. g_F is a dimensionless factor dependent to the specific atomic state considered. Concerning the $^1S_0$ ground state, since $S = L = 0$ the factor $g_{F|g\rangle} = -g_I \simeq -\mu_I/(\mu_B|I|) = -5.4 \times 10^{-4}$ [97]. μ_I is the nuclear magnetic moment, and for ^{171}Yb $\mu_I = 0.4919\mu_N$ [98], with μ_N being the nuclear magneton. For the excited $^3P_0$ state the factor $g_{F|e\rangle}$ is different because of an additional contribution δg_F arising from the hyperfine state mixing so that $g_{F|e\rangle} = g_{F|g\rangle} + \delta g_F$.

The eigenvalues of the Hamiltonian (3.3) allows to determine the first order term of the Zeeman frequency shift for a single state, which is linear in the magnetic field intensity and depends on the quantum number M_F according to

$$\frac{\Delta E_{\mathrm{Z}}}{h} = \frac{1}{h} g_F \mu_{\mathrm{B}} B M_F. \tag{3.4}$$

Therefore because of the external magnetic field the clock Zeeman sublevels are energy shifted with opposite sign. The inset in figure 3.1 shows the scheme of the clock energy levels and the resulting Zeeman transitions when an external magnetic field is present. Transitions with $\Delta M_F = \left| M_{F|g\rangle} - M_{F|e\rangle} \right| = 0$ are called π transitions, otherwise they are called σ transitions.

The two clock π transitions between the Zeeman states with either $M_F = 1/2$ or $M_F = -1/2$ are frequency shifted from the unperturbed frequency by the linear Zeeman shift according to

$$Z = \frac{\Delta E_{\mathrm{Z}|e\rangle} - \Delta E_{\mathrm{Z}|g\rangle}}{h} = \pm \frac{1}{2h} (g_{F|e\rangle} - g_{F|g\rangle}) \mu_{\mathrm{B}} B = \pm \frac{1}{2h} \delta g_F \, \mu_{\mathrm{B}} B, \tag{3.5}$$

δg_F has been theoretically calculated in [44], and experimentally measured at NIST in 2012 to be $\delta g_F = -2.73(10) \times 10^{-4}$ [99]. Using this experimental result, the linear Zeeman shift is $Z(M_F = \pm 1/2) = \mp 1910(70)$ Hz $\times (B/\mathrm{mT})$. A recent new evaluation performed at NIST found $Z = \mp 1995.16(2)$ Hz $\times (B/\mathrm{mT})$ [25], while an experimental evaluation at NMIJ found $Z = \mp 2105(69)$ Hz $\times (B/\mathrm{mT})$ [100].

Zeeman transitions couple to light fields with specific polarisation properties. A simple classical model, whose visual representation is drawn in figure 3.1, is sufficient to intuitively understand the phenomenon [95]. In this picture, the atom is considered an oscillator with the same resonance frequency for the three spatial directions.

Assuming an external magnetic field aligned along the z-axis, the atom electrons because of the field acquire a circular motion around that axis, in either one or the opposite direction. If the probing light propagates along the magnetic field axis with circular polarisation (case A), it couples with the electrons circular motion and can excite one of the two σ transitions, according to the direction of the polarisation rotation. The two σ transitions are frequency detuned from the unperturbed frequency because of the additional or lesser energy provided by the circular motion. In this case, the light does not interact with the π transitions, which instead are related to the electron oscillation along the quantization axis.

If the probing radiation propagates perpendicular to the magnetic field, and it is linearly polarized along z (case B), it interacts just with the π transitions, as it cannot couple with the circular motion. Assuming instead that the light polarisation is linear and laying on the (x, y) plane (case C), the light couples with the electron circular motion, which is on the (x, y) plane a linear sinusoidal oscillation, and excites the σ transitions.

When operating a ^{171}Yb frequency standard it is possible to neglect the linear Zeeman shift by adopting some expedients [101]. Firstly the Zeeman splitting is clearly resolved applying an external magnetic field ($B \sim 0.1$ mT) which is also used to define the quantization axis. Secondly, according to the qualitative model introduced above the clock transition is interrogated with a probe beam linearly polarized along the quantization axis, so that the σ transitions cannot be excited. Finally, both Zeeman π transitions are probed: since the first order frequency shift is equal in magnitude but has opposite sign for the two π components, then the mean frequency between the two resonances does match the unperturbed frequency.

Measurement of the quadratic Zeeman shift coefficient at RIKEN

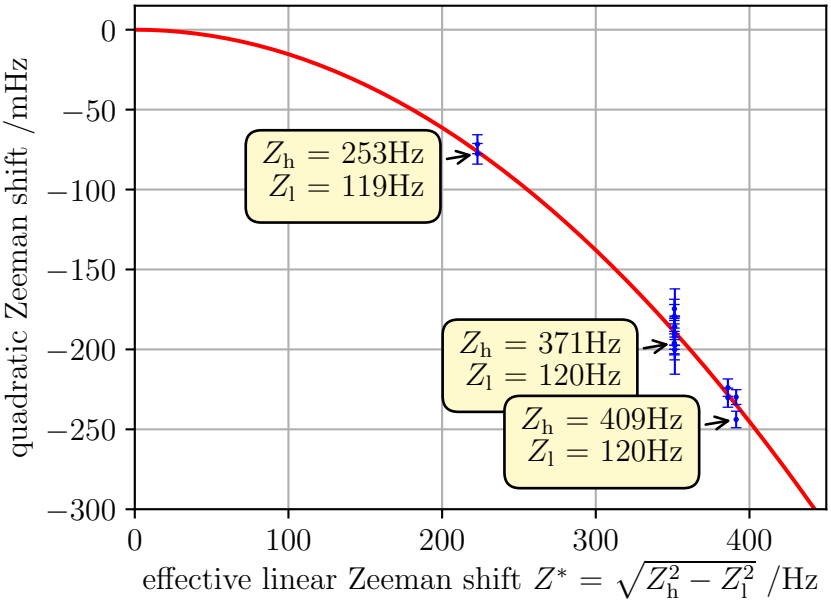

Figure 3.2: Quadratic Zeeman shift measurements at different linear shifts $Z^* = \sqrt{Z_h^2 - Z_l^2}$, with Z_l the reference condition and Z_h corresponding to the high field setting. The curve is a quadratic fit of the experimental data.

When implementing the Zeeman shift cancellation technique, as highlighted above, the first order Zeeman shift can be neglected. As a consequence the second order contribution in the Taylor expansion becomes relevant and requires to be measured. This is predominantly determined by the mixing of the ^{3}P$_0$ state with the near ^{3}P$_1$ state [96]. Since the shift depends on M_F^2 all ^{3}P$_0$ Zeeman sublevels are shifted with the same sign, therefore the shift-cancellation technique applied for the linear Zeeman shift does not remove this additional contribution.

The quadratic Zeeman shift can be experimentally evaluated by measuring the difference in clock frequency when applying different values for the external magnetic field B. This is performed interleaving the clock operation between two modes which differ by just the magnitude of the external field: all systematic frequency shift contributions which are not dependent to the magnetic field are common mode between the two clock operations, and thus they cancel when taking the frequency difference of the resulting clock frequencies.

A significant issue in the evaluation of the frequency shift is the calibration of the magnetic field affecting the atoms, since the atom exact location cannot be accessed with a probe for the magnetic field intensity. Instead of developing a method to directly measure the magnetic field, we can use the sensitivity of the atoms to the magnetic field as an in-situ measurement of the field. Since the linear Zeeman shift can be evaluated as the half of the frequency separation between the two π transitions, it can be used for an indirect calibration of the magnetic field.

At RIKEN we perform several measurements of the quadratic Zeeman shift using a reference *low* field setting corresponding to a linear Zeeman shift $Z_{\mathrm{l}} = 120$ Hz and a *high* field setting from $Z_{\mathrm{h}} = 253$ Hz to $Z_{\mathrm{h}} = 409$ Hz (see figure 3.2). The field is varied changing the current of the bias magnetic field coils.

The limit to the maximum available field intensity is provided by the stability of the current in the coils: with a current of about 4.5 A the field is not stable because of the temperature behaviour of the coil wires, which start heating critically at these high current settings.

When changing the magnitude of Z_{h} the bias fields along the three spatial directions are tuned to maintain the orientation of the quantization axis as initially set, i.e. to avoid field components not aligned along the lattice and probe laser polarisation. This is achieved minimizing the excitation of the σ transitions.

During the clock cycle of operation the magnetic field value is changed from the initial low value used during the atom loading into the lattice to the final setting at least 250 ms before the clock interrogation, so as to assure that Eddy currents are not present when atoms are probed. The interrogation time is chosen to be $T_{\mathrm{i}} = 300$ ms for the best clock stability available to reduce the required measuring time.

Measurements of the differential quadratic Zeeman shift $\Delta\nu_{\mathrm{Z}}$ are shown in figure 3.2. Plotting the measurement results against the effective linear Zeeman shift $Z^* = \sqrt{Z_{\mathrm{h}}^2 - Z_{\mathrm{l}}^2}$ corresponding to the measurement conditions allows to fit the data with a parabola crossing zero at $Z^* = 0$, thus avoiding other fitting parameters than the quadratic coefficient a_{Z}:

$$\Delta\nu_{\mathrm{Z}} = a_{\mathrm{Z}} Z_{\mathrm{h}}^2 - a_{\mathrm{Z}} Z_{\mathrm{l}}^2 = a_{\mathrm{Z}} Z^{*2}. \tag{3.6}$$

The linear Zeeman shifts $Z_{\mathrm{h,l}}$ are evaluated as the average of half the splitting between the two π transitions, whose frequencies are continuously acquired when

locking the clock local oscillator to the atoms. In the calculation linear drifts of the local oscillator are considered applying data linear interpolation. The white nature of the instability of the linear Zeeman shift allows to assign a statistical uncertainty to $Z_{\mathrm{h,l}}$ as the standard error of the mean, which results to be about 6 mHz for each measurement.

An additional uncertainty to Z^* arises taking the square of the averages $\langle Z_{\mathrm{h,l}}\rangle^2$ instead of $\langle Z^2_{\mathrm{h,l}}\rangle$ when applying eq. (3.6) to the experimental data. Since

$$\langle Z^2_{\mathrm{h,l}}\rangle = \langle Z_{\mathrm{h,l}}\rangle^2 + \sigma^2(Z_{\mathrm{h,l}}), \tag{3.7}$$

where $\sigma^2(Z_{\mathrm{h,l}})$ is the variance of the shift dataset, a correction factor equal to the data variance $\sigma^2(Z_{\mathrm{h,l}}) \sim (6\ \mathrm{mHz})^2$ is applied with an uncertainty of 100% to the linear Zeeman shifts squared used for the analysis.

Lattice vector light shift. Since the first order Zeeman shift Z is estimated measuring half of the frequency splitting between the two π clock transitions, its evaluation may be affected by a systematic error incurring because of the lattice vector light shift $\Delta\nu_{\mathrm{vls}}$. The effect leading to a vector light shift arises from a residual lattice elliptical polarisation and depends on the lattice intensity (or equivalently the lattice depth U_0), and can be considered as an apparent magnetic field $\boldsymbol{B}_{\mathbf{vls}} = k_{\mathrm{v}} U_0 \boldsymbol{u}_{\mathbf{kL}}$ aligned along the lattice wavevector $\boldsymbol{u}_{\mathrm{kL}}$ (i.e. the lattice axis) [102]; as a consequence, the total effective magnetic field results from the vector sum $\tilde{\boldsymbol{B}} = \boldsymbol{B} + \boldsymbol{B}_{\mathbf{vls}}$, and its magnitude reads

$$\tilde{B} = \sqrt{B^2 + 2BB_{\mathrm{vls}}\cos(\theta) + B^2_{\mathrm{vls}}}, \tag{3.8}$$

where θ is the angle between the external magnetic field $\boldsymbol{B}$ and the lattice axis, thus the effective half-splitting between the two π transition is [103]

$$\begin{aligned}\tilde{Z} &= \sqrt{Z^2 + 2Zk_{\mathrm{v}}U_0\cos(\theta) + k_{\mathrm{v}}^2U_0^2} \\ &\approx Z + k_{\mathrm{v}}\cos(\theta)\,U_0 + \sin^2(\theta)\,\frac{k_{\mathrm{v}}^2}{2Z}U_0^2 = Z + \Delta\nu_{\mathrm{vls}},\end{aligned} \tag{3.9}$$

where a Taylor expansion to the second order in U_0 has been performed. The factor k_{v} depends on the degree of the lattice elliptical polarisation $\mathcal{A}$ ($\mathcal{A} = \pm 1$ for fully circular, $\mathcal{A} = 0$ for linear polarization), on the differential lattice vector polarizability at the magic wavelength $\tilde{\alpha}^{\mathrm{V}} = \Delta\alpha^{\mathrm{V}}_{\mathrm{E1}}/\alpha^{\mathrm{S}}_{\mathrm{E1}}$ and on the hyperfine quantum numbers F, M_F such that

$$k_{\mathrm{v}} = -\frac{\tilde{\alpha}^{\mathrm{V}}}{h}\frac{M_F}{2F}\mathcal{A}. \tag{3.10}$$

The vector light shift can then be written at the first order as $\Delta\nu_{\mathrm{vls}} \approx k_{\mathrm{v}}\cos(\theta)\,U_0$. It results that the shift at the first order cancels by aligning the external magnetic field orthogonally to the lattice axis, and in general it totally cancels with a perfectly

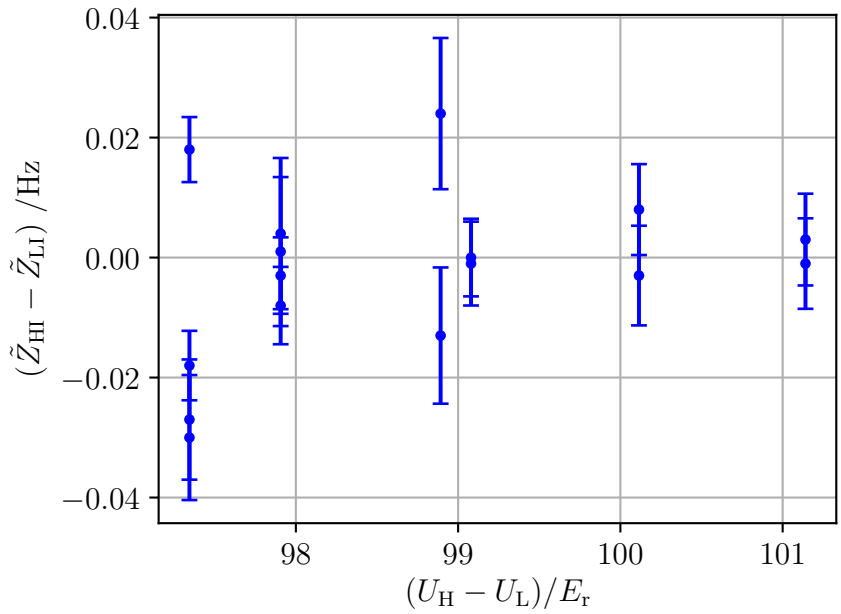

Figure 3.3: Differential vector light shift measured as the difference between the half-splitting of the two π transitions at high (H) and low (L) lattice intensity.

linear lattice polarization. Typically both conditions are desired in the standard clock operation. The lattice polarization is linearised using for example a Glan-Thompson polariser just before the lattice entrance to the experimental chamber, while the external magnetic field and the lattice wavevector are made orthogonal by suppressing the excitation of the σ transitions. These techniques ensure that the vector light shift is much smaller then the linear Zeeman shift, but they do not rule out the presence of a residual vector light shift contribution.

We constrain the vector light shift effect on the linear Zeeman shift determination by acquiring in interleaved operation measurements of the quadratic Zeeman shift at either a *high* lattice intensity of $U_0^{\mathrm{high}} = U_{\mathrm{H}} \sim 190\ E_{\mathrm{r}}$ or at a *low* lattice intensity of $U_{\mathrm{L}} \sim 75\ E_{\mathrm{r}}$. Taking the difference between the half-splitting $\tilde{Z}$ between high ($\tilde{Z}_{\mathrm{HI}}$) and low ($\tilde{Z}_{\mathrm{LI}}$) lattice intensity conditions at fixed external magnetic field

$$\tilde{Z}_{\mathrm{HI}} - \tilde{Z}_{\mathrm{LI}} = k_{\mathrm{v}} \cos(\theta)\ (U_{\mathrm{H}} - U_{\mathrm{L}}) + \sin^2(\theta)\, \frac{k_{\mathrm{v}}^2}{2Z} \left(U_{\mathrm{H}}^2 - U_{\mathrm{L}}^2\right) \tag{3.11}$$

it is possible to extract the differential vector light shift contribution and calculate the correction to be applied to the determination of Z. Figure 3.3 shows the measured differential vector stark shift. With the typical trap depths employed in the experiment is not possible to exclude contributions from the quadratic term, therefore we perform a data fit using as model the entire equation (3.11). To scale the experimental data to the specific external magnetic field, in the quadratic term

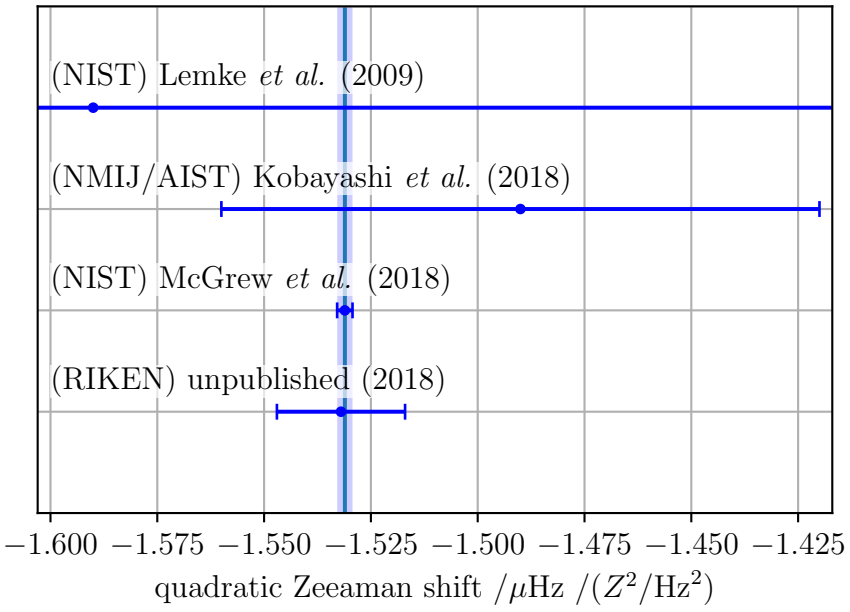

Figure 3.4: Quadratic Zeeman shift in units of the linear Zeeman shift squared Z^2, as independently measured by different research groups [25, 100, 104]. The vertical line and the shaded region represent the weighted mean and its uncertainty range.

it has been assumed $Z \approx \tilde{Z}$. Despite the extracted linear and quadratic coefficients are correlated and not meaningful when considered separately, it is possible to use them to evaluate a vector light shift at the operating conditions: for example $\Delta\nu_{\mathrm{vls}} = -4(6)$ mHz at $U_0 = 190\ E_{\mathrm{r}}$ and $Z = 160$ Hz.

A similar investigation of the vector light shift coefficients has been performed with splitting data taken from a earlier set of light shift measurements performed with a similar clock configuration. In that case the external magnetic field was unchanged during the entire campaign. Results confirm a vector light shift compatible with zero: at $U_0 = 190\ E_{\mathrm{r}}$ and $Z = 165$ Hz the shift is evaluated to be $\Delta\nu_{\mathrm{vls}} = -50(80)$ mHz.

The vector light shift is calculated for each of the different operating conditions of the quadratic Zeeman shift measurements, and it is used to correct the linear Zeeman shift data used in the analysis for the extraction of the quadratic Zeeman coefficient.

The final uncertainty on Z^* results to be about 10 mHz for each of the measurements performed, that corresponds to a negligible uncertainty in the determination

of the quadratic Zeeman shift coefficient when compared to the statistical uncertainty of the measured quadratic Zeeman shifts.

The final quadratic Zeeman shift is evaluated as

$$\Delta\nu_{\mathrm{Z}} = a_{\mathrm{Z}} Z^{*2} = a_{\mathrm{Z}}(Z_{\mathrm{h}}^2 - Z_{\mathrm{l}}^2) = -1.532(15)\ \mu\mathrm{Hz}(Z^2/\mathrm{Hz}^2). \tag{3.12}$$

The obtained value is in agreement with the recent results obtained at NIST [25] and NMIJ (AIST) [100] of

$$a_{\text{Z-NIST}} = -1.5311(18)\ \mu\mathrm{Hz}/\mathrm{Hz}^2$$
$$a_{\text{Z-NMIJ}} = -1.49(7)\ \mu\mathrm{Hz}/\mathrm{Hz}^2,$$

as shown in figure 3.4.

Final evaluation of the Zeeman shift at RIKEN

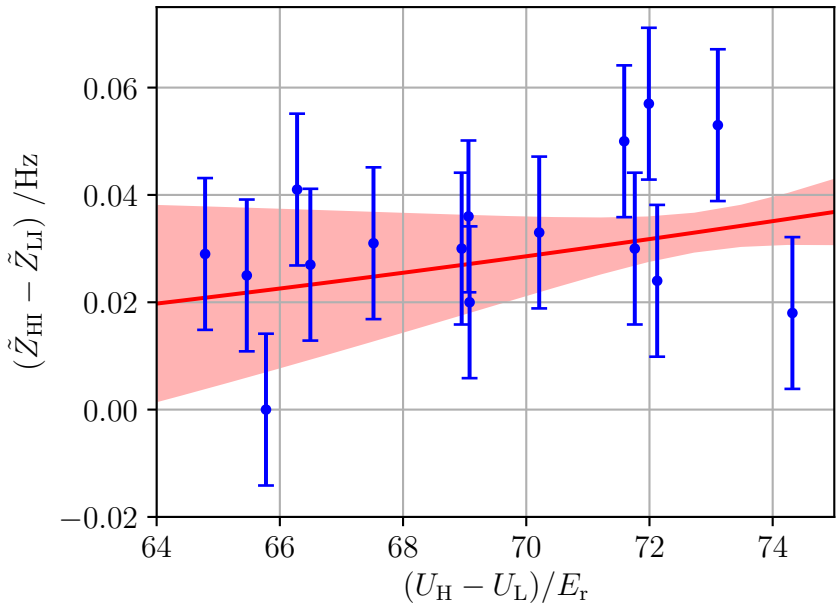

Figure 3.5: Differential vector light shift measured as the difference between the half-splitting of the two π transitions at high (H) and low (L) lattice intensity.

At RIKEN we evaluate the second order Zeeman shift in the standard operating conditions during the frequency ratio campaign reported in chapter 4 using eq. (3.12) and the acquired Zeeman half-splitting data. For a typical measurement duration of more than three hours and a clock instability of about $\sigma(\tau) = 6 \times 10^{-16}\ /\sqrt{\tau/\mathrm{s}}$ the linear Zeeman shift is evaluated with a statistical uncertainty

below 10 mHz. The statistical analysis performed is same as described in the previous section.

Since the vector light shift depends on the clock geometry and set-up, it has to be characterised in the specific operating conditions. We evaluate its contribution at the experimental conditions of the ratio measurements using the values of $\tilde{Z}_{\mathrm{HI(LI)}}$ acquired during the lattice light shift measurements (discussed in section 3.2.1), which are performed in between the frequency ratio measurements.

Figure 3.5 shows the results of the differential vector Stark shift, which are obtained and analysed with the same approach discussed in the previous paragraph. In this case with the typical trap depth of $U_0 = 90\ E_\mathrm{r}$ and $Z \simeq 162$ Hz we evaluate a vector light shift of $\Delta\nu_{\mathrm{vls}} = -20(110)$ mHz, which is applied as a correction to the linear Zeeman shift. When evaluating the quadratic Zeeman shift, such correction results in an additional uncertainty contribution of 1 % to the total uncertainty, which is dominated by the contribution of the shift coefficient.

3.2 AC Stark shift

The AC Stark frequency shift, or simply light shift, arises from the atom-light interaction. The oscillating light fields couple with the Yb atomic transitions inducing both line broadening and the shift of the involved energy levels. The effect can be described in the dressed atom picture [105]. An atomic two-level system (in free space) with ground state $|g\rangle$, excited state $|e\rangle$ and transition frequency $\omega_0 = 2\pi\nu_0 = (E_\mathrm{e} - E_\mathrm{g})/\hbar$ interacting with $N+1$ photons at frequency ω_l is coupled to the light field if a photon is absorbed and the atom is excited. The resulting light-coupled ground $|1(N)\rangle$ and excited $|2(N)\rangle$ dressed states can be described as a linear superposition of the original ground state $|g, N+1\rangle$ and the excited state $|e, N\rangle$ defined in the absence of coupling. The coupling potential V_{E1} is proportional to the atom electric dipole moment μ_E and the electric field E_l.

It is useful to introduce here the atomic transition Rabi frequency Ω_R,

$$\langle e, N|\, V_{\mathrm{E1}}\, |g, N+1\rangle = \langle e, N|\, \mu_\mathrm{E}\, |g, N+1\rangle\, E_\mathrm{l} = \frac{\hbar\Omega_\mathrm{R}}{2}, \tag{3.13}$$

assuming the electric field polarisation is aligned along the atomic dipole moment.

The time evolution of this system and its eigenvalues can be extracted from the Hamiltonian

$$H_{\mathrm{E1}} = \hbar \begin{pmatrix} \Delta\omega & \Omega_\mathrm{R}/2 \\ \Omega_\mathrm{R}/2 & -i\Gamma/2 \end{pmatrix}, \tag{3.14}$$

where $\Delta\omega = \omega_\mathrm{l} - \omega_0$ is the frequency detuning of the light field from resonance and $\Gamma = 2\pi\gamma$ is the excited state decay rate due to spontaneous emission, which can be expressed in terms of the transition linewidth γ.

Weak coupling limit. In the weak coupling limit, where $\Delta\omega \gg \Omega_R$ (or $\Omega_R \ll \Gamma$), the effect of the light field can be considered a small perturbation of the original states. The energy shifts of the dressed states $|1(N)\rangle$ and $|2(N)\rangle$ with respect to the original uncoupled states are

$$\Delta E_1 = \frac{\hbar\Omega_R^2}{4(\Delta\omega + i\Gamma/2)} = \hbar\delta\omega_{ls} - i\hbar\frac{\gamma_{broad}}{2} \tag{3.15}$$

$$\Delta E_2 = -\hbar\delta\omega_{ls} + i\hbar\frac{\gamma_{broad}}{2}, \tag{3.16}$$

where

$$\delta\omega_{ls} = \frac{\Delta\omega}{4\Delta\omega^2 + \Gamma^2}\Omega_R^2 \quad \text{and} \quad \gamma_{broad} = \frac{\Gamma}{4\Delta\omega^2 + \Gamma^2}\Omega_R^2 \tag{3.17}$$

are the light shift and the light broadening, respectively. As a result of the light coupling the original states $|g, N+1\rangle$ and $|e, N\rangle$ are shifted by the same amount $\delta\omega_{ls}$ but with opposite sign. The line broadening results from contamination of $|g, N+1\rangle$ by $|e, N\rangle$ and can be interpreted as a photon absorption rate from the ground state.

When considering far off resonance light fields, such that $|\Delta\omega| \gg \Gamma$, the equation for the light shift reduces to

$$\delta\omega_{ls} = \pm\frac{\Omega_R^2}{4\Delta\omega} \tag{3.18}$$

with "+" for the ground state and "−" for the excited state.

A semiclassical treatment of the interaction between an atomic two-level system and a far-detuned light field leads to the same result, but with the feature of explicitly showing the dependency to the light intensity I and the damping rate Γ [48]. In this picture, the damping rate Γ can be expressed as

$$\Gamma = \frac{\omega_0^3}{3\pi\epsilon_0\hbar c^3}|\langle e|\,\mu_E\,|g\rangle|^2. \tag{3.19}$$

As a consequence, it is possible to rewrite eq. (3.18) using eq. (3.13) as

$$\delta\omega_{ls} = \pm\frac{|\langle e|\,\mu_E\,|g\rangle|^2}{\hbar^2\Delta\omega}\left|E_l^2\right| = \pm\frac{3\pi c^2}{2\hbar\omega_0^3}\frac{\Gamma}{\Delta\omega}I. \tag{3.20}$$

The sign is determined with the same rule presented in (3.18).

For multi-level atoms equations (3.18) and (3.20) can be generalized by accounting for all dipole-allowed transitions involving the energy level concerned (this treatment does not include multipolar and two-photon transitions, providing a smaller but relevant contribution, as discussed in section 3.2.1). The light shift induced by a far-off resonance laser field of frequency ω_l affecting the energy level $|i\rangle$ is

$$\delta\omega_{ls} = \frac{3\pi c^2}{2\hbar}\left(\sum_j \frac{\Gamma_{ij}}{\omega_{ij}^3\Delta\omega_{ij}} - \sum_k \frac{\Gamma_{ki}}{\omega_{ki}^3\Delta\omega_{ki}}\right)I, \tag{3.21}$$

where the summations are over all possible excited states $|j\rangle$ identifying the transitions of frequency ω_{ij} where the state $|i\rangle$ is involved as ground level, and all possible ground states $|k\rangle$ of optical transitions where $|i\rangle$ is the excited state; $\Delta\omega_{ij} = \omega_{\mathrm{l}} - \omega_{ij}$.

The same generalization can also be performed on equation (3.18) by replacing the Rabi frequency and the frequency detuning $\Delta\omega$ by the summation over the corresponding values for all transitions coupled to the laser light.

High coupling limit. Considering the case where $\Delta\omega = 0$, when $\Omega_{\mathrm{R}} \gg \Gamma$ the two dressed states $|1(N)\rangle$ and $|2(N)\rangle$ become the linear symmetric and antisymmetric combinations of $|g, N+1\rangle$ and $|e, N\rangle$ and their energy splitting equals the Rabi frequency $\hbar\Omega_{\mathrm{R}}$. The two dressed stated are entangled. The time evolution of the system is described by a damped oscillation of the atom between $|g, N+1\rangle$ and $|e, N\rangle$ at the frequency Ω_{R} in a sequence of absorption and stimulated emission processes. The evolution is named Rabi oscillation and it is described by the phase term $\exp(\mp i\Omega_{\mathrm{R}} t/2)\exp(-\Gamma t/4)$, where the oscillating imaginary term is dumped with a rate $\Gamma/2$.

When the atoms are interrogated on the clock transition with a single Rabi pulse they undergo the Rabi oscillation as depicted above. A Rabi π-pulse, as introduced in section 2.4, is satisfied for an interrogation time T_{i} corresponding to a quarter of an oscillating period (where the excitation probability is maximal), thus with $\Omega_{\mathrm{R}} T_{\mathrm{i}} = \pi$.

If the light field is frequency detuned from resonance ($\Delta\omega \neq 0$) the high coupling limit is reached with $\Omega_{\mathrm{R}} \gg |\Delta\omega + i\Gamma/2|$. Then the oscillation happens at the effective Rabi frequency

$$\widetilde{\Omega}_{\mathrm{R}} = \sqrt{\Omega_{\mathrm{R}}^2 + \Delta\omega^2}; \tag{3.22}$$

in the frequency domain this leads to the spectrum of equation 2.5.

During the clock interrogation the probe laser and the lattice laser are present and couple with the atom energy levels inducing light shifts. In the following sections these systematic frequency shift are discussed in detail.

3.2.1 Lattice light shift

The optical lattice where neutral atoms are trapped is realised as a standing wave generated by two counterpropagating laser beams whose frequency ν_{L} is red-detuned from the atomic transition frequencies ν_0 such that $\nu_{\mathrm{L}} < \nu_0$, so as to confine the atoms in the lattice intensity maxima [48].

As discussed in the previous section, a far off resonance laser field, falling in the weak coupling limit, interacts with the clock states inducing a frequency shift proportional to the field intensity according to eq. (3.21) (a calculation of the expected shift can be found for example in [78]): since the lattice intensity I_{L} is spatially

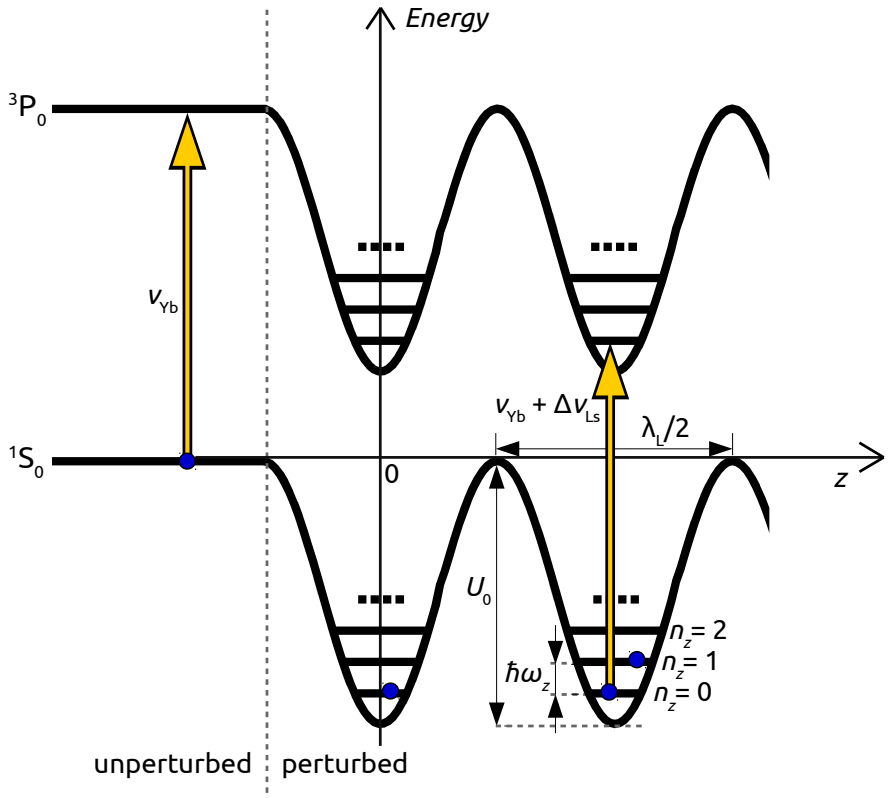

Figure 3.6: Drawing of the clock transition states unperturbed (left side of the picture) and modified by the presence of the lattice dipole potential (right side). Along the lattice propagation axis z the energy levels are affected by a spatially dependent light shift which modifies them according to the shape of the potential $U(z,r) \propto I_L(z,r)$, where I_L is the lattice intensity.

inhomogeneous it modifies the clock energy levels according to its shape, realising a trapping potential.

Assuming the lattice beams are Gaussians and propagate along the z-axis, the intensity profile varies along the z-axis with the beam radius $w(z)$ size because of the beam focusing. In the (x,y) plane the intensity varies according to a Gaussian profile of the form $\exp(-2r^2/w(z)^2)$, where r is the radial coordinate in the lattice transverse plane. Thus, if $P_L = I_0 \pi w_0^2/2$ is the optical power of each of the two beams

$$I_L = \frac{2P_L}{\pi w(z)^2} e^{-\frac{2r^2}{w(z)^2}}, \quad \text{with} \quad w(z) = w_0 \sqrt{1 + \left(\frac{z}{z_R}\right)^2}, \tag{3.23}$$

where the minimum radius w_0 is called the beam waist and $z_R = \pi w_0^2/\lambda_L$ is the Rayleigh range. In addition, the standing wave interference pattern provides a modulation of the intensity according to $\cos^2(k_L z)$, with k_L the lattice wavevector.

The resulting spatially dependent light shift generates a potential $U(z,r) \approx$

$-\alpha_{\mathrm{E1}} I_{\mathrm{L}}(z,r)$, where the proportionality constant α_{E1} is the lattice electric dipole (E1) polarizability, which defines the light-atom dipole coupling strength and depends on the properties of electric-dipole transitions according to (3.21), such that $\alpha_{\mathrm{E1}} = \hbar\delta\omega_{\mathrm{ls}}(z,r)/I_{\mathrm{L}}(z,r)$. A complete formulation of the potential, as discussed later, has also to account for the light coupling with other atomic transitions than the electric dipole ones, which however are the dominating contributions.

The potential shape can thus be written

$$U(z,r) \approx -\alpha_{\mathrm{E1}} I_{\mathrm{L}}(z,r) = -U_0 \cos^2(k_{\mathrm{L}} z) \left(\frac{w_0}{w(z)}\right)^2 e^{-\frac{2r^2}{w(z)^2}}, \tag{3.24}$$

and allows to trap the atoms through the restoring force $\boldsymbol{F} = -\boldsymbol{\nabla} U$ if the atom kinetic energy is small enough when compared to the depth of the potential well. For the atomic ensemble this translates as the thermal energy $(3/2)k_{\mathrm{B}}T$ being much smaller that the maximum trap depth U_0. While the strong longitudinal confinement does not have significant dependence to the lattice orientation, the radial confinement can be significantly affected by gravity. Aligning the lattice vertically, along gravity, solves the issue and suppresses the probability of atom tunnelling between lattice sites [106]. On the contrary an horizontal lattice or a lattice tilted by a certain angle θ from gravity has a radial confinement reduced by $U_{\mathrm{gravity}}(r) = m_{\mathrm{Yb}} g\, r \sin(\theta)$, thus in this case a deeper lattice is required to trap the atoms.

With the confinement condition satisfied the extension of the cloud of atoms is much smaller than w_0 and z_{R}, therefore the potential can be approximated in the vicinity of the intensity maxima by a cylindrically symmetric harmonic oscillator

$$\begin{aligned} U(r,z) &\approx -U_0 \cos^2(k_{\mathrm{L}} z) \left(1 - 2\frac{r^2}{w_0^2} - \frac{z^2}{z_{\mathrm{R}}^2}\right) \\ &\approx -U_0 \left(1 - k_{\mathrm{L}}^2 z^2 - 2\frac{r^2}{w_0^2} - 2\frac{k_{\mathrm{L}}^2 z^2 r^2}{w_0^2}\right) \end{aligned} \tag{3.25}$$

leading to a sequence of harmonic potential wells. In figure 3.6 these are shown for $r = 0$: the maximum trap depth is denoted U_0 and the resulting axial vibrational levels are identified by the quantum numbers n_z and separated in energy by $\hbar\omega_z$, where ω_z is the axial trap frequency.

Modelling the lattice light shift

Equation (3.21) for the light shift calculation has been obtained accounting for the coupling V_{E1} of the light field to the dipole allowed transitions involving the clock states through the atomic electric dipole moment μ_{E}. The interaction strength is expressed with the electric dipole polarizability α_{E1}. Since a laser electric

field oscillates over time, α_{E1} is a dynamic polarizability and in general can be decomposed into a scalar, vector and tensor components according to [107]

$$\begin{aligned}\alpha_{\mathrm{E1}} =& \alpha^{\mathrm{S}}_{\mathrm{E1}} + (\boldsymbol{u}_{\mathbf{kL}} \cdot \boldsymbol{u}_{\mathbf{B}}) \frac{M_F}{2F} \mathcal{A} \alpha^{\mathrm{V}}_{\mathrm{E1}} \\ &+ \frac{1}{2}(3|\boldsymbol{\epsilon} \cdot \boldsymbol{u}_{\mathbf{B}}|^2 - 1) \frac{3M_F^2 - F(F+1)}{F(2F-1)} \alpha^{\mathrm{T}}_{\mathrm{E1}},\end{aligned} \tag{3.26}$$

where the superscripts S, V, and T distinguish the scalar, vector, and tensor components of the polarizability. $\boldsymbol{u}_{\mathbf{kL}}$ and $\boldsymbol{u}_{\mathbf{B}}$ are the unit vectors of the lattice wavevector and the external magnetic field, and $\boldsymbol{\epsilon}$ is the polarisation. The parameter $\mathcal{A}$ is the degree of circular polarisation of the lattice light ($\mathcal{A} \pm 1$ for fully circular, $\mathcal{A} = 0$ for linear polarisation). Since $F = 1/2$ and $M_F = \pm 1/2$ for the clock states, the tensor part of the polarizability cancels out. Furthermore, as already discussed in section 3.1, the vector component is expected to be negligible because of $\mathcal{A} \simeq 0$ and $\boldsymbol{u}_{\mathbf{kL}} \perp \boldsymbol{u}_{\mathbf{B}}$, and it can be completely cancelled by averaging over the two π clock transition frequencies. As a consequence, $\alpha_{\mathrm{E1}} \simeq \alpha^{\mathrm{S}}_{\mathrm{E1}}$ and the other terms will be neglected in the following.

The E1 polarizability provides the dominant contribution of the lattice light shift, however when taking the differential lattice light shift between the excited $|e\rangle$ and the ground $|g\rangle$ clock states this term can be cancelled by choosing the lattice frequency so that the differential dipole polarizability $\Delta\alpha_{\mathrm{E1}} = \alpha^{\mathrm{e}}_{\mathrm{E1}}(\nu_{\mathrm{L}}) - \alpha^{\mathrm{g}}_{\mathrm{E1}}(\nu_{\mathrm{L}}) = 0$ [23]. This relation is true when $\nu_{\mathrm{L}} = \nu_{\mathrm{E1}} \simeq 394\,798.3$ GHz, which is called the E1-magic frequency[a].

With this condition satisfied, the approach of eq. (3.21) is not sufficient to model the lattice light shift accurately, since other minor contributions to the light shift require to be considered. Firstly, a higher-order electric dipole interaction proportional to I_{L}^2 arises from the light coupling with two-photon resonances between the clock $6s6p\,^3P_0$ state and higher lying $6s8p\,^3P_J$ and $6s5f\,^3F_2$ states [108]. Secondly, non-negligible interactions V_{E2} and V_{M1} exist because of the light coupling with multipolar transitions, respectively the electric quadrupole (E2) transitions and the magnetic dipole (M1) transitions. These interactions give rise to additional atomic polarizabilities termed hyperpolarizability β and E2 (M1) polarizability α_{E2} (α_{M1}).

Assuming the atom lays in a region of the potential well close to the centre, so that its position $|z| \ll \lambda_{\mathrm{L}}$ (see the coordinate system in figure 3.6), the lattice potential $U(z, I_{\mathrm{L}})$ can be expanded around $z = 0$ as [109, 110]

$$\begin{aligned}U(z, I_{\mathrm{L}}) &\approx -I_{\mathrm{L}} \left(\alpha_{\mathrm{E1}} \cos^2 k_{\mathrm{L}} z + \alpha^{\mathrm{qm}} \sin^2 k_{\mathrm{L}} z \right) - I_{\mathrm{L}}^2 \beta \cos^4 k_{\mathrm{L}} z \\ &\approx -\alpha_{\mathrm{E1}} I_{\mathrm{L}} - \beta I_{\mathrm{L}}^2 + u^{(2)}(I_{\mathrm{L}}) z^2 - u^{(4)}(I_{\mathrm{L}}) z^4 + \cdots ,\end{aligned} \tag{3.27}$$

[a] In general there are many possible magic frequencies [91, 107], but the chosen one satisfies some experimental conditions, for example the feasibility of a laser source at such frequency, and a corresponding differential polarizability less sensitive to lattice frequency variations.

Terms $u^{(2)}$ and $u^{(4)}$ depends on the combined E2-M1 polarizability $\alpha^{\mathrm{qm}} = \alpha_{\mathrm{E2}} + \alpha_{\mathrm{M1}}$, in addition to α_{E1} and β. The harmonic term $u^{(2)} = \frac{1}{2} m_{\mathrm{Yb}} \omega_z^2$ determines the axial vibrational frequency ω_z in terms of the lattice recoil energy E_{r}, while $u^{(4)}$ is the lowest-order anharmonic correction.

The energy shift of an atom in the n^{th} axial vibrational state is obtained with the equation [110]

$$h\delta\nu_{\mathrm{Ls}} = -\alpha_{\mathrm{E1}} I_{\mathrm{L}} - \beta I_{\mathrm{L}}^2 + \hbar\omega_z(I_{\mathrm{L}}) \left(n_z + \frac{1}{2}\right) - E^{(4)}(I_{\mathrm{L}}) \left(n_z^2 + n_z + \frac{1}{2}\right). \tag{3.28}$$

The final lattice light shift, obtained as the differential shift affecting the excited and ground clock state, can be expanded in the vicinity of $\nu_{\mathrm{L}} \approx \nu_{\mathrm{E1}}$ and written [58]

$$\begin{aligned} h\Delta\nu_{\mathrm{Ls}} &= h\left(\delta\nu_{\mathrm{Ls}}^{\mathrm{e}} - \delta\nu_{\mathrm{Ls}}^{\mathrm{g}}\right) \\ &= \left[\tilde{\alpha}'(\nu_{\mathrm{L}} - \nu_{\mathrm{E1}}) - \tilde{\alpha}^{\mathrm{qm}}\right] \left(\bar{n}_z + \frac{1}{2}\right) \sqrt{\left(\zeta - \frac{1}{2}\delta_2\right) \frac{U_0}{E_{\mathrm{r}}}} \\ &\quad - \left[\tilde{\alpha}'(\nu_{\mathrm{L}} - \nu_{\mathrm{E1}}) + \frac{3}{4}\tilde{\beta}(2\bar{n}_z^2 + 2\bar{n}_z + 1)\right] \zeta \frac{U_0}{E_{\mathrm{r}}} \\ &\quad + \tilde{\beta}(2\bar{n}_z + 1) \left[\left(\zeta + \frac{1}{2}\delta_2\right) \frac{U_0}{E_{\mathrm{r}}}\right]^{3/2} \\ &\quad - \tilde{\beta} \left[(\zeta + \delta_2) \frac{U_0}{E_{\mathrm{r}}}\right]^2 . \end{aligned} \tag{3.29}$$

With respect to eq. (3.28), here the lattice intensity has been replaced with the trap depth, which is easier to be measured than the lattice intensity at the atom location as discussed in a later paragraph. Since atoms undergo different confinement strengths because of their radial energy, the individual trap depths U vary across the atomic ensemble; thus in equation (3.29) the trap depth is included in terms of the effective trap depth U_{e}, which represents an average value over the atomic ensemble, so that for a generic power m

$$U_{\mathrm{e}}^m \approx \int U^m \sigma(U)\, \mathrm{d}U\,. \tag{3.30}$$

The function $\sigma(U)$ represents how the individual trap depths U for each atom are distributed (for more detail see ref. [58]). The effective trap depth is related to the on-axis maximum depth U_0 through the fractional depths ζ and δ_m, so that $U_{\mathrm{e}}^m \approx \left[(\zeta + \delta_m) U_0\right]^m$, with $\delta_1 = 0$, $\delta_{1/2} \approx -\frac{1}{2}\delta_2$ and $\delta_{3/2} \approx \frac{1}{2}\delta_2$ (see ref. [111] for a complete derivation).

In equation (3.29) the axial vibrational quantum number $\bar{n}_z$ is taken as the average of the individual n_z characterizing each atom of the ensemble. The model

coefficients are defined and experimentally measured [58] as follows:

$$\begin{aligned}\frac{\tilde{\alpha}'}{h} &\equiv \frac{\partial\Delta\alpha_{\mathrm{E1}}}{\partial\nu_{\mathrm{L}}}\frac{E_{\mathrm{r}}}{\alpha_{\mathrm{E1}}}\frac{1}{h} = 25.74(54)\ \mu\mathrm{Hz\,MHz^{-1}},\\ \frac{\tilde{\alpha}^{\mathrm{qm}}}{h} &\equiv \Delta\alpha^{\mathrm{qm}}\frac{E_{\mathrm{r}}}{\alpha_{\mathrm{E1}}}\frac{1}{h} = -1030(380)\ \mu\mathrm{Hz},\\ \frac{\tilde{\beta}}{h} &\equiv \Delta\beta\frac{E_{\mathrm{r}}}{\alpha_{\mathrm{E1}}}\frac{1}{h} = -1.194(89)\ \mu\mathrm{Hz}\end{aligned} \tag{3.31}$$

Here $\Delta\alpha_{\mathrm{E1}} = \alpha^{\mathrm{e}}_{\mathrm{E1}} - \alpha^{\mathrm{g}}_{\mathrm{E1}}$ and $\Delta\alpha^{\mathrm{qm}} = \alpha^{\mathrm{qm,e}} - \alpha^{\mathrm{qm,g}}$ refer to the E1 and the combined E2-M1 differential polarizabilities between the excited and the ground clock states, while $\Delta\beta = \beta^{\mathrm{e}} - \beta^{\mathrm{g}}$ is the differential hyperpolarizability.

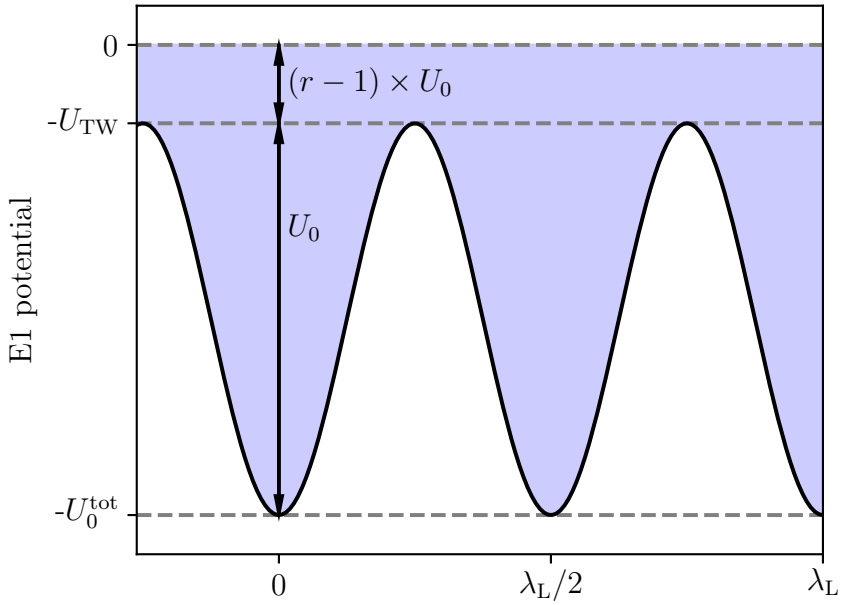

Figure 3.7: Drawing of the on-axis E1 lattice potential in the presence of a travelling wave. The drawing is inspired on the one included in [58].

This model assumes that the lattice is a perfect standing wave. Nevertheless, an eventual intensity imbalance between the two counter-propagating lattice beams determines the presence of a residual travelling wave (TW) contamination in the optical lattice, which leads to additional unexpected contributions to the light shift [109]. This may arise either if the two lattice beams have different optical power or if there is an alignment mismatch leading to imperfect beam overlap. As shown in figure 3.7, the main effect of the TW is a reduction of the on-axis modulation depth U_0 compared to the total lattice depth U_0^{tot}.

If $I_{1(2)}$ is the on-axis intensity of the first(second) lattice beam, and α_{E1} is the single beam dipole polarizability such that $U_0^{1(2)} = \alpha_{\mathrm{E1}} I_{1(2)}$ the total trap depth is obtained as

$$U_0^{\mathrm{tot}} = \alpha_{\mathrm{E1}}(I_1 + I_2 + 2\sqrt{I_1 I_2}). \tag{3.32}$$

An intensity imbalance produces a TW whose intensity depends on the difference between the electric field amplitudes of the two beams, thus

$$U_{\mathrm{TW}} = \alpha_{\mathrm{E1}}(I_1 + I_2 - 2\sqrt{I_1 I_2}). \tag{3.33}$$

In the presence of a TW contamination, the lattice on-axis modulation depth U_0, which is the only quantity experimentally accessible and measurable among the three listed here (i.e. U_0^{tot}, U_{TW}, and U_0), is smaller than the total trap depth such that

$$U_0 = U_0^{\mathrm{tot}} - U_{\mathrm{TW}} = \alpha_{\mathrm{E1}} 4\sqrt{I_1 I_2}. \tag{3.34}$$

In [58] an expanded version of the light shift model accounting for an intensity imbalance is discussed. Defining a TW correction $r = U_0^{\mathrm{tot}}/U_0 \geq 1$, the light shift model then becomes

$$\begin{aligned} h\Delta\nu_{\mathrm{Ls}} = {} & [\tilde{\alpha}'(\nu_{\mathrm{L}} - \nu_{\mathrm{E1}}) - \tilde{\alpha}^{\mathrm{qm}}] \left(\bar{n}_z + \frac{1}{2}\right) \sqrt{\left(\zeta - \frac{1}{2}\delta_2\right) \frac{U_0}{E_{\mathrm{r}}}} \\ & - \left[\tilde{\alpha}'(\nu_{\mathrm{L}} - \nu_{\mathrm{E1}}) r - \tilde{\alpha}^{\mathrm{qm}}(r-1) + \frac{3}{4}\tilde{\beta}(2\bar{n}_z^2 + 2\bar{n}_z + 1)\right] \zeta \frac{U_0}{E_{\mathrm{r}}} \\ & + \tilde{\beta}(2\bar{n}_z + 1) r \left[\left(\zeta + \frac{1}{2}\delta_2\right) \frac{U_0}{E_{\mathrm{r}}}\right]^{3/2} \\ & - \tilde{\beta} \left[r(\zeta + \delta_2) \frac{U_0}{E_{\mathrm{r}}}\right]^2 . \end{aligned} \tag{3.35}$$

The main difference from the light shift model of equation 3.29 is the appearance of an additional term $+\tilde{\alpha}^{\mathrm{qm}}(r-1)\zeta\frac{U_0}{E_{\mathrm{r}}}$ linear in the lattice intensity: if this term is not included, the effect of the TW contamination would mainly show up as a shift in the effective value of the E1-magic frequency.

In the RIKEN clock, the lattice is realised with two independent counter-propagating beams (see section 2.8), thus it is more prone to intensity imbalances compared to retro-reflected configurations. In order to contain intensity imbalances, we ensure that the two beams have the same optical power of 0.5 W when accessing the vacuum chamber, and we operate active power stabilization controls on both beams. Imperfect beam overlap is contained optimizing the beam throughput coupling in the fibre of the opposite beam, which we confirm to yield the largest observed trap depth.

A residual power imbalance may be due to different transmittances of the windows through which lattice beams access the vacuum chamber. This would lead

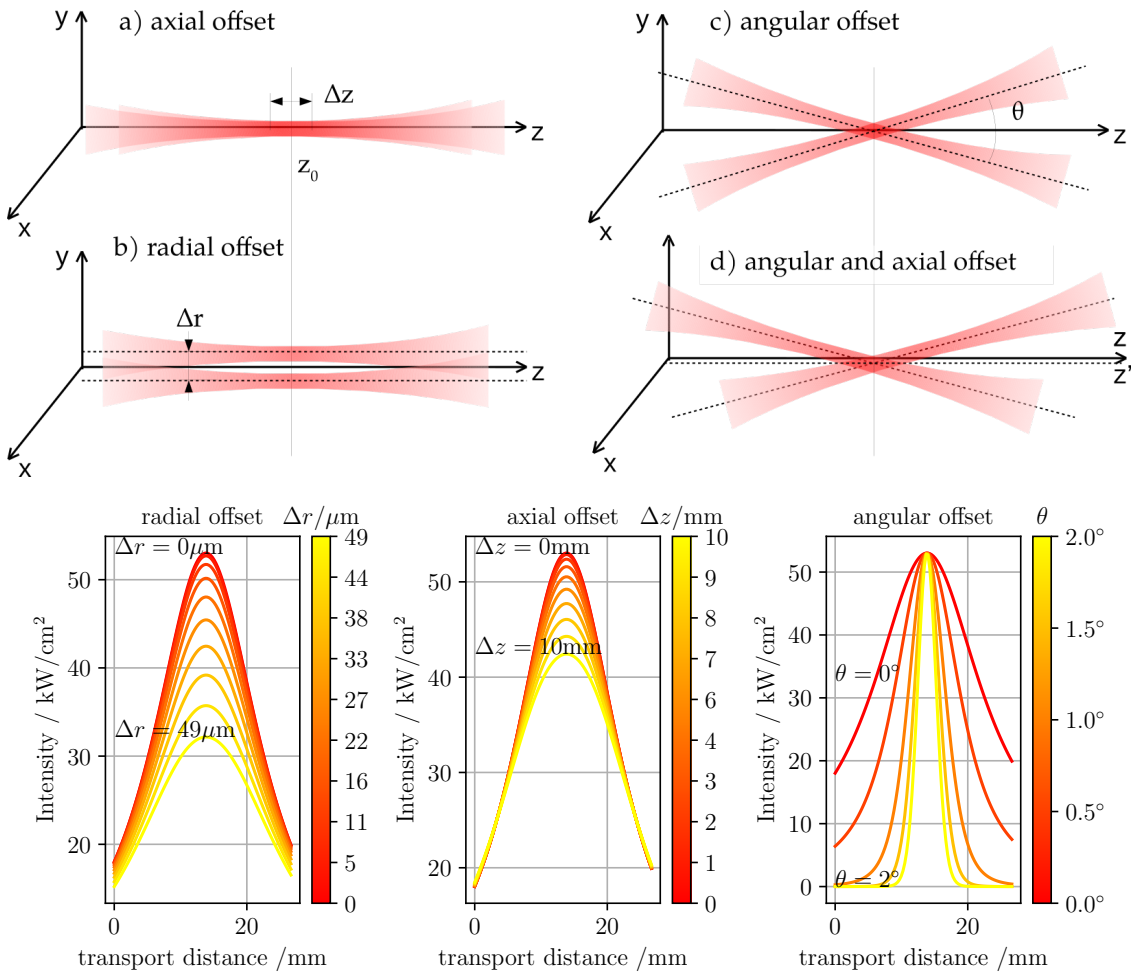

Figure 3.8: Above: hypothetical scenarios of a misalignment between the two lattice beams, leading to an imperfect beam overlap. Atoms are assumed to lie on the z-axis for cases a–c, while in case d atoms are assumed to be on the z'-axis. In cases a and d the beam mismatch leads to an intensity imbalance for a defined position z, while that does not happen in cases b and c because of the symmetry of the geometry. Below: plots of the simulated intensity profiles according to eq. (3.23) with lattice wavelength $\lambda_L = 759$ nm, beam waist $w_0 = 49$ µm and power for each beam of 0.5 W are shown for different magnitudes of the alignment offsets between the two beams, as indicated by colours and the respective labels of the colour bar. Transport distance refer to the on-axis position at which atoms are transported along the z-axis from the initial position where they are loaded in the lattice (see section 2.8 for details).

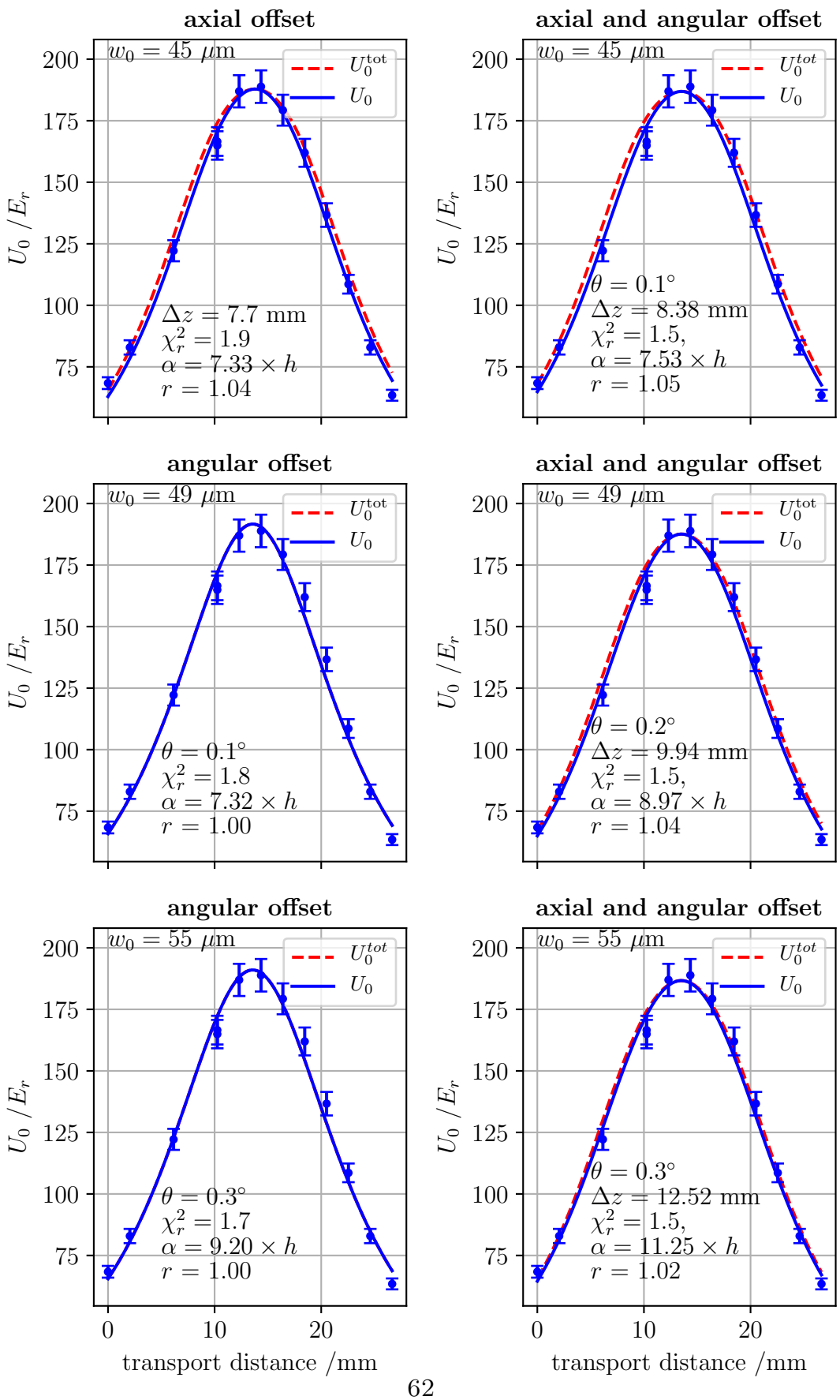

Figure 3.9: Agreement of the experimental distribution for U_0 with models (blue) accounting for misalignments, assuming different values for the beam waist w_0. red curves show the corresponding profile for $U_0^{\rm tot}$ assuming the parameters extracted from the blue fit; $\alpha \equiv \alpha_{\rm E1}$ is the polarizability in units of kHz/(kW/cm^2) extracted from the fit.

to a relative attenuation $a_r = I_1/I_2$ between the two beams, corresponding to $r = (1 + \sqrt{a_r})^2/(4\sqrt{a_r})$. A 10 % imbalance ($a_r = 0.9$) leads to a TW correction of $r = 1.0007$ with negligible effect on the final evaluation of the light shift.

In order to estimate the value of the TW correction r in our experimental conditions due to imperfect beam overlap we characterise the shape of the lattice potential within the Rayleigh range measuring the on-axis lattice modulation depth U_0 at different transport distances to map U_0 along the lattice region of interest (see fig. 2.18 in chapter 2, and figure 3.9). We compare the experimental distribution of U_0 with the expected profile of eq. (3.34) either according to perfect overlap or including in the model different hypothetical beam misalignments. We consider as possible residual misalignments radial (Δr), axial (Δz) or angular (θ) offsets between the two beams. Figure 3.8 (upper figure) shows the magnified effect of such misalignments on the lattice geometry as displacements between the two beams. In figure 3.8 (lower figure) the lattice intensity over the transport distance is simulated for different values of the spatial misalignment, as indicated by the colour scale, to predict the effect on the modulation depth: axial and radial offsets mainly lead to a drop of the intensity near the lattice waist, while angular offsets lead to a fast decrease of the intensity when moving away from the lattice waist.

We fit the experimental distribution of U_0 with models of the form of eq. (3.34) allowing in the equations of the intensity profiles $I_{1(2)}$ free parameters describing alignment offsets. We allow as a free parameter also the electric dipole polarizability α_{E1} providing the scaling factor (for this analysis we ideally assume no attenuation of the overall lattice intensity from the chamber windows, which would lead to different scaling factors). While the lattice beam waist is estimated to be $w_0 \simeq 49$ µm as extracted from the fit setting $r = 1$, we allow a 10% possible variability in its determination; therefore we perform the analysis fixing the waist at $w_0 = 45$ µm, 49 µm and 55 µm. Among all the cases investigated, we report in figure 3.9 the results showing an improved agreement between the model (blue curve) and the data (blue dots) according to the value of χ^2_{red} with respect to case with a negligible TW (i.e. $r = 1$, in this case the fit provides $\chi^2_{red} = 2.1$). In the plots the red dashed curve represent the corresponding profile of U_0^{tot} according to eq. (3.32) evaluated with the parameters extracted from the fit.

Based on this analysis we estimate the TW fraction to be $r = 1.03(3)$. We fit the light shift model of eq. (3.35) leaving ν_{E1} as free parameter to a series of light shift measurements performed interleaving operation at $U_e^{high} = 111\ E_r$ and $U_e^{low} = 49\ E_r$. Figure 3.10 (above) shows the extracted value for ν_{E1} for each of the light shift measurements performed, while the figure below shows the deviations of the measured shifts from the light shift model. We finally evaluate $\nu_{E1} = 394\,798\,266.5(9)$ MHz. Within the standard conditions at which we operate the RIKEN Yb clock (the same of the Yb/Sr frequency ratio measurement discussed in chapter 4 where we operate the lattice at $U_0 \sim 90\ E_r$), the largest effect in the inclusion of this factor r in the light shift model is the shift in the estimated E1

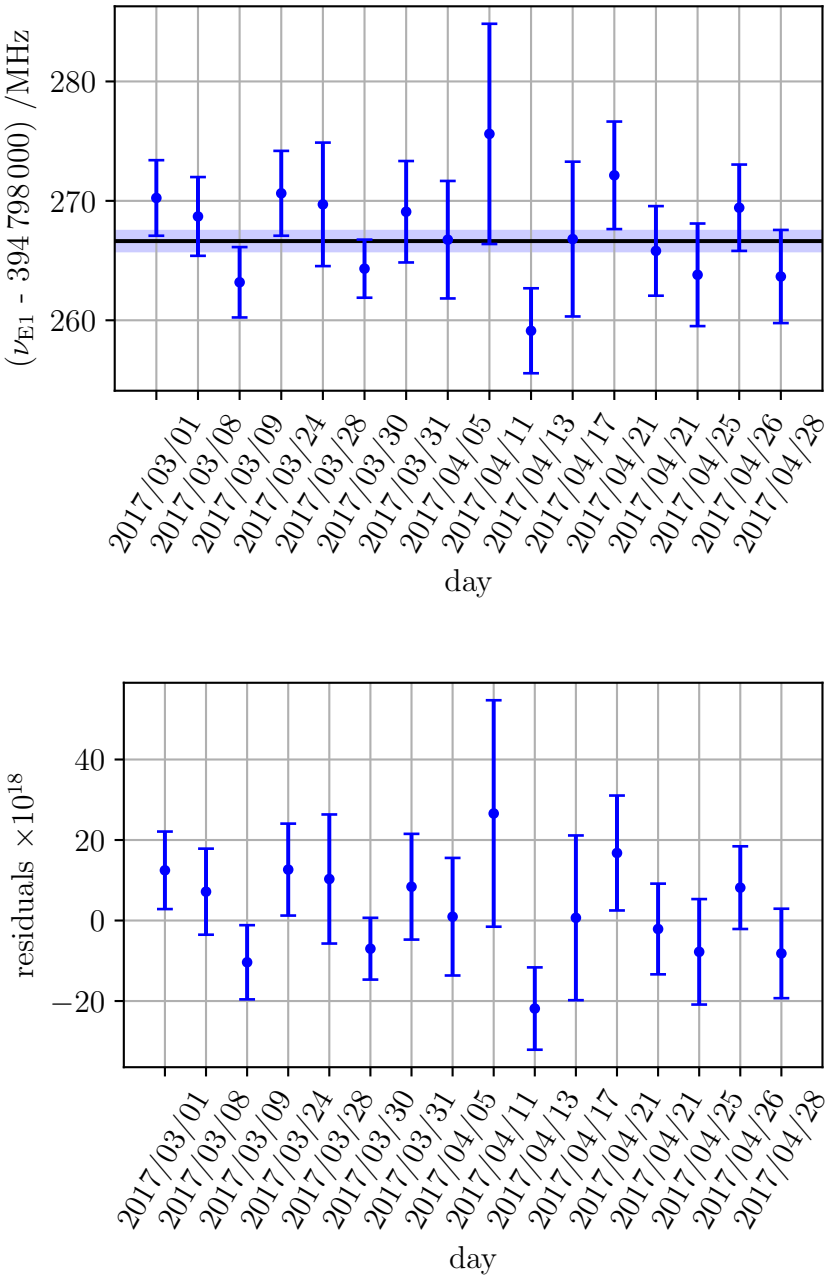

Figure 3.10: Above: extracted value for the E1-magic frequency ν_{E1} for each of the light shift measurements performed. Note that the extracted ν_{E1} may differ from its true value if residual unaccounted shifts linear in the lattice intensity are present. Below: fractional deviation of the light shift measurement results from the light shift model.

magic frequency of −1 MHz.

In the earlier work we performed operating the lattice in a retro-reflected configuration and described in [58], the E1-magic frequency was found to be $\nu_{E1} = 394\,798\,261(1)$ MHz.

At INRIM, where a retro-reflected lattice is operated, in 2018 we performed renewed light shift measurements and evaluated a E1-magic frequency of $\nu_{E1} = 394\,798\,265(3)$ MHz. The determinations at INRIM and at RIKEN are in agreement with results in [51, 112, 113] within few megahertz.

Other evaluations of the magic frequency by other research groups [51, 104, 113–115] provide results which differ by up to 100 MHz. We believe that such differences in the magic frequency determinations are related to spectral impurities on the lattice laser in addition to unaccounted TW contributions, leading to light shifts that show the same linear dependence on intensity as the differential E1 polarizability. We conclude that a determination of ν_{E1} in the specific experimental conditions of operation is required.

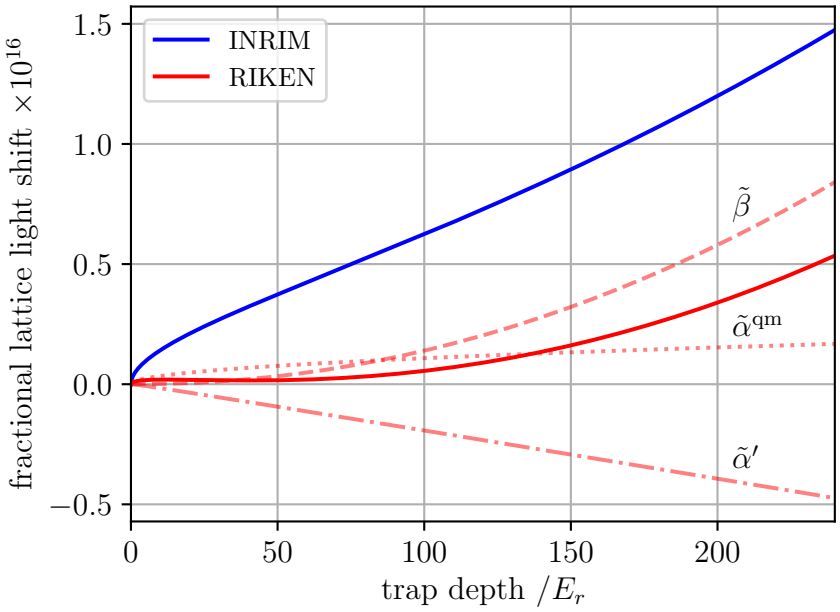

Figure 3.11: Expected fractional light shift according to the model of eq. (3.29) for standard operating conditions at INRIM and at RIKEN. Lattice parameters are respectively ($\zeta = 0.7$, $\delta_2 = 0$, $\bar{n}_z = 2.1$, $\nu_L = 394\,798\,267$ MHz, $\nu_{E1} = 394\,798\,265$ MHz) and ($\zeta = 0.8$, $\delta_2 = 0$, $\bar{n}_z = 0.1$, $\nu_L = 394\,798\,273$ MHz, $\nu_{E1} = 394\,798\,267$ MHz). Red dashed lines represent the different light shift terms related to either the dipole, multipolar or hyper-polarizability (as indicated by the labels) for the RIKEN trap parameters.

The expected lattice light shift at typical trap depth values is reported in figure 3.11. The trapping parameters ζ and $\bar{n}_z$ used for the simulation represent typical

operation at $U_0 \sim 240\ E_\mathrm{r}$ at INRIM and at $U_0 \sim 90\ E_\mathrm{r}$ at RIKEN. The figure clearly shows the non-linearity of the shift, especially at small trap depths. The shift simulated for the usual RIKEN trapping parameters is decomposed among the different contributions from the different lattice polarizabilities: by appropriately choosing ν_L, and thus the contribution from $\tilde{\alpha}'$, it is possible to compensate the contribution from $\tilde{\beta}$ to reduce the magnitude of the total shift below 10^{-17}.

Tuning the lattice frequency and trap depth it is possible to find a set of trapping parameters at which the total lattice light shift cancels out together with its derivative [52]. Using the E1-magic frequency found in [58] for Yb, at the typical operating conditions of the RIKEN Yb clock the cancellation point is found at a trap depth $U_0 = 56\ E_\mathrm{r}$ and a lattice frequency $\nu_\mathrm{L} = 394\,798\,267$ MHz.

A different model of the lattice light shift has been proposed in [51]. If the axial atomic temperature scales linearly with the trap depth $T_z \propto U_0$, it is found that the lattice light shift based on the potential of equation (3.27) simplifies to

$$\frac{\Delta\nu_\mathrm{Ls}}{\nu_\mathrm{Yb}} = -\alpha^* \frac{U_0}{E_\mathrm{r}} - \beta^* \left(\frac{U_0}{E_\mathrm{r}}\right)^2, \tag{3.36}$$

where the parameters $\alpha^* = (\nu_\mathrm{L} - \nu_\mathrm{zero})\frac{\partial\alpha^*}{\partial\nu_\mathrm{L}}$ and β^* have to be measured in the specific experimental conditions related to the clock operation. ν_zero is the lattice frequency at which the total light shift is cancelled. The Authors of [51] report the value of their coefficients converted in atomic properties, in order to allow direct comparison with (3.31). Taking into account thermal effects they obtain $\tilde{\alpha}'/h \approx 20$ µHz MHz^{-1} and $\tilde{\beta}/h \approx -0.5$ µHz. They also perform a theoretical calculation to evaluate $\tilde{\alpha}^\mathrm{qm}/h = -80(80)$ µHz.

The advantage of using the simple model (3.36) is counterbalanced by the experimental requirement of the temperature linear scaling with the lattice depth, which is not valid in general and needs to be confirmed with the specific system in use.

Extraction of the lattice parameters. The lattice trapping parameters, namely the lattice on-axis modulation depth U_0, the mean axial vibrational quantum number $\bar{n}_z$ and the trap depth corrections ζ and δ_2, in addition to the lattice frequency ν_L, require to be measured in order to evaluate the lattice light shift at the operating conditions.

The extraction of such parameters is possible performing axial sideband spectroscopy, where interrogation pulses are applied with an optical power and a frequency detuning from the clock electronic resonance sufficient to excite the lattice vibrational sidebands with $\Delta n_z = n_z^\mathrm{e} - n_z^\mathrm{g} \neq 0$. In these conditions the clock electronic transition ($\Delta n_z = 0$) is overdriven with a pulse area several times larger than π: this results in saturation broadening and a maximum excitation probability $P \approx 0.5$.

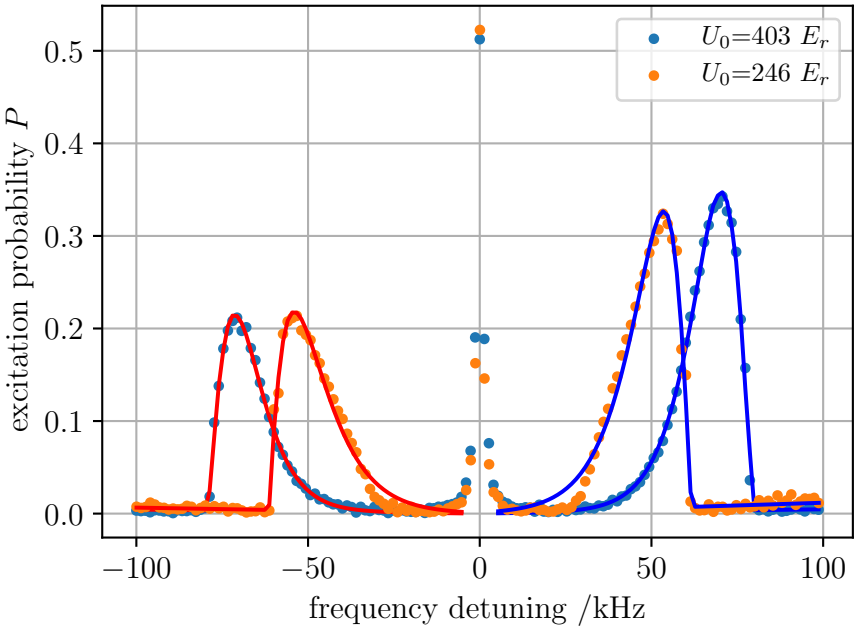

Figure 3.12: Sideband spectra acquired at INRIM at usual operating conditions. Data is fitted with the thermal model discussed in the text. The extracted trap parameters at high/low trap depth are respectively ($U_0 = 403\ E_\mathrm{r}$, $\zeta = 0.72$, $\bar{n}_z = 1.3$) and ($U_0 = 246\ E_\mathrm{r}$, $\zeta = 0.73$, $\bar{n}_z = 2.1$).

Figures 3.12 and 3.13 show typical experimental sideband spectra acquired at INRIM and at RIKEN respectively at different trap depths. The red sideband at lower frequencies than the carrier (i.e. the electronic transition) accounts for the $\Delta n_z = -1$ transitions, while the blue sideband at higher frequencies accounts for the $\Delta n_z = 1$ transitions. The shape of the sidebands can be interpreted imagining of taking an instant picture of the atoms oscillating in the radial (x, y) plane within the trapping potential well: according to their individual radial energy they will reside at different distances from the lattice axis. Experimentally, this picture can be acquired performing sideband spectroscopy with pulses of duration smaller than the radial oscillation period.

In this framework, an atom located at $r = 0$ undergoes the on-axis lattice depth U_0, while an atoms in a higher radial state undergoes a shallower trap depth. It is then possible to assign to every trapped atom i a trap depth $0 < U_i \leq U_0$ and a frequency detuning $\delta\nu^i_\mathrm{sb}(U_i)$ from the carrier at which the atom is excited on the blue sideband [89]

$$\delta\nu^i_\mathrm{sb} = \nu^i_z - (n^i_z + 1)\frac{E_\mathrm{r}}{h} = \left(2\sqrt{U_i E_\mathrm{r}} - (n^i_z + 1)E_\mathrm{r}\right)\frac{1}{h}, \tag{3.37}$$

with ν^i_z being the axial trap frequency, and n^i_z is the longitudinal vibrational state

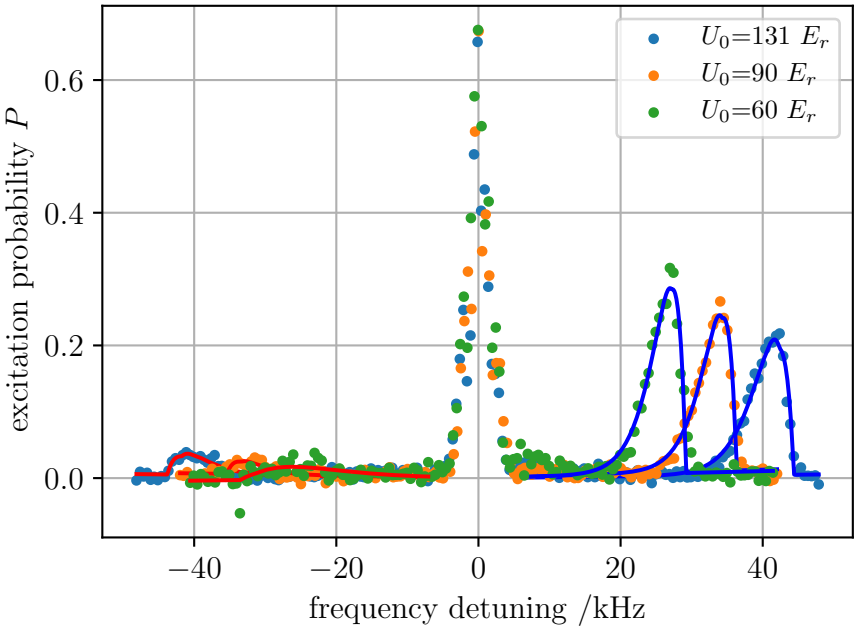

Figure 3.13: Sideband spectra acquired at RIKEN at usual operating conditions. Data is fitted with the thermal model discussed in the text. The extracted trap parameters at high/intermediate/low trap depth are respectively ($U_0 = 131\ E_\mathrm{r}$, $\zeta = 0.72$, $\bar{n}_z = 0.3$), ($U_0 = 90\ E_\mathrm{r}$, $\zeta = 0.76$, $\bar{n}_z = 0.2$) and ($U_0 = 60\ E_\mathrm{r}$, $\zeta = 0.73$, $\bar{n}_z = 0.1$).

of the individual atom. The Rabi frequency Ω^i_sb of the sideband transition ($n^i_z \leftrightarrow n^i_z - 1$) is related the strength of the confinement through the Lamb-Dicke parameter $\eta^i = \sqrt{E_\mathrm{r}^\mathrm{Yb}/(h\nu^i_z)}$ according to [20]

$$\Omega^i_\mathrm{sb} \approx \sqrt{n^i_z + 1}\,\eta^i\,\Omega_\mathrm{R}, \tag{3.38}$$

where Ω_R is the Rabi frequency of the electronic clock transition ($\Delta n_z = 0$).

The shape of the red sideband is symmetric to that of the blue sideband about the carrier, apart from the fact that atoms in the ground vibrational state $n_z = 0$ do not contribute to the red sideband excitation. Thus the height of the red sideband, besides the contribution from the different Rabi frequencies, is suppressed with respect to that of the blue sideband according to the axial temperature T_z, which can be calculated from the ratio between the areas below the two sidebands (see ref. [89]). At RIKEN we perform axial sideband cooling to cool atoms down to the lowest vibrational state so that $\bar{n}_z \simeq 0.1$, leading to a residual temperature $T_z < 1$ µK, instead at INRIM we do not perform this additional cooling stage: the mean vibrational quantum number is found to be $\bar{n}_z > 1$ and $T_z \sim 7$ µK at 240 E_r. These conditions explain the difference in the shape of the red sideband in the two figures.

The sideband spectrum can be modelled considering the potential shape of equation 3.25 and assuming that atoms are thermally distributed among radial states [89]. The red and blue fitting curves in figures 3.12 and 3.13 are obtained applying this thermal model. In some operating conditions this approach leads to satisfactory results, however if the radial motional energies are not much smaller than the trap depth the atoms probe regions of the trapping potential where the assumption of a harmonic radial potential is not valid. In this case the thermal model underestimates the density of high energy radial modes near the edge of the trap, and thus it underestimates the occupation of such energetic states.

We observe that with this thermal model the fit of a sideband spectrum acquired probing a radially hot atomic sample fails to reproduce the zero-excitation profile near the carrier, where the trap depth U_i is too small to allow confinement; this is due to the larger-than-expected signal corresponding to radially energetic atoms which appears along the sideband slope towards the carrier and cannot be modelled. This is partially visible in figure 3.12 for the low intensity case (orange dots), where no radial cooling methods are implemented. A discussion of this effect can be found in ref. [58]: we find that a truncated thermal distribution among transverse states might effectively describe the sideband shape of a radially hot atomic sample.

In order to contain this issue, high radial atomic energies are tried to be avoided by loading the atoms from the MOT cloud in a shallow lattice and ramp the lattice intensity to the final value in a second step. In fig. 3.12, sideband spectroscopy performed for the high lattice intensity case is acquired loading the atoms at $U_0 \sim 240\ E_\mathrm{r}$, and then ramping the trap depth to 403 E_r for the interrogation, while the low intensity case is measured with a fixed trap depth at $U_0 \sim 240\ E_\mathrm{r}$ during the loading and the interrogation (the sequence is also discussed in section 2.7). The sideband spectra acquired at RIKEN and shown in fig. 3.13 are obtained with the three lattice intensity sequences discussed in section 2.8; atoms are loaded at maximum lattice intensity, however the loading is performed at about 13 mm from the lattice focusing position, at a trap depth 20 % lower than at the position for the interrogation. In addition we include before interrogation a dip in the lattice intensity to an intensity level at least 10 % lower than during interrogation.

A different approach has also been proposed to model the axial sidebands without relying on assumptions over the atom distribution across the lattice radial modes [58]. If atoms are axially cooled to the lowest vibrational state so that $\bar{n}_z \simeq 0$, than the frequency detuning $\delta\nu^i_{\mathrm{BSB}}(U_i)$ is not ambiguous, as it depends only on U_i, and the sideband shape can be fitted numerically assuming that atoms are excited with the Rabi frequency Ω^i_{sb} of eq. (3.38). This approach does not require any assumption about the potential shape since it directly relates the observed trap frequencies to trap depths.

Investigation of the lattice dipole polarizability and hyperpolarizability at INRIM

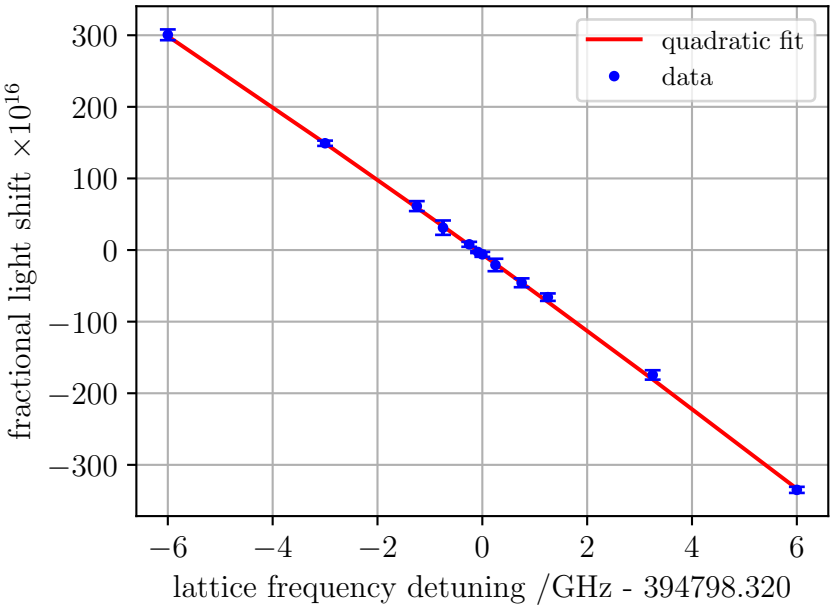

Figure 3.14: Lattice light shft measurements performed interleaving operation between a trap depth of $U_0^{\text{low}} = 208(1)\ E_\text{r}$ and a trap depth of $U_0^{\text{high}} = 333(2)\ E_\text{r}$ at different lattice frequencies. Shift results are dominanted by the light shift component linear in the lattice intensity. The linear shift scaling with the lattice frequency detuning is extracted as the linear coefficient of a polynomial fit of the data set.

The linear component of the lattice light shift of equation (3.29) is dominated by the term proportional to $(\nu_\text{L} - \nu_{\text{E1}})$, representing the lattice frequency detuning from the E1-magic frequency. Therefore it can be investigated acquiring light shift measurements between *high* and *low* lattice intensity conditions at different lattice frequencies. We perform this measurements interleaving the clock operation between a trap depth of $U_0^{\text{low}} = 208(1)\ E_\text{r}$ and a trap depth of $U_0^{\text{high}} = 333(2)\ E_\text{r}$. Results, linearly scaled at a trap depth of $U_0 = 200\ E_\text{r}$, are shown in figure 3.14.

From the experimental data it is possible to extract the slope of α_{E1} near the E1-magic frequency as $\tilde{\alpha}'/h = -27(3)\ \mu\text{Hz}\,\text{MHz}^{-1}$ (reported in ref. [114]), which is in in agreement with the result obtained with a similar investigation at RIKEN [58] (see figure 3.16).

The lattice differential hyperpolarizability $\tilde{\beta}$ can be investigated performing light shift measurements at fixed frequency ν_L and varying the trap depth (see the model 3.29). Nonetheless, because of the large shift contribution linear in the lattice intensity, in order to resolve the curvature of the shift due the hyperpolarizability

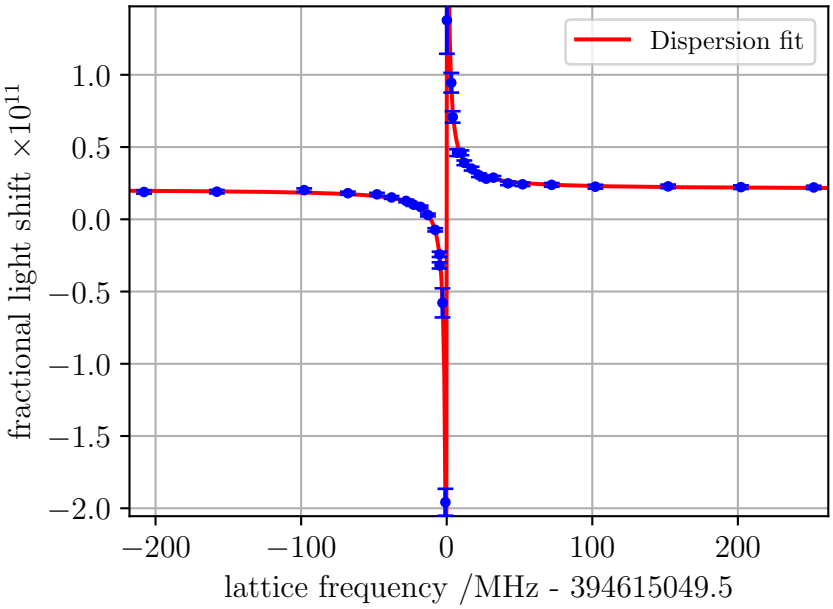

Figure 3.15: Lattice light shift induced by the $6s6p\,^3P_0$–$6s8p\,^3P_0$ two-photon transition.

it is required to explore a large range of trap depths; for example, at RIKEN light shift measurements are performed in a range of trap depths between 90 E_r and 600 E_r [58].

In our experiment we cannot afford such large range of trap depths. Firstly, the lattice provides at maximum an output power of about 2.5 W and we do not use an enhancement cavity; secondly, the lattice of waist $w_0 = 45$ µm is realised transversally with respect to gravity, thus the gravitational potential modifies the trap shape reducing the effective depth in which atoms can be confined. As a result we manage to trap atoms and operate the clock within a range of trap depth between 200 E_r and 400 E_r, not sufficient to resolve the effect of hyperpolarizability.

Two-photon transition	resonance frequency ν_{2ph} /MHz
$6s6p\,^3P_0$–$6s8p\,^3P_2(F = 3/2)$	397 484 603.3(3)
$6s6p\,^3P_0$–$6s8p\,^3P_2(F = 1/2)$	397 480 706.7(1)
$6s6p\,^3P_0$–$6s8p\,^3P_0$	394 615 049.5(1)
$6s6p\,^3P_0$–$6s5p\,^3F_2(F = 7/2)$	391 910 851(10)
$6s6p\,^3P_0$–$6s5p\,^3F_2(F = 5/2)$	391 908 676(4)

Table 3.1: Relevant two-photon transitions and their resonance frequency measured at INRIM.

Since the hyperpolarizability results from the coupling of the lattice light with two-photon resonances at frequencies $\nu^i_{2\mathrm{ph}}$ involving the $^3\mathrm{P}_0$ clock state, its effect is maximally visible when $\nu_\mathrm{L} \approx \nu^i_{2\mathrm{ph}}$. Therefore another approach to investigate the shift quadratic coefficient is to measure the clock frequency shift with ν_L close to the relevant two-photon resonances (listed in table 3.1) and extrapolate the shift at $\nu_\mathrm{L} = \nu_{\mathrm{E1}}$ [108, 116].

We measure the lattice light shift at $U_0 \sim 360\ E_\mathrm{r}$ using the local oscillator optical cavity as frequency reference for different values of ν_L around the two-photon resonances. We account for daily linear drifts of the reference cavity through linear interpolation of data acquired at $\nu_\mathrm{L} = \nu_{\mathrm{E1}}$ before and after the experiments at different lattice frequencies. Shift results are shown in figures 3.15 and 3.17 together with a dispersion fit approximated with the hyperbolic light shift model of eq. (3.17) (as done also in ref. [108, 117]) accounting for the detuning $\Delta\omega = 2\pi|\nu_\mathrm{L} - \nu_{2\mathrm{ph}}|$, the two-photon transition linewidth $\Gamma_{2\mathrm{ph}}$, its Rabi frequency $\Omega_{2\mathrm{ph}}$ and an additional offset accounting for the linear light shift contribution, assumed constant in the frequency range investigated:

$$\Delta\omega_{2\mathrm{ph}}(\omega_\mathrm{L}) = 2\pi\Delta\nu_{2\mathrm{ph}}(\nu_\mathrm{L}) = \frac{\Delta\omega}{4\Delta\omega^2 + \Gamma^2_{2\mathrm{ph}}}\Omega^2_{2\mathrm{ph}} + 2\pi\Delta\nu_{\mathrm{lin}} = \frac{\Delta\omega A}{4\Delta\omega^2 + D^2} + B, \tag{3.39}$$

with A, B, D and the two-photon frequency $\nu_{2\mathrm{ph}}$ as free parameters.

Two-photon resonances can be identified at the lattice frequency where the clock excited state population cannot be measured as the $^3\mathrm{P}_0$ state is totally depleted by the two-photon excitation, which expels the atoms from the trap.

According to the weak coupling limit equations (3.17), the lattice-atom interaction leads to both a frequency shift and a spectral line broadening. As a consequence the clock transition when $\nu_\mathrm{L} \approx \nu_{2\mathrm{ph}}$ has a linewidth of several kilohertz for the chosen lattice intensity and its spectral shape can be acquired by frequency scans across the resonance without strict requirements in terms of laser stability. The signal is acquired as a depletion of the trap. The line shape results to be asymmetric as far as the atoms are distributed among multiple vibrational levels n_z [118]: a superposition of Lorentzian profiles is used as fitting model for the line and the resonance central frequency is calculate as a weighted average over the spectroscopy frequency scan using the line shape as weighting distribution. This extracts the light shift corresponding to atoms in the average vibrational quantum number $\bar{n}_z$, which is evaluated acquiring the sideband spectra at $\nu_\mathrm{L} \approx \nu_{\mathrm{E1}}$.

The light shift $\Delta\nu_{\mathrm{hyper}}$ induced by the hyperpolarizability, evaluated from the dispersion fits after removing the offset and rescaling at the E1-magic frequency, is used to evaluate the coefficient $\tilde{\beta}$ from equation (3.29):

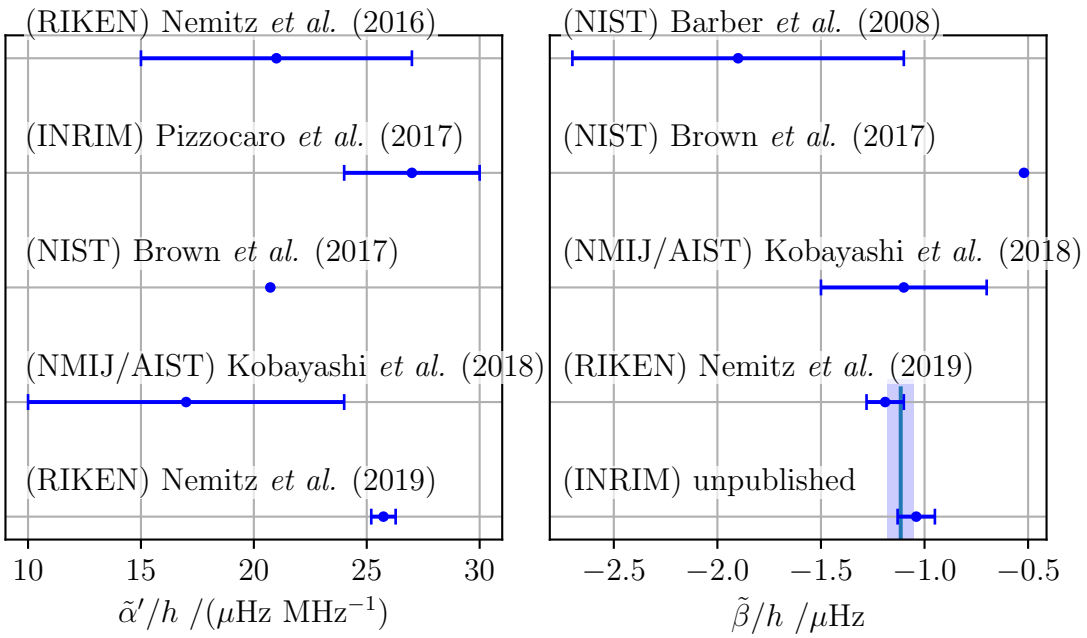

Figure 3.16: Summary of the measurements performed by different research groups worldwide of the slope of the E1 differential polarizability around ν_{E1} ($\tilde{\alpha}'$) [51, 58, 100, 112, 114] and of the differential hyperpolarizability $\tilde{\beta}$ [51, 58, 100, 108]. The result of Barber *et al.* [108] is taken from [112] where a conversion of the original number based on a model similar to (3.40) has been performed. Uncertainties are not reported for results of Brown *et al.* [51]. The weighted mean of the two most accurate values of the hyperpolarizability coefficient, measured independently at RIKEN and INRIM, is $\tilde{\beta}/\hbar = -1.12(6)$ µHz, as shown by the vertical line.

$$\begin{cases} \Delta\nu_{\mathrm{hyper}} = -\sum_i \left(\delta\nu^i_{\mathrm{2ph}}(\nu_{\mathrm{E1}}) - \Delta\nu^i_{\mathrm{lin}}\right) \approx -\sum_i \dfrac{A^i}{4(\nu_{\mathrm{E1}} - \nu^i_{\mathrm{2ph}})} \\ h\Delta\nu_{\mathrm{hyper}} = \tilde{\beta}\left[\dfrac{3}{4}\left(2\bar{n}_z^2 + 2\bar{n}_z + 1\right)\dfrac{U_{\mathrm{e}}}{E_{\mathrm{r}}} + (2\bar{n}_z + 1)\left(\dfrac{U_{\mathrm{e}}}{E_{\mathrm{r}}}\right)^{3/4} - \left(\dfrac{U_{\mathrm{e}}}{E_{\mathrm{r}}}\right)^2\right] \end{cases} \tag{3.40}$$

where the sum runs over all relevant two-photon transitions as listed in table 3.1. U_{e} is the effective trap depth at $\nu_{\mathrm{L}} \approx \nu_{\mathrm{E1}}$. We finally evaluate the hyperpolarizability coefficient $\tilde{\beta}/h = -1.04(9)$ µHz, in agreement with the result obtained at RIKEN and discussed in ref. [58]. We also find agreement with the result obtained at NMIJ investigating the two-photon resonance with a similar approach: they evaluate the coefficient to be $\tilde{\beta}_{\mathrm{NMIJ}}/h = -1.1(4)$ µHz [100]. See figure 3.16 for the summery of the results obtained by the different research groups.

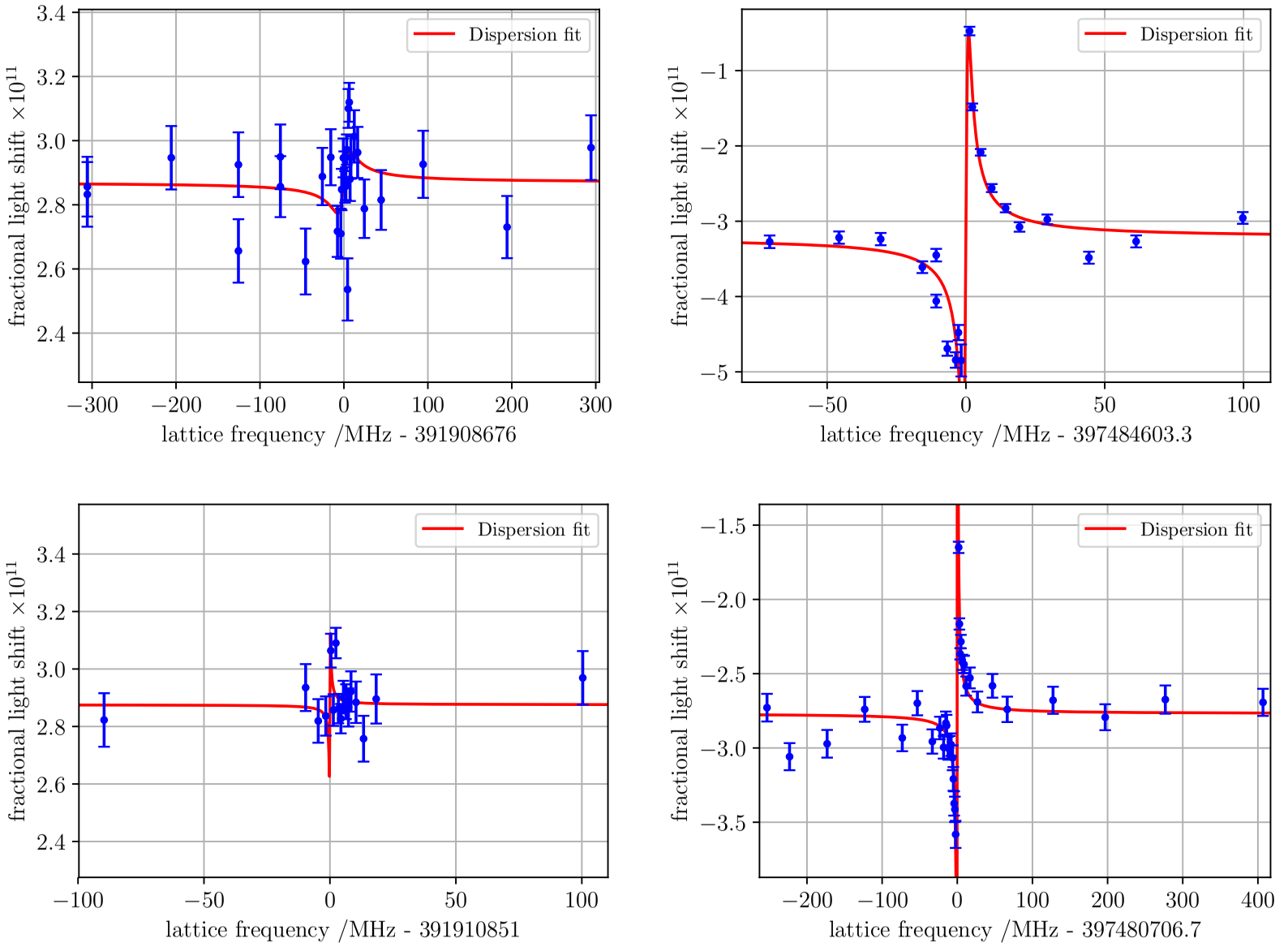

Figure 3.17: Lattice light shift induced by the $6s6p\,^3P_0$–$6s5p\,^3F_2$ transitions (left side of the page) and the $6s6p\,^3P_0$–$6s8p\,^3P_2$ transitions (right side of the page).

3.2.2 Probe light shift

The clock Rabi interrogation is performed through a single π-pulse of duration T_i of the probe laser, which is frequency tuned to the resonance of the clock transition. In the work presented here the Rabi frequency $\Omega_\mathrm{R} = \pi/T_\mathrm{i}$ ranges from 50 rad/s to 10 rad/s, with typical interrogation times between 60 ms to 300 ms. Since the Yb $^1\mathrm{S}_0$–$^3\mathrm{P}_0$ clock transition has a natural damping rate $\Gamma_\mathrm{Yb} = 4.42(35)\ \mathrm{s}^{-1} < 10\ \mathrm{s}^{-1}$ [47], the probe laser satisfies the relation of $\Omega_\mathrm{R} > \Gamma/2$ for the clock transition, which is the threshold to fall in the high coupling regime discussed at the beginning of the section.

The coupling of the resonant probe light to the clock transition does not induce a frequency shift. Nevertheless, the probe light couples with other off-resonance transitions involving the clock transition states, and induce a frequency shift according to eq. (3.17): table 3.2 summarizes the relevant transitions ($|i\rangle \rightarrow |j\rangle$) and the calculated light shift contributions to the total shift when applying a Rabi π-pulse of duration T_i. The calculation is performed extracting the probe intensity during the interrogation pulse I_p from equations (3.13) and (3.19):

$$I_\mathrm{p} = 2\epsilon_0 c|E_\mathrm{l}|^2 = \frac{\hbar}{6\pi c^2}\frac{\omega_\mathrm{Yb}^3\Omega_\mathrm{R}^2}{\Gamma_\mathrm{Yb}}, \tag{3.41}$$

where $\omega_\mathrm{Yb} \approx 2\pi \times 518$ THz is the Yb clock frequency. The clock energy level frequency shifts are then calculated from (3.20):

$$\delta\omega_{\mathrm{p},ij} = \pm\frac{1}{8\pi}\frac{\Gamma_{ij}}{\omega_{ij}^3\Delta\omega_{ij}}\frac{\omega_\mathrm{Yb}^3\Omega_\mathrm{R}^2}{\Gamma_\mathrm{Yb}}, \tag{3.42}$$

with $\Delta\omega_{ij} = \omega_\mathrm{l} - \omega_{ij} = \omega_\mathrm{Yb} - \omega_{ij}$, since the probe laser is approximately resonant to the clock transition. The final probe light shift contributions from the different transitions $|i\rangle$–$|j\rangle$ listed in table 3.2 are obtained from (3.42) accounting for the correct sign: if the frequency of the clock transition excited state decreases, the clock transition frequency decreases as well, while for the ground state the opposite is true.

Combining these shifts (resulting from the modification of either the ground or the excited clock state) it is possible to evaluate the expected probe light shift of the clock transition $\Delta\nu_\mathrm{p} = 1.2 \times 10^{-19}$ for a 120 ms interrogation pulse, or $\Delta\nu_\mathrm{p} = 1.9 \times 10^{-20}$ for a 300 ms pulse.

Measurement of the probe light shift coefficient at RIKEN

The standard approach to measure a frequency shift affecting the clock transition frequency is to interleave the clock operation between two experimental conditions which differ by just the magnitude of the physical effect generating the shift. The resulting frequency difference between the clock frequencies extracted

Transition ($\|i\rangle \rightarrow \|j\rangle$)	λ_0 /nm	ν_0 /THz	Γ /(rad/s)	fractional shift $\frac{\Delta\nu_p}{\nu_{Yb}} \times 10^{20}$ $T_i = 120$ ms	$T_i = 300$ ms
$^1S_0$–$^1P_1$	398.9	751	1.8×10^8	4.9	0.78
$^1S_0$–$^3P_1$	555.8	539	1.2×10^6	0.91	0.15
$^1S_0$–$^3P_0$	578.4	518	4.4	-	-
$^3P_0$–$^3S_1$	649.1	462	9.7×10^6	4.6	0.74
$^3P_0$–$^3D_1$	1388.8	216	1.7×10^6	1.5	0.24

Table 3.2: Relevant atomic transitions which are coupled by the probe light with their wavelength λ_0, decay rate Γ [119, 120] and the expected light shift contribution to the total probe light shift of the clock transition according to the theoretical model (assuming the probe laser is resonant with the clock transition).

from the two operating conditions directly provides information about the induced frequency shift of interest, as all other perturbations are common between the two experimental settings and cancel out from the frequency difference.

The probe light shift, according to this method, can be measured by interleaving the clock operation with either a reduced probe beam intensity or a maximized intensity. However, using the Rabi interrogation this approach is problematic since a variation in the probe intensity leads to a variation of the Rabi frequency. Since the clock operation requires that atoms are interrogated with a π-pulse, reducing the probe intensity means that a longer interrogation pulse T_i needs to be implemented, but this reduces the linewidth of the clock transition spectroscopy feature to the point that the local oscillator instability does not allow the lock to the atomic resonance any more. Concerning the opposite case, where the probe Rabi frequency is increased, the resulting spectral line shape used to lock the laser is broader than in the standard operation, with a consequent reduction in clock stability. Furthermore, if an unsuppressed frequency shift related to the spectral line shape, such as a line pulling effect or the shift from cold collisions, is present, it does not cancel out from the resulting frequency difference between the interleaved modes of operation and will affect the measurement results.

In order to overcome this issues, we perform the shift characterization applying the interleaved clock method with a Ramsey interrogation scheme (see section 2.4 and fig. 2.5), without turning off the laser beam during the dark time T_{dark}. If the probe laser is active and frequency detuned during the dark time, it induces a light shift also during this additional interrogation time, included between the two resonant pulses of duration T_p.

The linewidth of the Ramsey spectroscopy fringe used to lock the local oscillator to the atomic reference is determined by the Ramsey time $T_r = T_p + T_{dark}$, defined as the time separation between the centre of the two short pulses (see fig. 2.5), such that the linewidth (as the full width at half maximum) $\gamma \approx 1/(2T_r)$. As

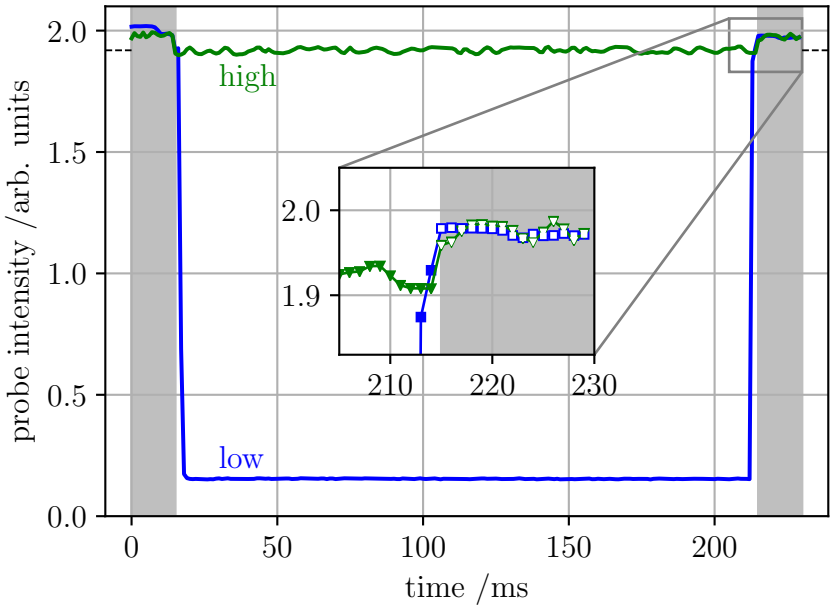

Figure 3.18: Probe beam intensity measured with a photodetector during the Ramsey interrogation while performing probe light shift interleaved measurements. Blue(green) data show a typical acquisition for a clock cycle at low(high) probe intensity. The shown data is obtained after taking the average by 1 ms segments of the signal collected with a 10 kHz sampling rate. The quantization error due to the signal sampling is below the 0.05%. White-filled open markers show the recorded signal during the resonant pulses, which are highlighted as grey-shaded areas. During the free evolution period of $T_{\mathrm{dark}} = 200$ ms, the intensity is either maintained at full level (green) or attenuated to approximately 8% (blue). Dashed lines illustrate the intensity outside of the interrogation sequence, for which no data is recorded

a consequence T_{p} can be chosen as short as possible to deliver the maximum available probe intensity, while compensating with a longer dark time to maintain the Ramsey time unchanged and avoid losing in clock stability. In addition the probe intensity can be varied just within T_{dark} to measure the induced frequency shift, so that the Rabi frequency, which depends on the probe intensity during the resonant pulses, is unchanged between the two operating conditions (see fig. 3.18). With this approach the light shift during the short resonant pulses is common between the two operating conditions and does not contribute to the final result.

Interrogation $\pi/2$-pulses of 15 ms lead to a Rabi frequency $\Omega_{\mathrm{R}} \approx 100$ rad/s ten times larger than in the standard operation, that translates in a probe intensity and light shift a hundred times larger. The experiment is performed with a dark time of either $T_{\mathrm{dark}} = 100$ ms or $T_{\mathrm{dark}} = 200$ ms, thus $\gamma \sim 4$ Hz, leading to the best clock stability with the available local oscillator.

In the low intensity mode of operation the probe laser is not turned off during the dark time, instead its intensity is decreased to a low level (see fig. 3.18). This is required because the probe laser is delivered to the atoms through an optical fibre and a small in-air path which are affected by environment-induced phase noise, which is compensated for by a Doppler noise cancellation (DNC) technique exploiting the double pass of the beam light along the affected path (see also section 3.5.1); turning off the laser would interrupt the DNC active stabilization.

The probe intensity is modulated acting on the efficiency of the AOM used for the DNC feedback loop. The variation in the AOM RF power level induces thermal gradients in the crystal leading to frequency chirps, which however are actively compensated by the DNC system as the AOM is part of the compensated path.

Nonetheless the intensity variation changes the DNC lock point because of a residual DC voltage in the DNC error signal, and this makes the DNC undergo a phase jump which may lead to a Doppler frequency shift. Therefore the trigger for the variation in probe intensity at the beginning (end) of the dark time is deliberately delayed (anticipated) from the laser frequency detuning (see fig. 3.18) to be sure that the intensity ramp is performed with the laser out of resonance, avoiding frequency shifts of the clock transition.

As can be seen from the zoomed area in figure 3.18 the probe intensity slightly varies in both the high and low intensity cycles in accordance with the laser frequency modulation because of a change in the fibre coupling efficiency. This is due to the single-pass AOM used for the frequency modulation, which is located before the beam injection into the fibre delivering the probe light to the clock apparatus and has a frequency dependent deflection angle. The small intensity change due to the frequency modulation is used to calibrate the timings of the interrogation sequence and to check that the intensity ramp is indeed delayed from the frequency step.

Since the probe intensity varies along the interrogation time, both because of the applied intensity modulation and because of intensity fluctuations due to unstabilised optical power, his perturbative effect has to be weighted with the Ramsey interrogation sensitivity function $g(t)$ (as discussed in section 2.4).

A time-dependent external perturbation such as the probe intensity $I_\mathrm{p}(t)$ affects the atomic energy levels inducing time-dependent frequency shifts $\Delta\nu_\mathrm{p}(t) = c_\mathrm{p} I_\mathrm{p}(t)$ which lead to variations ΔP in the excitation probability when probing the clock transition. These variations can be written according to eq. (2.6) [59]

$$\Delta P = \frac{1}{2}\int_0^{T_\mathrm{i}'} 2\pi\Delta\nu_\mathrm{p}(t) g(t)\,\mathrm{d}t = \pi c_\mathrm{p}\int_0^{T_\mathrm{i}'} I_\mathrm{p}(t) g(t)\,\mathrm{d}t\,, \tag{3.43}$$

while the derivative of the excitation probability calculated at the lock points is

$$\left.\frac{\mathrm{d}P}{\mathrm{d}\nu}\right|_{P=0.5} = \pi\int_0^{T_\mathrm{i}'} g(t)\,\mathrm{d}t\,. \tag{3.44}$$

The final frequency shift induced by the perturbation is then [59, 121]

$$\Delta\nu_\mathrm{p} = \frac{\Delta P}{\mathrm{d}P/\mathrm{d}\nu} = \frac{\pi c_\mathrm{p} \int_0^{T_\mathrm{i}'} I_\mathrm{p}(t) g(t)\,\mathrm{d}t}{\pi \int_0^{T_\mathrm{i}'} g(t)\,\mathrm{d}t}. \tag{3.45}$$

Thus the measured frequency shifts $\Delta\nu_\mathrm{p}$ (see figure 3.20, discussed later) obtained interleaving the two clock modes of operation shown in figure 3.18 are linearly proportional to the integrated time-dependent frequency shift induced by $I_\mathrm{p}(t)$

$$\tilde{I}_\mathrm{p} = \frac{\int_0^{T_\mathrm{i}'} I_\mathrm{p}^\mathrm{high}(t) g(t)\,\mathrm{d}t - \int_0^{T_\mathrm{i}'} I_\mathrm{p}^\mathrm{low}(t) g(t)\,\mathrm{d}t}{\int_0^{T_\mathrm{i}'} g(t)\,\mathrm{d}t}, \tag{3.46}$$

where $I_\mathrm{p}^\mathrm{high(low)}(t)$ is the measured probe intensity during the high (low) intensity clock cycles, as shown in figure 3.18 for sample clock cycles. The shift coefficient c_p can then be calculated as $c_\mathrm{p} = \Delta\nu_\mathrm{p}/\tilde{I}_\mathrm{p}$.

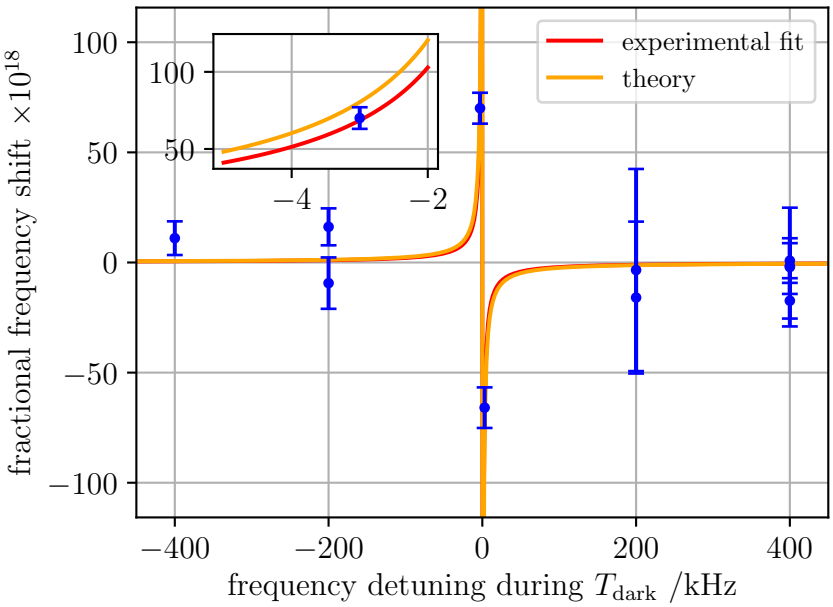

Figure 3.19: Probe light shift measurements $\Delta\nu_\mathrm{p}$ performed in interleaved operation and plotted against the laser frequency detuning from resonance during the dark time to resolve the contribution of the light coupling to the clock transition.

As a side remark note that if the probe intensity is constant over time, or varies with a time scale much longer than the interrogation time, the frequency shift would not depend on the interrogation sequence: in this case I_p would be moved out of the integrals in eq. 3.46, and $\tilde{I}_\mathrm{p}$ would drop its dependency to the sensitivity

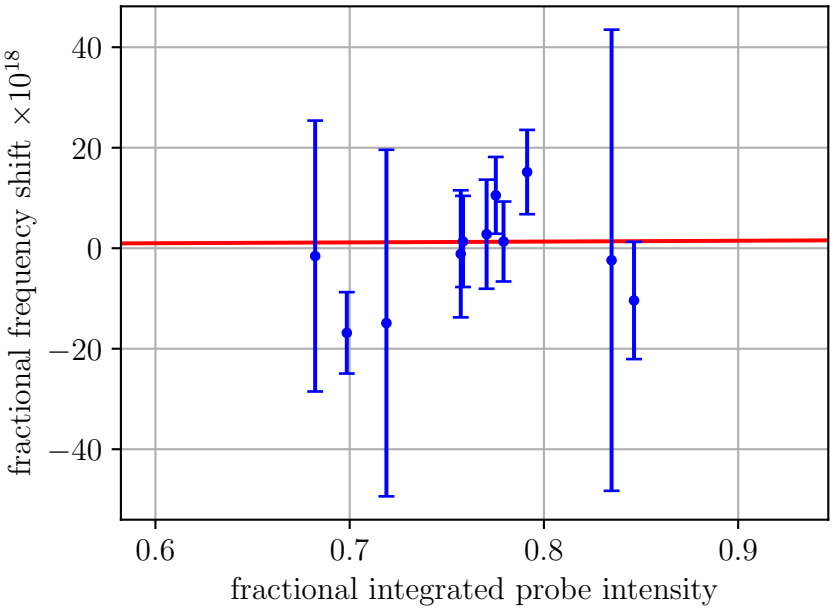

Figure 3.20: Probe light shift measurements $\Delta\nu_\mathrm{p}$ corrected by the contribution arising from the light coupling to the clock transition. These results are used to evaluate the shift from a probe intensity $I_{\mathrm{p},\pi/2} \propto \Omega^2_{\mathrm{R},\pi/2} = (\pi/(2T_\mathrm{p}))^2$ through a linear fit (red curve).

function so that $\tilde{I}_\mathrm{p} = I_\mathrm{pH} - I_\mathrm{pL}$. This case is realised for several other frequency shifts, such as the Zeeman shift and the lattice light shift.

Since the probe laser frequency detuning $\Delta\omega$ from resonance during the dark time is usually large enough so that the relation of the weak coupling limit $\Omega_\mathrm{R} \ll \Delta\omega$ stands, the probe light coupling with the clock transition induce an additional light shift of the clock states according to equation (3.18). This shift is not present when performing Rabi interrogation, hence it results in a systematic error when applying the extracted shift coefficient to standard operation. Because of the small clock transition damping rate $\Gamma_\mathrm{Yb}/(2\pi) \sim 7$ mHz [47] and $\Gamma \ll \Delta\omega$ the light coupling with the clock transition is predicted to provide a fractional light shift smaller than the one induced by the other transitions listed in table 3.2.

Nevertheless, in order to contain this issue the measurements are performed with frequency detunings during the dark time of ±200 kHz or ±400 kHz: since the shift induced by the coupling with the clock transition changes sign according to the sign of the detuning, performing measurements with both positive and negative detunings helps in averaging out a residual contribution. Moreover, two additional measurements with a detuning of ±3 kHz are acquired to clearly resolve the contribution from the light coupling with the clock transition, which dominates

at these values of frequency detuning. Figure 3.19 shows the raw measurement results $\Delta\nu_\mathrm{p}$ plotted against the laser frequency detuning during the dark time. This data is fitted with an hyperbolic model (the red curve) which is compared with the theoretical expectation for large frequency detuning according to eq. (3.18) (orange curve). The parameter extracted from the fit is used to apply corrections to the measurement results to remove the contribution arising from the light coupling with the clock transition.

Corrected data is shown in fig. 3.20 plotted against the average integrated probe intensity $\tilde{I}_\mathrm{p}$ normalized over $I_{\mathrm{p},\pi/2}$, which is the probe intensity delivered during the resonant pulses and shown as open markers in fig. 3.18.

The frequency shift $\Delta\nu_{\mathrm{p},\pi/2}$ generated by a probe laser with $\Omega_{\mathrm{R},\pi/2} = \pi/(2T_\mathrm{p})$ ($T_\mathrm{p} = 15$ ms), corresponding to an intensity $I_{\mathrm{p},\pi/2}$, can be directly evaluated from a linear fit of the data in figure 3.20 (red curve) as

$$\frac{\Delta\nu_{\mathrm{p},\pi/2}}{\nu_\mathrm{Yb}} = \frac{1}{\nu_\mathrm{Yb}} \frac{\Delta\nu_\mathrm{p}}{\tilde{I}_\mathrm{p}/I_{\mathrm{p},\pi/2}} = 1.6(42) \times 10^{-18}. \tag{3.47}$$

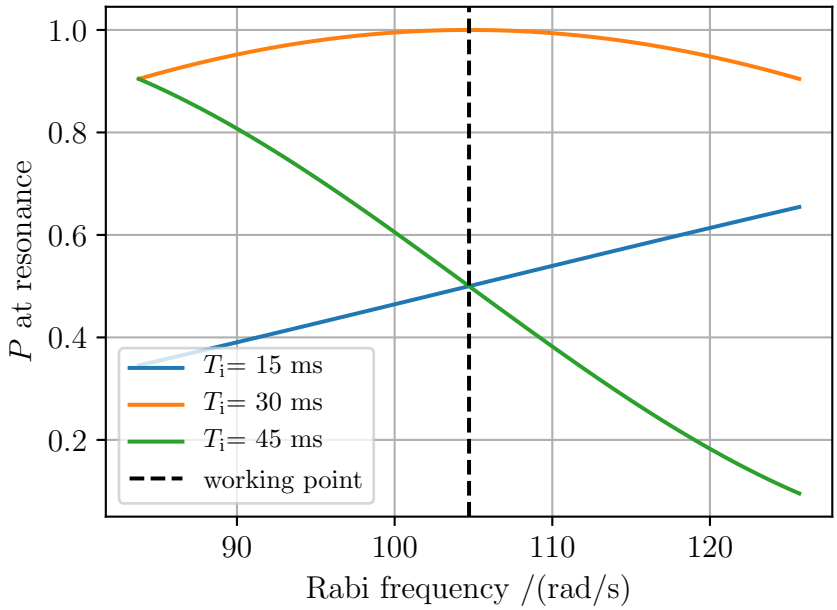

Figure 3.21: Expected excitation probability P for a resonant probe laser as a function of the Rabi frequency, which variates according to the intensity fluctuations. At the operating conditions a Rabi interrogation pulse of $T_\mathrm{i} = 15$ ms has a pulse area $\Omega_\mathrm{R} T_\mathrm{i} = \pi/2$.

In order to rescale the measured probe light shift to generic operating conditions, it is possible to calculate the coefficient $c_\mathrm{p} = \Delta\nu_{\mathrm{p},\pi/2}/I_{\mathrm{p},\pi/2}$ and apply it to the actual probe intensity I_p. However, the probe intensity at the atom location directly

affecting the atomic energy levels is difficult to determine. Since the probe laser Rabi frequency can instead be estimated in a easier way, and $I_\mathrm{p} \propto \Omega_\mathrm{R}^2$, it is possible to evaluate a new coefficient c_p^* normalized over the Rabi frequency squared.

In the following I will discuss the measurement of the Rabi frequency to apply the proper normalization factor in the determination of c_p^*.

Photodetector reading instability and Rabi frequency evaluation. The probe light intensity is acquired through a photodetector monitoring a signal extracted from the main beam before it accesses the vacuum chamber. The inability to measure the probe intensity at the exact location where atoms are interrogated, together with a non-ideal photodetector acquisition mainly due to its sensitivity to polarisation changes, introduce the possibility for a reading instability which could partially invalidate the expected correlation between the measured probe intensity and the actual Rabi frequency according to $\Omega_\mathrm{R} \propto \sqrt{I_\mathrm{p}}$.

During the experiment we independently track variations of the Rabi frequency through the monitor of the maximum excitation probability while probing the atoms with a resonant Rabi pulse. By correlating the measured intensity signal and the measured Rabi frequency fluctuations we retrieve information about the photodetector reading instability.

The Rabi frequency relates with the expected excitation probability P after a single Rabi interrogation pulse of duration T_i according to eq. (2.5), repeated here for convenience:

$$P = \frac{\Omega_\mathrm{R}^2}{\Omega_\mathrm{R}^2 + \Delta\omega^2} \sin^2\left(\sqrt{\Omega_\mathrm{R}^2 + \Delta\omega^2}\frac{T_\mathrm{i}}{2}\right), \tag{3.48}$$

where $\Delta\omega$ is the probe laser frequency detuning from the transition resonance in angular units.

As discussed earlier, at the operating conditions the probe laser delivers a $\pi/2$-pulse for an interrogation time $T_\mathrm{i} = 15$ ms, thus $\Omega_\mathrm{R} \sim 105$ rad/s. As can be seen in figure 3.21 the expected excitation probability P for a Rabi $\pi/2$-pulse or a Rabi $3\pi/2$-pulse ($T_\mathrm{i} = 45$ ms) is $P = 0.5$ and a variation in probe intensity, translating in a variation in Rabi frequency, would show clearly in a variation of P with a different sign relation according to positive or negative intensity changes, as shown in figure 3.21. This is not true for a π-pulse, which is thus unfit to extract the desired information.

Equation 3.48 does not account for an incorrect measurement of the $^3\mathrm{P}_0$ state population due to an inefficient pumping of the excited atoms to the ground state as part of the detection process. In the clock operation the issue is partially solved by accounting for a repumping efficiency $\eta_\mathrm{rep} = 0.9$ in the calculation of the atom population. Nevertheless, if the efficiency is not set properly or it fluctuates over time it could result in a measurement error. While this is usually a non-critical issue, this specific experiment may incur significant outcome biases, which are avoided

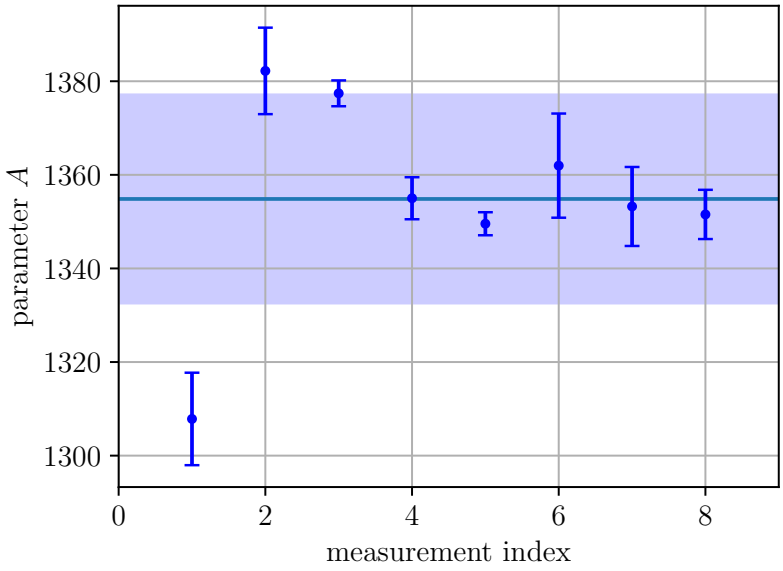

Figure 3.22: Parameter A obtained from datasets acquired performing interrogation with either a $\pi/2$-pulse or a $3\pi/2$-pulse. The standard deviation of the plotted values (shaded area), which is the 1.7% of the average (solid horizontal line), is used to assess the uncertainty in the photodetector reading.

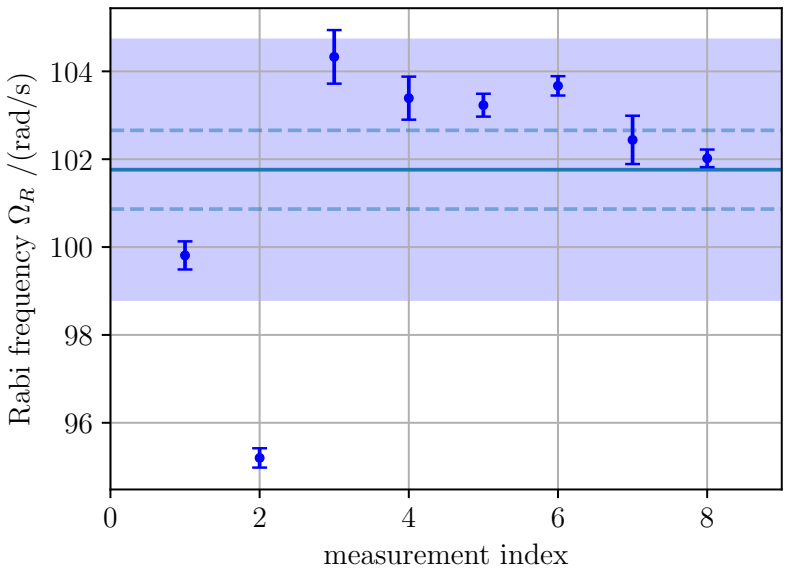

Figure 3.23: Extracted Rabi frequency for a $\pi/2$ Rabi pulse as $\Omega_{\mathrm{R}} = \sqrt{AI_p}$. Horizontal line and shared area are the average value and its uncertainty. Dashed lines represent the uncertainty contribution from the photodetector instability (extracted from the A parameter).

by including in equation (3.48) a free parameter $B > 0$ related to the repumping efficiency, where $B = 1$ for an actual efficiency $\eta_{\mathrm{rep}} = 0.9$.

If N_{g} and N_{e} are the populations of the ground and excited states respectively, the effective excitation probability can be written as

$$P^* = \frac{BN_{\mathrm{e}}}{BN_{\mathrm{e}} + N_{\mathrm{g}}} = \frac{B}{1/P - (1-B)}, \tag{3.49}$$

where $P = N_{\mathrm{e}}/(N_{\mathrm{e}} + N_{\mathrm{g}})$. Thus at resonance ($\Delta\omega = 0$) equation (3.48) can be written as

$$\frac{P^*}{B(1-P^*) + P^*} = \sin^2\left(\Omega_{\mathrm{R}}\frac{T_{\mathrm{i}}}{2}\right). \tag{3.50}$$

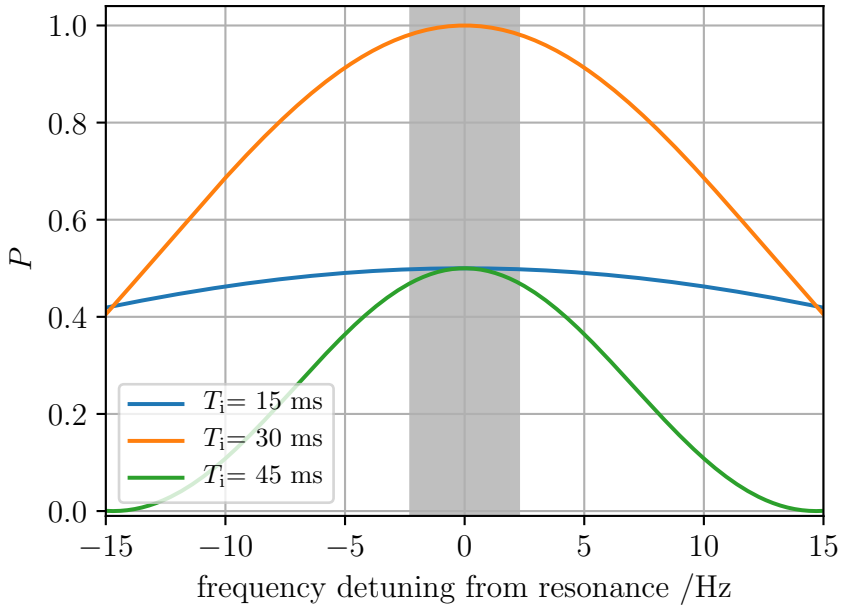

Figure 3.24: Clock transition spectroscopy lineshape close to resonance for a interrogation pulse of duration T_{i} at the operational Rabi frequency $\Omega_{\mathrm{R}} = \pi/(2(15\ \mathrm{ms}))$ satisfying a $\pi/2$-pulse for $T_{\mathrm{i}} = 15$ ms. Grey shaded area depicts the frequency range around the clock resonance explored by the probe laser according to an instability of $\sigma_{\mathrm{adev}}(\tau) = 4.7 \times 10^{-15}/\sqrt{\tau/\mathrm{s}}$ and a clock cycle of 1.18 s.

According to the relation between the Rabi frequency and the probe intensity, it is possible to write $\Omega_{\mathrm{R}} = \sqrt{AI_{\mathrm{p}}}$ with A a proportionality constant. The stability of A over multiple experiments carries the information about the photodetector reading stability, since fluctuation of Ω_{R} are expected to be totally correlated to fluctuations of I_{p}.

To gain information on the Rabi frequency, we measure the excitation probability at resonance with either a single Rabi $\pi/2$-pulse ($T_\mathrm{i} = 15$ ms) or a $3\pi/2$-pulse ($T_\mathrm{i} = 45$ ms) and we correlate the result with the probe intensity. We perform such measurements of the excitation probability at the same time as the measurements of the probe-induced light shifts. During these experiments, the lock to the clock transition provides the information needed to apply resonant light pulses.

The measured value of P^* is used to extract A by solving equation (3.50) for the two datasets. Parameter A for several of the probe light shift measurements is shown in figure 3.22 and it is used to evaluate the Rabi frequency for a $\pi/2$-pulse plotted in figure 3.23.

The residual instability of the local oscillator while locked to the atomic reference leads to an error in the evaluation of the Rabi frequency. The probe laser frequency noise moves the laser out of resonance, where P is not maximised. Figure 3.24 shows the theoretical spectroscopy line shapes of interest, namely for a $\pi/2$-pulse of duration $T_\mathrm{i} = 15$ ms and a $3\pi/2$-pulse of duration $T_\mathrm{i} = 45$ ms. In the figure the frequency range explored by the probe laser because of a frequency instability of $\sigma_\mathrm{adev}(\tau) = 4.7 \times 10^{-15}/\sqrt{\tau/\mathrm{s}}$, the worst observed during the probe light shift measurements, is highlighted as a grey shaded-area. Such instability leads to an additional uncertainty of 0.3% in the determination of the Rabi frequency.

The average Rabi frequency of the probe laser as evaluated for the calibration of the photodetector is thus $\Omega_{\mathrm{R},\pi/2} = \sqrt{\bar{A} I_{\mathrm{p},\pi/2}} = 102(1)$ rad/s, where $\bar{A}$ is the average of A; here the uncertainty just accounts for the photodetector instability, which is the only contribution relevant in the determination of the shift coefficient. In general the evaluation of the average Rabi frequency is also affected by the variability of the day-to-day pulse area because of variations of the overall probe intensity (which instead is measured and included in the calculation of the shift coefficient); accounting for this source of uncertainty we get $\Omega_{\mathrm{R},\pi/2} = 102(3)$ rad/s.

The final coefficient c_p^* is evaluated as

$$c_\mathrm{p}^* = \frac{\Delta\nu_{\mathrm{p},\pi/2}}{\Omega_{\mathrm{R},\pi/2}^2} = \frac{\Delta\nu_\mathrm{p}}{\tilde{I}_\mathrm{p}/I_{\mathrm{p},\pi/2}} \frac{1}{\bar{A} I_{\mathrm{p},\pi/2}} = 0.8(22) \times 10^{-7} \, \frac{\mathrm{Hz}}{(\mathrm{rad/s})^2}. \tag{3.51}$$

The photodetector reading instability contributes to this final result with an uncertainty of 1×10^{-8} Hz/(rad/s)^2, one order of magnitude smaller than the statistical uncertainty of the probe light shift measurements.

In figure 3.25 the experimental coefficient (3.51) is used to calculate the fractional probe light shift resulting from a Rabi interrogation of duration T_i. In the figure, the experimental result is compared with the calculation obtained from eq. (3.42): the experimental result is found in close agreement with expectations.

Table 3.3 compares the result provided by NIST in 2009 [104] and 2018 [25] with the corresponding result obtained applying the coefficient of eq. 3.51 to the Rabi frequency reported in their operating conditions. We find agreement between the results.

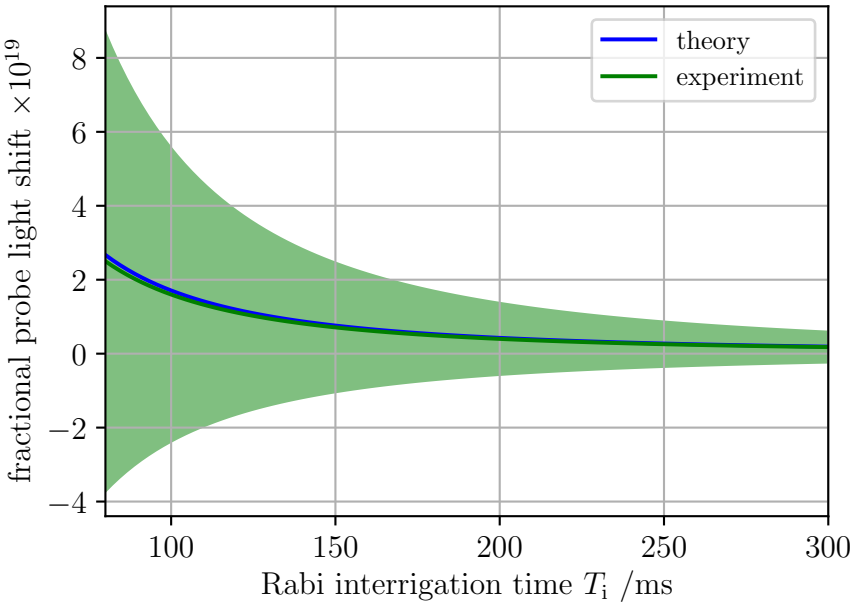

Figure 3.25: Probe light shift resulting from a Rabi interrogation with pulse area $\Omega_R T_i = \pi$, where T_i is the interrogation time. Blue: expected shift from theoretical calculations. Green: shift applying the experimental coefficient of eq. (3.51). Green-shaded area represents the 1-σ uncertainty range.

	T_i /ms	Ω_R /(rad/s)	fractional shift $\Delta\nu_p/\nu_{Yb}$ published	fractional shift $\Delta\nu_p/\nu_{Yb}$ calc. with eq. (3.51)
Lemke *et al.* [104]	80	39.3	$5(20) \times 10^{-18}$	$0.2(6) \times 10^{-18}$
McGrew *et al.* [25]	560	5.6	$2(1) \times 10^{-20}$	$0.5(13) \times 10^{-20}$
RIKEN	300	10.4(7)	-	$2(4) \times 10^{-20}$

Table 3.3: Comparison of probe light shift results evaluated and published by other research groups with the corresponding result obtained applying the coefficient of eq. 3.51 to their operating conditions. We list also the result evaluated at RIKEN for the frequency ratio measurement discussed in section 4.3.

3.3 Blackbody radiation shift

The blackbody radiation (BBR) emitted by the environment at temperature T surrounding the atomic ensemble affects the atomic energy levels inducing a Stark shift, in a similar way as discussed in the previous section for the electromagnetic radiations of lattice and probe lasers. In this case the radiation frequencies are small enough when compared to the clock relevant dipole transitions so that the

interacting electric field can be approximated to a static field, coupling with the atomic states through a static polarizability α_0 and inducing a shift $h\delta\nu_{\mathrm{BBR}} \propto \alpha_0 I_{\mathrm{BBR}}$, where I_{BBR} is the BBR intensity.

A residual dynamic component is however non-negligible, thus a parameter η_{BBR} accounting for this addition contribution is included in the calculation of the BBR-induced systematic frequency shift of the clock transition [122]:

$$\Delta\nu_{\mathrm{BBR}} = -\frac{1}{2}\frac{\Delta\alpha_0}{h}\langle E^2_{\mathrm{BBR}}\rangle_T(1+\eta_{\mathrm{BBR}}(T)), \tag{3.52}$$

where

$$\Delta\alpha_0 = \alpha_0^{\mathrm{e}} - \alpha_0^{\mathrm{g}} = h \times 3.626\,12(7) \times 10^{-6}\ \mathrm{Hz/(V/m)^2} \tag{3.53}$$

is the differential static polarizability experimentally measured at NIST, $\langle E^2_{\mathrm{BBR}}\rangle_T$ is the average electric field radiated by a blackbody at temperature T [123, 124]

$$\langle E^2_{\mathrm{BBR}}\rangle_T = (831.9430(15)\ \mathrm{V\,m^{-1}})^2 \left(\frac{T/\mathrm{K}}{300}\right)^4, \tag{3.54}$$

and the dynamic term [124, 125] is

$$\begin{aligned}\eta_{\mathrm{BBR}} &\approx \eta_1 \left(\frac{T/\mathrm{K}}{300}\right)^2 + \eta_2 \left(\frac{T/\mathrm{K}}{300}\right)^4 = \\ &= 0.017\,45(38)\left(\frac{T/\mathrm{K}}{300}\right)^2 + 0.000\,593(16)\left(\frac{T/\mathrm{K}}{300}\right)^4.\end{aligned} \tag{3.55}$$

Evaluation of the BBR shift at INRIM

There are two main sources of BBR radiation: the vacuum package surrounding the trapped atoms and the Yb oven generating the atomic collimated beam. The largest contribution in the uncertainty of the total BBR shift is provided by the evaluation of the effect due to the vacuum package temperature. The temperature of the vacuum package is continuously monitored by ten platinum resistance thermometers (RTD) Pt1000 placed on the package outer surface: eight sensors surrounds the main vacuum chamber, while two others are located either close to the oven or very far from it.

RTD Pt1000 sensors are characterized by a sensitivity of 3.850(63) $\Omega\,\mathrm{K^{-1}}$ and a temperature reading uncertainty at room temperature of 0.2 K. The temperature is acquired through a 4-wires resistance reading with a Keysight multimeter. While the 4-wire reading technique avoids additional uncertainty due to the wires' own resistance, the instrument contributes with an uncertainty of 0.06 K related to a measurement error, a switching error and a transducer conversion error.

The experimental apparatus has not been designed to control the vacuum package temperature, thus it is not possible to apply a specific model for the temperature

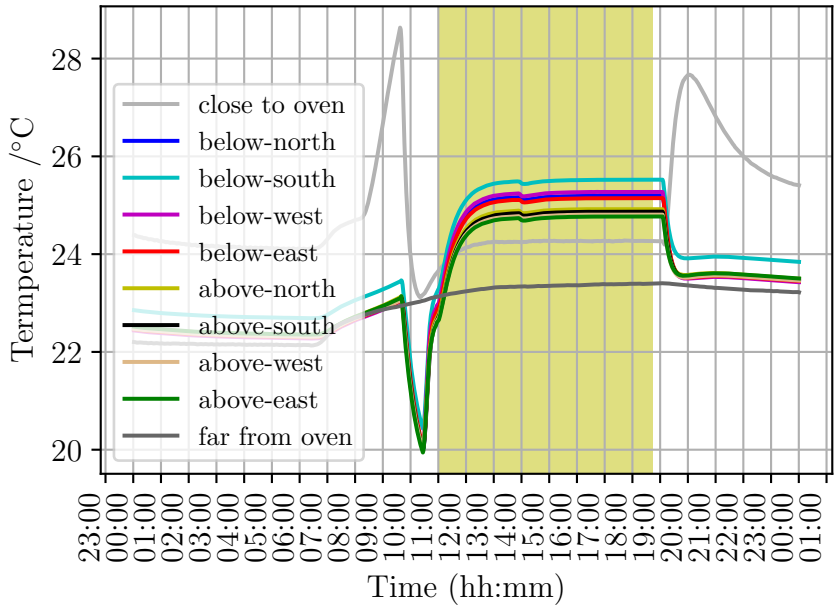

Figure 3.26: Typical temperature profile acquired through the ten thermistors on the vacuum package. Gradients are related to turning on/off the MOT coils current drivers and their water cooling chillers. Shaded area represents the time interval where the clock is operated.

distribution sampled by the RTD sensors. We can just assume that the temperature of the system lays within the temperature range defined by the minimum and maximum values acquired by the sensors, according to a uniform probability distribution. We evaluate the average temperature $T = (T_{\max} + T_{\min})/2$ and its uncertainty $\sigma_T = (T_{\max} - T_{\min})/\sqrt{12}$ for each day of operation, using $T_{\max}$ and $T_{\min}$ as the maximum and minimum temperature reading measured by the sensors over the operation time. In figure 3.26 it is shown a typical temperature profile measured during a day of operation.

The apparatus area where the oven is contained is separated from the main vacuum chamber through a narrow differential-vacuum tube made of copper: the tube has a length of 15 cm and a inner diameter of 0.5 cm. The BBR radiation emitted by the oven propagates through the tube to the main vacuum chamber where atoms are trapped.

In order to quantify the effect of the BBR radiation emitted by the oven we estimate the effective solid angle Θ_{oven} corresponding to the atom line of sight of the oven-generated BBR radiation. This is performed through a ray back-tracing analysis accounting for the radiation incoming from the oven and either directly interacting with the atoms or reflecting within the copper tube before the interaction

(up to two reflections are considered).

In order to evaluate the contributions of the radiation reflections we assume a copper emissivity $\epsilon = 0.4(2)$, and we neglect the BBR re-emission from the tube surface.

The oven temperature is measured with a Thermocoax NiAl thermocouple located within the oven package at the edge of the Yb reservoir [77]. The thermocouple has a sensitivity of 41 $\mu V\,K^{-1}$, and provides temperature measurements with an uncertainty of the 0.75 %.

For a typical oven temperature of $T_{\text{oven}} = 400(10)$ °C the resulting frequency shift is calculated using eq. (3.52) scaled by the normalized solid angle $\Theta_{\text{oven}}/(4\pi) = 3(1) \times 10^{-4}$ to be $\Delta\nu^{\text{oven}}_{\text{BBB}}/\nu_{\text{Yb}} = -2.1(8) \times 10^{-17}$. The large uncertainty on the oven temperature is determined by a lack of knowledge about the oven thermal distribution. We plan to include in the experimental apparatus an atomic shutter in between the atomic oven and the differential-vacuum tube to block the atom flow during the interrogation process: this will also block the BBR radiation and remove this contribution to the total BBR shift.

Methods to overcome the BBR shift

At RIKEN the BBR frequency shift is controlled below the 10^{-18} level by performing the atom interrogation within a cryogenic environment.

The entire clock apparatus is at room temperature, while a small copper chamber within the main vacuum chamber is kept at $T \leq 100$ K through a Stirling refrigerator [24]. The chamber, with a volume of about 6 cm^3, has two small apertures of diameter 0.5 mm and 1 mm, so that it can be crossed by the optical lattice (see section 2.8 for details on the clock apparatus and operation).

Since the frequency shift scales with the forth power of the temperature, reducing the environmental temperature by a factor 2 is already sufficient to control the BBR shift in the low 10^{-18} uncertainty regime without strong requirements in the temperature stabilization control and monitor. The Yb clock cryogenic chamber is usually operated at a temperature $T = 100.0(1)$ K, which would lead to a fractional BBR shift of $\Delta\nu_{\text{BBR}}/\nu_{\text{Yb}} = -2.995(12) \times 10^{-17}$. However, the residual environmental radiation accessing the cryogenic chamber though the two holes contributes significantly to the final uncertainty, so that the final shift is assessed to be $\Delta\nu_{\text{BBR}}/\nu_{\text{Yb}} = -3.176(49) \times 10^{-17}$.

Working in a cryogenic environment directly suppresses the BBR shift and potentially allows to make the shift totally negligible with a proper experimental design. Nonetheless, it introduces several technical difficulties. The current design of the RIKEN cryogenic clocks requires the lattice being generated by two independent counter-propagating laser beams, thus the lattice laser optical power needs to be twice the one used when establishing the lattice in a retro-reflected configuration: in the RIKEN Yb clock the lattice laser is a 4 W Ti:Sa injected by

a 18 W pump laser. In addition, this lattice geometry does not allow to implement an enhancement resonator to built-up the lattice power as done in other systems (see for example ref. [51, 52, 116]). Finally, the Stirling refrigerator is a source of vibrational noise close to the optical setup.

A different approach to tackle the BBR shift has been proposed in ref. [124] and consists in the implementation of a thermal shield enclosing the area where atoms are trapped. The shield can be described as a copper chamber within the main vacuum chamber, and differently from the cryogenic chamber described earlier it has several viewports to allow the access of laser beams along the three spatial dimensions. It is designed to provide temperature uniformity: materials are highly thermally conductive and the inner surface is coated with carbon nanotubes to avoid reflections. As a result, the temperature can be measured accurately to the point that the BBR shift uncertainty will be limited by the knowledge of the coefficients in equation 3.52.

At INRIM we are designing a renewed vacuum chamber which satisfies these requirements for the monitoring and control of the BBR. We expect that with this improved design we will be able to evaluate the BBR frequency shift with an uncertainty $< 10^{-17}$, as demonstrated in ref. [25].

Finally, a third option has been implemented in ref. [126]. They locate in-vacuum temperature sensors at the exact location of the atomic trap. Since the sensor blocks the beam access, it is placed on a movable device so that it can be removed when the clock is operated. This method does not require large modifications of the vacuum package, but it still undergoes technical difficulties such as the installation of temperature sensors in a high vacuum environment and close enough to the small region where atoms are trapped. Furthermore it requires the accurate characterization of the sensor readings and their stability over time. Finally, this technique does not allow real time monitoring of the BBR while the clock is operated.

3.4 Collisional shift

3.4.1 Cold atoms density shift

Cold atoms confined in the potential wells of the optical lattice collide with each other generating a frequency shift of the measured clock frequency. The interaction between colliding particles is usually distinguished between s-wave and p-wave, corresponding to the first and second order in the partial wave expansion of the interaction waveform. Higher order contributions can generally be neglected at the typical atomic temperatures in lattice clocks.

When optical lattice clock based on fermions, e.g. the ^{171}Yb clock, were firstly proposed, they were expected to be collisional shift free [127]: since spin polarized

fermions are undistinguishable, the s-wave scattering should have been prevented by the Pauli exclusion principle according to the Fermi statistics, while higher-order partial waves should have been frozen out by the low atomic temperatures [128] ($T_z \lesssim 30$ µK). As discussed in this section, it has been shown that this is not true, and instead the density shift is among the most significant contributions in lattice clock systematic frequency shifts.

In the typical operating conditions where most of the lattice sites are singly or doubly occupied, the shift magnitude scales linearly with the atomic density, as shown by theoretical many-body models [57, 129, 130] and experiments [131, 132], and depends on several other parameters which are discussed in this section.

Two-body collisions of cold Yb atoms depends on their internal state: the colliding pair of atoms can be either in the singlet state $|eg+\rangle = 1/\sqrt{2}(|eg\rangle - |ge\rangle)$ ($|g\rangle$ and $|e\rangle$ refer to the clock states), with interaction potential U^{eg}, or they can be in one of the triplet states $|gg\rangle$, $|ee\rangle$ or $|eg-\rangle = 1/\sqrt{2}(|eg\rangle + |ge\rangle)$, whose interaction parameters are V^{gg}, V^{ee} and V^{eg} respectively. Pairs of atoms in the singlet state may collide through a s-wave interaction, while in the other states they interact through p-waves [133]. If the clock interrogation coherently excite all atoms from $|g\rangle$ to $|e\rangle$, which can be possible if all atoms have the same Rabi frequency $\Omega_{\mathrm{R}} = \pi/T_{\mathrm{i}}$ (with T_{i} the duration of the Rabi pulse), then the s-wave collisions are strongly suppressed as the singlet state is expected not to be populated.

Nevertheless, if the atomic sample is characterized by a Rabi frequency inhomogeneity with spread $\Delta\Omega_{\mathrm{R}}$ ($\equiv$ the root-mean-square Rabi frequency), when the clock interrogation is performed atoms evolve in the Bloch sphere at different speeds: as they fall in different superpositions of the two clock states they become distinguishable; s-wave interactions are allowed and lead to a density shift [89, 134]. A Rabi frequency inhomogeneity occurs for several reasons: firstly, atoms may be affected by a different probe beam intensity according to their position into the lattice. This is due to the finite size of the probe beam, and by its Gaussian intensity profile, in addition to residual angular misalignments between the lattice and probe beams. Secondly, the inhomogeneity $\Delta\Omega_{\mathrm{R}}$ depends on both the radial T_r and axial T_z atomic temperatures [135], which determine the atomic distribution across the lattice vibrational levels.

Besides, s-wave collisions may appear if the spin polarisation process is not efficient, and both clock ground Zeeman states result populated: in that case atoms residing in one Zeeman state are distinguishable from those occupying the other state, and collisions between the two are allowed, as discussed later with the experimental results shown in fig. 3.32.

Furthermore, it has been experimentally demonstrated that in ^{171}Yb lattice clock p-wave collisional shifts are not negligible, and instead they represent the dominant contribution in the clock transition density shift [133] even in lattices with temperatures $T_{z,r} \sim 1$ µK to 10 µK. p-wave collisions, differently from s-waves, may occur even with $\Delta\Omega_{\mathrm{R}} = 0$.

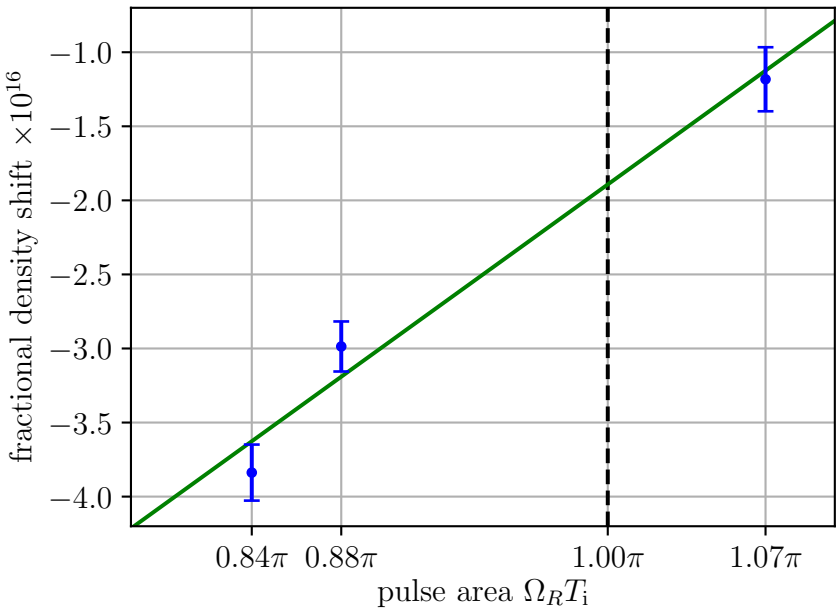

Figure 3.27: Fractional density shift $\Delta\nu_{\mathrm{coll}}/\nu_{\mathrm{Yb}}$ scaled for a number of atoms N_0 (corresponding to a fluorescence signal of 35 mV) at different pulse areas with a Rabi interrogation time of $T_\mathrm{i} = 80$ ms and final excitation probability $P \sim 0.5$. The green line is a linear fit showing a scaling law of $1.1(2) \times 10^{-15}/(\Omega_\mathrm{R} T_\mathrm{i})$. These measurements are acquired at a trap depth $U_0 \sim 400\ E_\mathrm{r}$.

In general both the s-wave and p-wave collisions are dependent to the fractions of atoms populating the ground and the excited clock states during the clock interrogation, thus the final excitation fraction P at the end of the interrogation pulse and the time-averaged excitation fraction over the pulse duration $\langle P \rangle_{T_\mathrm{i}}$ are both parameters of the collisional frequency shift. This means that variations in the pulse area $\Omega_\mathrm{R} T_\mathrm{i}$ or in the probe laser frequency detuning from resonance $\Delta\nu_{\mathrm{step}}$ when performing the clock interrogation lead to a variation of the density shift [89, 133, 136].

At INRIM we measure the sensitivity of the density shift to variations of the probe intensity, and thus to the pulse area, near the typical operating point delivering a π-pulse. This is realised performing a series af density shift measurements at different probe intensities. The Rabi interrogation time of $T_\mathrm{i} = 80$ ms and the modulation step $\Delta\nu_{\mathrm{step}} = 5$ Hz are fixed for all measurements and provide a final excitation probability $P \sim 0.5$ and $\langle P \rangle_{T_\mathrm{i}} \sim 0.36$. The atom density is changed for interleaved clock cycles by changing the time duration in which atoms interact and are slowed by the 399 nm slower beam, while keeping the total clock cycle time unchanged. Results, scaled to a total number of trapped atoms in the lattice

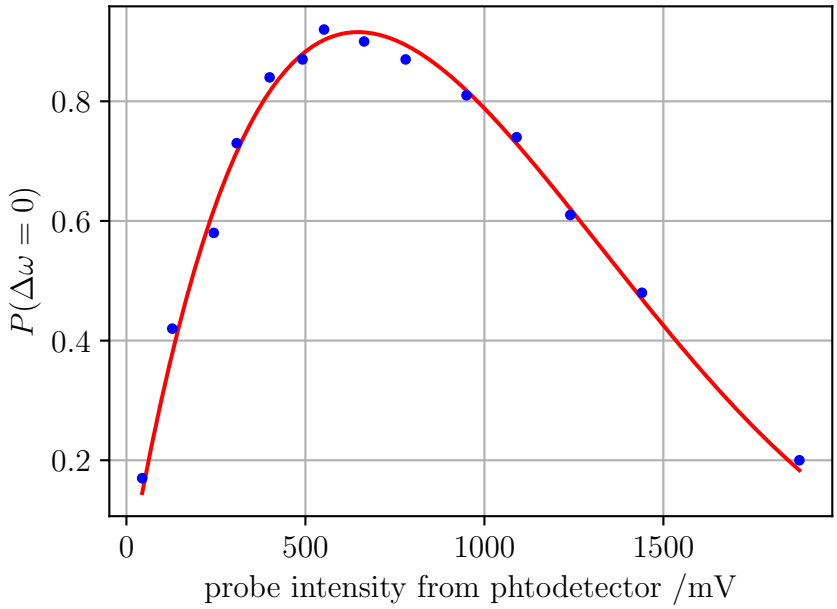

Figure 3.28: Calibration of the pulse area with the probe laser intensity measured by a photodetector. Experimental data is obtained as the maximum excitation registered while scanning the probe laser frequency across resonance. The fit (red) is performed according to eq. (3.48) with $\Delta\omega = 0$.

$N_0 \sim 450$ (corresponding to an integrated detection fluorescence signal of 35 mV), are shown in figure 3.27. From the graph it is possible to see that at the high operating trap depth $U_0 \sim 400\ E_\mathrm{r}$ even small variations of the pulse area lead to a significant change of the density shift.

The Rabi frequency used to evaluate the pulse area is calibrated with a specific measurement shown in figure 3.28: for several values of the probe beam intensity acquired with a photodiode the excitation fraction P at resonance ($\Delta\omega = 0$) is acquired as the maximum excitation registered while scanning the laser frequency over the spectroscopy line. The fit shown in figure 3.28, obtained from eq. (3.48) for the resonant condition, allows to relate the Rabi frequency with the probe intensity I_p measured with a photodetector, such that $\Omega_\mathrm{R} = 1.544(9)\sqrt{I_\mathrm{p}/(\mathrm{mV})}\,\mathrm{rad/s}$. Thus, a π-pulse with $T_\mathrm{i} = 80$ ms is performed with a probe intensity corresponding to a photodetector signal of 647 mV.

In figure 3.29 are shown density shift measurements performed at INRIM changing P and $\langle P\rangle_{T_\mathrm{i}}$ by tuning the modulation step. While the pulse area $\Omega_\mathrm{R} T_\mathrm{i} = \pi$ is same for all measurements (with $T_\mathrm{i} = 120$ ms), the lock points on the Rabi spectroscopy line shape are changed varying the laser detuning $\Delta\nu_\mathrm{step}$ from resonance:

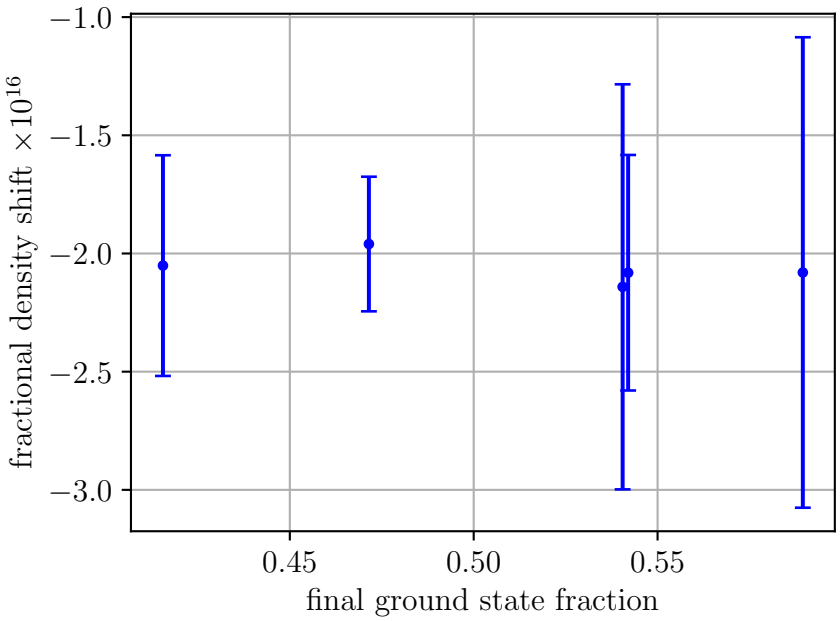

Figure 3.29: Density shift scaled to a number of atoms N_0 measured at different final excitation fractions P. The final ground state fraction is calculated as $(1-P)$. Plotted measurements corresponds to detunings $|\Delta\nu_{\text{step}}| = 2.96$ Hz, 3.20 Hz, 3.51 Hz, 3.50 Hz, 3.7 Hz. Trap parameters: $U_{\text{e}} = \zeta \times U_0 = 0.7 \times 376\ E_{\text{r}}$, $T_z = 6$ µK, $n_z = 1.1$.

in the standard operation $\Delta\nu_{\text{step}} = \pm 3.3$ Hz leading to a final excitation probability $P(|\Delta\nu_{\text{step}}|) = 0.5$. All measurements are consistent with each other within the uncertainty, showing that the sensitivity of the density shift to $\Delta\nu_{\text{step}}$ close to the lock points is not visible at this level of uncertainty.

Density shift dependence to trap conditions. The density shift strongly depends on the way atoms are loaded from the MOT cloud in the lattice. The atom transfer into the lattice determines the lattice volume occupied by the atoms, and thus the atom density. At INRIM, the third and final stage of the green MOT sequence is tuned in terms of laser frequency and magnetic field intensity to optimise the overlap of the MOT cloud on the lattice and consequently optimise the atom loading into the lattice; the optimisation is performed maximising the number of atoms trapped in the lattice, with an uncertainty in the determined frequency set point of about 100 kHz.

We investigate the density shift sensitivity to the green MOT final stage frequency f_{gMOT3} varying the set point around typical standard operation.

We measure the density shift setting either the frequency $f_{\text{3MOT}} = 139.38$ MHz, which optimizes the atom transfer to a *high* intensity lattice with trap depth of

about 400 E_r, or a detuned frequency within a range in which we observe up to 40 % decrease of the number of atoms loaded in the lattice with respect to the peak value corresponding to the starting condition (see inset in 3.30). As shown in figure 3.30, detunings of f_{gMOT3} within 1 MHz, which are significant when compared to a natural linewidth of the $^1S_0$-$^3P_1$ transition of 182 kHz, determine a significant variation in the measurement outcome. In the figure each density shift measurement is normalized to the corresponding measured number of atoms, and then linearly scaled to the standard value of $N_0 \sim 450$; this allows to observe the variation of the systematic shift because of the variation in confinement conditions, and not arising from the different overall atom number.

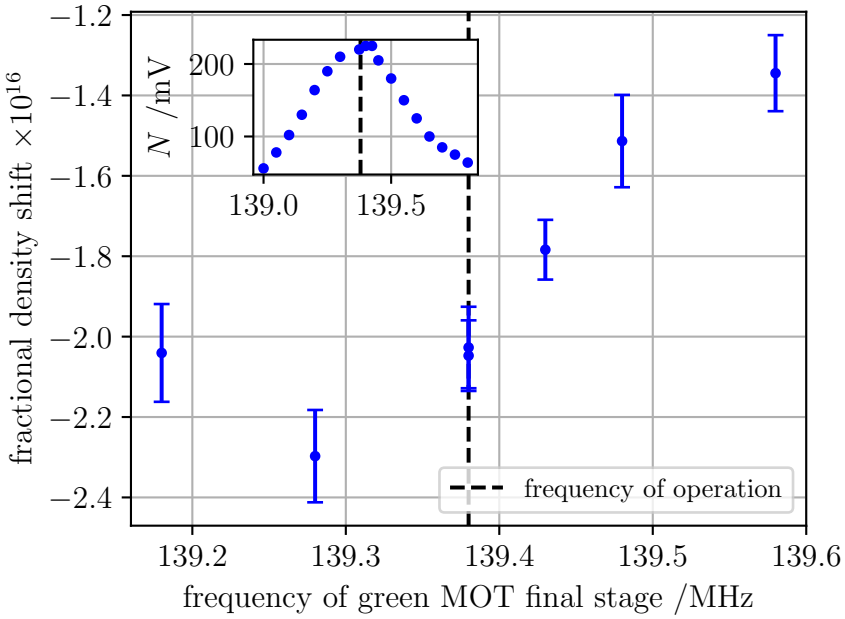

Figure 3.30: Density shift scaled to a number of atoms $N_0 \sim 450$ (fluorescence signal of 35 mV) measured varying the frequency f_{3MOT} of the third (final) stage of green MOT. Measurements are taken at trap depth $U_0 \sim 400\ E_r$. Inset: Atom number (in terms of fluorescence signal) in the lattice at different f_{3MOT}.)

The observed dependence of the atom number with the final MOT frequency (inset in figure 3.30) may be explained in terms of balance between two competing effects: a more compact MOT leads to higher atomic density overlapping the lattice, but also to an higher temperature, leading to worse transfer efficiency in the lattice. This finds an optimal point for the maximum density with atomic temperature low enough to guarantee an efficient capture rate in the lattice.

The definition of the interaction parameters V^{gg}, V^{ee} and V^{eg}, and U^{eg} (see the supplementary material of ref. [133]) allows to extract the expected dependency of

the density shift $\Delta\nu_{\mathrm{coll}}$ from the lattice trap frequencies ω_z and ω_r. Since the lattice intensity $I_{\mathrm{L}} \propto U_0 \propto \omega_{z,r}^2$, it results that [57]

$$\Delta\nu_{\mathrm{coll}}(p\text{-wave}) \propto V^{\alpha\beta} \propto I_{\mathrm{L}}^{5/4}, \tag{3.56}$$

$$\Delta\nu_{\mathrm{coll}}(s\text{-wave}) \propto U^{eg} \propto I_{\mathrm{L}}^{3/4}. \tag{3.57}$$

These laws predict the scaling of the density shift with trap depth if the atom distribution across vibrational levels remains constant despite changes in lattice depth. This is satisfied in our experimental conditions both at INRIM and at RIKEN. At INRIM the atom loading in the lattice is always performed at the same trap depth $U \sim 230\ E_{\mathrm{r}}$, which is then ramped to the final desired level after the transfer of atoms in the lattice is concluded. Similarly, also at RIKEN we load atoms at fixed, low lattice depth and then increase it to the desired level for the interrogation with an intensity ramp. If instead the ensemble motional energy is maintained while changing the lattice depth, p-wave atomic interactions scale as $\propto I_{\mathrm{L}}^{3/2}$ [126].

At INRIM we investigate the density shift dependence to the lattice intensity measuring the density shift over several months at different lattice trap depths ranging from $U_0 \sim 230\ E_{\mathrm{r}}$ to $410\ E_{\mathrm{r}}$. Most of the measurements are performed at either $U_0 \sim 230\ E_{\mathrm{r}}$, which is the clock standard operating conditions, or at $U_0 \sim 400\ E_{\mathrm{r}}$ to increase the leverage in the investigation of the trap depth dependence.

Loading the atoms in a lattice of fixed depth $U \sim 230\ E_{\mathrm{r}}$ for all measurements ensures the same lattice condition for the atom loading. The clock interrogation is performed with either $T_{\mathrm{i}} = 120$ ms or $T_{\mathrm{i}} = 80$ ms Rabi pulses. The longer interrogation time reflects the interest in pushing for the best clock stability with the available LO, however this results in an unreliable lock to the clock transition, with frequent unlocks. For some measurements we thus operate the clock with a shorter interrogation time. Results are plotted in figure 3.31.

Initial data (light blue points in figure 3.31) are acquired without implementing specific clock optimisation procedures aimed at maintaining the same experimental conditions over repeated measurements. By contrast, following measurements marked in dark blue are obtained after optimising the clock operation to reproduce experimental conditions as similar as possible over multiple days. Firstly, the recovery of ideally the same optimized conditions of the green laser beams for all measurements is performed tuning the green master frequency every day of operation to compensate for the drift of the reference optical cavity: the frequency optimization can be performed tuning the shape of the time of flight fluorescence signal for a colder sample, with a sensitivity of about 100 kHz; instead, we tune the green master frequency for maximum efficiency in the spin polarisation process, with a sensitivity of about 20 kHz. This avoids the tuning of the green MOT final stage to recover optimised transfer in the lattice as well as the tuning of the spin polarisation parameters. The frequency of the green MOT final stage is fixed for

all measurements at $f_{\mathrm{gMOT3}} = 139.18$ MHz, as optimal for the atom transfer in a lattice of $U \sim 230\ E_{\mathrm{r}}$.

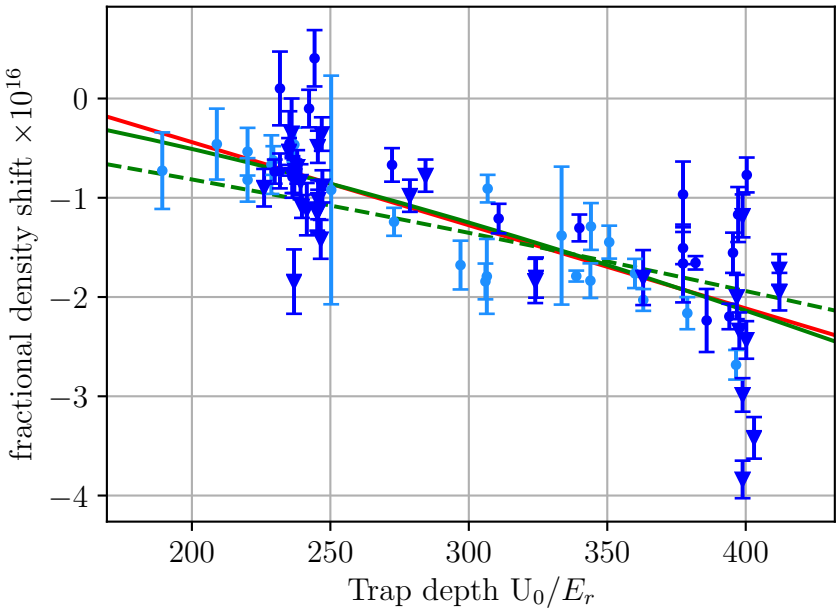

Figure 3.31: Density shift scaled to an atom number N_0 at different trap depth U_0. Dark blue points are obtained implementing specific clock optimisation procedures aimed at maintaining the same experimental conditions over repeated measurements, while light blue points not. Circles are acquired with an interrogation Rabi time of $T_{\mathrm{i}} = 120$ ms, while triangles with $T_{\mathrm{i}} = 80$ ms. Green dashed curve is the best fit of the model $c_1(U_0/E_{\mathrm{r}})^{5/4}$, expected for p-wave collisions. Green solid curve is the best fit with a model accounting for both s-wave and p-wave collisions according to $c_1(U_0/E_{\mathrm{r}})^{5/4} + c_2(U_0/E_{\mathrm{r}})^{3/4}$ (see text). The red curve is a linear fit, providing a scaling law of $-8.4(8) \times 10^{-19}\ /(U_0/E_{\mathrm{r}})$, and a crossing of the zero-shift axis at $U_0 = 148\ E_{\mathrm{r}}$.

In addition, the probe beam intensity is set to deliver a π-pulse using a characterization of the photodetector reading as performed in figure 3.28 and it is unchanged over all experiments; a probe beam active power stabilization control compensates power fluctuations. If this stabilisation were not being implemented, a drift or fluctuation of the probe intensity by 2 %, which is reasonable in a time scale of some days because for instance of degraded fibre coupling, would lead to a variation of the pulse area of $\sim$ 12 % (assuming $T_{\mathrm{i}} = 80$ ms), resulting in a variation of the density shift as large as 4×10^{-16} according to the measurements of fig. 3.27.

The results of fig. 3.31 show that this level of experimental parameter control is not sufficient and measured shifts are still affected by a significant variability, possibly related to residual uncontrolled parameters in the transfer and confinement of the atoms in the lattice. The large variability of the results at large depths

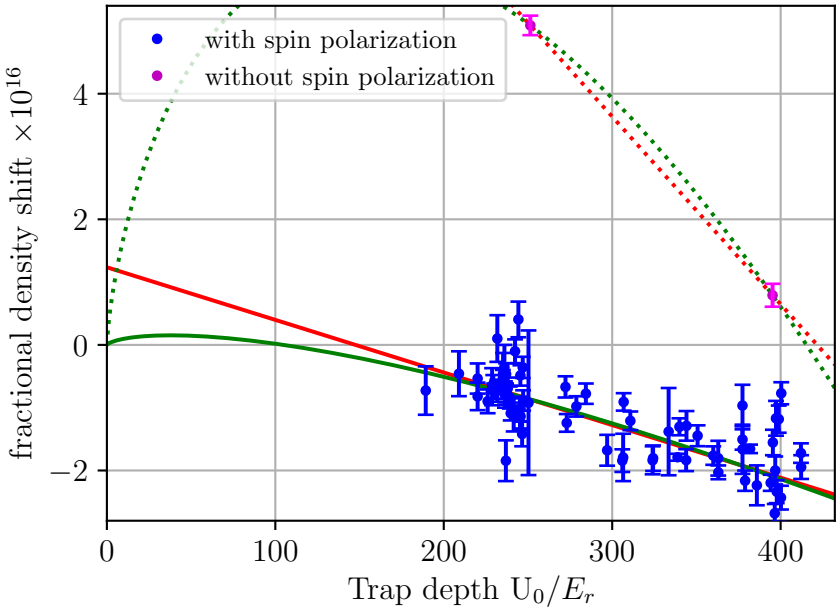

Figure 3.32: Density shift scaled to an atom number N_0 at different trap depth U_0. Pink data are obtained without spin polarizing atoms to a specific clock ground state: as a result, fermions in the two hyperfine ground states are not indistinguishable and the s-wave collisional shift is strongly enhanced. Green (dotted and solid) curves are obtained with the model $c_1 U_0^{5/4} + c_2 U_0^{3/4}$, while the red (dotted and solid) curves are linear fit (see text).

may suggest a stronger sensitivity of the density shift at such trap depths to the experimental parameters, in addition to the variability provided by statistics.

Data plotted in figure 3.31 is compared with the theoretical expectation of eq. (3.56) assuming that p-wave collisions dominate in the Yb clock (green dashed line). In this case a model $\Delta\nu_{\rm coll}(U_0)/\nu_{\rm Yb} = c_1(U_0/E_{\rm r})^{5/4}$ provides best fit of the data for $c_1 = -0.056(2)$. The green solid line represents a model which accounts for a residual presence of s-wave collisions according to $\Delta\nu_{\rm coll}(U_0)/\nu_{\rm Yb} = c_1(U_0/E_{\rm r})^{5/4} + c_2(U_0/E_{\rm r})^{3/4}$, with $c_1 = -0.13(2)$ and $c_2 = 1.3(4)$.

A similar investigation of the density shift dependence to the trap depth is performed at RIKEN and discussed in ref. [58]. Both analyses find that the shift becomes strongly negative at increasing trap depths, with a curvature that cannot be explained by the expected scaling of $\propto U_0^{5/4}$. A possible explanation of the negative higher-order contribution can be found in the cold collisions with atoms returned from the excited state to a non-coherent ground state because of off-resonance scattering of lattice photons [137], as the scattering rate increases with the lattice intensity and leads to an additional intensity-dependent collisional shift

term.

Another (or additional) possible explanation is the presence of a residual positive s-wave collisional shift which becomes significant at trap depths where the p-wave contribution is small. In order to visualize the effect of the s-wave collisional shift we enhance its contribution without spin polarizing the atoms to a specific hyperfine clock ground state. This is achieved removing from the clock cycle the sequence of optical pumping pulses, so as to leave atoms populating both $M_F = \pm 1/2$ ground state levels. As discussed earlier, in these conditions fermions are distinguishable and s-wave collisions may occur between atoms with opposite spin.

Measurements results taken at two different lattice trap conditions are shown in figure 3.32 (pink), in comparison with data taken in standard operating conditions and already shown in figure 3.31 (blue). The effect of s-waves is clearly resolved, as both the magnitude and sign of the density shift have changed. This same behaviour is observed and reported by the NIST group [25].

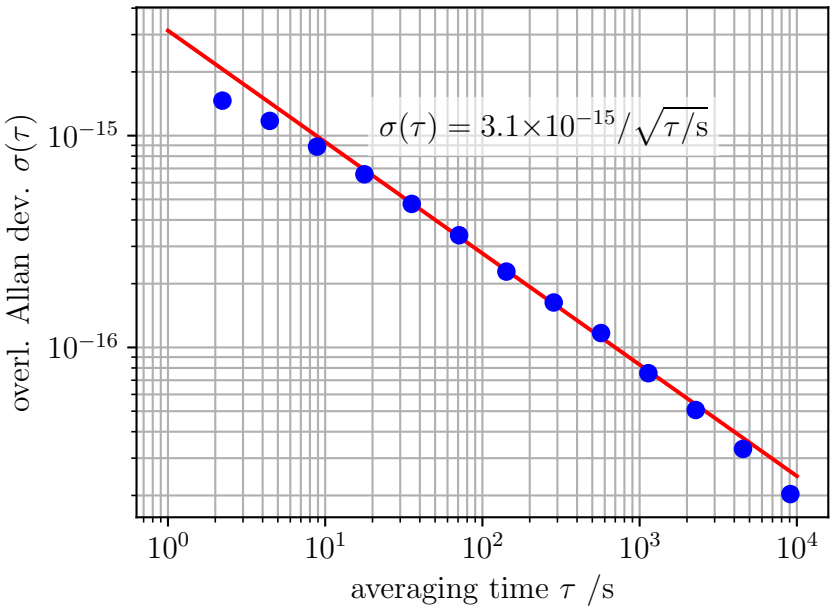

Figure 3.33: Instability of an interleaved density shift measurement lasting $\sim$ 15 h performed at INRIM. The measurement is affected by white frequency noise, which is highlighted with the red linear fit corresponding to a stability of $3.1 \times 10^{-15}\ /\sqrt{\tau/\mathrm{s}}$. The stability does not deteriorate over the time scale of the experiment.

Green dotted curve is obtained as best fit with the model $\Delta\nu_{\mathrm{coll}}(U_0)/\nu_{\mathrm{Yb}} = c_1(U_0/E_\mathrm{r})^{5/4} + c_2(U_0/E_\mathrm{r})^{3/4}$, with coefficients $c_1 = -0.9$ and $c_2 = 19$ (uncertainties cannot be computed because of the few data points). Dotted red line is obtained with linear data fitting. The coefficient c_1 is not in agreement with the coefficient

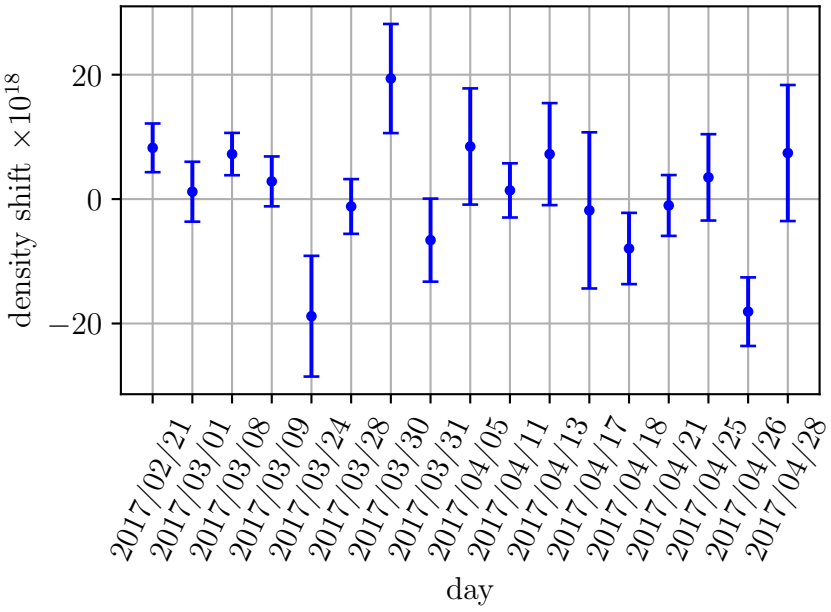

Figure 3.34: Density shift measured at RIKEN at a trap depth $U_0 \simeq 130\ E_r$ and rescaled to a typical atom number $N \simeq 300$ corresponding to 4000 camera counts.

obtained for the spin polarized case. A fit with just c_2 left as a free parameter, and with c_1 fixed at the value found earlier for the spin polarized case, does not converge. Despite the observed s-wave collisional shift may provide an interpretation of the stronger than expected density shift scaling with trap depth, further investigation is required.

Considering the variability of the results even when providing special care in the control of the experimental parameters, and the difficulty to find an appropriate model describing our results, both at INRIM and at RIKEN we decide not to rely on any model for the evaluation of the density shift. Instead, we daily measure the shift to characterize it in the specific experimental conditions of operation. Over a single day of operation we do not observe drifts of the experimental parameters leading to a variation of the density shift over time; this is confirmed by the stability of the density shift interleaved measurements, which does not deteriorate after several hours of operation (see figure 3.33 for a measurement performed at INRIM).

At INRIM we characterize the density shift at the lattice operating depth of $U_0 \sim 230\ E_r$ achieving for each measurement a typical statistical uncertainty of 2×10^{-17}. The horizontal geometry of the lattice limits our operating conditions in terms of trap depth and waist size, which is currently set to $w_0 \sim 45$ µm; this does not allow the suppression of the density shift which is evaluated for a single measurement at the typical number of atoms $N \sim 450$ to be $\sim -7 \times 10^{-17}$. In the

future we plan to implement a vertical cavity-enhanced lattice, allowing to trap the same number of atoms in a larger volume and smaller trap depth.

At RIKEN, the clock is typically operated loading $N \sim 300$ atoms in a vertical lattice of depth $U_0 \sim 90\ E_\mathrm{r}$ and radius $w \sim 60$ µm. In these conditions the density shift in a single day of operation is found compatible with zero, within an uncertainty of about 2×10^{-18}. Density shift measurements performed during the Yb/Sr frequency ratio campaign discussed in section 4.3 are shown in figure 3.34.

3.4.2 Background-gas collisional shift

The clock vacuum chambers where Yb atoms are trapped and interrogated are usually characterized by a residual vacuum pressure below 10^{-7} Pa. Ion pumps installed and operating in the vacuum system usually provide a rough reading of the vacuum pressure, which is assessed to be 4×10^{-8} Pa in the INRIM setup, while at RIKEN it is about 7×10^{-9} Pa.

The presence of a residual background gas in the chamber is of concern, since background atoms and molecules can interact with the trapped Yb atoms. Such collisions may induce the ejection of Yb atoms from the trap, determining in most of the lattice clock apparatuses the dominant and limiting contribution to the Yb atom lifetime in the lattice. Other possible contributions to the lifetime are the cold collisions between trapped Yb atoms and lattice-induced heating provided by the scattering of the lattice photons with Yb atoms [48] and/or parametric heating from the lattice phase and intensity noise [138].

During the clock interrogation, Yb atoms are in a coherent superposition of the ground $^1\mathrm{S}_0$ state ($|g\rangle$) and the excited $^3\mathrm{P}_0$ state ($|e\rangle$). When they collide with a background atom or molecule their coherent superposition experiences a phase shift, because the scattering amplitude is different for the two clock states. This phase shift affects the excitation probability outcome. As a result, if these atoms after the collision are not ejected from the trap, they induce a clock-transition frequency shift which requires to be estimated.

The model to calculate the background gas shift has been proposed by K. Gibble [139]. The model assumes that background-gas collisions with cold atoms are dominated by long-range van der Waals interactions, which scale as $-C_6 r^{-6}$, where r is the relative distance between the colliding particles and C_6 is the long-range interaction coefficient, which depends on the atom internal structure and state. Secondly, it assumes that the frequency shift is proportional to the atom loss rate τ_lt^{-1} from the lattice because of background gas collisions, where τ_lt is the background collision-limited lifetime of Yb atoms in the lattice.

Relevant C_6 coefficients are those describing interactions between a generic background-gas species $\mathrm{X}_{|g\rangle}$ and Yb atoms in either the ground or excited state. These coefficient will be denoted $C_6(\mathrm{Yb}_{|g(e)\rangle}\text{–}\mathrm{X}_{|g\rangle})$.

According to the model in ref. [139], as also discussed in ref. [55] the shift $\Delta\nu_\mathrm{bkg}$

can be calculated using the lifetime τ_{lt} of the atoms in the lattice:

$$\Delta\nu_{\mathrm{bkg}} = -\frac{1}{13.8\pi}\frac{\left|C_6(\mathrm{Yb}_{|g\rangle}\text{–}\mathrm{X}_{|g\rangle}) - C_6(\mathrm{Yb}_{|e\rangle}\text{–}\mathrm{X}_{|g\rangle})\right|}{C_6(\mathrm{Yb}_{|g\rangle}\text{–}\mathrm{X}_{|g\rangle})}\frac{1}{\tau_{\mathrm{lt}}}. \tag{3.58}$$

The C_6 coefficients describing interactions between two Yb atoms have been calculated [91, 140] and experimentally measured in the case of ground-ground interactions [141, 142]. The coefficients reported in ref. [140] are

$$\begin{aligned} C_6(\mathrm{Yb}_{|g\rangle} - \mathrm{Yb}_{|g\rangle}) &= 1929(39) \\ C_6(\mathrm{Yb}_{|g\rangle} - \mathrm{Yb}_{|e\rangle}) &= 2561(95) \\ C_6(\mathrm{Yb}_{|e\rangle} - \mathrm{Yb}_{|e\rangle}) &= 3746(180); \end{aligned} \tag{3.59}$$

with these coefficients the shift due to collisions with background hot Yb atoms can be calculated

$$\frac{\Delta\nu_{\mathrm{bkg}}}{\nu_{\mathrm{Yb}}} = -1.46(25)\times 10^{-17}\ (\tau_{\mathrm{lt}}/\mathrm{s})^{-1}, \tag{3.60}$$

where the uncertainty reflects just the uncertainties of the C_6 coefficients. The composition of the background gas is typically dominated by hot Yb atoms continuously flowing from the atomic source. If the design of the clock physical package avoids the interaction of the Yb atomic flux with the cold atoms during the interrogation process, the residual background gas is mainly composed by molecules released by the chamber inners surfaces. Collisions with hot Yb atoms can be avoided either including in the vacuum package an atomic shutter blocking the flux of atoms, or moving the atoms in a separate environment for the interrogation, as performed at RIKEN and in the INRIM Sr clock [143]. With residual vacuum pressure of $\sim 10^{-7}$ Pa the gas released by the chamber material is expected to be mainly molecular hydrogen H_2.

An experimental investigation of the background-gas collisional shift in a Yb lattice clock has been performed at NIST [25, 55]. They confirm linear scaling of the loss rate $1/\tau_{\mathrm{lt}}$ with the vacuum pressure, which they find largely dominated by H_2 with a residual gas analysis. They measure the frequency shift of the clock transition changing the residual vacuum pressure in their vacuum package, using as frequency reference a separate clock. They find a shift

$$\frac{\Delta\nu_{\mathrm{bkg}}}{\nu_{\mathrm{Yb}}} = -1.64(12)\times 10^{-17}\ (\tau_{\mathrm{lt}}/\mathrm{s})^{-1}. \tag{3.61}$$

Measurement of the Yb lattice lifetime and calculation of the background gas collisional shift at RIKEN

In the RIKEN Yb clock operation the clock interrogation is performed after moving the trapped atoms from the loading position into the cryogenic chamber,

which shields them from the Yb flux of hot atoms coming from the oven. The cryogenic environment usually at 100 K is expected to be characterized by a vacuum pressure smaller than in the outer region of the atomic vacuum chamber, further reducing the background gas collision rate. This is due to the cryogenic pumping provided by a Stirling cryocooler which works as a reversed heat pump.

In the lifetime measurement experimental sequence atoms moved into the cryogenic chamber are axially cooled through sideband cooling (SBC) and held into the lattice for a holding time Δt. Finally they are moved back outside the cryogenic chamber and detected. The atom lifetime in the lattice is evaluated measuring the number of the ground state atoms in the lattice while changing their holding time before the detection process.

The lattice trap depth varies along the transport distance, from a shallower trap at the loading position to a deeper trap into the cryogenic chamber (see section 2.8). During the clock standard operation in the cryogenic chamber atoms are held at a lattice depth $U_0 \simeq 90\ E_\mathrm{r}$, while they are loaded and detected at $U_0 \simeq 60\ E_\mathrm{r}$.

While the atoms are held in the cryogenic chamber, they may experience an increase in their mean energy $\langle E \rangle$ because of lattice-induced heating. The scattering rate Γ_s between the atoms and the lattice photons provided by the coupling of the lattice light to some atomic transitions leads to an heating rate of the atomic ensemble [48]. The dominant contribution to the scattering rate is given by the light coupling with the $^1\mathrm{S}_0$-$^1\mathrm{P}_1$ transition, calculated at $U_0 = 90\ E_\mathrm{r}$ as

$$\Gamma_\mathrm{s} \approx \frac{\Gamma}{\hbar \Delta\omega} U_0 \approx 0.09\ \mathrm{s}^{-1}, \tag{3.62}$$

where Γ is the transition damping rate, and $\Delta\omega = 2\pi(\nu_\mathrm{L} - \nu_0)$ is the frequency detuning between the lattice frequency and the transition frequency. The average heating rate of the thermal motion along the transverse and longitudinal axes are

$$\frac{\mathrm{d}\langle E \rangle_\mathrm{transv}}{\mathrm{d}t} = \frac{1}{2} \frac{\mathrm{d}\langle E \rangle_\mathrm{long}}{\mathrm{d}t} \approx \frac{2}{3} \Gamma_\mathrm{s} E_\mathrm{r} \approx 0.06\ E_\mathrm{r}\,\mathrm{s}^{-1}. \tag{3.63}$$

In addition, frequency components of the lattice intensity noise near the lattice vibrational frequencies may induce the excitation of the atoms to higher radial and axial vibrational levels, with a consequent heating of the atomic ensemble [138]. This effect, usually referred as parametric heating, is suppressed implementing an active lattice power stabilization control loop. Both heating effects are expected to be negligible under the typical operating conditions, otherwise they may lead to the loss of the most energetic atoms from the trap. To further reduce the probability of atom losses it is desirable to work with a cold atomic sample in a sufficiently deep lattice so that $\langle E \rangle \ll U_0$ over the relevant time scales.

The radial temperature of the atomic ensemble is controlled loading the atoms at lower lattice depth $U_0^\mathrm{load} \sim 65\ E_\mathrm{r}$ than in the cryogenic chamber $U_0^\mathrm{cryo} \sim 90\ E_\mathrm{r}$.

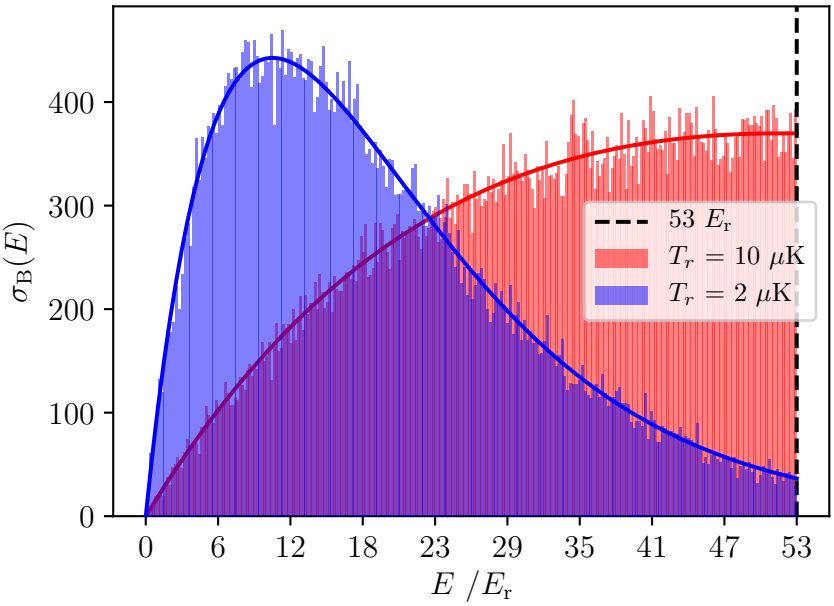

Figure 3.35: Simulated distribution of the atomic radial energies E according to a mean radial temperature T_r and a cut-off energy $E_{max} = U_0^{dip}$ (atoms with larger energies are intentionally lost from the trap). Solid lines show the analytic model of eq. (3.64), while shaded areas are the numerically simulated distributions.

Furthermore a 15 ms lattice intensity dip to $U_0^{dip} \sim 53\ E_r$ is included in the operational sequence after the transport into the cryogenic chamber is concluded; this allows the removal of radially hot atoms from the trap. We control the axial temperature $T_z \sim 1$ µK through SBC; additionally some of the measurements are performed adding a SBC pulse just before the detection process; this cools along the axial direction atoms heated up by the interaction with lattice photons during the holding time. Since this second SBC pulse does not lead to a significant increase of the atoms detected, we confirm that lattice-induced atomic heating along the axial direction does not lead to atom losses. Both measurements with and without the second SBC pulse are included in the lifetime analysis.

Assuming that SBC avoids atom losses because of the lattice-induced longitudinal heating, we investigate the effect of transverse heating. We assume that atoms at the initial radial temperature T_r are radially distributed according to the Boltzmann distribution [58]

$$\sigma_B(E) = \left(\frac{2}{k_B T_r}\right)^2 E e^{-2\frac{E}{k_B T_r}} \tag{3.64}$$

truncated at the maximum radial energy $E_{max} = U_0^{dip}$ (atoms with larger energies are not trapped). Figure 3.35 show the simulated distribution of the atomic radial

energies for an initial radial temperature $T_r = (1-\zeta)U_0^{\mathrm{cryo}}/k_{\mathrm{B}} \approx 2$ µK (with $\zeta \sim 0.8$ as measured in the cryogenic chamber with sideband spectroscopy). The radial energy then varies with time because of the lattice photon scattering and the transport to a shallower lattice for the detection process, which leads to adiabatic cooling according to $\sqrt{(U_0^{\mathrm{detect}}/U_0^{\mathrm{cryo}})(w_{\mathrm{cryo}}/w_{\mathrm{detect}})}$ (with w the lattice radius) and leads to a smaller cut-off energy $E_{\mathrm{max}} = U_0^{\mathrm{detect}} = U_0^{\mathrm{load}} < U_0^{\mathrm{cryo}}$. According to the simulation, lattice-induced losses from the trap becomes visible for holding times Δt of several hundreds seconds, hence they are negligible in the relevant holding times < 50 s.

The standard clock operation is affected by atom number fluctuations induced for example by fluctuations of the 399 nm slower beam intensity or other effects difficult to track and control. If the atom number undergoes a significant variation in the experiment time-scale, the measurement is affected by a systematic error. In order to avoid that, measurements at long and short holding times were interleaved in order to extract an unbiased value.

Measurements of the background offset signals were acquired at each holding time Δt by turning off the lattice laser while keeping the clock running in the standard mode of operation: without lattice beams atoms are not trapped and cannot generate signals, while all other signal sources are in place. The measured background signal (~ 5 % at $\Delta t = 10$ s) is removed from the measurement results. This avoids the inclusion of a parameter accounting for an offset in the model applied to fit the data.

The measured atom number at each value of Δt was calculated taking the average and standard deviation of the acquired dataset if more than ten samples were available and if the event frequencies could be described with a normal distribution. In all other cases samples are assumed uniformly distributed.

All data is normalized according to the atom number measured at $\Delta t = 0.5$ s, so that acquisitions performed over multiple days can be merged together.

The ensemble of the measurements at each holding time is modelled with an exponential decay of the form $y = \exp(a - (\Delta t/\tau_{\mathrm{lt}}))$, with a scaling factor a (see fig. 3.36). The atom lifetime is evaluated to be $\tau_{\mathrm{lt}} = 8.6(2)$ s, where the uncertainty has been inflated according to $\chi^2_{\mathrm{red}} = 11.5$.

The agreement of a single exponential decay model with the data supports the result that background gas collisions are the dominant limitation of the atom lifetime, and atom lifetimes induced by other effects are longer and not visible from the acquired data.

In order to further confirm this conclusion, we perform some additional measurements. We check the atom lifetime dependence to the lattice trap depth performing repeated measurements with fixed Δt at different lattice depths. Results, plotted in figure 3.37, do not show the presence of a correlation between atom counts and trap depth. The result at very small trap depth is performed at $U_0^{\mathrm{cryo}} = U_0^{\mathrm{dip}}$: in

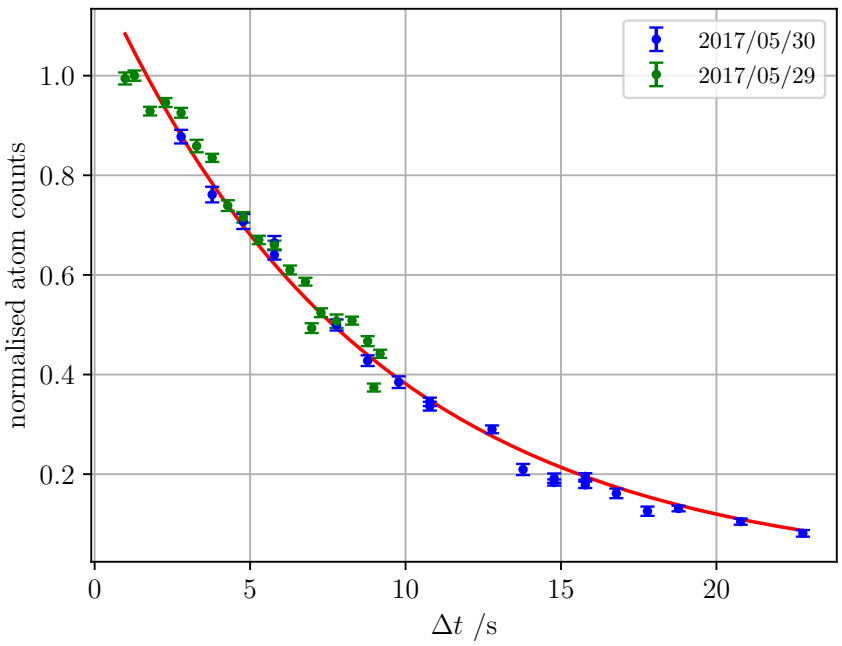

Figure 3.36: Residual atom counts at holding time Δt measured over two consecutive days (green and blue dots). Red curve is the exponential decay used to extract the atom lifetime in the lattice.

this case the simulation discussed above predicts a lattice-induced losses of 2 ‰ which is not compatible with the larger signal observed and requires further investigation (the simulation does not predict losses for the other data points in figure 3.37). Nonetheless the clock standard operation is carried out with a lattice depth between 65 E_r and 100 E_r, where results are found to be consistent.

Moreover, we perform specific lifetime measurements with increased lattice depth at detection to confirm the absence of heating-induced losses allowed by the smaller cut-off energy at detection than in the cryogenic chamber. In the standard clock operation (see section 2.8), atoms are moved from the loading region by 20.5 mm by gradually detuning the frequency of one of the lattice beams, reaching a peak detuning of 2 MHz. The opposite frequency detuning is usually applied at the end of the clock cycle to bring the atoms back to the loading position to perform detection. In this experiment the atom lifetime is measured again while changing the peak frequency detuning of the back-transport to either 1.8 MHz or 1.65 MHz, leading to a shortened return move of 18.45 mm or 16.92 mm respectively. This allows to perform the detection process closer to the lattice waist, where the trap depth is larger. The duration of the transport cycle phase is unchanged. Because of a technical problem with the lattice laser the overall available laser intensity is reduced with respect to earlier measurements; the lattice depths are evaluated to be

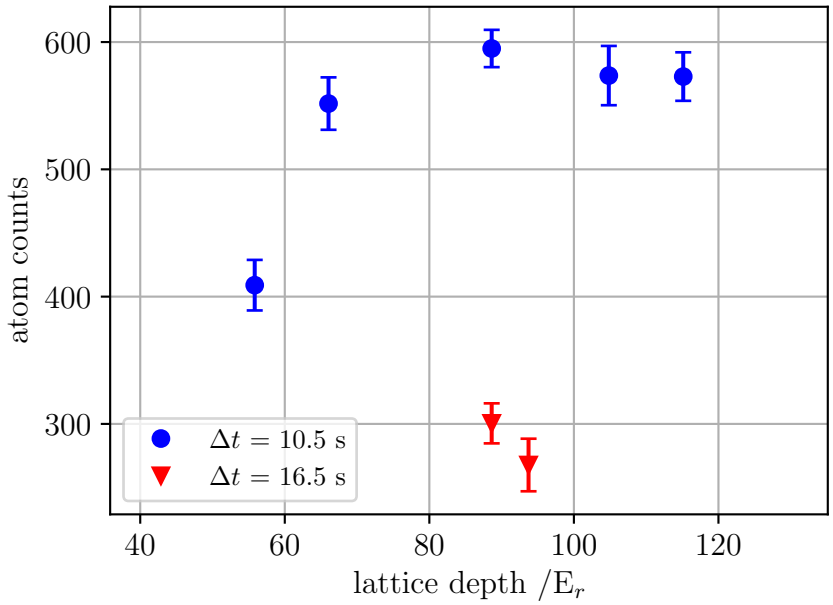

Figure 3.37: Residual raw atom counts after a holding time of either $\Delta t = 10.5$ s or $\Delta t = 16.5$ s while changing the lattice depth.

$U_0^{\text{load}} \sim U_0^{\text{dip}} \sim 53\ E_\text{r}$, $U_0^{\text{cryo}} \sim 88\ E_\text{r}$ and at the two locations for the atom detection $U_0^{\text{detect}} \sim 64\ E_\text{r}$ and $U_0^{\text{detect}} \sim 74\ E_\text{r}$ respectively. The measured lifetime in these two operating conditions (see fig.3.38) are $\tau_{1.8} = 8.8(3)$ s and $\tau_{1.65} = 8.3(4)$ s respectively, consistent with previous results. This further confirms that our lifetime measurement is not limited by heating-induced losses.

We investigate the variation of the atom lifetime in the lattice in two additional operating conditions. Firstly, the effect of holding the atoms in a cryogenic environment at 100 K is investigated measuring the atom lifetime with the cryogenic chamber at 297 K after turning off the cryocooler (see fig. 3.39a). In this condition the lifetime decreases to $\tau_{297\text{K}} = 5.3(8)$ s. This reduction in the measured lifetime is attributed to the decreased cryogenic pumping, and also supports the fact that the lifetime limit is provided by the collisions with the background gas.

We also investigate the lifetime of the atoms if held outside the cryogenic chamber. In order to avoid background collisions of the atoms with hot Yb atoms we exploit a mechanical shutter blocking the atomic flux outside of the MOT loading sequence. In addition, atoms are transported 3.6 mm away from the loading position to move them out from the oven line of sight. The distance is short enough not to let atoms access the cryo-chamber. The transport is performed applying a peak frequency detuning of the lattice beam of 350 kHz. Results shown in fig. 3.39b lead to a lifetime $\tau_{\text{out}} = 7.4(2)$ s.

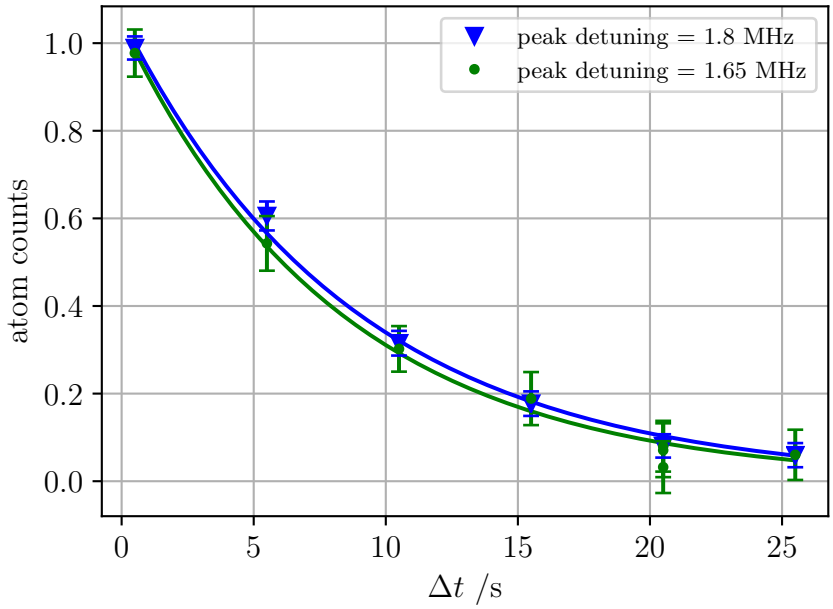

Figure 3.38: Residual atom counts at holding time Δt detecting at a reduced back-transport distance of 18.45 mm (blue triangles) and 16.92 mm (green dots), corresponding to lattice beam peak transport detuning of 1.8 MHz and 1.65 MHz respectively. The measured lifetime in these two operating conditions are $\tau_{1.8} = 8.8(3)$ s and $\tau_{1.65} = 8.3(4)$ s respectively.

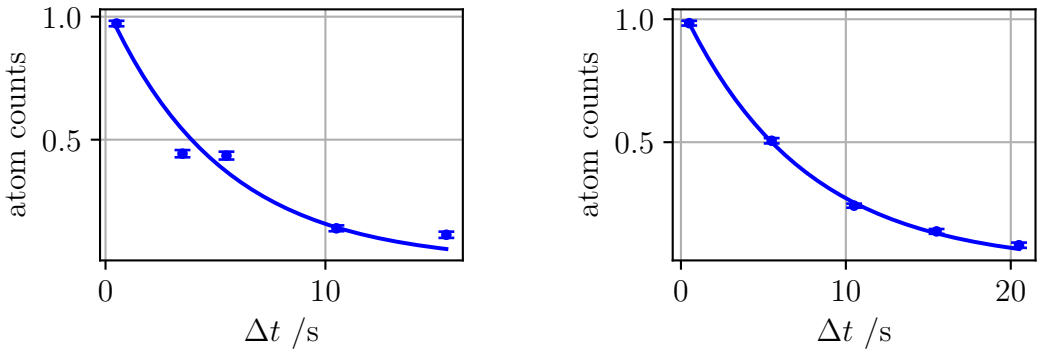

(a) Residual atom counts at holding time Δt with the cryo-chamber at room temperature of 297 K. In this condition the lifetime is $\tau_{297\mathrm{K}} = 5.3(8)$ s.

(b) Residual atom counts at holding time Δt with atoms outside the cryo-chameber, avoiding background collisions with hot Yb atoms. In this condition the lifetime is $\tau_{\mathrm{out}} = 7.4(2)$ s.

Figure 3.39: Atom lifetime at different operating conditions.

These results show that the vacuum pressure inside the cryo-chamber is larger than in the outer region when cryogenic cooling is inactive; this may be explained by the fact that the vacuum pumps are not located close to the cryogenic chamber and the vacuum in the volume enclosed by the cryogenic chamber is not pumped as efficiently as in the outer region.

Calculation of the background gas collisional shift. With a residual vacuum pressure of $\sim 10^{-8}$ Pa, we expect that the composition of the background gas in our vacuum chamber is dominated by H_2. Using equation (3.61) we calculate a frequency shift of $\Delta\nu_{\mathrm{bkg}}/\nu_{\mathrm{Yb}} = -1.91(15) \times 10^{-18}$. We account for residual differences in the background gas composition relative to the NIST system by inflating the uncertainty of the shift coefficient to match the maximum deviation between the coefficient experimentally measured and those calculated from the theoretical model (3.58) for either Yb-Yb collisions (taken as upper bound for collisions with heavy atoms) and Yb-H_2 collisions. To include the theoretical expectations accounting for H_2 background gas we make use of the approximation reported in [55] (page 121). We finally establish the frequency shift to be $-1.9(3) \times 10^{-18}$.

Measurement of the Yb lattice lifetime and calculation of the background gas collisional shift at INRIM

At INRIM we measure the lifetime of the ground state atoms in the lattice in a similar way as previously discussed: we load the atomic sample in the lattice and after a holding time Δt we measure the ground state population through a detection pulse. Results, shown in figure 3.40, are fitted with an exponential decay to extract the lifetime τ_{lt}.

As discussed in section 2.7, we operate an horizontal retro-reflected lattice; the need to counterbalance gravity defines a minimum operational trap depth $U_0^{\mathrm{min}} > 200\ E_{\mathrm{r}}$. We ensure that the atoms are held and detected in a deeper lattice than during the atom loading (as discussed in the previous section), by loading the atoms in a lattice of depth $U_0 = 248\ E_{\mathrm{r}}$, which we then increase to $U_0 = 270\ E_{\mathrm{r}}$ for the following cycle phase.

During the clock operation trapped cold atoms are in the line of sight of the hot flow of Yb atoms emitted by the atomic oven. Since we currently do not implement an atomic shutter, we expect that collisions between cold Yb atoms with background hot Yb atoms are the dominant contribution to the atom lifetime in the lattice, beside the presence of collisions with H_2 molecules. In the typical operating conditions the oven is kept at a temperature $T \sim 378$ °C, and the residual vacuum pressure in the main vacuum chamber is $P \sim 6 \times 10^{-8}$ Pa, as measured by the ion pump incorporated in the physical package.

From an exponential fit of data shown in figure 3.40, we measure a lifetime of $\tau_{\mathrm{lt}} = 4.0(2)$ s.

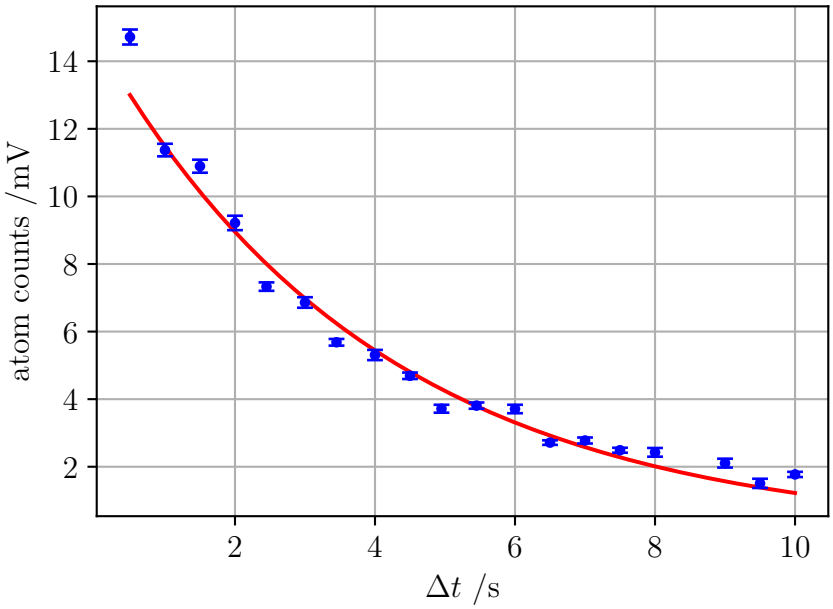

Figure 3.40: Residual atom counts at holding time Δt in terms of the fluorescence signal acquired by a photomultiplier. Red curve is the exponential decay used to extract the atom lifetime in the lattice.

Using the model of equation (3.58) and the C_6 coefficients in ref. [140] we can calculate the shift expected for collisions with background hot Yb atoms to be $-3.6(7) \times 10^{-18}$, while the theoretical calculation of the shift accounting for collisions with background H_2 molecules, performed with the approximation reported in ref. [55], provides a result of $-4.4(5) \times 10^{-18}$.

We finally evaluate the frequency shift to be $\Delta\nu_{\mathrm{bkg}}/\nu_{\mathrm{Yb}} = -4.0(4) \times 10^{-18}$ assuming that the shift coefficient c_{bkg} describing the background gas composition of our system is included between the determinations accounting from collisions with Yb and H_2 background gases, which are considered borderline cases for collisions with heavy and light background particles. We estimate c_{bkg} assuming it is distributed according to a curvilinear trapezoid probability density function (see ref. [144], page 20) such that its expected value and variance are

$$E(c_{\mathrm{bkg}}) = \frac{a+b}{2}, \quad V(c_{\mathrm{bkg}}) = \frac{(b-a)^2}{12} + \frac{d^2}{9}, \tag{3.65}$$

where a and b are the two theoretically calculated coefficients and d represents their variability, which is taken as the largest between the uncertainties of a and b.

3.5 Other shifts

3.5.1 Doppler shift

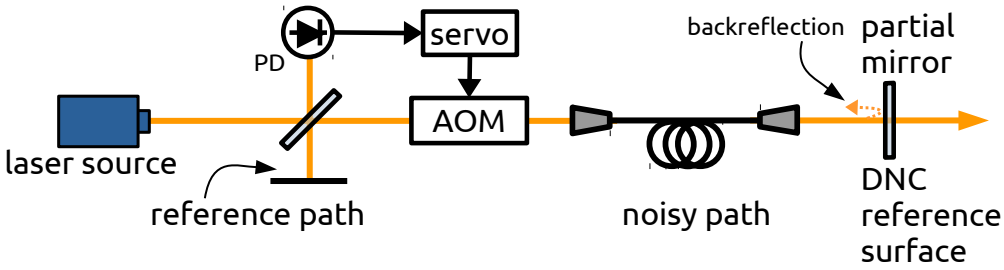

Figure 3.41: Scheme of the Doppler noise cancellation (DNC) setup. PD: photodiode.

The optical lattice where neutral atoms are trapped is designed to confine the atoms in the so-called *Lamb-Dicke* regime [49], where the atoms are effectively fixed in the reference frame of the probe light (see also section 2.1).

A Doppler frequency shift may however still be present. While the probe laser propagates, it can accumulate a phase noise related to either the interaction with air molecules or because of the delivering through optical fibres which translate environmental seismic noise and temperature fluctuations into phase noise. Therefore, even if atoms are well localized the probe laser noise induces a Doppler frequency shift and line broadening.

A Doppler noise cancellation (DNC) scheme is implemented to avoid such shift contributions [30, 145]. The cancellation scheme consists of an interferometer comparing the optical signal propagating through the noise-affected path with a reference signal propagating in a small unperturbed path: the beatnote between the two beams carries information about the integrated phase noise which is actively compensated for with an acousto-optic modulator (AOM). The acquisition of the signal affected by the noise is performed retroreflecting a portion of the light back on the same path (see fig. 3.41).

In order to avoid residual uncompensated optical paths, the backreflecting mirror is usually integral with the optical lattice reference surface, so as to provide the DNC with the atomic reference system. While this is true in the RIKEN clock, in the INRIM clock the DNC backreflecting mirror is currently not linked to the lattice reference frame, and it is located about 30 cm far from the lattice mirror (see figure 2.7); even if the two mirrors are placed on the same table, a residual phase noise synchronous to the clock cycle affecting the two surfaces in a different way may lead to a Doppler shift. For example the ON/OFF switching of the MOT coils driving current may add a seismic noise to the table synchronous with the clock cycle. We constrain the magnitude of this residual Doppler shift replacing the lattice retro-reflecting curved mirror with a flat mirror and acquiring the phase

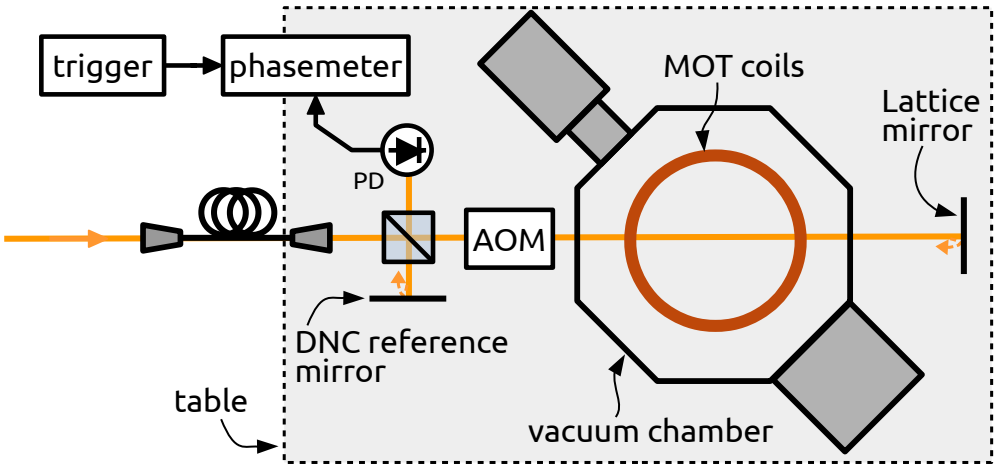

Figure 3.42: Scheme of the Doppler noise cancellation (DNC) setup. PD: photodiode.

noise of the interferometric beatnote between the beams retro-reflected on either that mirror or the DNC reference mirror, as shown in figure 3.42. The measurement is performed running a fake clock cycle where the standard switching of the MOT coils is either allowed or interrupted. The phase noise during the interrogation pulse is acquired with a phasemeter and converted in a frequency shift applying the Rabi sensitivity function. We finally estimate $\Delta\nu_{\mathrm{Doppler}}/\nu_{\mathrm{Yb}} = 0(5) \times 10^{-17}$.

Limits in the DNC performance may lead to a residual Doppler frequency shift, thus the DNC active control requires to be tested and characterized; this yields a INRIM Yb clock residual shift of $\Delta\nu_{\mathrm{Doppler}}/\nu_{\mathrm{Yb}} = 0(1) \times 10^{-18}$ (see ref. [54] for details), while the shift affecting the RIKEN Yb clock is assessed to be $\Delta\nu_{\mathrm{Doppler}}/\nu_{\mathrm{Yb}} = 0(2) \times 10^{-18}$.

3.5.2 AOM chirp and switching shift

During the clock operation the probe laser is frequency modulated to be on resonance during the clock transition interrogation and detuned usually by 200 kHz from resonance outside of the interrogation process not to interact with the atoms. Frequency modulation is performed with an acousto-optic modulator (the clock AOM), which is also in charge to apply the frequency corrections required for the frequency stabilization on the clock transition.

The AOM exploits an external radio-frequency (RF) signal to drive a piezoelectric transducer, which generates sound waves inside a crystal to realise a diffractive grating. According to the amplitude of the RF signal, the crystal warms up and thermalise to a certain temperature. The AOM RF frequency switching, implemented to bring the laser on resonance, triggers the heating or cooling of the crystal, which experiences a thermal gradient before stabilising to the new temperature

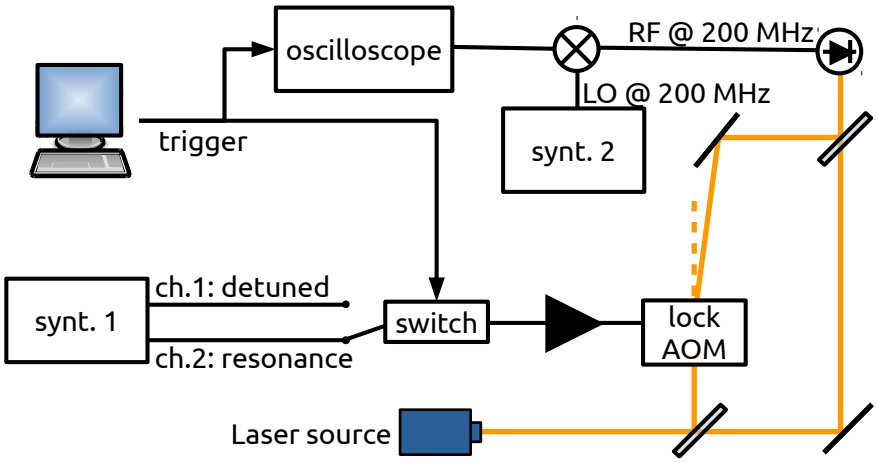

Figure 3.43: Experimental setup for the acquisition of the AOM phase chirp.

equilibrium.

This leads to a slow phase drift of the laser field going through the device. The drift consists of an exponential decay with a time constant of several seconds and thus it can be considered linear within the interrogation pulse. When the frequency modulation brings the laser on resonance the phase variation, which can be interpreted as a frequency shift of the probe laser, happens while probing the clock transition. Since the phase drifts during the clock interrogation over repeated clock cycles have always the same sign (as the thermal behaviour is always the same), the AOM chirp and switching effect results in a systematic frequency shift [121] which does not average out over time and requires to be estimated.

The time-resolved phase noise $\delta\phi(t)$ produced by the AOM can be investigated by acquiring the interferometric beatnote between the laser beam going through the AOM and a reference optical signal (see figure 3.43). The RF beatnote acquisition can be performed either directly by a frequency counter or by an oscilloscope after downmixing it to a DC signal.

To identify the timing of the interrogation pulse and extract the relevant phase data a trigger signal is delivered to both the switch implementing the AOM frequency modulation and the acquisition device.

The frequency shift $\Delta\nu_{\mathrm{AOM}}$ can then be calculated in a similar way as the probe light shift with eq. (3.45), rewritten to account for a phase noise instead of a frequency noise [121] such that

$$\Delta\nu_{\mathrm{AOM}} = \frac{-\frac{1}{2}\int_0^{T_\mathrm{i}} \delta\phi(t)\frac{\partial g(t)}{\partial t}\,\mathrm{d}t}{\int_0^{T_\mathrm{i}} g(t)\,\mathrm{d}t}. \tag{3.66}$$

Here we assume the time origin to be at the beginning of the interrogation pulse

of duration T_i, and $g(t)$ is the sensitivity function for a Rabi π-pulse interrogation, discussed in section 2.6.

At RIKEN we evaluate the frequency shift for the typical interrogation time $T_\mathrm{i} = 300$ ms taking the mean of multiple acquisitions, performed implementing the scheme shown in figure 3.43 with the same AOM used for the clock frequency steering. We find $\Delta\nu_\mathrm{AOM}/\nu_\mathrm{Yb} = 0.2(6) \times 10^{-18}$.

In our system the frequency modulation of the probe laser is realised switching the AOM driving signal between two channels of a synthesizer. If the RF driving signal were turned off instead of switched to a detuned signal the AOM chirp effect would have been more visible. In this later case we evaluate a corresponding frequency shift larger than 1×10^{-17}. While the frequency modulation varies just the frequency of the driving signal, turning the signal on and off also varies the RF power injected into the crystal, leading to more significant thermal effects.

Since the probe light which propagates through the lock AOM then crosses the beam splitter for Doppler noise cancellation (DNC, see section 3.5.1) shown in figure 3.41, the frequency switching of the AOM RF signal leads to a phase jump: the frequency variation happens in a shorter time than required for the light to propagate in a round-trip of the DNC interferometer long branch, thus it results in a phase difference between the light signals from the long and short DNC branches. This difference is proportional to the frequency modulation step and to the length of the round-trip path. The DNC AOM zeros the phase difference, which however is not due to a real phase noise, leading to a phase chirp.

To avoid this DNC behaviour we apply phase-shift keying (PSK) on the DNC frequency reference signal, setting a phase modulation step which counter-balances the phase difference accumulated after the AOM switching. Since the phase jump due to this effect is observed as a glitch in the DNC AOM error signal, we minimise this signal tuning the PSK modulation step size.

3.5.3 Servo error shift

The local oscillator is frequency stabilized on the clock transition by probing it at the half-maximum points, where the slope of the spectroscopy signal is approximately the steepest and the excitation probability is $P \approx 0.5$ (see also section 2.4). The error signal is generated by modulating the probe frequency ν_l with a positive or a negative fixed detuning $\Delta\nu_\mathrm{step}$ from resonance ν_0. The frequency stabilisation control loop applies additional small frequency corrections $\Delta\nu_\mathrm{corr}$ (i.e. servo errors) to the probe laser frequency to satisfy the lock condition such that $\nu_\mathrm{l} = \nu_0 \pm \Delta\nu_\mathrm{step} + \Delta\nu_\mathrm{corr}$. The servo error shift is obtained as the average probe laser detuning from resonance:

$$\Delta\nu_\mathrm{servo} = \langle\nu_\mathrm{l}\rangle - \nu_0 = \langle\Delta\nu_\mathrm{corr}\rangle \approx 0. \tag{3.67}$$

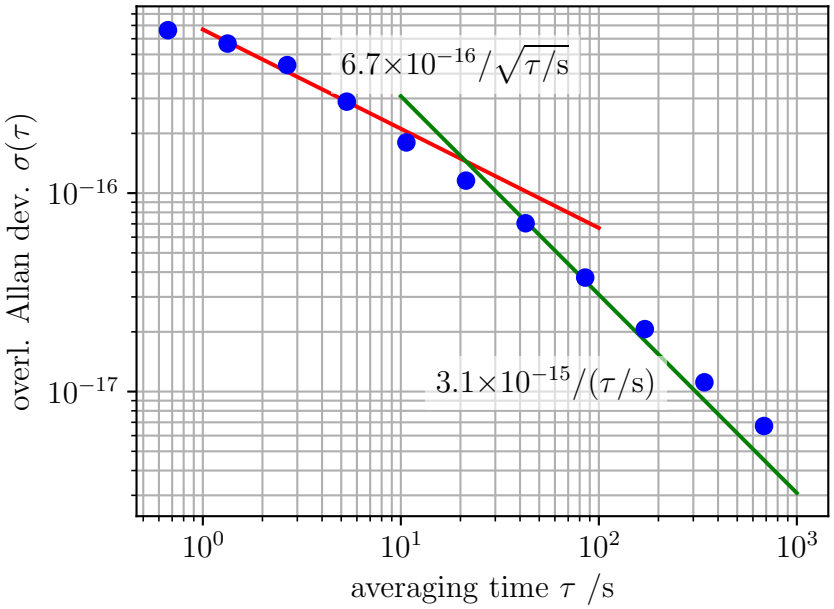

Figure 3.44: Overlapping Allan deviation of servo error data for a typical operating condition of the RIKEN Yb clock.

Figure 3.44 shows the typical stability for servo error data collected with the RIKEN clock during the Yb/Sr frequency ratio measurement discussed in section 4.3. The initial stability almost reflects that of the frequency measurement, while for longer averaging times the data correlation due to the lock integrator makes the data instability fall faster than the white profile.

A conservative approach to establish the servo error shift uncertainty is to take the servo error data standard deviation. We apply this approach in the characterization of the INRIM Yb clock for the measurements discussed in chapter 4, where we assess the shift to be $\Delta\nu_{\mathrm{servo}}/\nu_{\mathrm{Yb}} = 0(1) \times 10^{-17}$.

In the characterization of the RIKEN Yb clock for the Yb/Sr frequency ratio (discussed in chapter 4) we employ a different approach to establish the shift uncertainty. Since the Yb LO is phase referenced to the Sr LO, servo errors are expected to be partially correlated; therefore analysing the servo data of the Yb and Sr clocks singularly leads to an overestimation of the servo error shift uncertainty. In addition, the extracted clock frequency data is corrected by servo errors in real-time, thus the servo shift does not need to account for a statistical uncertainty contribution.

A residual systematic uncertainty contribution arises from an imperfect calculation of the servo errors, which are evaluated converting the observed excitation probability deviations δP according to the clock transition line shape. We

combine the Yb and Sr servo error data $\Delta\nu_{\mathrm{corr,combined}} = \Delta\nu_{\mathrm{corr,Yb}} - R\Delta\nu_{\mathrm{corr,Sr}}$ to remove correlations, where $R \approx \nu_{\mathrm{Yb}}/\nu_{\mathrm{Sr}}$ is used to scale the Sr data, and we calculate the combined shift uncertainty assuming a 25 % uncertainty in the applied line shape slope value. The final frequency shift for the Yb clock results $\Delta\nu_{\mathrm{servo}}/\nu_{\mathrm{Yb}} = 0.5(9) \times 10^{-18}$.

3.5.4 Gravitational redshift

General relativity predicts that time is affected by gravity. As a consequence, the clock frequency is affected by the Earth gravity (gravitational plus centrifugal) potential at the site where the clock is located.

The gravitational redshift effect arises when two frequency standards at respective locations A and B are compared. If the frequency of the clock in A is measured from the location B, it differs from the proper frequency measured at location A. For an observer in B (i.e. a receiver) the frequency of the clock in A (i.e. an emitter) is shifted according to the difference in gravity potential $\Delta W = W_B - W_A$, such that the fractional gravitational redshift can be evaluated as [35]

$$\frac{\Delta\nu_{\mathrm{redshift}}}{\nu_{\mathrm{Yb}}^{\mathrm{rec}}} = \frac{\nu_{\mathrm{Yb}}^{\mathrm{rec}} - \nu_{\mathrm{Yb}}^{\mathrm{em}}}{\nu_{\mathrm{Yb}}^{\mathrm{rec}}} = \frac{\Delta W}{c^2} = -\frac{1}{c^2}\int_A^B g\,\mathrm{d}H \tag{3.68}$$

where $c = 299\,792\,458\ \mathrm{m\,s^{-1}}$ is the speed of light in vacuum and g is the magnitude of the gravity vector, which is integrated along the plumb line connecting A and B and intersecting orthogonally the equipotential surfaces. Defining

$$\bar{g} = \frac{1}{H}\int_A^B g\,\mathrm{d}H \tag{3.69}$$

as the mean value of gravity along the plumb line between A and B, it is possible to write the redshift in terms of the orthometric height H [146] such that

$$\frac{\Delta\nu_{\mathrm{redshift}}}{\nu_{\mathrm{Yb}}^{\mathrm{rec}}} = -\frac{\bar{g}H}{c^2}. \tag{3.70}$$

Since the computation of $\bar{g}$ requires the knowledge of the Earth's interior gravity field, it is not a convenient parameter. Usually gravity potential differences are expressed instead in terms on the normal gravity $\bar{\gamma}$ and normal height H^{N} (see ref. [146]).

When measuring the frequency ratio between two frequency standards is thus required to correct the result by the relativistic redshift effect. This can be performed by measuring the difference in gravity potential between the positions where atoms are confined in the two experiments; a fractional uncertainty at the 10^{-18} level in the redshift evaluation is reached measuring ΔW with an uncertainty of about 0.1 $\mathrm{m^2\,s^{-2}}$, equivalent to a knowledge of H at the centimetre level. If the

distance between the locations of the two standards is within a kilometre, it is possible to determine H with an uncertainty of about 1 mm applying geometric levelling, which is a differential technique directly providing a measurement of ΔW. For longer distances it is possible to use the Global Navigation Satellite System (GNSS)/geoid approach, which combines field modelling and GNSS position measurements to determine absolute potential values with an uncertainty in a best-case scenario corresponding to about 2 cm in the value of H [35].

The RIKEN Yb/Sr frequency ratio measurement discussed in section 4.3 is realised comparing two frequency standards sharing the same construction and located on the same optical table. While atoms in the two clocks are expected to be loaded in the lattice at the same elevation from the table surface, a different transport distance into the cryogenic chamber (see section 2.8) leads to the interrogation of the atomic sample at different gravity potentials. Since the lattice is tilted by $\theta = 15°$ from gravity, a transport distance for the Yb[Sr] clock of 20.5(15) mm[22.7(15) mm] leads to a differential redshift of the Yb frequency as observed at the Sr location of $\Delta\nu_{\mathrm{redshift}}/\nu_{\mathrm{Yb}}^{\mathrm{rec}} = 2(2) \times 10^{-19}$. In this case the gravity acceleration can be considered same for the two systems, and the difference in the elevation of the two atomic clouds from the optical table surface is sufficient to determine the frequency shift.

In order to provide atomic clock contributions to the international atomic time (TAI), the redshift requires to be computed with respect to the conventional zero gravity potential value of

$$W_0 = 62\,636\,856.00\ \mathrm{m^2\,s^{-2}},$$

which has been defined in the year 2000 by the Resolution B1.9 of the International Astronomical Union (IAU) [33, 35] based on the value recommended by the International Association of Geodesy (IAG) [147]. Measurements of the absolute gravity potential W, evaluated with respect to the reference level W_0, can be performed with the GNSS/geoid approach. The geometric levelling approach can also be employed, but leads to results that are just valid locally [35].

In Europe measurements of the absolute gravity potential W have been performed at each national metrology institute (NMI) to allow the comparison of frequency standards operated at different NMIs and to allow the evaluation of the redshift correction of absolute frequency measurements. This has been performed in 2015 in the context of the European project *International timescales with optical clocks* (ITOC) [148].

At INRIM, the absolute gravity potential has been measured in the Yb optical frequency standard laboratory applying the GNSS/geoid approach to be $W(\mathrm{Yblab}) = 2333.59(23)\ \mathrm{m^2\,s^{-2}}$. Accounting for the residual height $h \approx 30$ cm of the atomic cloud from the reference marker, the gravity potential is evaluated to be $W(\mathrm{Yb}) = 2336.28(25)\ \mathrm{m^2\,s^{-2}}$. The corresponding gravitational redshift is $\Delta\nu_{\mathrm{redshift}}/\nu_{\mathrm{Yb}}^{\mathrm{rec}} = 2599.5(3) \times 10^{-17}$.

Chapter 4

Frequency measurements

4.1 Absolute frequency of the ^{171}Yb $^1S_0$-$^3P_0$ clock transition

At INRIM we have performed the absolute frequency measurement of the ^{171}Yb $^1S_0$-$^3P_0$ clock transition by comparing our optical lattice clock with the cryogenic ^{133}Cs fountain clock [13], developed and operated at INRIM as the Italian primary frequency standard.

The Yb frequency has been measured to be

$$\nu_{\mathrm{Yb}} = 518\,295\,836\,590\,863.59(31)\ \mathrm{Hz}.$$

The result, published in ref. [114], is in agreement with the recommended value by CIPM of [158]

$$\nu_{\mathrm{Yb}}^{\mathrm{CIPM}} = 518\,295\,836\,590\,863.6(5)\ \mathrm{Hz},$$

which has been obtained as the mean of frequency measurements performed worldwide by research groups up to year 2017.

Figure 4.1 shows all measurements performed to date by worldwide research groups of the Yb clock frequency. The ^{171}Yb $^1S_0$-$^3P_0$ clock frequency has been obtained with absolute frequency measurements performed either directly against primary Cs standards or against the international atomic time (TAI). In addition, it has been measured with respect to other optical frequency standards based on ^{87}Sr, whose absolute frequency has been evaluated independently; in this case the Yb frequency has been extracted from the measured frequency ratio multiplied by the CIPM recommended value of the ^{87}Sr clock frequency [157]

$$\nu_{\mathrm{Sr}}^{\mathrm{CIPM}} = 429\,228\,004\,229\,873.0(4)\ \mathrm{Hz}.$$

The metrological chain used to measure the Yb absolute frequency against the Cs primary standard is shown in figure 4.2. The Yb LO is split in two main

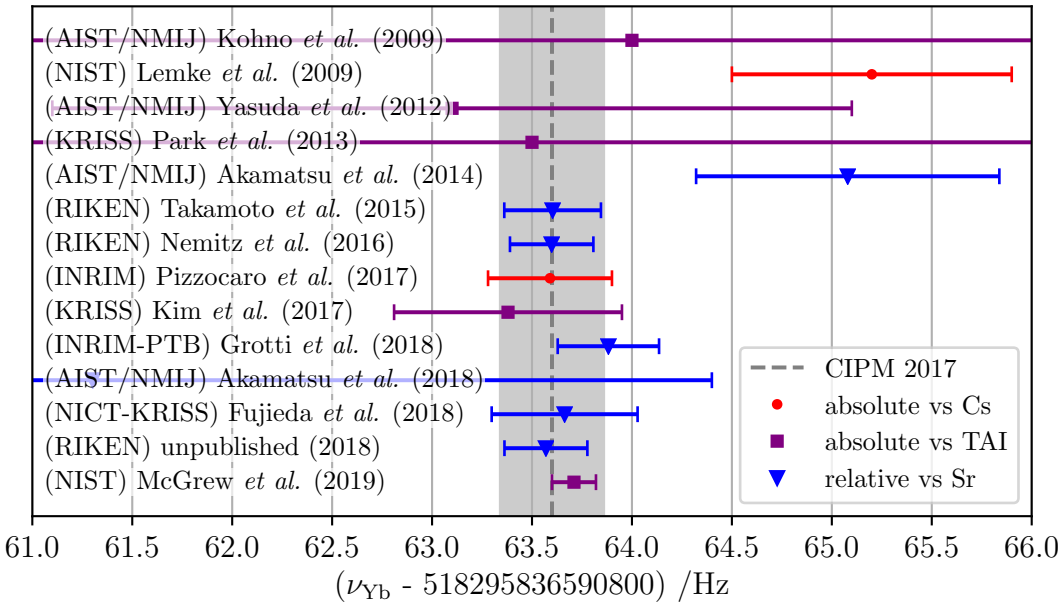

Figure 4.1: Collection of measurements of the Yb clock frequency performed by different research groups [42, 104, 112–114, 149–156]. Absolute measurements are performed either directly against Cs primary standards or against the time scale TAI, while results relative to Sr frequency standards are extracted using the CIPM recommended value for the Sr clock frequency [157]. Dashed line and grey shaded area represent the value and the uncertainty range of the CIPM Yb frequency recommended value [158] obtained averaging the shown data up to year 2017 (included).

branches: the first is delivered to the clock apparatus, providing the probe laser; the second is delivered to the optical frequency comb (see chapter 1), a Menlo System's Er fiber frequecy comb where a beat note f_b with a frequency duplicated portion of the comb spectrum is acquired. Frequency duplication is realised with second harmonic generation using a non-linear cristal, and allows to expand the frequency comb emission to the visible domain at the Yb LO frequency of 518 THz; this explains the factor 2 in front of f_{CEO} in figure 4.2. This factor is added in front of f_{CEO} in equation (1.1) when calculating the Yb frequency.

During the measurements the frequency comb is referenced to a hydrogen maser (H Maser) delivering a 10 MHz calibration signal, and the maser frequency is periodically measured against the Cs fountain to maintain traceability to the SI second.

The beat note f_b between the Yb clock LO and the frequency comb is measured and acquired with a K+K frequency counter [159]. In order to detect glitches in the frequency counting due to occasional excessive phase noise or a decrease in the beat note signal-to-noise ratio, the RF beat note is split in two signals which are down-mixed, filtered and measured independently in two separate channels of the

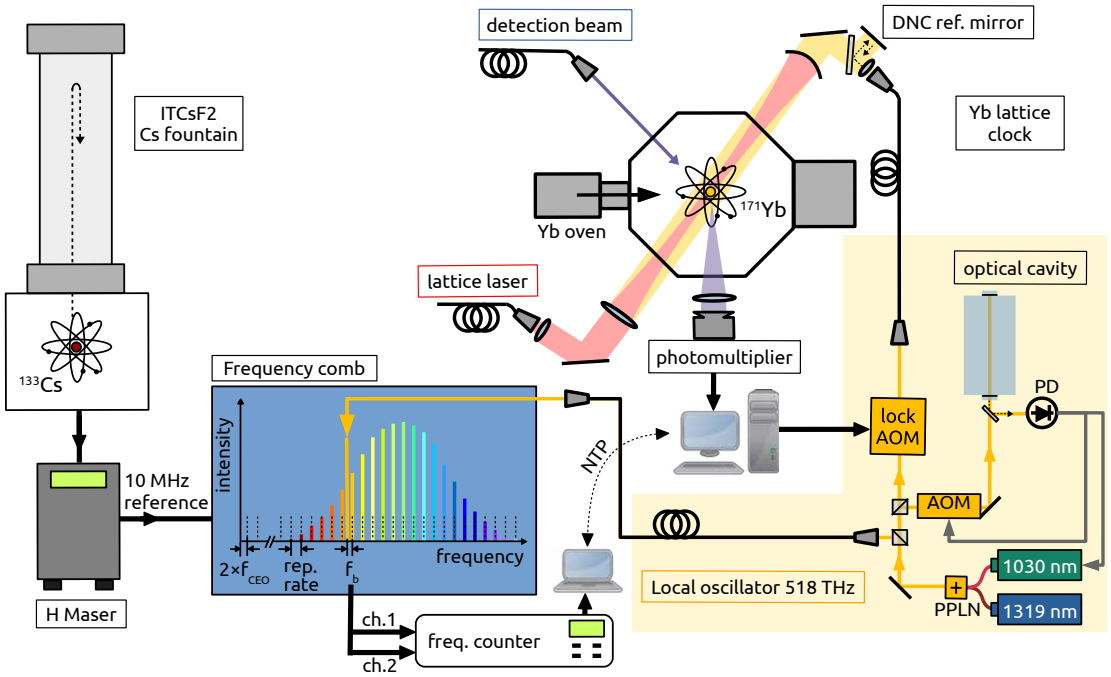

Figure 4.2: Metrological chain of the absolute frequency measurement of the Yb clock frequency.

counter: acquired data is discarded if the difference between channel 1 and channel 2 is larger than 200 mHz. Although the values of f_{CEO} and f_{rep} are known and fixed during the measurement campaign, they are continuously measured with the K+K counter for monitor and debugging reasons.

The Yb clock probe laser is locked to the atomic reference continuously applying frequency corrections $\Delta\nu_{\mathrm{corr}}$ to the lock AOM driving frequency f_{lockAOM} (see fig. 4.2). The AOM is located along the probe laser path, and does not modify the frequency of the laser delivered to the frequency comb, which measures the frequency of the reference cavity. These frequency corrections are computed, applied and recorded by a computer, whose time reference is synchronized with the one collecting the frequency comb data through the INRIM's network time protocol (NTP) server. The comb measurements and the frequency corrections are then combined to evaluate the Yb clock frequency.

Time synchronization is required to avoid mismatches when merging the two datasets through interpolation. We assess an uncertainty in the time synchronization of 3 ms.

Since frequency corrections $\Delta\nu_{\mathrm{corr}}$ are applied after two clock cycles, the cavity frequency drift during this time is not properly characterised against the atomic reference and results in a frequency error even with perfect timestamp synchronisation. Accounting for a maximum cavity drift of 0.1 Hz s^{-1} we estimate a total

uncertainty related to synchronisation of 6×10^{-19}.

From the measured beat note frequency f_b it is possible to evaluate the Yb clock frequency $\nu_\mathrm{Yb}^\mathrm{H}$ against the H maser:

$$\left(\nu_\mathrm{Yb}^\mathrm{H} - \Delta f\right) = f_\mathrm{b} + \left(2f_\mathrm{CEO} + m_\mathrm{Yb} f_\mathrm{rep}\right), \tag{4.1}$$

$$\text{with} \quad \Delta f = f_\mathrm{lockAOM} + \Delta\nu_\mathrm{corr} + \Delta\nu_\mathrm{syst}. \tag{4.2}$$

The systematic frequency shifts $\Delta\nu_\mathrm{syst}$ affecting the atomic transition are considered in the calculation as a correction frequency offset. The sign of the beat note frequency depends whether the beat note is generated with the comb tooth at higher frequency than the laser frequency (in this case $f_\mathrm{b} < 0$) or with the tooth at lower frequency ($f_\mathrm{b} > 0$). In our experiment $f_\mathrm{b} \approx +40.9$ MHz, $f_\mathrm{lockAOM} = 2\times -82.15$ MHz (the factor 2 accounts for a double-pass AOM), $f_\mathrm{CEO} = -20$ MHz, $f_\mathrm{rep} = 250$ MHz and $m_\mathrm{Yb} = 2\,073\,184$.

The final absolute frequency of the Yb clock transition is evaluated including in the calculation the calibration of the maser by the primary standard.

$$\nu_\mathrm{Yb} \equiv \nu_\mathrm{Yb}^\mathrm{Cs} = \left(\frac{\nu_\mathrm{maser}^\mathrm{Cs} - \nu_\mathrm{maser}^\mathrm{H}}{\nu_\mathrm{maser}^\mathrm{H}} + 1\right) \nu_\mathrm{Yb}^\mathrm{H}, \tag{4.3}$$

where $\nu_\mathrm{maser}^\mathrm{Cs}$ is the measured absolute frequency of the H maser and $\nu_\mathrm{maser}^\mathrm{H}$ is the expected maser frequency, thus the term $(\nu_\mathrm{maser}^\mathrm{Cs} - \nu_\mathrm{maser}^\mathrm{H})$ represents the deviation of the maser frequency from the SI second.

The measurement campaign consists of 31 measurements performed between January 2016 and May 2016, for a total of 227 h of measurement time, with a final statistical uncertainty of 3.9×10^{-16} (see table 4.1).

The measurement instability was limited by the Cs fountain white frequency noise, which depends on the number of atoms probed by the microwave oscillator. For the first part of the campaign the clock is operated in a low atomic density regime, contributing with a statistical uncertainty in terms of Allan deviation of $3.6 \times 10^{-13}\ /\sqrt{\tau/\mathrm{s}}$. In these conditions the systematic frequency shift due to the cold collisions is contained and the total fractional systematic uncertainty is 3.0×10^{-16}. For the second part of the campaign we decide to increase the atomic density to improve the signal-to-noise ratio and therefore also the clock instability to $2.5 \times 10^{-13}\ /\sqrt{\tau/\mathrm{s}}$, however the higher density leads to an increase of the uncertainty budget to 4.8×10^{-16}, which worsen the ultimate limit in the final measurement uncertainty.

We characterise the frequency comb uncertainty contribution to the total uncertainty by measuring the Yb absolute frequency with also a second frequency comb, and we take the deviation between the two results of 1×10^{-16} at 10^4 s averaging time as the uncertainty.

The Yb lattice clock contributes to the accuracy budget with a systematic uncertainty of 1.6×10^{-16} (see table 4.1 for the detailed budget, discussed in ref. [114]).

The dominant contribution is provided by the lattice light shift, whose evaluation is limited by the knowledge at the time of the measurement of the atomic hyperpolarizability and multipolar polarizabilities to the lattice light. The non-linear light shift contribution listed in the table includes the correction for the non-linearity of the differential shift measured interleaving the clock operation between different lattice depth conditions, and used to extract the linear component of the lattice shift.

The magnitude of the uncertainty related to non-linear light shifts has triggered the interest in investigating the hyperpolarizability coefficient separately, in a specific experiment performed later and discussed in section 3.2.1. The recent investigations of these higher order lattice shift contributions discussed in the previous chapter now allow to evaluate the light shift in the INRIM Yb clock at the 10^{-17} level.

The large uncertainty contribution arising from the collisional density shift is limited by the statistical uncertainty, which can be reduced in future measurements either performing more density shift measurements or implementing a lattice design able to trap atoms in a large volume in order to effectively reduce the shift magnitude.

The blackbody radiation (BBR) frequency shift (discussed in section 3.3) is the ultimate limit of the INRIM Yb clock accuracy, as its evaluation is limited by the design of the vacuum package which does not allow to accurately control and evaluate the temperature of the atomic environment.

a) Yb clock systematic shifts

Contribution	Shift$\times 10^{16}$	Unc.$\times 10^{16}$
Linear lattice light	-0.4	0.8
Non-linear lattice light	-1.2	1.0
BBR room	-23.53	0.25
BBR oven	-0.21	0.08
Zeeman	-2.7	0.4
Collisions	-0.2	0.6
Probe light	0.1	0.35
AOM phase chirp and switching	-	0.04
Background gas	-	0.15
1^{st} order Doppler	-	0.5
Servo error	-	0.1
DC Stark	-	0.1
Tunneling	-	0.04
Fibre links	-	0.01
Line pulling	-	0.04
Total	-28.1	1.6
Gravitational redshift	259.97	0.06
Total	231.9	1.6

b) Absolute frequency measurement uncertainty budget

Contribution	Unc. $\times 10^{16}$
Cs fountain	4.0
Statistics	3.9
Yb clock	1.6
Frequency comb	1.0
Differential gravitational redshift	0.02
Fibre link	0.01
Synchronization	0.006
Total	5.9

Table 4.1: a) Uncertainty budget of the INRIM Yb lattice clock in fractional units for the absolute frequency measurement [114]. The gravitational redshift is separated from the other frequency shifts as it is considered separately when compiling the uncertainty budget of the frequency measurement, where just the differential redshift is relevant. b) Uncertainty budget of the absolute frequency measurement of the Yb clock transition in fractional units [114].

4.2 ^{171}Yb/^{87}Sr frequecy ratio with a transportable lattice clock

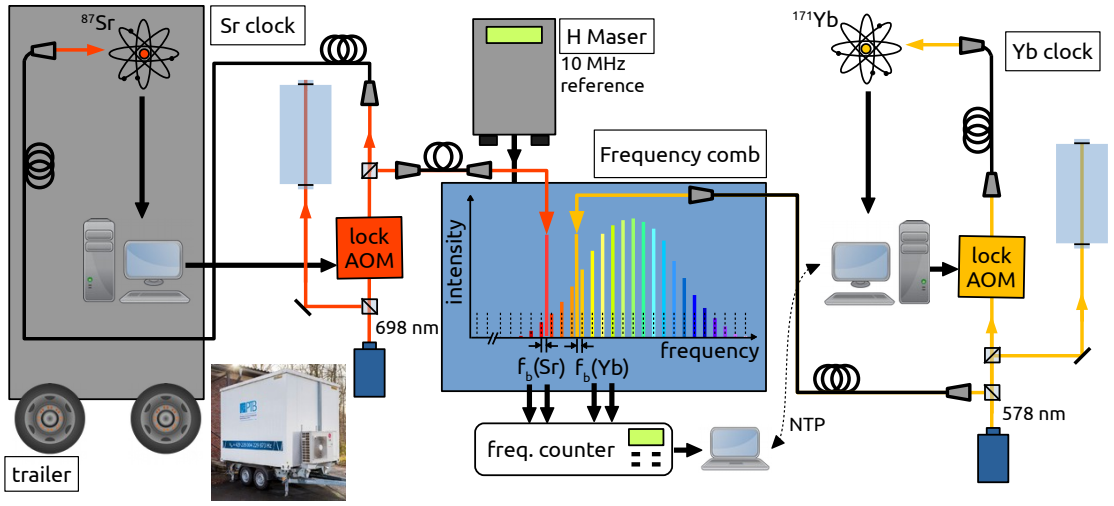

Figure 4.3: Metrological chain of the Yb/Sr frequency ratio measurement performed between the INRIM stationary clock and the PTB transportable clock. The small photo, taken from ref. [160], shows the actual PTB trailer housing the clock.

Within the German National Metrology Institute, the Physikalisch-Technische Bundesanstalt[a] (PTB), researchers have developed a transportable optical lattice clock based on ^{87}Sr atoms [161]. The interest in the development of transportable optical clocks arises from the need to compare optical frequency standards taking advantage of their stability performances.

The standard approach to compare remote atomic clocks employs GNSS[b] satellites. However, the satellite frequency transfer technique deteriorates the measurement stability, leading to a statistical uncertainty of 10^{-10} $/(\tau/\mathrm{s})$.

Optical fibre frequency transfer techniques overcome the issue and succeed to transfer the stability of the optical standards over distances of several hundred kilometres without degradation [32]. Networks of fibre links have been realised [162], connecting selected locations. Nonetheless, the installation, maintenance and operation of fibre links is expensive and often not possible.

Transportable optical clocks may be physically moved to either locations where a fibre link is available, or directly close to another optical frequency standard,

[a] https://www.ptb.de/cms/en.html

[b] Global navigation satellite system, including the GPS (American), GLONASS (Russian), Galileo (European) and BeiDou (Chinese) systems.

with no major limits on the transport distance. The PTB Sr transportable lattice clock has been moved to INRIM to perform an optical frequency ratio measurement between the $^1S_0$-$^3P_0$ clock transitions of ^{171}Yb and ^{87}Sr [154]. This was the first in-field measurement for a transportable optical lattice clock.

The PTB transportable clock is installed in a car trailer, which can be described as a small transportable laboratory. The trailer is parked next to the INRIM building where the Yb stationary clock is located, in an area protected from direct sun light to contain overheating. The clock local oscillator is moved out from the trailer and located inside the building next to the frequency comb, and it is delivered to the clock apparatus with a 50 m Doppler-noise compensated optical fibre. Figure 4.3 shows the metrological chain implemented to perform the frequency ratio measurement.

Contribution	Unc.$\times 10^{16}$
Sr systematics	1.8
Yb systematics	1.6
Statistics	1.1
Differential gravitational redshift	0.1
Frequency comb	1.0
Fibre link	0.01
Synchronization	0.006
Total	2.8

Table 4.2: Frequency ratio measurement uncertainty budget. The gravitational redshift accounts for a difference in height between the Yb and Sr clocks of $\Delta h = 3.6(1)$ m.

The frequency ratio measurement is performed synchronously acquiring through a K+K frequency counter the beat note signals f_b of the Yb and Sr clocks' local oscillators with the frequency comb, which is referenced to a hydrogen maser (see the previous section for details). Since the optical frequencies of the two local oscillators $\nu_\mathrm{Yb} = 518$ THz and $\nu_\mathrm{Sr} = 429$ THz lay in the yellow and red visible regions respectively, the frequency comb intensity is optimised in these frequency ranges to maximise the beat note signals.

The beat note frequencies $f_\mathrm{b,Yb}$ and $f_\mathrm{b,Sr}$, which are redundantly measured with two pairs of counter channels to discard data affected by cycle slips, are used to directly evaluate the optical frequency ratio between the Yb and Sr clock transitions according to [163, 164]

$$R = \frac{\nu_\mathrm{Yb}}{\nu_\mathrm{Sr}} = \frac{m_\mathrm{Yb}}{m_\mathrm{Sr}} + \left(\frac{(2f_\mathrm{CEO} + f_\mathrm{b,Yb} + \Delta f_\mathrm{Yb}) - (2f_\mathrm{CEO} + f_\mathrm{b,Sr} + \Delta f_\mathrm{Sr}) \frac{m_\mathrm{Yb}}{m_\mathrm{Sr}}}{\nu_\mathrm{Sr}} \right), \tag{4.4}$$

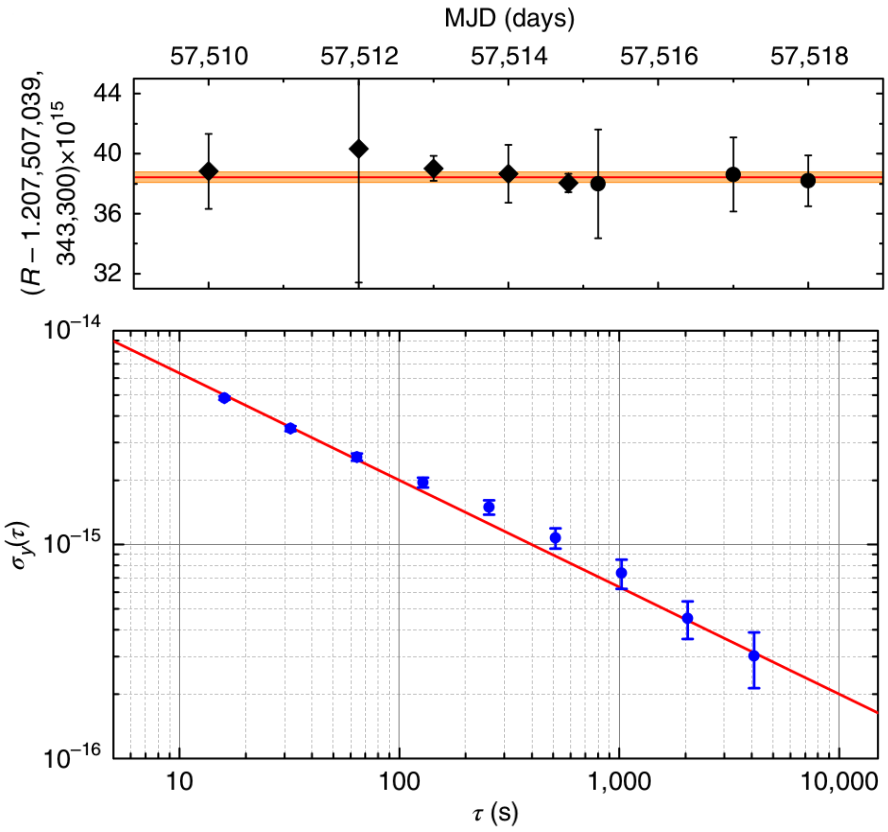

Figure 4.4: Above: frequency ratio measurements on different day of operation. Diamonds (circles) denote the operation of the Sr lattice clock with a shallow (deep) lattice. The line is the overall average. Below: fractional instability of R/R_0, where $R_0 = 1.207\,507\,039\,343\,338\,122$ is calculated from the CIPM 2015 recommended values for the Yb and Sr frequencies; the red line depicts a white frequency noise of $2 \times 10^{-14}\,/\sqrt{\tau/\mathrm{s}}$. Both figures are taken from ref. [154].

using the notation of eq. 4.2. In our experiment we have $f_{\mathrm{b,Sr}} = +44.2$ MHz, $m_{\mathrm{Sr}} = 1\,716\,912$, $f_{\mathrm{b,Yb}} = +40.9$ MHz and $m_{\mathrm{Yb}} = 2\,073\,184$, while all other parameters are same as for the absolute frequency measurement discussed in the previous section.

Despite the evaluation of the individual optical frequencies is limited by the stability of the term $m \times f_{\mathrm{rep}}$, where the factor m brings the noise of the RF repetition rate referenced to the H maser to the optical domain, the frequency ratio of eq. 4.4 is calculated independently of f_{rep}. Therefore, the stability of the H maser does not limit the evaluation of R, which can effectively be interpreted as a virtual beat note of the two optical frequencies.

The optical frequency ratio is measured to be [154]

$$R = \frac{\nu_{\mathrm{Yb}}}{\nu_{\mathrm{Sr}}} = 1.207\,507\,039\,343\,338\,41(34).$$

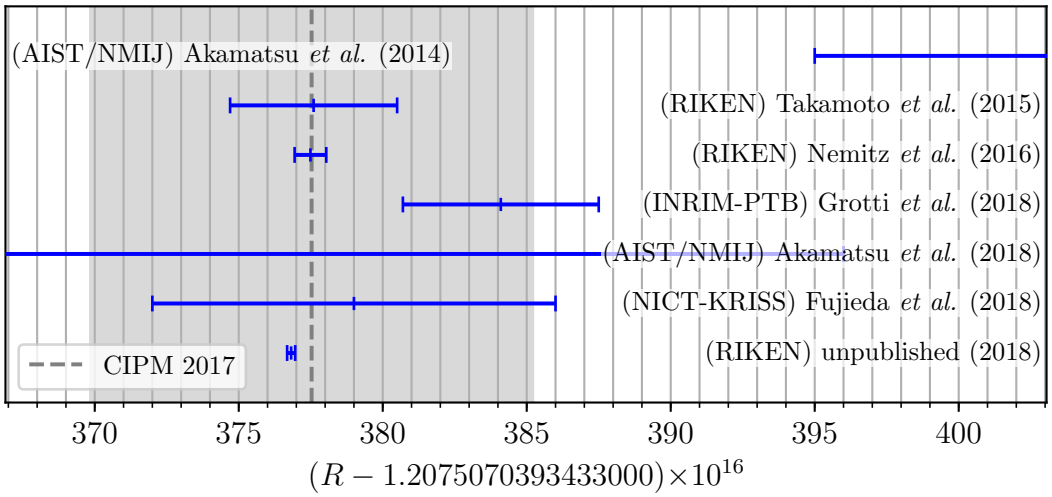

Figure 4.5: Collection of the ^{171}Yb/^{87}Sr frequecy ratio measurements performed so far [112, 152–156]. Dashed line and grey shaded area represents the value and uncertainty range resulting from the frequency ratio of the CIPM 2017 recommended values $R_{\mathrm{CIPM}} = 1.207\,507\,039\,343\,337\,75(77)$ [157, 158]. The frequency ratio discussed in this section is reported in the paper of J. Grotti and co-authors [154].

Table 4.2 summarises the measurement uncertainty budget. Since the ratio measurements are performed in the same period of the Yb absolute frequency measurement, the accuracy budget of the Yb lattice clock, together with its experimental conditions, are unchanged from that reported in the previous section and in table 4.1. Concerning the Sr lattice clock, although it was firstly characterized against a stationary Sr lattice clock at PTB with an uncertainty of 7.4×10^{-17} [161], the re-evaluation of the uncertainty budget after moving the clock to INRIM met technical and time-schedule difficulties leading to a larger final uncertainty. The temperature and ventilation control inside the trailer was challenging, and the clock operation time was not sufficient to perform a complete renewed characterization of the lattice light shift in the new experimental conditions, potentially different from those at PTB [160].

As shown in figure 4.4 the final frequency ratio value results from seven measurements performed over multiple days within two weeks in May 2016. The total measurement time amounts to 31 000 s, with a ratio instability of $2 \times 10^{-14}\ /\sqrt{\tau/\mathrm{s}}$.

Figure 4.5 compares the final result with the results of the Yb/Sr frequency ratio measurements performed by other research groups. Our result is within two standard deviations of the most accurate previous evaluation [112]. We do not have a justification for the disagreement, and further investigation is required.

As shown in figure 4.5, the ^{171}Yb/^{87}Sr frequency ratio has been measured by

four independent research groups worldwide, namely NICT-KRISS (Japan-Korea), NMIJ/AIST (Japan), RIKEN (Japan), INRIM-PTB (Italy-Germany), and to our knowledge this is the first time a direct optical frequency ratio undergoes such metrological characterization.

The independent validation of frequency measurements is necessary in order to demonstrate reliability and build confidence in the optical frequency standards. As a consequence, even if this frequency measurement result does not reach the accuracy demonstrated by other optical clocks worldwide, it is an important contribution to the generation of an internationally consistent clock frequency value to be considered as a candidate for the redefinition of the unit of time.

4.3 ^{171}Yb/^{87}Sr frequecy ratio at RIKEN

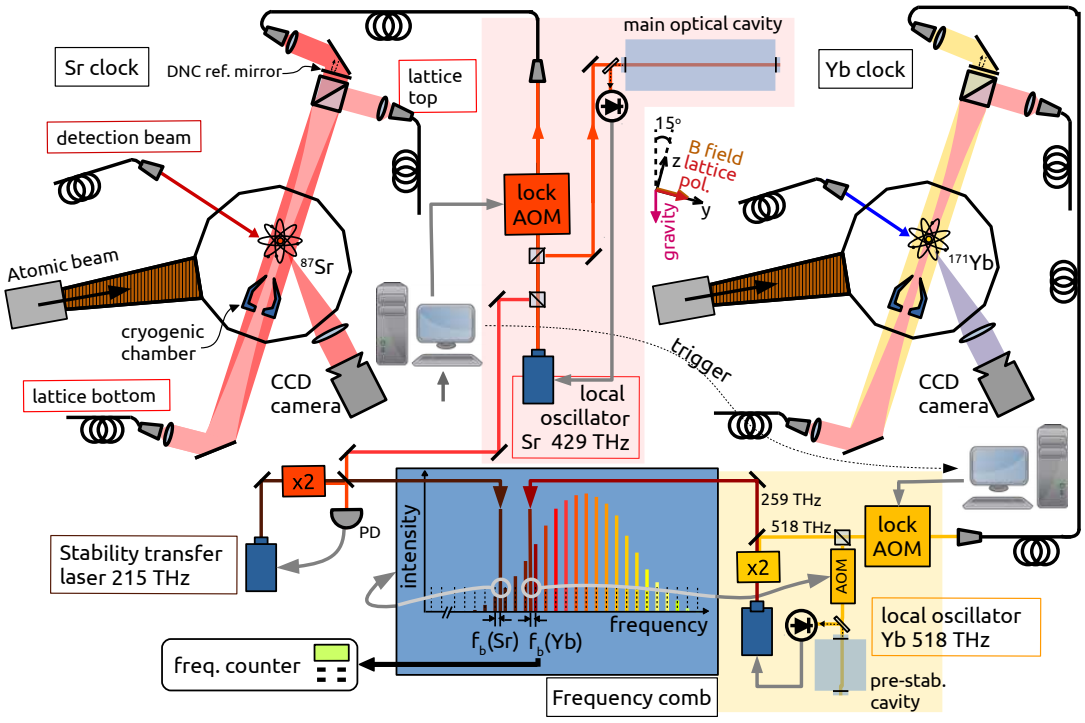

Figure 4.6: Metrological chain of the ^{171}Yb/^{87}Sr frequecy ratio performed at RIKEN.

The most accurate ^{171}Yb/^{87}Sr frequency ratio value published to date has been obtained at RIKEN in 2016, with a fractional uncertainty of 4.6×10^{-17} [112] (see fig. 4.5). In this measurement the uncertainty budget is dominated by the lattice light shift of the Yb lattice clock, which is evaluated with a fractional uncertainty in terms of the Yb frequency of 3.3×10^{-17}.

A new evaluation of the Yb lattice light shift coefficients [58], discussed in section

3.2.1, now allows for an evaluation of the lattice light shift below 10^{-17}. We take advantage of a renewed evaluation of the Yb uncertainty budget at 6.0×10^{-18} to perform an improved measurement of the ^{171}Yb/^{87}Sr frequency ratio comparing the RIKEN Sr and Yb lattice clocks.

The frequency ratio is evaluated to be (see also fig. 4.5)

$$R = \frac{\nu_{\mathrm{Yb}}}{\nu_{\mathrm{Sr}}} = 1.207\,507\,039\,343\,337\,682(14).$$

The metrological chain implemented to perform the frequency measurement is shown in figure 4.6. The two lattice clocks based on either strontium (^{87}Sr) or ytterbium (^{171}Yb) are built with a similar design (see section 2.8 for details). Two counter-propagating lattice beams, delivered from the bottom and the top of the physical package, are overlapped and interfere to generate the lattice. The probe laser is delivered from the top of the package through a Doppler noise compensated (DNC) optical path.

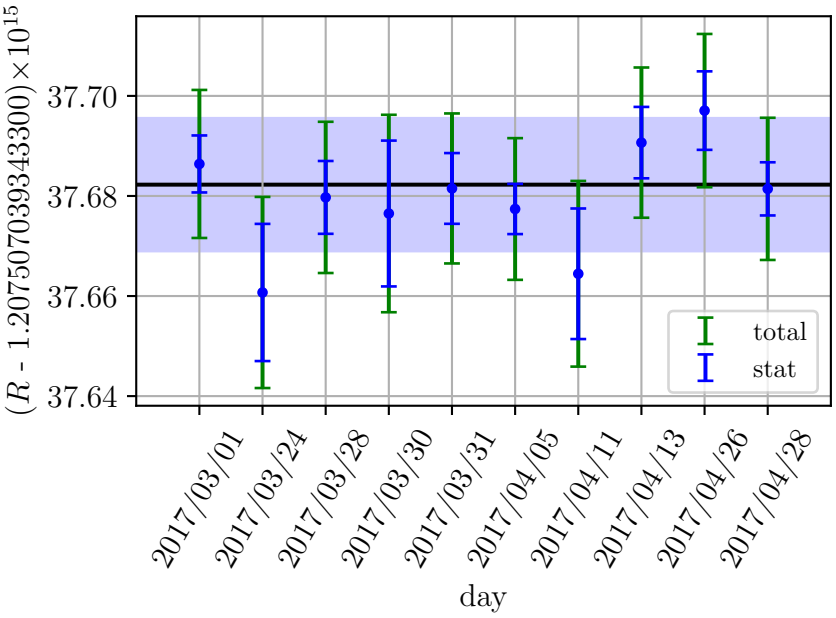

Figure 4.7: Yb/Sr frequency ratio measurements. Smaller red error bars show the measurement statistical uncertainty $\sigma_{i,\mathrm{stat}}$, while the larger blue bars are the total measurement uncertainties accounting both statistical and systematic contributions $\sigma_i^2 = \sigma_{i,\mathrm{stat}}^2 + \sigma_{i,\mathrm{syst}}^2$.

The frequency stability of the Sr local oscillator is transferred to the Yb oscillator at $\nu_{\mathrm{Yb}} = 518$ THz through the optical frequency comb, as shown in figure 4.6 and discussed in section 2.8.

The instability of the spectral purity transfer system, dominated by the phase drift of the frequency comb in-fibre uncompensated optical paths affected by long term temperature variations, is assessed to be smaller than 7×10^{-18} at 1 s averaging time through out-of-loop beat note measurements between different comb output branches with independent amplification and spectral broadening. For the relevant experimental time scales of $\tau = 10^3$ s to 10^4 s, we find an instability smaller than 5×10^{-19}, in agreement with results obtained in a different environment using a single-branch reference comb system [165]. In the frequency ratio measurement discussed here, the beat notes of the transfer laser and Yb laser are generated using the same output branch of the frequency comb to further reduce non-common phase drifts.

We perform a series of 10 frequency ratio measurements between the RIKEN Sr and Yb lattice clocks over April and May 2017 (see fig. 4.7). The duration of each measurement, between 8000 s and 25 000 s, allows us to reach a fractional statistical uncertainty varying between 1.2×10^{-17} and 4.4×10^{-18} with a Rabi interrogation of duration $T_\mathrm{i} = 300$ ms. The typical measurement instability, evaluated with the data total deviation [166], is characterised with a white frequency noise falling as $6 \times 10^{-16}\ /\sqrt{\tau/\mathrm{s}}$ (see fig. 4.8).

Most of the Dick effect contribution (see section 2.6.2) to this measurement instability is suppressed under the current operating conditions, as the Yb and Sr LOs are phase referenced to each other. Performing synchronous clock interrogations of same duration T_i the cavity instability is correlated between the two frequency standards, therefore also the deviations in the measured clock transition probabilities are mostly correlated. As a consequence when combining the acquired data from the two clocks to evaluate the frequency ratio the correlated noise contributions cancel out, allowing frequency measurements beyond the Dick limit [67, 76].

The limit in the ratio instability is provided by residual noise sources uncommon between the two frequency standards, such as the noise of the spectral purity transfer chain and the technical detection noise due to the signal acquisition devices.

The contribution of the quantum projection noise (QPN) [65] (see section 2.6) to the clock instability can be estimated according to equation (2.19).

With a Rabi π-pulse of duration $T_\mathrm{i} = 300$ ms, and assuming a maximum excitation probability of 0.97, according to eq. (2.5) the clock transition linewidth is calculated to be $\gamma = 2.7$ Hz. Since the Yb standard interrogates about $N_\mathrm{Yb} \sim 300$ atoms, the QPN contribution to the instability is evaluated to be $\sigma_y^\mathrm{QPN}(\tau) = 1.2 \times 10^{-16}\ /\sqrt{\tau/\mathrm{s}}$. In the Sr frequency standard a larger atomic sample of $N_\mathrm{Sr} \sim 1000$ is probed, thus $\sigma_y^\mathrm{QPN}(\tau) = 7.9 \times 10^{-17}\ /\sqrt{\tau/\mathrm{s}}$. Hence, the instability due to QPN is not a limiting factor in the current experimental system.

We assign a statistical uncertainty $\sigma_{i,\mathrm{stat}}$ to each of the ratio measurements based on their measured instability, including a statistical contribution arising from

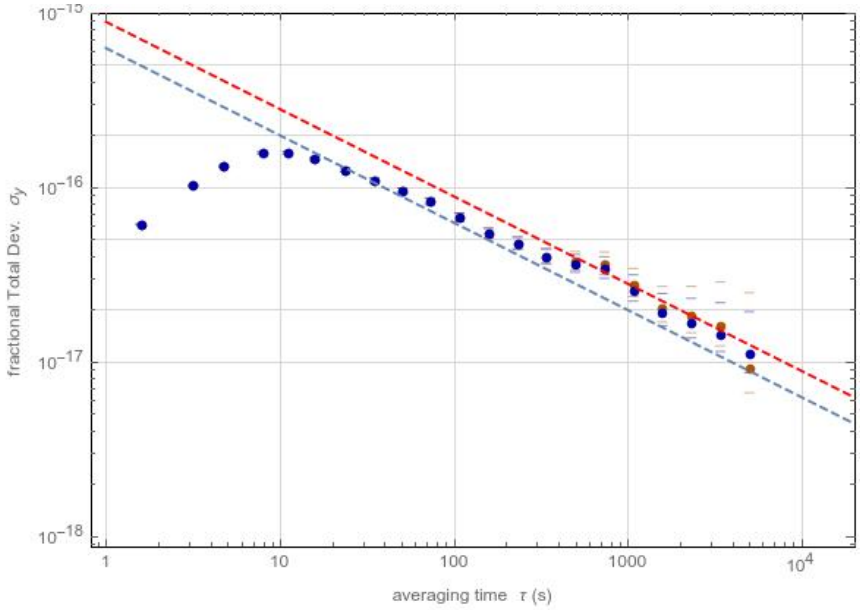

Figure 4.8: Typical ratio measurement instability according to the data total deviation. Dashed lines show the most optimistic (blue) and most pessimistic (red) linear fit according to a white frequency noise falling as either 6.2×10^{-16} $/\sqrt{\tau/\mathrm{s}}$ or 8×10^{-16} $/\sqrt{\tau/\mathrm{s}}$. The difference between the two results arises because of the large uncertainty in the calculation of the total deviation for long averaging times. To avoid this ambiguity we decide to calculate the measurement instability according to the standard deviation, which provides an equivalent estimation of the instability of data affected by white frequency noise. Because of the servo, the instability at averaging times $\tau < 10$ s is underestimated; hence we divide and average the dataset in bins of 16 data points each, corresponding to $\tau \sim 25$ s, and take the standard deviation of this modified dataset.

variations in experimental parameters between repeated measurements. These are the lattice trapping parameters, which are acquired through sideband spectroscopy before and after each measurement, the Zeeman linear shift, which is measured in real-time during the clock operation through the lock data, and the servo error, calculated from the applied frequency corrections.

Figure 4.7 highlights the statistical contributions with respect to the total measurement uncertainties; frequency ratio results are found to be in agreement between each other within statistical expectations, with $\chi^2_{\mathrm{red}} = 1.4$ (excluding parameters' variability $\chi^2_{\mathrm{red}} = 2.3$).

The overall ratio fractional statistical σ_{stat} and systematic σ_{syst} uncertainties are

calculated applying for each measurement weights w_i such that

$$\sigma_{\text{stat}} = \sqrt{\chi^2_{\text{red}} \sum_i \sigma^2_{i,\text{stat}} w_i^2} = 2.2 \times 10^{-18}, \tag{4.5}$$

$$\sigma_{\text{syst}} = \sqrt{\sum_i \sigma^2_{i,\text{syst}} w_i} = 1.1 \times 10^{-17}, \tag{4.6}$$

with weights defined according to the variance $\sigma^2_{i,\text{stat}}$ as

$$w_i = \frac{1}{\sigma^2_{i,\text{stat}}} \sum_j \frac{1}{\sigma^2_{j,\text{stat}}}. \tag{4.7}$$

The systematic frequency shifts of the Yb and Sr clock frequencies are listed in table 4.3.

Both the Yb and Sr clock uncertainty budgets are dominated by the contribution of the lattice light frequency shifts. These are evaluated through a series of light shift measurements interspersed with the ratio measurement and applying similar light shift models (see section 3.2.1 for the Yb clock and [52] for the Sr clock). Both evaluations take advantage of a renewed measurement of the lattice polarizabilities [52, 58]. Concerning the Sr standard, the shift is evaluated for the lattice trapping parameters of $U_{\text{e}} = 34(6)\ E_{\text{r}}$ and $\bar{n}_z \approx 0.01$, and the final shift uncertainty is dominated by the uncertainty of the measured lattice frequency $\nu_{\text{L}} = 368\,554\,473(4)$ MHz, due to the drift of the optical cavity used for its stabilization over the measurement period of about 2 months. Concerning the Yb clock, the lattice trap conditions are described by $U_{\text{e}} = 75.6(2)\ E_{\text{r}}$, $\zeta \approx 0.83$, $\bar{n}_z \approx 0.1$, $\delta_2 \approx 0.007$ and $\nu_{\text{L}} = 394\,798\,273.4(1)$ MHz. The shift uncertainty is limited by the uncertainty on the model coefficients. Both evaluations includes the estimation of the contribution from travelling wave (TW).

In future measurements, trap parameters can be deliberately tuned to operational magic conditions for frequency and intensity [52, 110] to further reduce the lattice light shift uncertainty contribution [52, 58].

a) Yb and Sr clock systematic fractional frequency shifts

	^{171}Yb		^{87}Sr	
Contribution	Shift$\times 10^{18}$	Unc.$\times 10^{18}$	Shift$\times 10^{18}$	Unc.$\times 10^{18}$
Lattice light	6.8	5.2	−2.8	7.9
Blackbody radiation	−32.1	0.5	−54.3	0.9
Zeeman	−77.9	0.7	−116.7	0.7
Collisions	1.1	1.5	−0.9	4.2
Probe light	0.02	0.04	−0.04	0.02
AOM chirp	0.2	0.6	0.0	0.2
Background gas	−1.9	0.3	−5.4	1.6
Doppler	0.0	2.0	0.0	0.5
Servo	0.5	0.9	2.5	1.1
Total	−104.3	6.0	182.8	9.2

b) Ratio uncertainty budget

Contribution	Unc.$\times 10^{18}$
Yb systematic effects	6.0
Sr systematic effects	9.2
Gravitational redshift	0.2
Statistical uncertainty	2.9
Frequency comb	0.4
RF reference	0.7
Total	11.2

Table 4.3: a) Uncertainty budget of the Yb and Sr frequency standards. b) Uncertainty budget of the frequency ratio.

4.4 2019 INRIM Yb clock uncertainty budget

At INRIM we are planning a renewed absolute frequency measurement of the ^{171}Yb $^1S_0$-$^3P_0$ clock transition against the International Atomic Time (TAI). This measurement will take advantage of a renewed evaluation of the Yb clock uncertainty budget, improved by more than a factor 4 from the one evaluated in 2016 [114]. Table 4.4 summarises the different uncertainty contributions.

The budget presented here is supported by the renewed investigations of the lattice light shift and density shift discussed in chapter 3. Other shift evaluations take advantage of results recently published by another research groups [25].

Contribution	Shift$\times 10^{17}$	Unc.$\times 10^{17}$
Lattice light	7.6	0.2
Blackbody radiation room	−235.0	1.2
Blackbody radiation oven	−1.7	0.8
Zeeman	−0.693	0.014
Collisions	−5.9	0.2
Probe light	0.09	0.05
Background gas	−0.53	0.18
DC Stark	−1.6	0.9
Servo	0.0	0.3
Others	0.0	0.6
Gravitational redshift	2599.5	0.3
Total	2361.8	2.8

Table 4.4: Uncertainty budget of the INRIM Yb lattice clock in fractional units as re-evaluated in 2019.

Chapter 5

Conclusion

The optical frequency standards have demonstrated performances which clearly surpass in both accuracy and stability the microwave Cs primary standards. Nowadays absolute frequency measurements of optical frequencies are limited by the realisation of the SI second, and optical frequency ratios have been measured with uncertainties beyond the SI limit. These results have been allowed also by the advent and continuous improvement of technologies for the frequency transfer and comparison, namely the optical frequency comb and the fibre frequency transfer infrastructures. These advances have supported the recommendation of several optical atomic transitions as secondary representations of the second, including the clock transition of neutral ^{171}Yb.

Results achieved by the optical frequency standards have opened the way for defining a roadmap towards the redefinition of the SI second on an optical atomic transition [37]. Requirements for a redefinition are the realisation of optical frequency standards characterised with uncertainties in the low 10^{-18} regime, and their comparison both against the best primary standards available and against other optical standards with similar uncertainties.

The activity of my Ph.D. in Metrology contributes on achieving these milestones. The work has been carried out at INRIM, the Italian National Metrology Institute, and at RIKEN, in Japan. At INRIM we have developed and characterised a ^{171}Yb lattice frequency standard with an uncertainty of 1.6×10^{-16} and we have performed the most accurate absolute frequency measurement of the ^{171}Yb clock transition directly against a Cs fountain primary standard to date, with a fractional uncertainty of 5.9×10^{-16} limited by the Cs standard. This result is already included in the calculation of the CIPM recommended frequency of ^{171}Yb. The work is published in *Metrologia* [114] and it has been included in the journal *Highlights of 2017* collection.

We also performed an optical frequency ratio measurement with the transportable lattice clock based of ^{87}Sr developed at PTB, which was the first demonstration of an in-field measurement for a transportable optical standard. Because

of the limited number of sites connected by the fibre links, transportable clocks represent the alternative solution to perform optical frequency comparisons between clocks independently developed by different institutes, as indicated in the roadmap. The results of this experiment has been published in *Nature Physics* [154].

We then improved the performances of our Yb clock both with updates in the optical setup including a new local oscillator, and investigating the limiting contribution to the clock uncertainty budget, namely the non-linear lattice light frequency shift. We have now characterised the total systematic uncertainty of our standard at 2.8×10^{-17} and we demonstrated improved robustness with $>$ 12 h of unattended continuous operation. We are performing a renewed improved measurement of the Yb absolute frequency.

At RIKEN we characterised a ^{171}Yb lattice frequency standard with a fractional uncertainty of 6.0×10^{-18}, close to the target uncertainty defined in the roadmap for the optical standards to become candidates for a redefinition. This has been possible through a renewed investigation of the lattice light frequency shift, in addition to a renewed investigation of the Zeeman shift and probe light shift. We confirm agreement between the lattice polarizabilities measured independently at INRIM and at RIKEN. We measured the frequency ratio between our Yb clock and the RIKEN ^{87}Sr lattice clock with an uncertainty of 1.1×10^{-17}, which to our knowledge is more accurate than any interspecies frequency ratio published to date.

The Yb/Sr frequency ratios measured at INRIM and at RIKEN add to similar measurements performed either at NMIJ/AIST (Japan) and between the Yb and Sr clocks developed at KRISS (Korea) and NICT (Japan). As a result, this frequency ratio has been independently investigated by four different research groups in the world, providing a deep metrological insight of this quantity as required by the roadmap.

At INRIM we are designing a new ^{171}Yb lattice clock we expect to characterise with an uncertainty $< 10^{-17}$. Besides, with other European partners we are involved in a project aimed at fulfilling additional steps in the roadmap towards the redefinition of the SI second. A network of fibre links connecting several European National Metrology Institutes will allow the simultaneous comparisons of several different optical clocks. The improvement of the clock robustness and automation will increase the clock unattended uptime and long term operation, so as to start to regularly contribute to the realisation of National and International time scales.

Appendix A

Characterization of the seismic isolation system at INRIM

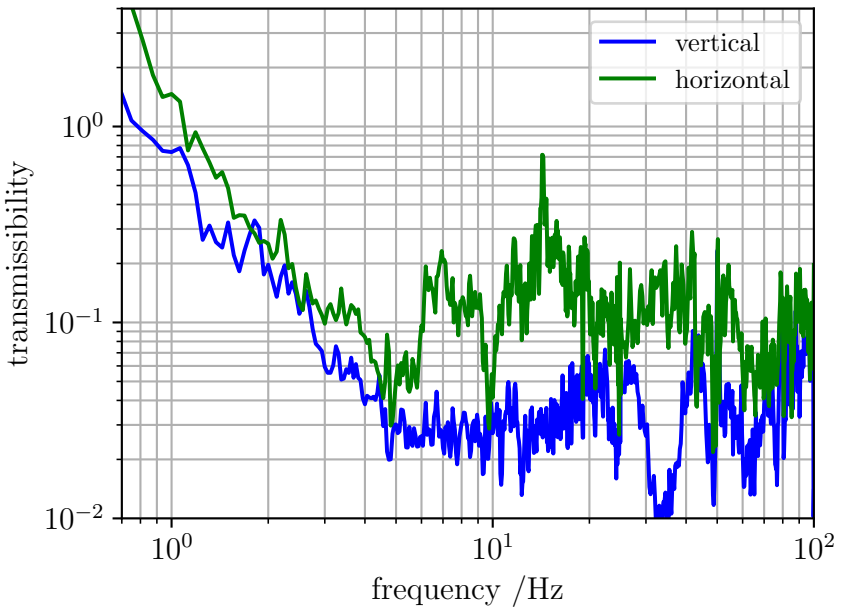

Figure A.1: Performance of the active seismic isolator OSDVIA-T45 in terms of the transmissibility, which is the ratio between the transmitted and the input seismic accelerations shown in figure A.2 and calculated from the seismic velocities measured with the seismometer. Measuremetns are acquired for the vertical axis along gravity and the horizontal axis, orthogonal to gravity.

This appendix provides some details about the performance of the seismic isolation system used at INRIM to improve the stability of the local oscillator reference optical cavity.

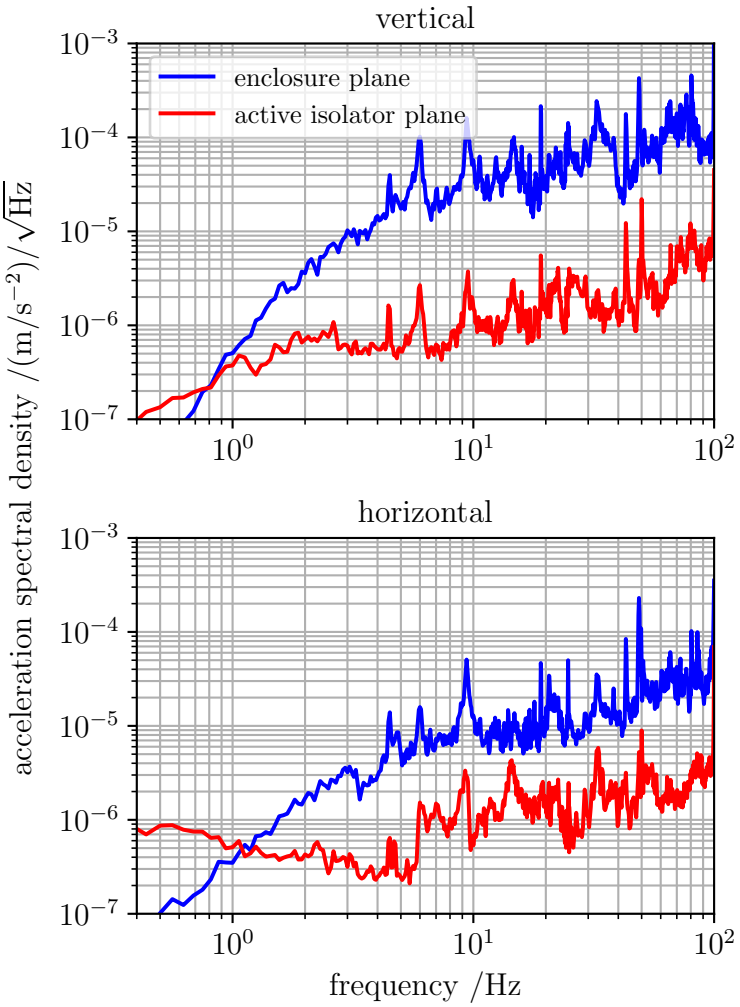

Figure A.2: Acceleration spectral density of the seismic noise measured either with the isolator in operation, or under the blocked mode. In the latter case the measured seismic noise represents the natural noise affecting the floor of the laboratory, where the acoustic enclosure is laying.

The seismic and acoustic noise affecting the cavity are suppressed installing the cavity vacuum package on an active vibration isolation platform (OSDVIA-T45, OptoSigma/DAEIL SYSTEMS) and enclosing the whole system in an acoustic enclosure (AEK-2002, HERZAN) laying directly on the floor. The performance of the active seismic isolator is shown in figure A.1 in terms of the platform transmissibility, defined as the ratio between the seismic acceleration transmitted by the

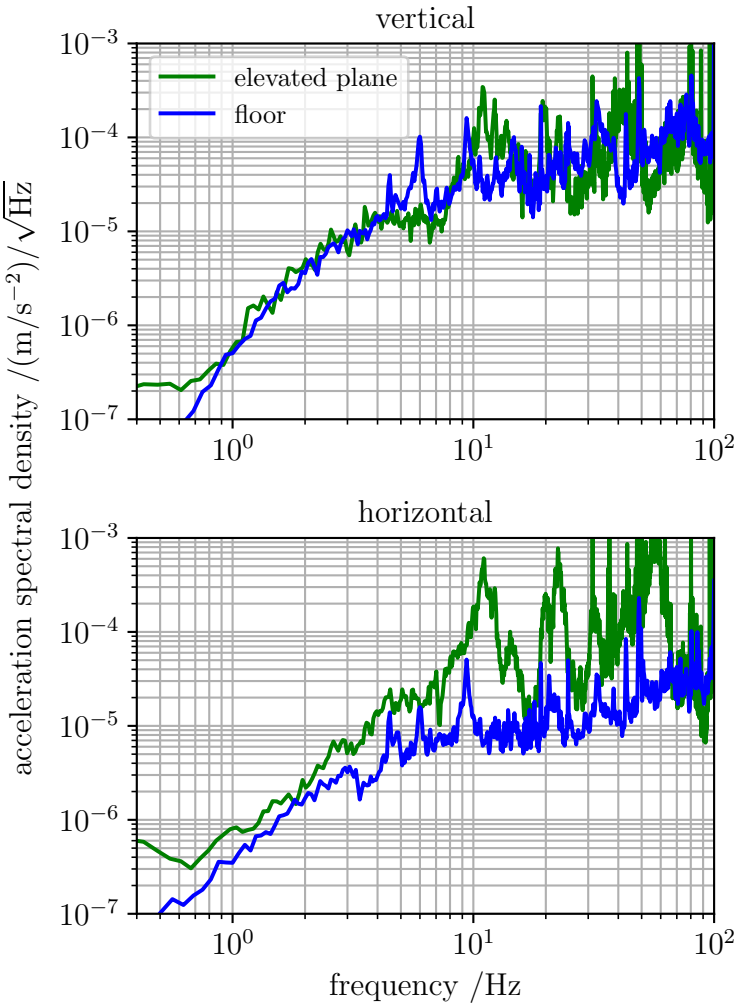

Figure A.3: Acceleration spectral density of the seismic noise on the acoustic enclosure elevated from the floor by ~ 75 cm compared to that of the floor.

isolator and the input seismic acceleration. Seismic noise is measured with a three-axes seismometer (LE-3Dlite, Lennartz Electronics), whose electric response signal transduction factor is 400 V/(m/s). Since the isolator can be hard blocked when turned off, the measurements are carried leaving the isolator on the platform and setting the isolator operation either as ON or as OFF and blocked. The individual absolute measurements of the seismic acceleration in the two conditions are shown in figure A.2.

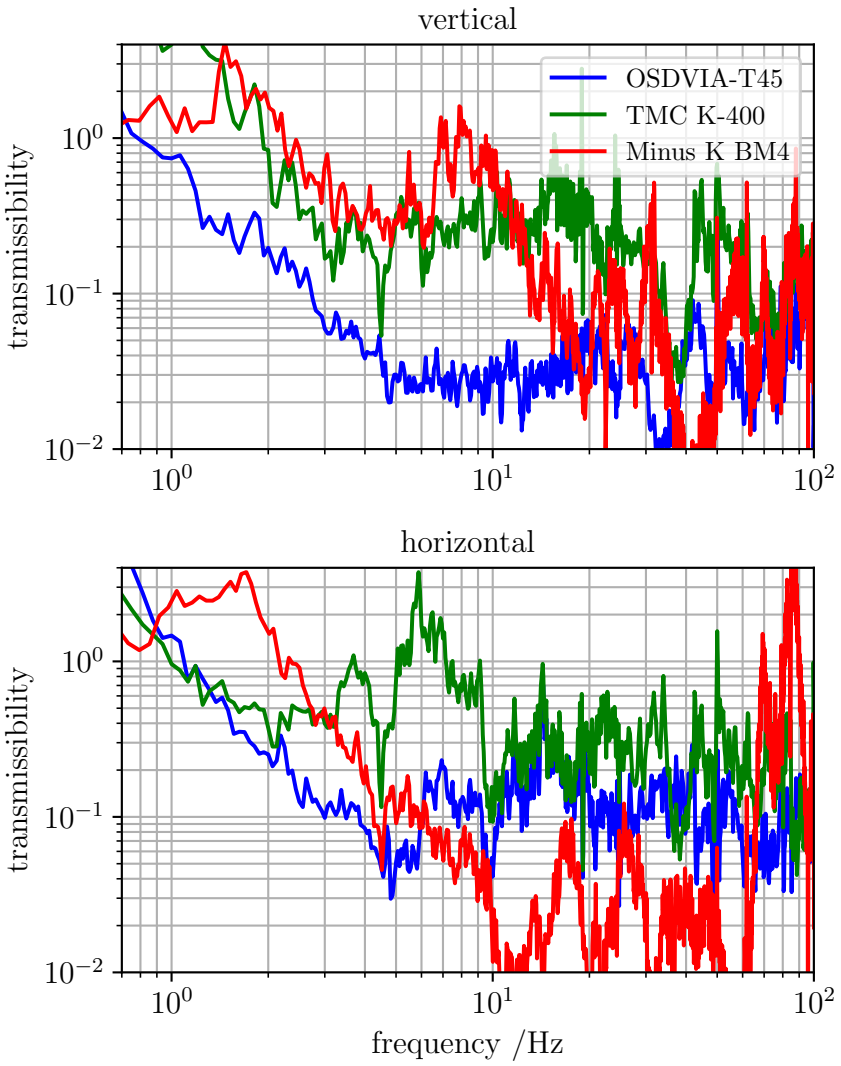

Figure A.4: Comparison of the performances in terms of transmissibility of different tested seismic isolators.

According to the manufacturer specifications[a], the isolator should start suppressing the seismic noise at 0.6 Hz, and reach an attenuation > 98 % at 10 Hz for the vertical axis (no data is available for the horizontal axis). A small disagreement of the measured performance from the expectation may be due to a non-ideal distribution of the payload on the platform plate: the centre of mass should be placed at the centre of the plate, that is non-trivial because of the complexity of

[a] https://america.optosigma.com/active-vibration-isolation-systems-13619.html

the vacuum and optical setup. Besides, we use as the input seismic noise the natural noise affecting the floor of the laboratory, while a proper performance measurement would have required the generation of a simulated strong broadband seismic noise to enhance the measurement resolution.

The acoustic enclosure was originally supported on four legs 75 cm high. In this condition we measure the seismic noise on the enclosure plate and compare the result with the floor noise, we observe that the enclosure supporting legs were introducing significant noise along the horizontal axis, as shown in figure A.3, thus they were removed laying the enclosure directly on the floor.

Figure A.4 shows the comparison of the performance of different seismic isolators. In addition to the OSDVIA-T45 isolator, we test the active isolator Everstill K-400 manufactured by TMC and the passive isolator BM4 manufactured by Minus K. The passive isolator shows a resonance frequency at about 1.5 Hz which deteriorates its performance in the range 1 Hz to 10 Hz, and it shows satisfactory performance at higher frequencies, even better than the active isolators as far as the horizontal isolation is concerned. Passive isolators can be fine tuned in terms of stiffness of the spring constants and weight balance to reduce the resonance frequency, however the process is non-trivial and it may be impossible to reduce the resonance frequency below a certain level. Passive isolator producers like Minus K or HERZ now claim systems with resonance frequency below 0.5 Hz, able to compete and eventually outperform active isolators.

Active isolators have the advantage against passive systems of a much simpler and reliable operation; they usually provide isolation starting from 0.5 Hz to 1 Hz, and they behave as passive isolators beyond 40 Hz. The TMC isolator we test does not match the performance declared by the producer's specifications, which claim a seismic noise attenuation starting at 0.6 Hz and an isolation > 97 % at frequencies > 4 Hz. We find that the isolator transport for the shipment is critical and led to some damages of the system, which we think may explain the difference in the measurement results.

Bibliography

[1] Boureau International des Poids et Mesures (BIPM), ed. *SI Brochure: The International System of Units (SI) [Draft of the 9th edition]*. 2019. eprint: https://www.bipm.org/utils/en/pdf/si-revised-brochure/Draft-SI-Brochure-2019.pdf (cit. on p. 1).

[2] Bureau International des Poids et Mesures (BIPM), ed. *SI Brochure: The International System of Units (SI) [8th edition]*. Bureau International des Poids et Mesures. http://www.bipm.org/en/publications/si-brochure/second.html. 2006. eprint: https://www.bipm.org/utils/common/pdf/si_brochure_8.pdf (cit. on p. 1).

[3] Andreas Bauch. «Caesium atomic clocks: function, performance and applications». In: *Meas. Sci. Technol.* 14.8 (July 2003), pp. 1159–1173. DOI: 10.1088/0957-0233/14/8/301 (cit. on p. 1).

[4] A. Bauch, S. Weyers, D. Piester, E. Staliuniene, and W. Yang. «Generation of UTC(PTB) as a fountain-clock based time scale». In: *Metrologia* 49.3 (2012), pp. 180–188. DOI: 10.1088/0026-1394/49/3/180 (cit. on p. 1).

[5] G. D. Rovera, S. Bize, B. Chupin, J. Guéna, Ph. Laurent, P. Rosenbusch, P. Uhrich, and M. Abgrall. «UTC(OP) based on LNE-SYRTE atomic fountain primary frequency standards». In: *Metrologia* 53.3 (2016), S81–S88. DOI: 10.1088/0026-1394/53/3/s81 (cit. on p. 1).

[6] Gérard Petit, Felicitas Arias, and Gianna Panfilo. «International atomic time: Status and future challenges». In: *Comptes Rendus Physique* 16.5 (2015), pp. 480–488. DOI: 10.1016/j.crhy.2015.03.002 (cit. on p. 1).

[7] Gianna Panfilo, Aurelie Harmegnies, and Laurent Tisserand. «A new prediction algorithm for the generation of International Atomic Time». In: *Metrologia* 49.1 (2011), pp. 49–56. DOI: 10.1088/0026-1394/49/1/008 (cit. on p. 1).

[8] Comité Consultatif des Longueurs. *2004 Report of the 11th meeting (11–12 September 2003) to the International Committee for Weights and Measures*. Comité international des poids et mesures (CIPM), 2003 (cit. on p. 2).

[9] V. Gerginov, N. Nemitz, S. Weyers, R. Schröder, D. Griebsch, and R. Wynands. «Uncertainty evaluation of the caesium fountain clock PTB-CSF2». In: *Metrologia* 47.1 (2009), pp. 65–79. DOI: 10.1088/0026-1394/47/1/008 (cit. on p. 2).

[10] J. Guena, P. Rosenbusch, P. Laurent, M. Abgrall, D. Rovera, G. Santarelli, M. E. Tobar, S. Bize, and A. Clairon. «Demonstration of a dual alkali Rb/Cs fountain clock». In: *IEEE Transactions on Ultrasonics, Ferroelectrics and Frequency Control* 57.3 (2010), pp. 647–653. DOI: 10.1109/tuffc.2010.1461 (cit. on p. 2).

[11] Ruoxin Li, Kurt Gibble, and Krzysztof Szymaniec. «Improved accuracy of the NPL-CsF2 primary frequency standard: evaluation of distributed cavity phase and microwave lensing frequency shifts». In: *Metrologia* 48.5 (2011), pp. 283–289. DOI: 10.1088/0026-1394/48/5/007 (cit. on p. 2).

[12] Yu. S. Domnin, V. N. Baryshev, A. I. Boyko, G. A. Elkin, A. V. Novoselov, L. N. Kopylov, and D. S. Kupalov. «The MTsR-F2 fountain-type cesium frequency standard». In: *Measurement Techniques* 55.10 (2012), pp. 1155–1162. DOI: 10.1007/s11018-012-0102-0 (cit. on p. 2).

[13] Filippo Levi, Davide Calonico, Claudio E. Calosso, Aldo Godone, Salvatore Micalizio, and Giovanni A. Costanzo. «Accuracy evaluation of ITCsF2: a nitrogen cooled caesium fountain». In: *Metrologia* 51.3 (May 2014), pp. 270–284. DOI: 10.1088/0026-1394/51/3/270 (cit. on pp. 2, 119).

[14] Thomas P Heavner, Elizabeth A Donley, Filip.po Levi, Giovanni Costanzo, Thomas E Parker, Jon H Shirley, Neil Ashby, Stephan Barlow, and S R Jefferts. «First accuracy evaluation of NIST-F2». In: *Metrologia* 51.3 (2014), pp. 174–182. DOI: 10.1088/0026-1394/51/3/174 (cit. on p. 2).

[15] Fang Fang, Mingshou Li, Pingwei Lin, Weiliang Chen, Nianfeng Liu, Yige Lin, Ping Wang, Kun Liu, Rui Suo, and Tianchu Li. «NIM5 Cs fountain clock and its evaluation». In: *Metrologia* 52.4 (2015), pp. 454–468. DOI: 10.1088/0026-1394/52/4/454 (cit. on p. 2).

[16] Aishik Acharya, Vattikonda Bharath, Poonam Arora, Suchi Yadav, Ashish Agarwal, and Amitava Sen Gupta. «Systematic Uncertainty Evaluation of the Cesium Fountain Primary Frequency Standard at NPL India». In: *MAPAN* 32.1 (2016), pp. 67–76. DOI: 10.1007/s12647-016-0190-4 (cit. on p. 2).

[17] A. Jallageas, L. Devenoges, M. Petersen, J. Morel, L. G. Bernier, D. Schenker, P. Thomann, and T. Südmeyer. «First uncertainty evaluation of the FoCS-2 primary frequency standard». In: *Metrologia* 55.3 (2018), pp. 366–385. DOI: 10.1088/1681-7575/aab3fa (cit. on p. 2).

[18] Bureau International des Poids et Mesures (BIPM) Time Department FTP server, ed. *Circular T 373*. Feb. 2019. eprint: https://www.bipm.org/en/bipm-services/timescales/time-ftp/Circular-T.html (cit. on p. 2).

[19] Scott A. Diddams, David J. Jones, Jun Ye, Steven T. Cundiff, John L. Hall, Jinendra K. Ranka, Robert S. Windeler, Ronald Holzwarth, Thomas Udem, and T. W. Hänsch. «Direct Link between Microwave and Optical Frequencies with a 300 THz Femtosecond Laser Comb». In: *Phys. Rev. Lett.* 84 (22 May 2000), pp. 5102–5105. DOI: 10.1103/PhysRevLett.84.5102 (cit. on p. 3).

[20] D. J. Wineland and Wayne M. Itano. «Laser cooling of atoms». In: *Phys. Rev. A* 20 (4 Oct. 1979), pp. 1521–1540. DOI: 10.1103/PhysRevA.20.1521 (cit. on pp. 4, 68).

[21] Harold J. Metcalf and Peter Van der Straten. *Laser cooling and trapping*. Springer Science & Business Media, 1999. DOI: 10.1007/978-1-4612-1470-0 (cit. on pp. 4, 12, 15).

[22] F. Diedrich, J. C. Bergquist, Wayne M. Itano, and D. J. Wineland. «Laser Cooling to the Zero-Point Energy of Motion». In: *Phys. Rev. Lett.* 62 (4 Jan. 1989), pp. 403–406. DOI: 10.1103/PhysRevLett.62.403 (cit. on p. 4).

[23] Hidetoshi Katori, Masao Takamoto, V. G. Pal'chikov, and V. D. Ovsiannikov. «Ultrastable Optical Clock with Neutral Atoms in an Engineered Light Shift Trap». In: *Phys. Rev. Lett.* 91 (17 Oct. 2003), p. 173005. DOI: 10.1103/PhysRevLett.91.173005 (cit. on pp. 4, 10, 57).

[24] Ichiro Ushijima, Masao Takamoto, Manoj Das, Takuya Ohkubo, and Hidetoshi Katori. «Cryogenic optical lattice clocks». In: *Nat. Photonics* 9.3 (Feb. 2015), pp. 185–189. DOI: 10.1038/nphoton.2015.5 (cit. on pp. 4, 36–38, 42, 89).

[25] W. F. McGrew, X. Zhang, R. J. Fasano, S. A. Schäffer, K. Beloy, D. Nicolodi, R. C. Brown, N. Hinkley, G. Milani, M. Schioppo, T. H. Yoon, and A. D. Ludlow. «Atomic clock performance enabling geodesy below the centimetre level». In: *Nature* 564.7734 (2018), pp. 87–90. DOI: 10.1038/s41586-018-0738-2. arXiv: arXiv:1807.11282 [physics.atom-ph] (cit. on pp. 4, 5, 45, 50, 51, 85, 86, 90, 99, 102, 134).

[26] Christian Sanner, Nils Huntemann, Richard Lange, Christian Tamm, Ekkehard Peik, Marianna S. Safronova, and Sergey G. Porsev. «Optical clock comparison for Lorentz symmetry testing». In: *Nature* 567.7747 (2019), pp. 204–208. DOI: 10.1038/s41586-019-0972-2. arXiv: arXiv:1809.10742 [physics.atom-ph] (cit. on p. 4).

[27] M. Schioppo, R. C. Brown, W. F. McGrew, N. Hinkley, R. J. Fasano, K. Beloy, T. H. Yoon, G. Milani, D. Nicolodi, J. A. Sherman, N. B. Phillips, C. W. Oates, and A. D. Ludlow. «Ultrastable optical clock with two cold-atom ensembles». In: *Nat. Photonics* 11 (Jan. 2017), pp. 48–52. DOI: 10.1038/nphoton.2016.231. arXiv: 1607.06867 [physics.atom-ph] (cit. on pp. 4, 25).

[28] E. Oelker, R. B. Hutson, C. J. Kennedy, L. Sonderhouse, T. Bothwell, A. Goban, D. Kedar, C. Sanner, J. M. Robinson, G. E. Marti, D. G. Matei, T. Legero, M. Giunta, R. Holzwarth, F. Riehle, U. Sterr, and J. Ye. «Demonstration of 4.8×10^{-17} stability at 1 s for two independent optical clocks». In: *Nat. Photonics* (Feb. 7, 2019). DOI: 10.1038/s41566-019-0493-4. arXiv: arXiv:1902.02741 [physics.atom-ph] (cit. on pp. 4, 25).

[29] Antoine Rolland, Peng Li, Naoya Kuse, Jie Jiang, Marco Cassinerio, Carsten Langrock, and Martin E. Fermann. «Ultra-broadband dual-branch optical frequency comb with 10^{-18} instability». In: *Optica* 5.9 (2018), p. 1070. DOI: 10.1364/optica.5.001070 (cit. on p. 5).

[30] Long-Sheng Ma, Peter Jungner, Jun Ye, and John L. Hall. «Delivering the same optical frequency at two places: accurate cancellation of phase noise introduced by an optical fiber or other time-varyingpath». In: *Opt. Lett.* 19.21 (Nov. 1994), pp. 1777–1779. DOI: 10.1364/OL.19.001777 (cit. on pp. 5, 111).

[31] Anna Tampellini. «Coherent fibre-optic link: applications in Time and Frequency metrology, Geodesy, Radio Astronomy and Seismology». PhD thesis. Politecnico di Torino, 2019. eprint: http://hdl.handle.net/11583/2742522 (cit. on p. 5).

[32] C. Lisdat, G. Grosche, N. Quintin, C. Shi, S. M. F. Raupach, C. Grebing, D. Nicolodi, F. Stefani, A. Al-Masoudi, S. Dörscher, S. Häfner, J.-L. Robyr, N. Chiodo, S. Bilicki, E. Bookjans, A. Koczwara, S. Koke, A. Kuhl, F. Wiotte, F. Meynadier, E. Camisard, M. Abgrall, M. Lours, T. Legero, H. Schnatz, U. Sterr, H. Denker, C. Chardonnet, Y. Le Coq, G. Santarelli, A. Amy-Klein, R. Le Targat, J. Lodewyck, O. Lopez, and P.-E. Pottie. «A clock network for geodesy and fundamental science». In: *Nat. Commun.* 7 (Aug. 2016), p. 12443. DOI: 10.1038/ncomms12443 (cit. on pp. 5, 125).

[33] M. Soffel, S. A. Klioner, G. Petit, P. Wolf, S. M. Kopeikin, P. Bretagnon, V. A. Brumberg, N. Capitaine, T. Damour, T. Fukushima, B. Guinot, T.-Y. Huang, L. Lindegren, C. Ma, K. Nordtvedt, J. C. Ries, P. K. Seidelmann, D. Vokrouhlick, C. M. Will, and C. Xu. «The IAU 2000 Resolutions for Astrometry, Celestial Mechanics, and Metrology in the Relativistic Framework: Explanatory Supplement». In: *The Astronomical Journal* 126.6 (2003), pp. 2687–2706. DOI: 10.1086/378162 (cit. on pp. 5, 117).

[34] Gérard Petit and Brian Luzum. *IERS Conventions (2010)*. Tech. rep. International Earth Rotation and Reference Systems Service (IERS), 2010. eprint: https://www.iers.org/IERS/EN/Publications/TechnicalNotes/tn36.html/ (cit. on p. 5).

[35] Heiner Denker, Ludger Timmen, Christian Voigt, Stefan Weyers, Ekkehard Peik, Helen S. Margolis, Pacôme Delva, Peter Wolf, and Gérard Petit. «Geodetic methods to determine the relativistic redshift at the level of 10^{-18} in the context of international timescales: a review and practical results». In: *J. Geod.* 92.5 (2017), pp. 487–516. DOI: 10.1007/s00190-017-1075-1 (cit. on pp. 5, 116, 117).

[36] S. M. Brewer, J.-S. Chen, A. M. Hankin, E. R. Clements, C. W. Chou, D. J. Wineland, D. B. Hume, and D. R. Leibrandt. «$^{27}Al^+$ Quantum-Logic Clock with a Systematic Uncertainty below 10^{-18}». In: *Phys. Rev. Lett.* 123.3 (2019). DOI: 10.1103/PhysRevLett.123.033201. arXiv: http://arxiv.org/abs/1902.07694v1 [physics.atom-ph] (cit. on p. 5).

[37] Fritz Riehle, Patrick Gill, Felicitas Arias, and Lennart Robertsson. «The CIPM list of recommended frequency standard values: guidelines and procedures». In: *Metrologia* 55.2 (Feb. 2018). DOI: https://doi.org/10.1088/1681-7575/aaa302 (cit. on pp. 6, 137).

[38] C. Grebing, A. Al-Masoudi, S. Dörscher, S. Häfner, V. Gerginov, S. Weyers, B. Lipphardt, F. Riehle, U. Sterr, and C. Lisdat. «Realization of a time-scale with an optical clock». In: *Optica* 3.6 (May 2015), p. 563. DOI: 10.1364/optica.3.000563 (cit. on p. 6).

[39] Jérôme Lodewyck, Sławomir Bilicki, Eva Bookjans, Jean-Luc Robyr, Chunyan Shi, Grégoire Vallet, Rodolphe Le Targat, Daniele Nicolodi, Yann Le Coq, Jocelyne Guéna, Michel Abgrall, Peter Rosenbusch, and Sébastien Bize. «Optical to microwave clock frequency ratios with a nearly continuous strontium optical lattice clock». In: *Metrologia* 53.4 (2016), pp. 1123–1130. DOI: 10.1088/0026-1394/53/4/1123 (cit. on p. 6).

[40] Hidekazu Hachisu, Gérard Petit, Fumimaru Nakagawa, Yuko Hanado, and Tetsuya Ido. «SI-traceable measurement of an optical frequency at the low 10^-16 level without a local primary standard». In: *Optics Express* 25.8 (2017), p. 8511. DOI: 10.1364/oe.25.008511 (cit. on p. 6).

[41] Hidekazu Hachisu, Fumimaru Nakagawa, Yuko Hanado, and Tetsuya Ido. «Months-long real-time generation of a time scale based on an optical clock». In: *Scientific Reports* 8.1 (Mar. 2018). DOI: 10.1038/s41598-018-22423-5 (cit. on p. 6).

[42] W. F. McGrew, X. Zhang, H. Leopardi, R. J. Fasano, D. Nicolodi, K. Beloy, J. Yao, J. A. Sherman, S. A. Schäffer, J. Savory, R. C. Brown, S. Römisch, C. W. Oates, T. E. Parker, T. M. Fortier, and A. D. Ludlow. «Towards the optical second: verifying optical clocks at the SI limit». In: *Optica* 6.4 (2019), p. 448. DOI: 10.1364/optica.6.000448. arXiv: arXiv:1811.05885 [physics.atom-ph] (cit. on pp. 6, 120).

[43] Jian Yao, Jeff A. Sherman, Tara Fortier, Holly Leopardi, Thomas Parker, William McGrew, Xiaogang Zhang, Daniele Nicolodi, Robert Fasano, Stefan Schäffer, Kyle Beloy, Joshua Savory, Stefania Romisch, Chris Oates, Scott Diddams, Andrew Ludlow, and Judah Levine. «Optical-Clock-Based Time Scale». In: (Feb. 19, 2019). arXiv: http://arxiv.org/abs/1902.06858v1 [physics.app-ph] (cit. on p. 6).

[44] Sergey G. Porsev, Andrei Derevianko, and E. N. Fortson. «Possibility of an optical clock using the $6^1S_0 \rightarrow 6^3P_0^o$ transition in ^{171,173}Yb atoms held in an optical lattice». In: *Phys. Rev. A* 69.2, 021403 (2 Feb. 2004), p. 021403. DOI: 10.1103/PhysRevA.69.021403. arXiv: http://arxiv.org/abs/physics/0402124v2 [physics.atom-ph] (cit. on pp. 9, 45).

[45] V. A. Dzuba, V. V. Flambaum, and S. Schiller. «Testing physics beyond the standard model through additional clock transitions in neutral ytterbium». In: *Phys. Rev. A* 98.2 (2018), p. 022501. DOI: 10.1103/PhysRevA.98.022501 (cit. on p. 9).

[46] M. S. Safronova, S. G. Porsev, Christian Sanner, and Jun Ye. «Two Clock Transitions in Neutral Yb for the Highest Sensitivity to Variations of the Fine-Structure Constant». In: *Phys. Rev. Lett.* 120.17 (Apr. 2018), p. 173001. DOI: 10.1103/PhysRevLett.120.173001 (cit. on p. 9).

[47] C.-Y. Xu, J. Singh, J. C. Zappala, K. G. Bailey, M. R. Dietrich, J. P. Greene, W. Jiang, N. D. Lemke, Z.-T. Lu, P. Mueller, and T. P. O'Connor. «Measurement of the Hyperfine Quenching Rate of the Clock Transition in ^{171}Yb». In: *Phys. Rev. Lett.* 113 (3 July 2014), p. 033003. DOI: 10.1103/PhysRevLett.113.033003 (cit. on pp. 9, 75, 80).

[48] Rudolf Grimm, Matthias Weidemüller, and Yurii B. Ovchinnikov. «Optical Dipole Traps for Neutral Atoms». In: *Advances In Atomic, Molecular, and Optical Physics*. Ed. by Benjamin Bederson and Herbert Walther. Vol. 42. Advances In Atomic, Molecular, and Optical Physics. Elsevier, 2000, pp. 95–170. DOI: 10.1016/S1049-250X(08)60186-X. arXiv: arXiv:physics/9902072 [physics.atom-ph] (cit. on pp. 10, 53, 54, 101, 103).

[49] R. H. Dicke. «The Effect of Collisions upon the Doppler Width of Spectral Lines». In: *Phys. Rev.* 89.2 (Jan. 1953), pp. 472–473. DOI: 10.1103/PhysRev.89.472 (cit. on pp. 11, 111).

[50] Hidetoshi Katori, Koji Hashiguchi, E. Yu. Il'inova, and V. D. Ovsiannikov. «Magic Wavelength to Make Optical Lattice Clocks Insensitive to Atomic Motion». In: *Phys. Rev. Lett.* 103 (15 Oct. 2009), p. 153004. DOI: 10.1103/PhysRevLett.103.153004 (cit. on p. 11).

[51] R. C. Brown, N. B. Phillips, K. Beloy, W. F. McGrew, M. Schioppo, R. J. Fasano, G. Milani, X. Zhang, N. Hinkley, H. Leopardi, T. H. Yoon, D. Nicolodi, T. M. Fortier, and A. D. Ludlow. «Hyperpolarizability and Operational Magic Wavelength in an Optical Lattice Clock». In: *Phys. Rev. Lett.* 119.25 (25 Dec. 2017), p. 253001. DOI: 10.1103/PhysRevLett.119.253001 (cit. on pp. 12, 65, 66, 73, 90).

[52] Ichiro Ushijima, Masao Takamoto, and Hidetoshi Katori. «Operational Magic Intensity for Sr Optical Lattice Clocks». In: *Phys. Rev. Lett.* 121.26 (2018). DOI: 10.1103/PhysRevLett.121.263202 (cit. on pp. 12, 66, 90, 133).

[53] Takuya Ohkubo. «Frequency ratio measurement of ytterbium/strontium optical lattice clocks». PhD thesis. University of Tokyo, 2016 (cit. on pp. 12, 36, 42).

[54] B. Rauf, M. C. Vélez López, P. Thoumany, M. Pizzocaro, and D. Calonico. «Phase noise cancellation in polarisation-maintaining fibre links». In: *Rev. Sci. Instrum.* 89.3 (Mar. 2018), p. 033103. DOI: 10.1063/1.5016514 (cit. on pp. 12, 112).

[55] Gianmaria Milani. «Realization of advanced ^{171}Yb optical lattice frequency standard». PhD thesis. Politecnico di Torino, 2018. eprint: http://hdl.handle.net/11583/2706635 (cit. on pp. 12, 29, 101, 102, 109, 110).

[56] W. Neuhauser, M. Hohenstatt, P. Toschek, and H. Dehmelt. «Optical-Sideband Cooling of Visible Atom Cloud Confined in Parabolic Well». In: *Phys. Rev. Lett.* 41.4 (1978), pp. 233–236. DOI: 10.1103/physrevlett.41.233 (cit. on p. 13).

[57] Ryotatsu Yanagimoto. «(BSc) Characterization of collisional shifts in optical lattice clocks based on asymmetries in the Ramsey spectrum». Bachelor thesis. University of Tokyo, 2017 (cit. on pp. 14, 15, 91, 96).

[58] Nils Nemitz, Asbjørn Arvad Jørgensen, Ryotatsu Yanagimoto, Filippo Bregolin, and Hidetoshi Katori. «Modeling light shifts in optical lattice clocks». In: *Phys. Rev. A* 99.3 (2019). DOI: 10.1103/physreva.99.033424 (cit. on pp. 15, 40, 58–60, 65, 66, 69–71, 73, 98, 104, 129, 133).

[59] G. J. Dick, J. D. Prestage, C. A. Greenhall, and L. Maleki. «Local Oscillator Induced Degradation of Medium-Term Stability in Passive Atomic Frequency Standards». In: *22nd Annual Precise Time and Time Interval (PTTI) Applications and Planning Meeting*. May 1990, pp. 487–508 (cit. on pp. 18, 78, 79).

[60] G. Santarelli, C. Audoin, A. Makdissi, P. Laurent, G. J. Dick, and C. Clairon. «Frequency stability degradation of an oscillator slaved to a periodically interrogated atomic resonator». In: *Ultrasonics, Ferroelectrics, and Frequency Control, IEEE Transactions on* 45.4 (July 1998), pp. 887–894. DOI: 10.1109/58.710548 (cit. on pp. 18, 20, 24).

[61] G. J. Dick. «Local Oscillator Induced Instabilities in Trapped Ion Frequency Standards». In: *19th Annual Precise Time and Time Interval (PTTI) Applications and Planning Meeting*. Ed. by R. L. Sydnor. US Naval Observatory/Goddard Space Flight Center. Dec. 1987, pp. 133–147. eprint: http://www.dtic.mil/docs/citations/ADA502386 (cit. on pp. 18, 22, 24).

[62] D. B. Sullivan, D. W. Allan, D. A. Howe, and F. L. Walls. *NIST Technical Note 1337: Characterization of Clocks and Oscillators*. Tech. rep. National Institute of Strandard and Technology, 1990. eprint: https://tf.nist.gov/general/pdf/868.pdf (cit. on p. 21).

[63] Fritz Riehle. *Frequency Standards: Basics and Applications*. Wiley-VCH, 2004. ISBN: 3-527-40230-6 (cit. on pp. 21, 22).

[64] Andrew D. Ludlow, Martin M. Boyd, Jun Ye, E. Peik, and P. O. Schmidt. «Optical atomic clocks». In: *Rev. Mod. Phys.* 87.2 (June 2015), pp. 637–701. DOI: 10.1103/RevModPhys.87.637 (cit. on p. 21).

[65] W. M. Itano, J. C. Bergquist, J. J. Bollinger, J. M. Gilligan, D. J. Heinzen, F. L. Moore, M. G. Raizen, and D. J. Wineland. «Quantum projection noise: Population fluctuations in two-level systems». In: *Phys. Rev. A* 47 (5 May 1993), pp. 3554–3570. DOI: 10.1103/PhysRevA.47.3554 (cit. on pp. 22, 23, 131).

[66] G. Santarelli, Ph. Laurent, P. Lemonde, A. Clairon, A. G. Mann, S. Chang, A. N. Luiten, and C. Salomon. «Quantum Projection Noise in an Atomic Fountain: A High Stability Cesium Frequency Standard». In: *Phys. Rev. Lett.* 82.23 (1999), pp. 4619–4622. DOI: 10.1103/physrevlett.82.4619 (cit. on pp. 23, 24).

[67] Masao Takamoto, Tetsushi Takano, and Hidetoshi Katori. «Frequency comparison of optical lattice clocks beyond the Dick limit». In: *Nat. Photonics* 5 (May 2011), pp. 288–292. DOI: doi:10.1038/nphoton.2011.34 (cit. on pp. 24, 26, 131).

[68] Pasquale Maddaloni, Marco Bellini, and Paolo De Natale. *Laser-Based Measurements for Time and Frequency Domain Applications: A Handbook*. Series in Optics and Optoelectronics. CRC Press, 2013 (cit. on p. 24).

[69] M. Pizzocaro, G. A. Costanzo, A. Godone, F. Levi, A. Mura, M. Zoppi, and D. Calonico. «Realization of an ultrastable 578-nm laser for an Yb lattice clock». In: *IEEE Transactions on Ultrasonics, Ferroelectrics and Frequency Control* 59.3 (Mar. 2012), pp. 426–431. DOI: 10.1109/tuffc.2012.2211 (cit. on pp. 25, 32–34).

[70] G. Vallet, E. Bookjans, U. Eismann, S. Bilicki, R. Le Targat, and J. Lodewyck. «A noise-immune cavity-assisted non-destructive detection for an optical lattice clock in the quantum regime». In: *New J. Phys.* 19.8 (Aug. 2017), p. 083002. DOI: 10.1088/1367-2630/aa7c84 (cit. on p. 25).

[71] T. Nazarova, F. Riehle, and U. Sterr. «Vibration-insensitive reference cavity for an ultra-narrow-linewidth laser». English. In: *Appl. Phys. B* 83.4 (2006), pp. 531–536. ISSN: 0946-2171. DOI: 10.1007/s00340-006-2225-y (cit. on p. 25).

[72] S. A. Webster, M. Oxborrow, S. Pugla, J. Millo, and P. Gill. «Thermal-noise-limited optical cavity». In: *Phys. Rev. A* 77 (3 Mar. 2008), p. 033847. DOI: 10.1103/PhysRevA.77.033847 (cit. on p. 25).

[73] W. Zhang, J. M. Robinson, L. Sonderhouse, E. Oelker, C. Benko, J. L. Hall, T. Legero, D. G. Matei, F. Riehle, U. Sterr, and J. Ye. «Ultrastable Silicon Cavity in a Continuously Operating Closed-Cycle Cryostat at 4 K». In: *Phys. Rev. Lett.* 119.24 (Dec. 2017). DOI: 10.1103/PhysRevLett.119.243601 (cit. on p. 25).

[74] Kenji Numata, Amy Kemery, and Jordan Camp. «Thermal-Noise Limit in the Frequency Stabilization of Lasers with Rigid Cavities». In: *Phys. Rev. Lett.* 93 (25 Dec. 2004), p. 250602. DOI: 10.1103/PhysRevLett.93.250602 (cit. on p. 25).

[75] D. G. Matei, T. Legero, S. Häfner, C. Grebing, R. Weyrich, W. Zhang, L. Sonderhouse, J. M. Robinson, J. Ye, F. Riehle, and U. Sterr. «1.5 µm Lasers with Sub-10 mHz Linewidth». In: *Phys. Rev. Lett.* 118 (26 June 2017), p. 263202. DOI: 10.1103/PhysRevLett.118.263202 (cit. on p. 25).

[76] S. Bize, Y. Sortais, P. Lemonde, S. Zhang, P. Laurent, G. Santarelli, C. Salomon, and A. Clairon. «Interrogation oscillator noise rejection in the comparison of atomic fountains». In: *IEEE Trans. Ultrason. Ferroelectr. Freq. Control* 47.5 (Sept. 2000), pp. 1253–1255. DOI: 10.1109/58.869073 (cit. on pp. 26, 131).

[77] M. Schioppo, N. Poli, M. Prevedelli, St. Falke, Ch. Lisdat, U. Sterr, and G. M. Tino. «A compact and efficient strontium oven for laser-cooling experiments». In: *Rev. Sci. Instrum.* 83.10, 103101 (Oct. 2012), p. 103101. DOI: 10.1063/1.4756936 (cit. on pp. 26, 36, 89).

[78] Marco Pizzocaro. «Realization and characterization of optical frequency standards». PhD thesis. Politecnico di Torino, 2013. eprint: https://iris.polito.it/retrieve/handle/11583/2506152/59294/phdthesis-archive%20me.pdf (cit. on pp. 27, 33, 54).

[79] J. Huckans, W. Dubosclard, E. Maréchal, O. Gorceix, B. Laburthe-Tolra, and M. Robert de Saint-Vincent. «Note on the reflectance of mirrors exposed to a strontium beam». In: (Feb. 23, 2018). arXiv: http://arxiv.org/abs/1802.08499v2 [physics.atom-ph] (cit. on p. 27).

[80] B. J. Bloom, T. L. Nicholson, J. R. Williams, S. L. Campbell, M. Bishof, X. Zhang, W. Zhang, L. Bromley, and J. Ye. «An optical lattice clock with accuracy and stability at the 10^{-18} level». In: *Nature* 506.7486 (Jan. 2014), pp. 71–75. DOI: 10.1038/nature12941 (cit. on p. 29).

[81] Wolfgang Demtröder. *Laser Spectroscopy. Vol. 1: Basic Principles*. Vol. 56. Springer-Verlag Berlin Heidelberg, Oct. 2008, pp. 487–488. DOI: 10.1080/00107514.2015.1065907 (cit. on p. 29).

[82] Marco Pizzocaro, Davide Calonico, Pablo Cancio Pastor, Jacopo Catani, Giovanni A. Costanzo, Filippo Levi, and Luca Lorini. «Efficient frequency doubling at 399 nm». In: *Appl. Opt.* 53.16 (June 2014), pp. 3388–3392. DOI: 10.1364/AO.53.003388 (cit. on p. 29).

[83] T. W. Hänsch and B. Couillaud. «Laser frequency stabilization by polarization spectroscopy of a reflecting reference cavity». In: *Opt. Commun.* 35.3 (1980), pp. 441–444. ISSN: 0030-4018. DOI: 10.1016/0030-4018(80)90069-3 (cit. on p. 29).

[84] Gianmaria Milani, Benjamin Rauf, Piero Barbieri, Filippo Bregolin, Marco Pizzocaro, Pierre Thoumany, Filippo Levi, and Davide Calonico. «Multiple wavelength stabilization on a single optical cavity using the offset sideband locking technique». In: *Opt. Lett.* 42.10 (May 2017), pp. 1970–1973. DOI: 10.1364/OL.42.001970 (cit. on p. 29).

[85] R. W. P. Drever, J. L. Hall, F. V. Kowalski, J. Hough, G. M. Ford, A. J. Munley, and H. Ward. «Laser phase and frequency stabilization using an optical resonator». English. In: *Appl. Phys. B* 31.2 (1983), pp. 97–105. ISSN: 0946-2171. DOI: 10.1007/BF00702605 (cit. on p. 32).

[86] Eric D. Black. «An introduction to Pound-Drever-Hall laser frequency stabilization». In: *Am. J. Phys* 69.1 (2001), pp. 79–87. DOI: 10.1119/1.1286663 (cit. on p. 32).

[87] M. Pizzocaro, D. Calonico, C. Calosso, C. Clivati, G. A. Costanzo, F. Levi, and A. Mura. «Active disturbance rejection control of temperature for ultra-stable optical cavities». In: *IEEE Transactions on Ultrasonics, Ferroelectrics and Frequency Control* 60.2 (Feb. 2013), pp. 273–280. DOI: 10.1109/tuffc.2013.2563 (cit. on p. 33).

[88] Benjamin Rauf. «Absolute frequency measurement of an ^{171}Yb lattice clock and optical clock comparisons». PhD thesis. Politecnico di Torino, 2018. eprint: http://hdl.handle.net/11583/2708557 (cit. on p. 34).

[89] S. Blatt, J. W. Thomsen, G. K. Campbell, A. D. Ludlow, M. D. Swallows, M. J. Martin, M. M. Boyd, and J. Ye. «Rabi spectroscopy and excitation inhomogeneity in a one-dimensional optical lattice clock». In: *Phys. Rev. A* 80.5 (5 Nov. 2009), p. 052703. DOI: 10.1103/PhysRevA.80.052703 (cit. on pp. 35, 67–69, 91, 92).

[90] J. Lodewyck, M. Zawada, L. Lorini, M. Gurov, and P. Lemonde. «Observation and cancellation of a perturbing DC stark shift in strontium optical lattice clocks». In: *IEEE Trans. Ultrason., Ferroelectr., Freq. Control* 59.3 (2012), pp. 411–415. DOI: 10.1109/TUFFC.2012.2209 (cit. on p. 38).

[91] V. A. Dzuba and A. Derevianko. «Dynamic polarizabilities and related properties of clock states of the ytterbium atom». In: *J. Phys. B: At., Mol. Opt. Phys.* 43.7 (Mar. 2010), p. 074011. DOI: 10.1088/0953-4075/43/7/074011 (cit. on pp. 40, 57, 102).

[92] Kana Iwakuni, Hajime Inaba, Yoshiaki Nakajima, Takumi Kobayashi, Kazumoto Hosaka, Atsushi Onae, and Feng-Lei Hong. «Narrow linewidth comb realized with a mode-locked fiber laser using an intra-cavity waveguide electro-optic modulator for high-speed control». In: *Optics Express* 20.13 (2012), p. 13769. DOI: 10.1364/oe.20.013769 (cit. on p. 42).

[93] Wolfgang Hänsel, Heinar Hoogland, Michele Giunta, Sebastian Schmid, Tilo Steinmetz, Ralf Doubek, Peter Mayer, Sven Dobner, Carsten Cleff, Marc Fischer, and Ronald Holzwarth. «All polarization-maintaining fiber laser architecture for robust femtosecond pulse generation». In: *Appl. Phys. B* 123.1 (2017). DOI: 10.1007/s00340-016-6598-2 (cit. on p. 42).

[94] H. R. Telle, B. Lipphardt, and J. Stenger. «Kerr-lens, mode-locked lasers as transfer oscillators for optical frequency measurements». In: *Appl. Phys. B* 74.1 (2002), pp. 1–6. DOI: 10.1007/s003400100735 (cit. on p. 42).

[95] Christopher J. Foot. *Atomic Physics*. Ed. by Oxford University Press. 2005 (cit. on pp. 44, 45).

[96] Martin M. Boyd, Tanya Zelevinsky, Andrew D. Ludlow, Sebastian Blatt, Thomas Zanon-Willette, Seth M. Foreman, and Jun Ye. «Nuclear spin effects in optical lattice clocks». In: *Phys. Rev. A* 76.2 (2007). DOI: 10.1103/PhysRevA.76.022510 (cit. on pp. 43, 44, 46).

[97] B. H. Bransden and C. J. Joachain. *Physics of atoms and molecules*. Ed. by Longman Scientific & Technical. 1983 (cit. on p. 44).

[98] L. Olschewski. «Determination of the nuclear magnetic moments on free ^{43}Ca-, ^{87}Sr-, ^{135}Ba-, ^{137}Ba-, ^{171}Yb-, und ^{173}Yb-Atoms by means of optical pumping». In: *Z. Physik* 249.3 (1972), pp. 205–227. DOI: 10.1007/BF01400226 (cit. on p. 44).

[99] N. D. Lemke. «Optical Lattice Clock with Spin-1/2 Ytterbium Atoms». PhD thesis. University of Colorado, 2012 (cit. on p. 45).

[100] T. Kobayashi, D. Akamatsu, Y. Hisai, T. Tanabe, H. Inaba, T. Suzuyama, F. Hong, K. Hosaka, and M. Yasuda. «Uncertainty evaluation of an ^{171}Yb optical lattice clock at NMIJ». In: *IEEE Trans. Ultrason. Ferroelectr. Freq. Control* (2018). DOI: 10.1109/TUFFC.2018.2870937 (cit. on pp. 45, 50, 51, 73).

[101] Masao Takamoto, Feng-Lei Hong, Ryoichi Higashi, Yasuhisa Fujii, Michito Imae, and Hidetoshi Katori. «Improved Frequency Measurement of a One-Dimensional Optical Lattice Clock with a Spin-Polarized Fermionic 87Sr Isotope». In: *J. Phys. Soc. Jpn.* 75.10 (2006), p. 104302. DOI: 10.1143/JPSJ.75.104302 (cit. on p. 46).

[102] M. V. Romalis and E. N. Fortson. «Zeeman frequency shifts in an optical dipole trap used to search for an electric-dipole moment». In: *Phys. Rev. A* 59.6 (1999), pp. 4547–4558. DOI: 10.1103/physreva.59.4547 (cit. on p. 48).

[103] C. Shi, J.-L. Robyr, U. Eismann, M. Zawada, L. Lorini, R. Le Targat, and J. Lodewyck. «Polarizabilities of the ^{87}Sr clock transition». In: *Phys. Rev. A* 92.1 (2015). DOI: 10.1103/physreva.92.012516 (cit. on p. 48).

[104] N. D. Lemke, A. D. Ludlow, Z. W. Barber, T. M. Fortier, S. A. Diddams, Y. Jiang, S. R. Jefferts, T. P. Heavner, T. E. Parker, and C. W. Oates. «Spin-1/2 Optical Lattice Clock». In: *Phys. Rev. Lett.* 103.6 (6 Aug. 2009), p. 063001. DOI: 10.1103/PhysRevLett.103.063001 (cit. on pp. 50, 65, 85, 86, 120).

[105] C. Cohen-Tannoudji and D. Guéry-Odelin. *Advanced in Atomic Physics: An Overview*. World Scientific, Sept. 2011. DOI: 10.1142/9789812774989_0001 (cit. on p. 52).

[106] Pierre Lemonde and Peter Wolf. «Optical lattice clock with atoms confined in a shallow trap». In: *Phys. Rev. A* 72 (3 Sept. 2005), p. 033409. DOI: 10.1103/PhysRevA.72.033409 (cit. on p. 56).

[107] Andrei Derevianko and Hidetoshi Katori. «*Colloquium* : Physics of optical lattice clocks». In: *Rev. Mod. Phys.* 83 (2 May 2011), pp. 331–347. DOI: 10.1103/RevModPhys.83.331 (cit. on p. 57).

[108] Z. W. Barber, J. E. Stalnaker, N. D. Lemke, N. Poli, C. W. Oates, T. M. Fortier, S. A. Diddams, L. Hollberg, C. W. Hoyt, A. V. Taichenachev, and V. I. Yudin. «Optical Lattice Induced Light Shifts in an Yb Atomic Clock». In: *Phys. Rev. Lett.* 100.10 (10 Mar. 2008), p. 103002. DOI: 10.1103/PhysRevLett.100.103002 (cit. on pp. 57, 72, 73).

[109] V. D. Ovsiannikov, V. G. Pal'chikov, A. V. Taichenachev, V. I. Yudin, and Hidetoshi Katori. «Multipole, nonlinear, and anharmonic uncertainties of clocks of Sr atoms in an optical lattice». In: *Phys. Rev. A* 88.1 (July 2013). DOI: 10.1103/PhysRevA.88.013405 (cit. on pp. 57, 59).

[110] Hidetoshi Katori, V. D. Ovsiannikov, S. I. Marmo, and V. G. Palchikov. «Strategies for reducing the light shift in atomic clocks». In: *Phys. Rev. A* 91 (5 May 2015), p. 052503. DOI: 10.1103/PhysRevA.91.052503 (cit. on pp. 57, 58, 133).

[111] Asbjörn Arvad Jörgensen. «Characterizing the lattice induced light shifts of the Ytterbium optical lattice clock». MA thesis. University of Copenhagen, 2017. eprint: https://ultracold-atoms.nbi.ku.dk/research/theses_conference/ (cit. on p. 58).

[112] Nils Nemitz, Takuya Ohkubo, Masao Takamoto, Ichiro Ushijima, Manoj Das, Noriaki Ohmae, and Hidetoshi Katori. «Frequency ratio of Yb and Sr clocks with 5×10^{-17} uncertainty at 150 seconds averaging time». In: *Nat. Photonics* 10.4 (Nov. 2016), pp. 258–261. DOI: 10.1038/nphoton.2016.20. arXiv: 1601.04582 [physics.atom-ph] (cit. on pp. 65, 73, 120, 128, 129).

[113] Huidong Kim, Myoung-Sun Heo, Won-Kyu Lee, Chang Yong Park, Hyun-Gue Hong, Sang-Wook Hwang, and Dai-Hyuk Yu. «Improved absolute frequency measurement of the 171 Yb optical lattice clock at KRISS relative to the SI second». In: *Jpn. J. Appl. Phys.* 56.5 (Mar. 2017), p. 050302. DOI: 10.7567/jjap.56.050302 (cit. on pp. 65, 120).

[114] Marco Pizzocaro, Pierre Thoumany, Benjamin Rauf, Filippo Bregolin, Gianmaria Milani, Cecilia Clivati, Giovanni A. Costanzo, Filippo Levi, and Davide Calonico. «Absolute frequency measurement of the $^1S_0$ - $^3P_0$ transition of ^{171}Yb». In: *Metrologia* 54.1 (Jan. 2017), pp. 102–112. DOI: 10.1088/1681-7575/aa4e62 (cit. on pp. 65, 70, 73, 119, 120, 122, 124, 134, 137).

[115] Qi Gao, Min Zhou, Chengyin Han, Shangyan Li, Shuang Zhang, Yuan Yao, Bo Li, Hao Qiao, Di Ai, Ge Lou, Mengya Zhang, Yanyi Jiang, Zhiyi Bi, Longsheng Ma, and Xinye Xu. «Systematic evaluation of a ^{171}Yb optical clock by synchronous comparison between two lattice systems». In: *Sci. Rep.* 8.8022 (May 2018). DOI: 10.1038/s41598-018-26365-w (cit. on p. 65).

[116] Anders Brusch, Rodolphe Le Targat, Xavier Baillard, Mathilde Fouché, and Pierre Lemonde. «Hyperpolarizability Effects in a Sr Optical Lattice Clock». In: *Phys. Rev. Lett.* 96.10 (2006). DOI: 10.1103/PhysRevLett.96.103003 (cit. on pp. 72, 90).

[117] Zeb Barber. «Ytterbium Optical Lattice Clock». PhD thesis. University of Colorado, 2007 (cit. on p. 72).

[118] M. McDonald, B. H. McGuyer, G. Z. Iwata, and T. Zelevinsky. «Thermometry via Light Shifts in Optical Lattices». In: *Phys. Rev. Lett.* 114.2 (2015). DOI: 10.1103/physrevlett.114.023001 (cit. on p. 72).

[119] S. G. Porsev, Yu. G. Rakhlina, and M. G. Kozlov. «Electric-dipole amplitudes, lifetimes, and polarizabilities of the low-lying levels of atomic ytterbium». In: *Phys. Rev. A* 60.4 (Oct. 1999), pp. 2781–2785. DOI: 10.1103/PhysRevA.60.2781 (cit. on p. 76).

[120] Y. Takasu, K. Komori, K. Honda, M. Kumakura, T. Yabuzaki, and Y. Takahashi. «Photoassociation Spectroscopy of Laser-Cooled Ytterbium Atoms». In: *Phys. Rev. Lett.* 93 (12 2004), p. 123202. DOI: 10.1103/PhysRevLett.93.123202 (cit. on p. 76).

[121] S. Falke, M. Misera, U. Sterr, and C. Lisdat. «Delivering pulsed and phase stable light to atoms of an optical clock». In: *Appl. Phys. B* 107.2 (Mar. 2012), pp. 301–311. ISSN: 1432-0649. DOI: 10.1007/s00340-012-4952-6 (cit. on pp. 79, 113).

[122] J. A. Sherman, N. D. Lemke, N. Hinkley, M. Pizzocaro, R. W. Fox, A. D. Ludlow, and C. W. Oates. «High-Accuracy Measurement of Atomic Polarizability in an Optical Lattice Clock». In: *Phys. Rev. Lett.* 108 (15 Apr. 2012), p. 153002. DOI: 10.1103/PhysRevLett.108.153002 (cit. on p. 87).

[123] E. J. Angstmann, V. A. Dzuba, and V. V. Flambaum. «Frequency shift of hyperfine transitions due to blackbody radiation». In: *Phys. Rev. A* 74 (2 Aug. 2006), p. 023405. DOI: 10.1103/PhysRevA.74.023405 (cit. on p. 87).

[124] K. Beloy, N. Hinkley, N. B. Phillips, J. A. Sherman, M. Schioppo, J. Lehman, A. Feldman, L. M. Hanssen, C. W. Oates, and A. D. Ludlow. «Atomic Clock with 1×10^{-18} Room-Temperature Blackbody Stark Uncertainty». In: *Phys. Rev. Lett.* 113 (26 Dec. 2014), p. 260801. DOI: 10.1103/PhysRevLett.113.260801 (cit. on pp. 87, 90).

[125] K. Beloy, J. A. Sherman, N. D. Lemke, N. Hinkley, C. W. Oates, and A. D. Ludlow. «Determination of the $5d6s\ ^3D_1$ state lifetime and blackbody-radiation clock shift in Yb». In: *Phys. Rev. A* 86.5 (5 Nov. 2012), p. 051404. DOI: 10.1103/PhysRevA.86.051404 (cit. on p. 87).

[126] T. L. Nicholson, S. L. Campbell, R. B. Hutson, G. E. Marti, B. J. Bloom, R. L. McNally, W. Zhang, M. D. Barrett, M. S. Safronova, G. F. Strouse, W. L. Tew, and J. Ye. «Systematic evaluation of an atomic clock at 2×10^{-18} total uncertainty». In: *Nat. Commun.* 6 (Apr. 2015), p. 6896. DOI: 10.1038/ncomms7896 (cit. on pp. 90, 96).

[127] Kurt Gibble and Boudewijn J. Verhaar. «Eliminating cold-collision frequency shifts». In: *Phys. Rev. A* 52.4 (Oct. 1995), pp. 3370–3373. DOI: 10.1103/PhysRevA.52.3370 (cit. on p. 90).

[128] B. DeMarco, J. L. Bohn, J. P. Burke, M. Holland, and D. S. Jin. «Measurement of p-Wave Threshold Law Using Evaporatively Cooled Fermionic Atoms». In: *Phys. Rev. Lett.* 82.21 (May 1999), pp. 4208–4211. DOI: 10.1103/PhysRevLett.82.4208 (cit. on p. 91).

[129] A. M. Rey, A. V. Gorshkov, and C. Rubbo. «Many-Body Treatment of the Collisional Frequency Shift in Fermionic Atoms». In: *Physical Review Letters* 103.26 (Dec. 2009). DOI: 10.1103/PhysRevLett.103.260402 (cit. on p. 91).

[130] M. J. Martin, M. Bishof, M. D. Swallows, X. Zhang, C. Benko, J. von Stecher, A. V. Gorshkov, A. M. Rey, and J. Ye. «A Quantum Many-Body Spin System in an Optical Lattice Clock». In: *Science* 341.6146 (Aug. 2013), pp. 632–636. DOI: 10.1126/science.1236929 (cit. on p. 91).

[131] M. Bishof, Y. Lin, M. D. Swallows, A. V. Gorshkov, J. Ye, and A. M. Rey. «Resolved Atomic Interaction Sidebands in an Optical Clock Transition». In: *Phys. Rev. Lett.* 106.25 (June 2011). DOI: 10.1103/PhysRevLett.106.250801 (cit. on p. 91).

[132] Ryotatsu Yanagimoto, Nils Nemitz, Filippo Bregolin, and Hidetoshi Katori. «Decomposed description of Ramsey spectra under atomic interactions». In: *Phys. Rev. A* 98.1 (July 2018), p. 012704. DOI: 10.1103/PhysRevA.98.012704 (cit. on p. 91).

[133] N. D. Lemke, J. von Stecher, J. A. Sherman, A. M. Rey, C. W. Oates, and A. D. Ludlow. «p-Wave Cold Collisions in an Optical Lattice Clock». In: *Phys. Rev. Lett.* 107 (10 Aug. 2011), p. 103902. DOI: 10.1103/PhysRevLett.107.103902 (cit. on pp. 91, 92, 95).

[134] G. K. Campbell, M. M. Boyd, J. W. Thomsen, M. J. Martin, S. Blatt, M. D. Swallows, T. L. Nicholson, T. Fortier, C. W. Oates, S. A. Diddams, N. D. Lemke, P. Naidon, P. Julienne, Jun Ye, and A. D. Ludlow. «Probing Interactions Between Ultracold Fermions». In: *Science* 324.5925 (Apr. 2009), pp. 360–363. ISSN: 0036-8075. DOI: 10.1126/science.1169724. eprint: http://science.sciencemag.org/content/324/5925/360.full.pdf (cit. on p. 91).

[135] Masao Takamoto and Hidetoshi Katori. «Coherence of Spin-Polarized Fermions Interacting with a Clock Laser in a Stark-Shift-Free Optical Lattice». In: *J. Phys. Soc. Jpn.* 78.1 (Jan. 2009), p. 013301. DOI: 10.1143/JPSJ.78.013301. arXiv: arXiv:0901.1526 [physics.atom-ph] (cit. on p. 91).

[136] Sangkyung Lee, Chang Yong Park, Won-Kyu Lee, and Dai-Hyuk Yu. «Cancellation of collisional frequency shifts in optical lattice clocks with Rabi spectroscopy». In: *New J. Phys.* 18.3 (2016), p. 033030. DOI: 10.1088/1367-2630/18/3/033030 (cit. on p. 92).

[137] Sören Dörscher, Roman Schwarz, Ali Al-Masoudi, Stephan Falke, Uwe Sterr, and Christian Lisdat. «Lattice-induced photon scattering in an optical lattice clock». In: *Phys. Rev. A* 97.6 (June 2018), p. 063419. DOI: 10.1103/PhysRevA.97.063419 (cit. on p. 98).

[138] T. A. Savard, K. M. O'Hara, and J. E. Thomas. «Laser-noise-induced heating in far-off resonance optical traps». In: *Phys. Rev. A* 56.2 (1997), R1095–R1098. DOI: 10.1103/PhysRevA.56.R1095 (cit. on pp. 101, 103).

[139] Kurt Gibble. «Scattering of Cold-Atom Coherences by Hot Atoms: Frequency Shifts from Background-Gas Collisions». In: *Phys. Rev. Lett.* 110 (18 May 2013), p. 180802. DOI: 10.1103/PhysRevLett.110.180802 (cit. on p. 101).

[140] S. G. Porsev, M. S. Safronova, A. Derevianko, and Charles W. Clark. «Long-range interaction coefficients for ytterbium dimers». In: *Phys. Rev. A* 89.1 (Jan. 2014), p. 012711. DOI: 10.1103/PhysRevA.89.012711 (cit. on pp. 102, 110).

[141] K. Enomoto, M. Kitagawa, K. Kasa, S. Tojo, and Y. Takahashi. «Determination of the s-Wave Scattering Length and the C_6 van der Waals Coefficient of ^{174}Yb via Photoassociation Spectroscopy». In: *Phys. Rev. Lett.* 98 (20 May 2007), p. 203201. DOI: 10.1103/PhysRevLett.98.203201 (cit. on p. 102).

[142] Masaaki Kitagawa, Katsunari Enomoto, Kentaro Kasa, Yoshiro Takahashi, Roman Ciuryło, Pascal Naidon, and Paul S. Julienne. «Two-color photoassociation spectroscopy of ytterbium atoms and the precise determinations ofs-wave scattering lengths». In: *Phys. Rev. A* 77.1 (2008), p. 012719. DOI: 10.1103/PhysRevA.77.012719 (cit. on p. 102).

[143] M. G. Tarallo, D. Calonico, F. Levi, M. Barbiero, G. Lamporesi, and G. Ferrari. «A strontium optical lattice clock apparatus for precise frequency metrology and beyond». In: *2017 Joint Conference of the European Frequency and Time Forum and IEEE International Frequency Control Symposium (EFTF/IFCS)*. July 2017, pp. 748–750. DOI: 10.1109/FCS.2017.8089020 (cit. on p. 102).

[144] Joint Committee for Guides in Metrology (JCGM). *JCGM 101:2008 Evaluation of measurement data - Supplement 1 to the Guide to the expression of uncertainty in measurement (GUM)*. 2008. eprint: https://www.bipm.org/utils/common/documents/jcgm/JCGM_101_2008_E.pdf (cit. on p. 110).

[145] P. A. Williams, W. C. Swann, and N. R. Newbury. «High-stability transfer of an optical frequency over long fiber-optic links». In: *J. Opt. Soc. Am. B* 25.8 (2008), p. 1284. DOI: 10.1364/josab.25.001284 (cit. on p. 111).

[146] Bernhard Hofmann-Wellenhof and Helmut Moritz. *Physical Geodesy*. Springer-Verlag KG, Aug. 28, 2006. ISBN: 3211335447 (cit. on p. 116).

[147] Erwin Groten. «Report of Special Commission 3 of IAG». In: *International Astronomical Union Colloquium* 180 (2000), pp. 337–352. DOI: 10.1017/s0252921100000488 (cit. on p. 117).

[148] H. S. Margolis, R. M. Godun, P. Gill, L. A. M. Johnson, S. L. Shemar, P. B. Whibberley, D. Calonico, F. Levi, L. Lorini, M. Pizzocaro, et al. «International Timescales with Optical Clocks (ITOC)». In: *2013 Joint European Frequency and Time Forum & International Frequency Control Symposium (EFTF/IFC)*. IEEE. Institute of Electrical and Electronics Engineers (IEEE), July 2013, pp. 908–911. DOI: 10.1109/eftf-ifc.2013.6702183 (cit. on p. 117).

[149] Takuya Kohno, Masami Yasuda, Kazumoto Hosaka, Hajime Inaba, Yoshiaki Nakajima, and Feng-Lei Hong. «One-Dimensional Optical Lattice Clock with a Fermionic 171 Yb Isotope». In: *Appl. Phys. Express* 2.7 (2009), p. 072501. DOI: https://doi.org/10.1143/APEX.2.072501 (cit. on p. 120).

[150] Masami Yasuda, Hajime Inaba, Takuya Kohno, Takehiko Tanabe, Yoshiaki Nakajima, Kazumoto Hosaka, Daisuke Akamatsu, Atsushi Onae, Tomonari Suzuyama, Masaki Amemiya, and Feng-Lei Hong. «Improved Absolute Frequency Measurement of the ^{171}Yb Optical Lattice Clock towards a Candidate for the Redefinition of the Second». In: *Appl. Phys. Express* 5.10 (Sept. 2012), p. 102401. DOI: 10.1143/APEX.5.102401 (cit. on p. 120).

[151] Chang Yong Park, Dai-Hyuk Yu, Won-Kyu Lee, Sang Eon Park, Eok Bong Kim, Sun Kyung Lee, Jun Woo Cho, Tai Hyun Yoon, Jongchul Mun, Sung Jong Park, Taeg Yong Kwon, and Sang-Bum Lee. «Absolute frequency measurement of $^{1}S_{0}$ (F=1/2) $^{3}P_{0}$ (F=1/2) transition of ^{171}Yb atoms in a one-dimensional optical lattice at KRISS». In: *Metrologia* 50.2 (Feb. 2013), pp. 119–128. DOI: 10.1088/0026-1394/50/2/119 (cit. on p. 120).

[152] Daisuke Akamatsu, Masami Yasuda, Hajime Inaba, Kazumoto Hosaka, Takehiko Tanabe, Atsushi Onae, and Feng-Lei Hong. «Frequency ratio measurement of ^{171}Yb and ^{87}Sr optical lattice clocks». In: *Opt. Express* 22.7 (Apr. 2014). erratum 22, 32199–32199 (2014), pp. 7898–7905. DOI: 10.1364/OE.22.007898 (cit. on pp. 120, 128).

[153] Masao Takamoto, Ichiro Ushijima, Manoj Das, Nils Nemitz, Takuya Ohkubo, Kazuhiro Yamanaka, Noriaki Ohmae, Tetsushi Takano, Tomoya Akatsuka, Atsushi Yamaguchi, and Hidetoshi Katori. «Frequency ratios of Sr, Yb, and Hg based optical lattice clocks and their applications». In: *C. R. Phys.* 16.5 (2015). The measurement of time / La mesure du temps, pp. 489–498. ISSN: 1631-0705. DOI: 10.1016/j.crhy.2015.04.003 (cit. on pp. 120, 128).

[154] Jacopo Grotti, Silvio Koller, Stefan Vogt, Sebastian Häfner, Uwe Sterr, Christian Lisdat, Heiner Denker, Christian Voigt, Ludger Timmen, Antoine Rolland, Fred N. Baynes, Helen S. Margolis, Michel Zampaolo, Pierre Thoumany, Marco Pizzocaro, Benjamin Rauf, Filippo Bregolin, Anna Tampellini, Piero Barbieri, Massimo Zucco, Giovanni A. Costanzo, Cecilia Clivati, Filippo Levi, and Davide Calonico. «Geodesy and metrology with a transportable optical clock». In: *Nat. Phys.* 14.5 (Feb. 2018), pp. 437–441. DOI: 10.1038/s41567-017-0042-3 (cit. on pp. 120, 126–128, 138).

[155] Daisuke Akamatsu, Takumi Kobayashi, Yusuke Hisai, Takehiko Tanabe, Kazumoto Hosaka, Masami Yasuda, and Feng-Lei Hong. «Dual-mode operation of an optical lattice clock using strontium and ytterbium atoms». In: *IEEE Trans. Ultrason. Ferroelectr. Freq. Control* 65.6 (Mar. 2018), pp. 1069–1075. DOI: 10.1109/TUFFC.2018.2819888 (cit. on pp. 120, 128).

[156] M. Fujieda, S.-H. Yang, T. Gotoh, S.-W. Hwang, H. Hachisu, H. Kim, Y. K. Lee, R. Tabuchi, T. Ido, W.-K. Lee, M.-S. Heo, C. Y. Park, D.-H. Yu, and G. Petit. «Advanced Satellite-based Frequency Transfer at the 10^{-16} Level». In: *IEEE Trans. Ultrason. Ferroelectr. Freq. Control* 65.6 (June 2018), pp. 973–978. DOI: 10.1109/TUFFC.2018.2821159 (cit. on pp. 120, 128).

[157] *CIPM Recommended value: STRONTIUM 87 ATOM*. 2018. eprint: https://www.bipm.org/utils/common/pdf/mep/87Sr_429THz_2018.pdf (cit. on pp. 119, 120, 128).

[158] *CIPM Recommended value: YTTERBIUM 171 ATOM*. 2018. eprint: https://www.bipm.org/utils/common/pdf/mep/171Yb_518THz_2018.pdf (cit. on pp. 119, 120, 128).

[159] G. Kramer and W. Klische. «Extra high precision digital phase recorder». In: *18th European Frequency and Time Forum (EFTF 2004)*. IEE, 2004. DOI: 10.1049/cp:20040935 (cit. on p. 120).

[160] Jacopo Grotti. «A transportable optical lattice clock for metrology and geodesy». PhD thesis. Hannover : Gottfried Wilhelm Leibniz Universität, 2018. DOI: 10.15488/3480. eprint: https://www.repo.uni-hannover.de/handle/123456789/3510 (cit. on pp. 125, 128).

[161] S. B. Koller, J. Grotti, St. Vogt, A. Al-Masoudi, S. Dörscher, S. Häfner, U. Sterr, and Ch. Lisdat. «Transportable Optical Lattice Clock with 7×10^{-17} Uncertainty». In: *Phys. Rev. Lett.* 118.7 (Feb. 2017), p. 073601. DOI: 10.1103/PhysRevLett.118.073601 (cit. on pp. 125, 128).

[162] Fritz Riehle. «Optical clock networks». In: *Nat. Photonics* 11.1 (2017), pp. 25–31. DOI: 10.1038/nphoton.2016.235 (cit. on p. 125).

[163] Jörn Stenger, Harald Schnatz, Christian Tamm, and Harald R. Telle. «Ultraprecise Measurement of Optical Frequency Ratios». In: *Phys. Rev. Lett.* 88.7 (2002). DOI: 10.1103/physrevlett.88.073601 (cit. on p. 126).

[164] Steven T. Cundiff and Jun Ye. «*Colloquium* : Femtosecond optical frequency combs». In: *Rev. Mod. Phys.* 75 (1 Mar. 2003), pp. 325–342. DOI: 10.1103/RevModPhys.75.325 (cit. on p. 126).

[165] M. Giunta, W. Hänsel, M. Fischer, M. Lezius, and R. Holzwarth. «Simultaneous spectral purity transfer at three optical clock transitions using an ultra-low noise Er:Fiber frequency comb». In: *2017 Joint Conference of the European Frequency and Time Forum and IEEE International Frequency Control Symposium (EFTF/IFC)*. IEEE, 2017. DOI: 10.1109/FCS.2017.8089032 (cit. on p. 131).

[166] D. A. Howe. «An extension of the Allan variance with increased confidence at long term». In: *Proceedings of the 1995 IEEE International Frequency Control Symposium (49th Annual Symposium)*. IEEE, 1995. DOI: 10.1109/FREQ.1995.483917 (cit. on p. 131).

This Ph.D. thesis has been typeset by means of the TEX-system facilities. The typesetting engine was pdfLATEX. The document class was `toptesi`, by Claudio Beccari, with option `tipotesi=scudo`. This class is available in every up-to-date and complete TEX-system installation.